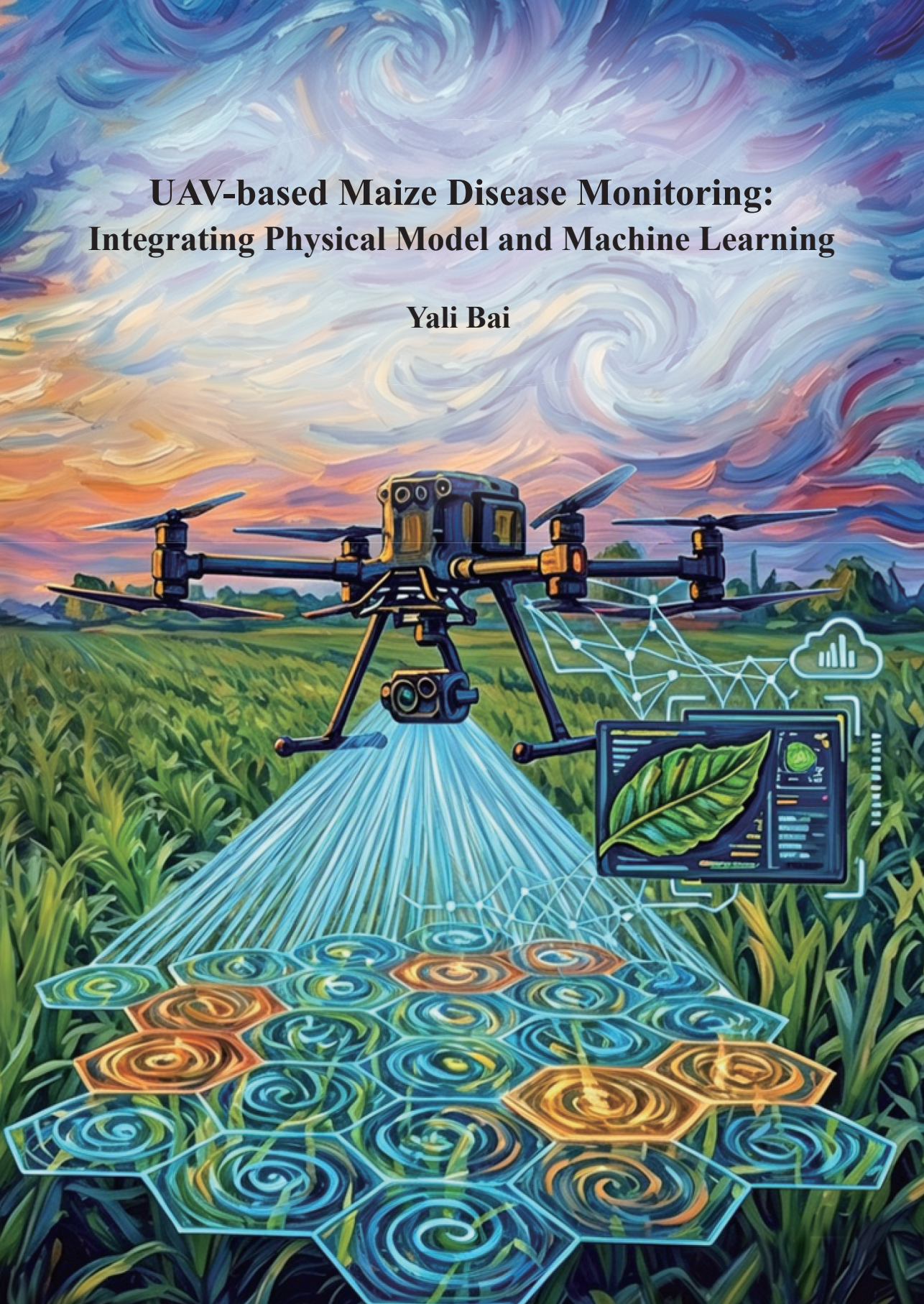
UAV-based Maize Disease Monitoring: Integrating Physical Model and Machine Learning

Yali Bai



Propositions

1. Physical models and deep learning are complementary tools for UAV-based crop disease monitoring. (this thesis)
2. Standardized feature selection improves the reproducibility and robustness of hyperspectral disease monitoring. (this thesis)
3. Generative AI's inability to ask original questions prevents it from ever replacing scientists.
4. The academic demand for hyper-specialization kills scientific creativity.
5. Perfect AI companions will destroy our ability to connect with real humans.
6. Social media platforms are designed to profit from user anxiety rather than user happiness.

Propositions belonging to the thesis, entitled
UAV-based Maize Disease Monitoring: Integrating Physical Model and Machine Learning

Yali Bai
Wageningen, June 3, 2026

UAV-based Maize Disease Monitoring: Integrating Physical Model and Machine Learning

Yali Bai

Thesis committee

Promotors
Prof. Dr Bedir Tekinerdogan
Professor of Information Technology
Wageningen University & Research

Prof. Dr Xiuliang Jin
Professor in Crop Phenomics Innovation
Institute of Crop Sciences, CAAS, Beijing, China

Co-promotor
Dr Qingzhi Liu
Assistant Professor of Information Technology
Wageningen University & Research

Other members
Prof. Dr Sytze de Bruin, Wageningen University & Research
Dr Gerrit Polder, Wageningen University & Research
Dr Estefanía Talavera Martínez, University of Twente, Enschede
Dr Yijian Zeng, University of Twente, Enschede

This research was conducted under the auspices of the Wageningen School of Social Sciences.

UAV-based Maize Disease Monitoring: Integrating Physical Model and Machine Learning

Yali Bai

Thesis

Submitted in fulfilment of the requirements for the degree of doctor
at Wageningen University
by the authority of the Rector Magnificus,
Prof. Dr C. Kroeze,
in the presence of the
Thesis Committee appointed by the Academic Board
to be defended in public
on Wednesday 3 June 2026
at time 1 p.m. in the Omnia Auditorium.

Yali Bai
UAV-based Maize Disease Monitoring: Integrating Physical Model and Machine Learning, 196 pages.

PhD thesis, Wageningen University, Wageningen, the Netherlands (2026)
With references, with summary in English
https://doi.org/10.18174/682139

Contents

Chapter 1: Introduction	1
Chapter 2: Hyperspectral Remote Sensing for Monitoring Crop Disease: Applications, Challenges, and Perspectives	9
Chapter 3: A novel disease sensitive index (DSI) for monitoring early maize leaf disease using PROSPECT-D and LESS models	37
Chapter 4: Comprehensive analysis of hyperspectral features for monitoring canopy maize leaf spot disease	63
Chapter 5: Physical model-guided deep learning (PGDL) for enhanced monitoring of maize leaf spot disease	91
Chapter 6: A synergistic UAV-driven deep learning and epidemic modeling framework for dynamic spatiotemporal prediction of maize leaf spot	123
Chapter 7: Conclusion	149
References	161
Summary	185
Acknowledgment	189
Short biography	191
Publications	193

1

Introduction

1.1 Food production and crop disease

One of the most pressing challenges today is answering the question, 'How to feed the world?', as outlined in the sustainable food and home food and agriculture by FAO in 2021. This challenge is particularly significant given that the global population is expected to reach 9.8 billion by 2050 (Leong et al., 2018). To meet this demand, global food production must increase by 70% to ensure nutritional security, accommodate changing diets, and support the rising need for biological products in sectors such as construction and energy (Galieni et al., 2021). In parallel, agriculture's environmental impact must be minimized to safeguard vital resources—water, climate, soil, and biodiversity—while reducing production risks for farmers (Gomiero et al., 2011). Climate change exacerbates these challenges, as extreme weather events and shifts in precipitation and temperature patterns are expected to become more frequent globally (Cogato et al., 2019). This will increase the frequency of abiotic stresses (e.g., heat and drought) and biotic stresses (e.g., diseases and pests), and their combinations (Govender et al., 2009), ultimately threatening crop productivity. Without swift and effective management strategies, these stresses will lead to significant yield losses (Atzberger, 2013). Therefore, early detection of crop stress is crucial to implementing appropriate agrotechnical solutions and minimizing yield losses.

Globally, crop losses due to pathogens—including oomycetes, viruses, bacteria, and fungi—are estimated to be 16% (Oerke, 2020). Timely and accurate monitoring of crop diseases is essential to mitigate these losses. Over the past 80 years, visual disease assessments have relied on conventional disease scales. More recently, quantitative methods using high-throughput-omic technologies have enabled sensitive molecular analyses of biological systems (Llanes et al., 2018). However, these techniques are not only destructive but also time-consuming and costly, limiting their use for continuous monitoring and large-scale study (Galieni et al., 2021). Thus, there is an increasing need for emerging technologies that provide effective and spatially continuous monitoring solutions.

1.2 Remote sensing for monitoring crop disease

In recent decades, remote sensing studies focused on agricultural applications have seen significant increases (Weiss et al., 2020). Remote sensing offers the advantage of large-scale coverage and high revisit frequency, making it a cost-effective tool for detecting crop stress and monitoring the spatiotemporal dynamics of agricultural landscapes. Additionally, remote sensing can provide global coverage, offering valuable insights that could contribute to improving food security in developing countries (Rembold et al., 2000).

The application of remote sensing for crop disease monitoring is grounded in the principle that crop pathogens alter the way light interacts with crop leaves and canopies. As noted by Bos and Parlevliet (1995), crop diseases caused by pathogens are dynamic processes that unfold in a series of stages. Once a pathogen triggers pathogenesis, a

sequence of events often follows autonomously. During host-pathogen interactions, changes occur in crop physiology and biochemistry, influenced by the ontogenesis, nutrition, and structure of the pathogen, such as fungal species. These processes affect the crop's optical properties, which can be detected by remote sensing (Mahlein et al., 2013).

Traditionally, crop diseases have been identified based on visible symptoms such as lesions, blight, galls, tumors, cankers, wilts, rots, or damping-off, as well as pathogen-specific signs like the urediniospores of *Pucciniales* or mycelium of *Erysiphales*. However, to gain a deeper understanding of these interactions, it is essential to explore different types of crop-pathogen relationships. Crop pathogens are generally classified into biotrophs, necrotrophs, and, more recently, hemibiotrophs. As explained in phytopathology literature, biotrophs obtain nutrients from living host tissues, while necrotrophs feed on dead or dying crop cells. Some pathogens can shift between these lifestyles, depending on their developmental stage or environmental conditions (Casadevall, 2008).

The complex processes behind each crop-pathogen interaction govern the appearance and progression of disease. Remote sensing can capture the changes in reflectance caused by these processes, such as alterations in leaf structure and chemical composition during pathogenesis. For instance, changes like chlorosis and necrosis, or the emergence of fungal structures like powdery mildew *hyphae* and *conidia*, are visible indicators of disease. Each crop-pathogen system has a distinct spatial and temporal dynamic, influencing different wavelength ranges at various stages of pathogenesis (Mahlein et al., 2012; Wahabzada et al., 2016; Zhang et al., 2020). Therefore, remote sensing can effectively capture the intricate presence of pathogens and crop-pathogen interactions.

1.3 Platforms of remote sensing

Remote sensing platforms vary widely depending on the application of the different scales of, ranging from cellular and tissue levels to regional and landscape scales. In agriculture, remote sensing platforms are typically categorized into four types: laboratory-based, field-based, low-altitude-based, and large-scale platforms.

Laboratory-based remote sensing platforms are ideal for high-resolution, high-accuracy evaluations of processes during pathogenesis under controlled conditions (Thomas et al., 2018). These platforms are particularly effective at scales such as the leaf, individual crop, and canopy levels (Abdulridha et al., 2018; Oerke et al., 2016). By using time-series analysis, researchers can track pathogen progression and spectral changes throughout disease development. These platforms offer the advantage of controlled environments, making them suitable for basic research in crop breeding and resistance gene analysis. However, their low throughput and inability to scale up for practical applications limit their broader use.

Field-based remote sensing platforms, often referred to as ground phenotyping platforms, include phenopoles, phenomobiles, and stationary platforms (Jin et al.,

2021b). Phenopoles use poles, typically made of aluminum, steel, or plastic, to mount sensors for direct data collection on crop phenotyping traits (Richardson et al., 2018). Phenomobiles encompass automatic, human-driven, and tractor-pulled platforms (Comar et al., 2012). Stationary platforms, such as those equipped with RGB cameras, multispectral and hyperspectral cameras, thermal cameras, and laser sensors, are fixed-site systems designed for simultaneous, fully automated phenotyping (Virlet et al., 2016). These platforms excel in capturing high-accuracy data at both the organ and canopy scales. However, they are limited in their ability to monitor crop diseases across large areas (Liu et al., 2020c).

Low-altitude remote sensing platforms, such as manned aircraft, helicopters, unmanned aerial vehicles (UAVs), and balloons, are lightweight, cost-effective, and highly mobile. UAVs, in particular, have become a prominent tool in agricultural remote sensing due to their flexibility, ease of use, and ability to perform high-resolution, high-throughput disease detection (Huang et al., 2012b; Vanegas et al., 2018). UAVs are particularly well-suited for canopy-scale analysis, although their mixed spectra make them less suitable for detailed research on crop resistance or gene analysis. Nevertheless, their high spatial resolution and ability to quickly monitor large areas make them invaluable for practical applications in crop disease detection.

Large-scale remote sensing platforms, such as airborne and satellite systems, have been used for decades in agriculture. Satellite platforms like Sentinel-2 A/B (since 2015) and Landsat (since 2008) provide easily accessible multispectral images (Berger et al., 2022). These platforms offer wide-area coverage, making them ideal for regional-scale research and studies based on environmental factors. However, they come with limitations, including low spatial and temporal resolution, poor timeliness, and lower accuracy, which reduce their effectiveness for precise crop disease monitoring.

UAV-based remote sensing technology stands out due to its ability to rapidly and accurately monitor crop health, making it a powerful tool for precision agriculture. While large-scale platforms, like satellites, provide broad coverage, they are too coarse for detailed farm- or field-scale studies. As such, UAVs offer significant potential for intelligent agriculture by enabling scalable, efficient disease detection and management.

1.4 Research objective and strategy

The primary aim of this thesis is to explore the remote sensing mechanisms involved in crop disease detection and to develop effective methods for early disease monitoring at the canopy scale. To achieve this goal, the study addresses five core research questions:

- RQ 1: What are the current applications, challenges, and perspectives in monitoring crop diseases using hyperspectral remote sensing?
- RQ 2: Can a disease-specific index monitor early maize leaf spot?
- RQ 3: How and when do remote sensing features respond to maize leaf spot disease?
- RQ 4: Can a physical model-guided deep learning approach improve early-stage

detection of maize leaf spot by leveraging the generalization strengths of physical models?

- RQ 5: Can hyperspectral remote sensing predict maize leaf-spot disease progression in both space and time?

To answer these questions, this thesis adopts a progressive research framework. First, a comprehensive review was conducted to assess the current applications, challenges, and future perspectives in monitoring crop disease (RQ 1). Building on this, a novel disease index was developed specifically for early detection of maize leaf diseases at the canopy scale (RQ 2). To enhance the ability of hyperspectral features for disease monitoring, a detailed analysis of hyperspectral features was performed to understand how remote sensing can detect maize leaf spot disease (RQ 3). To enhance the generalization of deep learning models for disease monitoring, a novel physical model-guided deep learning approach was developed and evaluated (RQ 4). Finally, to explore the potential of hyperspectral remote sensing in predicting disease progression in both space and time, a synergistic framework was proposed, which integrates a remote-sensing-driven deep learning model with a stochastic epidemic-spread model for predicting maize leaf-spot distribution in spatiotemporal dimensions (RQ 5).

In recent years, hybrid approaches that combine physically based and data-driven models have gained increasing attention for crop stress and disease monitoring. Physically based radiative transfer models (RTMs) provide mechanistic insights into canopy–radiation interactions, while machine learning offers efficiency and predictive flexibility. Integrating these two paradigms allows models to benefit from both physical interpretability and data-driven adaptability (Verrelst et al., 2015; Verrelst et al., 2021). Building on this principle, this thesis explores four hybrid strategies for UAV-based maize disease monitoring.

First, we develop disease-specific indices based on RTM-based simulations. These indices are designed by considering the spectral response mechanisms and serve as effective features for further modeling, facilitating more accurate disease detection.

Second, we use biophysical parameters, such as chlorophyll content, retrieved from RTMs as input features for machine learning models. As disease progresses, changes in pigment concentrations are indicative of disease severity and stage, making it essential to track these dynamics over time. RTMs can retrieve pigment information across the entire wavelength range, offering complementary features to traditional vegetation indices that are calculated using only a few bands (Baret et al., 2007; Berger et al., 2018).

Third, we propose a hybrid method involving pre-training deep learning models on RTM-based simulations, followed by fine-tuning on real field data. This approach uses a physical process-based model to generate high-quality simulation datasets with a broad range of values. Deep learning models are trained on these simulation datasets and then applied to real-world field data through transfer learning, enhancing the model's adaptability to actual conditions.

Finally, we propose a synergistic framework that pairs a remote sensing–driven deep

learning model (RS–deep learning) with a stochastic epidemic spread model to predict spatiotemporal maize leaf spot. The RS–deep learning provides spatially explicit probability maps used as initial states, and the epidemic model iteratively refines these estimates; their complementary strengths enhance overall prediction performance.

1.5 Thesis outline

To reach the objectives of the thesis, several studies were conducted. The structure of the remaining chapters of this thesis is illustrated in Fig. 1.1 and detailed as follows:

Chapter 2 provides a comprehensive review of the current state-of-the-art in hyperspectral remote sensing for crop disease monitoring. It synthesizes the literature on commonly used spectral and textural features, pigment- and fluorescence-based indicators, and multimodal approaches. This review highlights the challenges in feature selection, model development, and large-scale disease surveillance, setting the stage for the subsequent studies.

Chapter 3 presents the development of a novel Disease Sensitive Index (DSI), designed to detect early maize leaf diseases while remaining relatively insensitive to variations in crop spacing and canopy structure. Through simulations using the PROSPECT-D and LESS models, the DSI is rigorously tested and validated on field datasets. The results highlight its potential as a practical, scalable tool for early disease detection, even under varying cultivation conditions.

Chapter 4 focuses on the sensitivity of hyperspectral features for monitoring canopy maize leaf spot disease. It examines how biophysical parameters, spectral reflectance features, vegetation indices, and wavelet features evolve over time and across various disease severity levels. The chapter identifies which features emerge as the earliest indicators of disease severity and evaluates their complementary value in improving detection accuracy.

Chapter 5 introduces a novel methodology—Physical Model-Guided Deep Learning (PGDL)—that integrates radiative transfer simulations with advanced neural network architectures. By comparing different simulation strategies and transfer learning approaches, this chapter demonstrates how incorporating biophysical insights improves the model's ability to generalize and perform robustly across seasons and disease stages. The PGDL framework effectively bridges the gap between physically based and data-driven methods.

Chapter 6 presents an RS-DeepSpread model, a novel Synergistic Remote Sensing-Deep Learning and Epidemic framework that integrates a remote sensing-driven deep learning with a stochastic epidemic spread model to predict the progression of maize leaf spot in both space and time. The epidemic model constrains and refines the predictions generated by the remote sensing deep-learning module. RS-DeepSpread consistently outperforms standalone deep-learning models, achieving higher accuracy and lower rates of underestimation. The Synergistic framework trained on hyperspectral imagery offers a solution for timely and spatially explicit prediction of maize leaf spot disease dynamics.

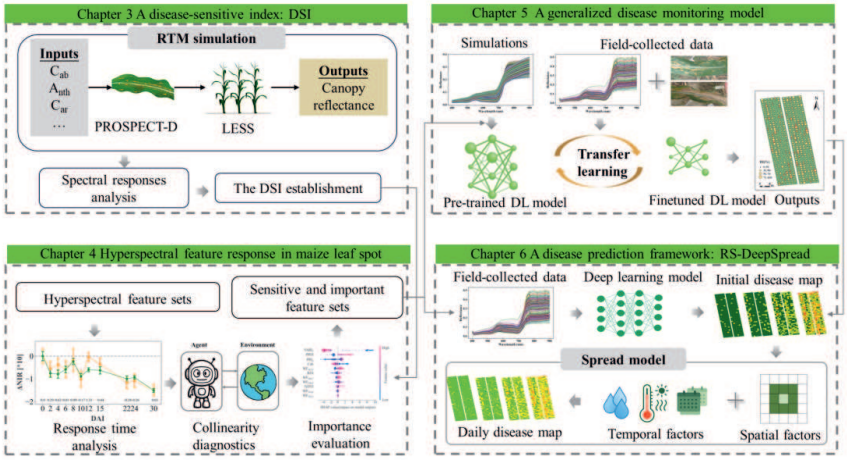


Fig. 1.1. *Overview of the research framework and chapter organization*

2

Hyperspectral Remote Sensing for Monitoring Crop Disease: Applications, Challenges, and Perspectives

This chapter is based on:
Bai, Y., Zarco-Tejada, P.J., Peñuelas, J., McCabe, M.F., Hawkesford, M.J., Atzberger, C., Poblete, T., Kumar, L., Reynolds, M.P., Nie, C. (2025). Hyperspectral Remote Sensing for Monitoring Crop Disease: Applications, challenges, and perspectives. IEEE Geoscience and Remote Sensing Magazine, 2-26
Bai, Y., Jin, X. (2024). Hyperspectral approaches for rapid and spatial plant disease monitoring. Trends in Plant Science, 29, 711-712

Abstract

Crop diseases present significant threats to global food security and agricultural sustainability. Traditional monitoring methods, reliant on visual inspections and laboratory analyses, are labor-intensive and unsuitable for large-scale implementation. Hyperspectral remote sensing has emerged as a promising tool for operational crop disease monitoring. Here we provide a broad review, starting with a hyperspectral-based description of observable symptoms of common crop diseases and then examining hyperspectral features, including spectral and textural features, pigments light absorption, solar-induced chlorophyll fluorescence, spatiotemporal information, and multimodal features. We also analyze the algorithms used for disease detection, including traditional statistical methods, machine learning, and physical-based approaches. Our findings highlight the effectiveness of these methods in distinguishing various stressors, detecting early diseases, assessing crop resistance, and monitoring large scale diseases. Based on a quantitative literature review, we summarize current research trends. Future research should emphasize integrating physical models with deep learning, ensuring sensitivity and robustness of spectral features, and promoting international data sharing.

2.1 Introduction

Crop diseases cause substantial economic damage globally, posing a serious risk to food security and agricultural sustainability (Boyd et al., 2013; Fisher et al., 2012; Paini et al., 2016). Early monitoring and assessments of crop diseases are essential for developing effective management strategies to mitigate their impact on crop productivity. Conventional methods for monitoring crop diseases primarily rely on in-situ visual inspections. This process requires a substantial number of skilled professionals, which is subjective, time-consuming, and labor-intensive. For monitoring disease objectively and rapidly, remote sensing techniques have been proposed. Remote sensing allows the collection of high spatial resolution information on large areas and rapidly analyzing a large number of crops and their related traits, which provides strong support for agricultural monitoring applications focused on food security (Martinelli et al., 2015).

Hyperspectral remote sensing, a subset of remote sensing technologies, offers high spectral resolution and has rapidly evolved into an effective tool for agricultural research (Adão et al., 2017; Baret et al., 1987; Jin et al., 2020). The hyperspectral sensors can generate a distinct spectral signature for each captured target at high spectral resolutions < 2.5 nm, consisting of reflectance measurements in hundreds of contiguous wavelength channels (Thenkabail et al., 2000). It is noted that a few commercial hand-held systems even achieve resolutions less than 1nm. Narrow wavebands of hyperspectral sensing systems explain their widespread use in phenotyping (Machwitz et al., 2021; Mishra et al., 2020). This unique property of hyperspectral remote sensing allows for high sensitivity to subtle crop changes caused by diseases, enabling the detection of various disease types and early-stage, asymptomatic infections (Zarco-Tejada et al., 2018; Zarco-Tejada et al., 2021). For instance, this technique has been widely used in monitoring root rot (Marzougui et al., 2019; Reynolds et al., 2012), leaf spot (Mahlein et al., 2010), bacterial blight (Gold et al., 2020b; Sterling and Di Rienzo, 2022) and yellow rust (Devadas et al., 2009; Ren et al., 2021a), etc.

As hyperspectral sensors and data analysis methods for crop disease monitoring have developed, numerous studies have reviewed advancements in this field from various perspectives. Mahlein et al. (2018) first explored the factors that make hyperspectral sensors more favorable for detecting crop diseases than other sensors and discussed the current interpretations of reflectance signatures from the crop-pathogen interactions. Zhang et al. (2020) provided a workflow for using hyperspectral technologies in analyzing crop diseases. Terentev et al. (2022a) analyzed the current state of hyperspectral remote sensing for the early detection of crop diseases in four types of crops, including oil palm, citrus crops, the Solanaceae (nightshade) family, and wheat. Paux et al. (2022) focused on identifying candidate genes that could be further characterized to identify relevant alleles for breeding programs. Zhu et al. (2024) highlighted the transformative potential of UAV-based remote sensing and deep

learning in crop disease and pest management. While these studies have contributed significantly to specific aspects of crop disease research, they lacked clear criteria for selecting hyperspectral features and do not provide objective assessments of future trends in the field based on quantitative literature analysis.

This review explores the capabilities of hyperspectral remote sensing features for crop disease monitoring and proposes a structured approach for selecting hyperspectral features sensitive to crop diseases. By analyzing the temporal patterns of keywords frequently used in publications related to hyperspectral sensing, we summarize the results and highlight the future challenges in monitoring crop diseases using this technology.

The remaining content of this paper is organized as follows. Section 2.2 provides an overview of the fundamental definitions and common symptoms associated with crop diseases. Section 2.3 explores a range of relevant hyperspectral features for monitoring crop diseases. Section 2.4 reviews the algorithms used in monitoring crop diseases through hyperspectral features. Section 2.5 presents several case studies demonstrating the practical application of hyperspectral monitoring in crop disease management. Section 2.6 discusses the challenges and future perspectives in utilizing hyperspectral remote sensing for disease monitoring. Finally, Section 2.7 summarizes a general overview and conclusion.

2.2 Plant disease basics

Crops are exposed to various environmental stresses, including biotic and abiotic pressures, which strongly affect their growth, development, and survival. Abiotic stresses, such as solar radiation, salinity, waterlogging, nutrient shortages, temperature extremes, and heavy metals, can affect metabolism, growth, and development (Minhas et al., 2017; Suzuki et al., 2014). In contrast, biotic stresses arise from interactions between crops and other living organisms, such as pathogens, weeds, insect pests, nematodes, protists, viruses, and viroids (Morkunas et al., 2018). For the purposes of this review, the term "crop disease" refers specifically to biotic stress, as defined in Nutter et al. (2006).

Disease responses in crops result from complex interactions between various organisms. These interactions can affect different crop components, including roots, stems, leaves, and fruits, and may have both direct and indirect impacts on crop physiology and biochemistry (Fig. 2.1A). For example, viruses can cause damage by inducing pigment degradation, structural wilting, and necrosis, which may lead to nutrient deficiencies, such as phosphorus deficiency (Chandrakar et al., 2018). Fungal pathogens have a broad diversity of effects on crops, ranging from early stimulation of photosynthesis to later reduction of photosynthetic capacity, leading to visible foliar lesions (Chang et al., 2013; Vergara-Diaz et al., 2015). The diversity of fungal pathogens can cause anthracnose, leaf spot, rust, and wilt. These symptoms can be monitored as changes in the properties of optical reflectance of the canopy (Singh et al., 2020). Microbes, such as those causing downy mildew, can also cause similar

symptoms, leading to biotic stress responses in crops. The temporal aspect of disease symptoms is also important. Short-term disease manifestations often reflect changes in photosynthesis, respiration, and transpiration rates, while long-term infections can have more persistent effects on crop growth and development (Damm et al., 2018).

Crop responses to disease are typically continuous but often exhibit nonlinear characteristics (Kranner et al., 2010). Responses to disease can be divided into three phases based on the severity and duration of the stressors. Using the case of rice leaf blast as an example, a few watery lesions (usually one or two) are initially observed in greenhouses on infected leaves. Still, these lesions are often difficult to monitor under field conditions. The mild stage of infection is characterized by several small brown spindle lesions that are easily visible on the surface of infected leaves. The foliar surface generally appears normal, except for the necrotic lesions. The stage of severe infection as the disease increases features multiple distinct fusiform plaques on the foliar surface, accompanied by wilting and yellowing around the lesions (Tian et al., 2021).

It is important to note that the same disease can produce different symptoms depending on environmental conditions and the developmental stage of the crop. As shown in Fig. S2.1, different diseases may also lead to similar symptoms. Therefore, a thorough understanding of the physiological responses of crops to specific diseases is crucial for accurate disease identification and effective mitigation strategies.

2.3 Hyperspectral features

Hyperspectral features refer to the specific spectral information extracted from hyperspectral data that can be used to identify, analyze, and classify different materials or conditions, such as crop diseases. Since the early hyperspectral work of Baret et al. (1987), numerous features have been proposed for qualitative or quantitative crop disease assessment and monitoring of crop structure and physiology changes. This review divides hyperspectral features into spectral, spatial, and bio-physical features such as pigment content and SIF (refer to Table 2.1). Other data sources that can enhance the precision of disease monitoring by supplementing hyperspectral information are also referred to as auxiliary data.

2.3.1 Spectral features

The visible (VIS) and near-infrared (NIR) spectral domains are commonly used to monitor crop diseases (Haagsma et al., 2020; Kurihara et al., 2022; Liu et al., 2020a; Sterling and Di Rienzo, 2022; Xiao et al., 2021). As can be seen from Fig. 2.1B, chlorophyll, accounting for the green color of vegetation, absorbs strongly in red (650–700 nm) and blue (400–500 nm) spectral regions and has maximum reflectance in green wavelengths (560 nm). Anthocyanins, reflecting strongly in red wavelengths, have an absorption maximum at approximately 530 nm, while the red-edge region (680–780 nm) is sensitive to changes in photosynthetic rate (Boegh et al., 2002; Cao et al., 2019) and the NIR region is sensitive to foliar and canopy structure. The SWIR region is particularly sensitive to water content in leaves and is crucial for detecting hydration changes in crops under biotic stress, as water is a key factor in the physiological

response to disease (Gold et al., 2020a; Huang et al., 2015; Meng et al., 2020).

Hyperspectral reflectance refers to an object's ability to reflect light across various wavelengths, which is captured and quantified by hyperspectral imaging sensors. Commercial hyperspectral sensors on the market have spectral capabilities that cover the entire range or selected portions of the electromagnetic spectrum between 400–2500 nm and can retrieve anywhere between 30–2000+ individual bands (Appeltans et al., 2020). Each object or material exhibits a unique reflectance pattern at specific wavelengths, forming a distinct spectral "fingerprint" that can be used to identify or differentiate between healthy pants or diseases. While hyperspectral reflectance provides rich spectral information, it is also complex to process and can be significantly influenced by environmental factors.

Table 2.1 Hyperspectral features for monitoring crop diseases

Spectral features	Advantages	Disadvantages	Related Studies
Hyperspectral reflectance **Spectrum transformation** **Wavelet features** **Vegetation indices**	Simple calculation	Poor transferability Mixed spectrum	(Gold et al., 2020b; Zhang et al., 2018)
Spatial features			
Textural features	Represents the spatial pattern	Affected by spatial resolution Requires imaging sensors	(Khan et al., 2021; Xuan et al., 2022)
Pigment concentration			
Anthocyanins **Chlorophylls** **Xanthophyll** **V+A+Z pool** **Carotenoids**	Early response Good transferability Robustness	Complexity of physically based models	(Zarco-Tejada et al., 2018; Zarco-Tejada et al., 2021)
Fluorescence emission			
Solar induced fluorescence	Early response	Weak signals High spectral resolution Lack of disease specificity	(Calderon et al., 2013; Mahlein et al., 2019)
Auxiliary data			
Vegetation temperature	Early response	Atmospheric correction issue Complex retrieval Lack of disease specificity	(Hornero et al., 2021; Mahlein et al., 2019)
Structural information	Surface penetrating	Lack of chemical information	(Yu et al., 2021a; Zhou et al., 2022)

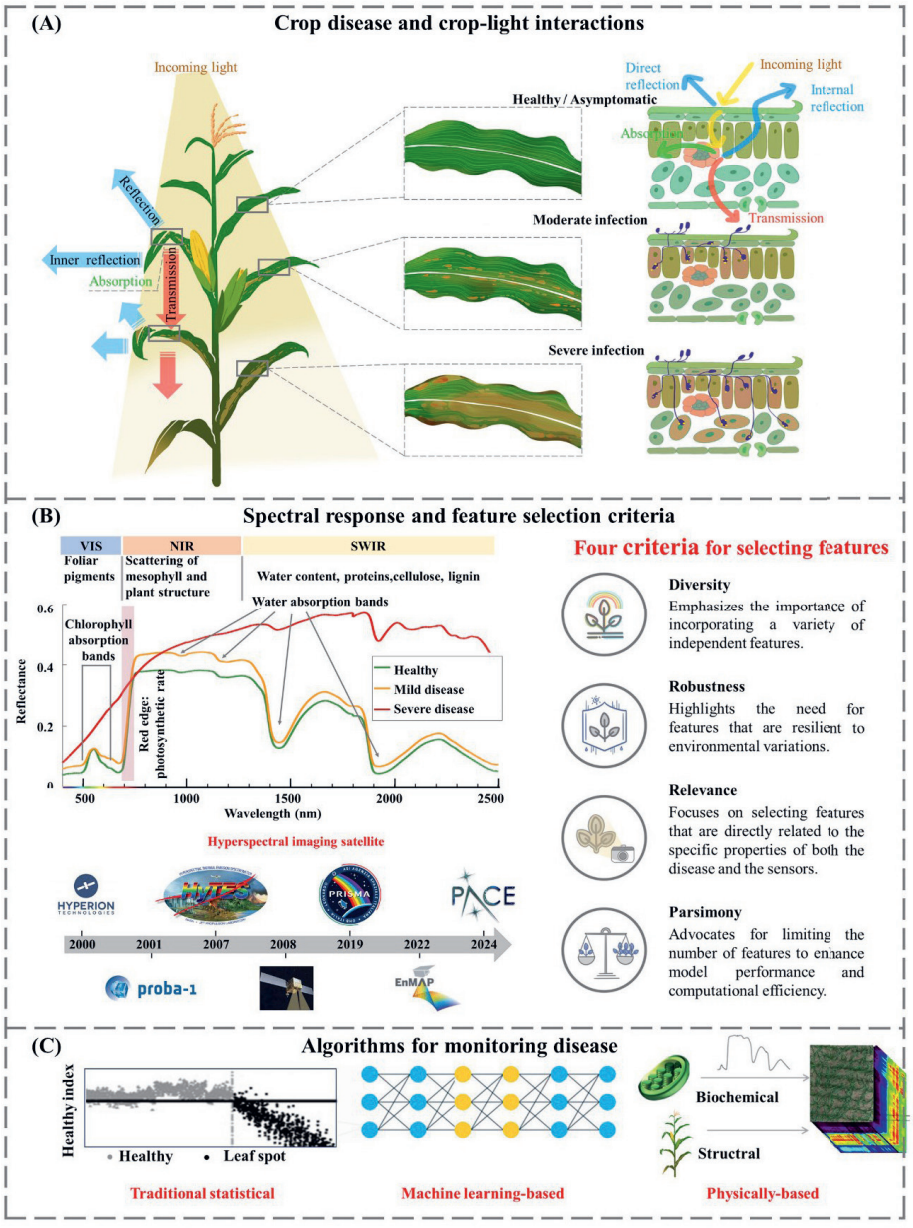


Fig. 2.1. *Comprehensive framework of remote sensing-based crop disease monitoring: from crop-disease interaction to disease feature and modeling analysis algorithms. (A) Crop-disease and crop-light interactions under different disease severity. (B) Spectral response and feature selection criteria. (C) Algorithms for monitoring disease. Note: VIS denotes visible reflectance; NIR denotes near-infrared reflectance; SWIR denotes shortwave infrared reflectance.*

Vegetation indices (VIs) have been used partly to compensate for some of these effects, widely employed to characterize crop information. Many VIs have been proposed to monitor crop biophysical, biochemical, and physiological properties since the early 1970s (Zeng et al., 2022). VIs are practical tools for monitoring diseases due to the correlations between these attributes and diseases (Table S2.1). The most basic vegetation indices are obtained from an algebraic combination of spectral reflectance (Baret and Guyot, 1991). Among these, the Photochemical Reflectance Index (PRI) is one of the most commonly used indices for quantifying spectral changes caused by disease. PRI is based on variations in xanthophyll concentration and pigment pool sizes, which allows it to effectively track light-use efficiency and photosynthetic performance (Gamon et al., 1992). Variants of PRI, such as normalized PRI (PRIn) and modified PRI, have also been widely adopted (Camino et al., 2021; Poblete et al., 2020; Zarco-Tejada et al., 2018). Additionally, several VIs sensitive to crop pigments, such as the normalized phaeophytinization index (NPQI), Vogelmann index, transformed chlorophyll absorption ratio/optimized soil adjusted vegetation index, Lichtenthaler 3, and pigment-specific normalized difference for chlorophyll a, have been employed for disease monitoring. Likewise, VIs sensitive to water content, including the water index, disease-water stress index, and normalized difference water index, have been utilized to monitor diseases caused by pathogens such as Phytophthora, downy mildew, fire blight, corn rust, wheat fusarium head blight, late blight, and early blight (Huang et al., 2021; Meng et al., 2020; Skoneczny et al., 2020). Although vegetation indices like PRI and NDSI are useful in many cases, they generally ignore the finer spectral details that hyperspectral data can offer. Thus, while these indices are practical, they are inherently sub-optimal for hyperspectral applications that require a more nuanced understanding of crop health (Berger et al., 2022).

The Red-edge Inflection Point (REIP) and three-edge parameters represent alternative vegetation indices also used to capture unique spectral characteristics of crop diseases. These indices encompass position, amplitude, and area within wavelength regions of substantial spectral variability (Broge et al., 2003; Darvishzadeh et al., 2009). For instance, Lin et al. (2020) investigated the sensitivity of 36 three-edge parameters to rice sheath blight, highlighting that the ratio index of the red-edge area to the green-peak area was the most important feature for distinguishing foliar sheath lesions from foliar blade lesions. Feng et al. (2016) demonstrated that the sum of the 1st derivatives within the blue edge was significantly correlated with the severity of wheat powdery mildew. Three-edge parameters have also been used for monitoring wheat fusarium head blight (Huang et al., 2021). While these commonly used vegetation indices can represent changes in crop health to some extent, they generally lack disease specificity. This means that they may be sensitive to various diseases, not just the target disease under study.

To monitor a particular disease, disease-specific indices are generally developed after evaluating their sensitivity to the specific symptom associated with the target disease. For example, the healthy index (HI) was created to monitor sugar beet diseases by

testing all possible combinations of a single wavelength and a normalized wavelength difference (Mahlein et al., 2013). The yellow rust spectral index was designed to estimate the severity of wheat yellow rust quantitatively (Huang et al., 2015), and the fusarium head blight classification index was developed to classify healthy and diseased areas of wheat spikelets (Zhang et al., 2019b). It would be beneficial to mention that creating such indices requires a clear understanding of the disease's spectral signature and the associated symptoms. A more direct method of building vegetation indices involves mimicking the mathematical form of classical indices and exhausting all possible band combinations. For example, Marzougui et al. (2019) calculated the normalized difference spectral indices (NDSIs) using the formula of NDVI and all combinations of wavelengths, and Meng et al. (2020) used the form of the healthy index to construct a three-band combination index. However, these disease-specific indices, derived from leaf spectral data, often do not account for the structural parameters of crops, leading to decreased accuracy when applied to canopy-level monitoring tasks (Asner and Martin, 2008). Future efforts should focus on developing robust, disease-specific indices that can be easily adapted to different crop species and environmental conditions, enabling real-time disease detection across agricultural landscapes.

Several transformations of the raw spectrum can also be applied to monitoring crop diseases, such as the derivative transformation (Chen et al., 2022a; Zhang et al., 2012b) and wavelet features (Huang et al., 2021; Huang et al., 2020; Shi et al., 2017; Zhang et al., 2018). These transformations often produce features equivalent to or even more numerous than the original reflectance data. Consequently, the sensitivity and specificity of these features to crop diseases require careful analysis.

2.3.2 Textural features

Image texture represents the distribution of pixel grayscale values and their spatial neighborhood relationships. Textural features have been applied in the detection and monitoring of various crop diseases, including wheat powdery mildew (Feng et al., 2022b; Khan et al., 2021; Xuan et al., 2022), fusarium head blight (Liu et al., 2020a; Xiao et al., 2021), and yellow rust (Guo et al., 2021a). A standard method for quantitatively describing textural features involves the construction of compelling grayscale images and the calculation of statistical properties using the gray-level co-occurrence matrix (GLCM) (Fig. S2.2). To generate compelling grayscale images, researchers have employed principal components of hyperspectral images (Xuan et al., 2022) or disease-sensitive bands (Khan et al., 2021). As a type of spatial feature, textural features can effectively monitor diseases that cause variations in leaf or canopy patterns. However, the performance of textural features is influenced by factors such as spatial resolution and the size of sliding windows used in the analysis. Addressing these challenges and optimizing the extraction and application of textural features will be critical for advancing the use of hyperspectral imaging in monitoring crop diseases.

2.3.3 Pigments light absorption

The absorption properties of crop pigments, quantitatively expressed as crop pigments concentration, are a critical indicator of crop diseases, as they reflect

symptoms such as discoloration, chlorosis, and changes in the dynamics of pigment pools (Osdaghi et al., 2020; Zarco-Tejada et al., 2018). Numerous studies have demonstrated that analyzing pigment concentration is essential for accurately detecting infected crops and distinguishing symptoms caused by pathogens from those induced by water stress. Zarco-Tejada et al. (2021) found that anthocyanin content was critical for distinguishing *Xylella fastidiosa* infections in olive trees from water-stress responses, while chlorophyll was relevant in almonds. Similarly, Poblete et al. (2021) found that carotenoid content was relevant for discriminating *Verticillium dahliae* infections from *Xylella fastidiosa* infections in olive trees, while xanthophyll-related indicators were relevant for discriminating *Xylella fastidiosa* infections. In a recent study, Poblete et al. (2023a) analyzed the progression of pigment concentration, comparing their contribution to detecting early, middle, and advanced stages of infection in a multi-date, multi-site, and multi-species assessment. They found that pigment concentrations played different roles depending on the stage of the infection. As diseases progress, changes in pigment concentrations evolve, making it crucial to monitor pigment dynamics over time to assess disease stage and severity. These pigments can be retrieved based on radiative transfer models (RTMs), which simultaneously leverage information from the entire wavelength range (Baret et al., 2007; Berger et al., 2018). Although changes in pigment concentrations are crucial physiological responses to crop diseases, inversion methods based on complex physical models may introduce errors (Wang et al., 2023b; Zhang et al., 2021).

2.3.4 Solar-induced chlorophyll fluorescence

SIF provides valuable information about photosynthetic activity, making it a crucial indicator for assessing crop health and detecting disease (Buschmann et al., 2000; Jones and Schofield, 2008; Moya and Cerovic, 2004). Several methods have been developed to quantify SIF at the foliar and canopy levels, including the Fraunhofer-line discrimination (FLD) method (Plascyk and Gabriel, 1975), RTMs (Gastellu-Etchegorry et al., 2017; van der Tol et al., 2009), spectral-fitting methods (Meroni et al., 2010), and singular vector decomposition (Yang et al., 2018). However, retrieving SIF from spectral images is challenging, as the SIF signal under natural light conditions constitutes less than 1% of the incident energy (Malenovský et al., 2009). Fortunately, recent work has shown the strong relationship between SIF quantified with subnanometer resolution (0.1–0.2 nm FWHM) and narrowband resolution (5.8 nm FWHM), showing that SIF can be tracked in relative terms, using broader resolution sensors (Belwalkar et al., 2022). This has allowed the use of SIF quantified using a broader-band imaging spectrometer to detect biotic stress with high accuracy (Poblete et al., 2020; Zarco-Tejada et al., 2018; Zarco-Tejada et al., 2021). Given the potential of SIF in disease monitoring, future research should focus on developing algorithms that can isolate SIF from other sources of variability, improving its specificity for biotic stress detection.

2.3.5 Auxiliary data

Multimodal collaboration is generally an efficient framework for monitoring crop

diseases, which must be versatile, user-friendly, and cost-effective to facilitate its integration into precision agriculture and breeding systems (Berger et al., 2022). Multimodal remote sensing data can provide a more comprehensive understanding of the complex interactions between diseases and crops. Among the most widely used data types to complement hyperspectral data for disease monitoring are thermal and LiDAR data.

1) Vegetation temperature

Vegetation temperature has proven helpful for determining transpiration rates and assessing crop health (Lu et al., 2020). Vascular pathogens colonize crop vessels, block sap flow, reduce transpiration, and increase canopy temperature (Calderon et al., 2013; Zarco-Tejada et al., 2018). Combining vegetation temperature with hyperspectral characteristics has been employed for early disease monitoring (Calderon et al., 2015; Feng et al., 2022b; Lopez-Lopez et al., 2016; Mahlein et al., 2019), discriminating pathogens with similar visual symptoms (Poblete et al., 2021), and disentangling biotic from abiotic sources of stress (Zarco-Tejada et al., 2021). Zarco-Tejada et al. (2018) conducted a pioneering study using multiple sensor acquisitions, including airborne hyperspectral and thermal data, to analyze trees experiencing early stress caused by the vector-transmitted bacterial crop pathogen *Xylella fastidiosa*. They derived indicators of vegetation temperature and the Crop Water Stress Index (CWSI) (Moran et al., 1997), estimated canopy structural and foliar biochemical traits using RTM inversion, and calculated the sensitivities of narrow-band spectral indices. All these indicators underwent multivariate analysis using machine learning algorithms to classify the pre-visual incidence and severity of the disease on a large field scale. Despite considerable advances in both satellite and UAV-based thermal sensing, challenges remain. The accuracy of thermal infrared data is often compromised by issues related to data correction. Therefore, it is a challenge to distinguish crop responses or stress from natural variability in vegetation (Stutsel et al., 2021) or the confounding effects of rapidly changing environmental conditions (Aragon et al., 2020).

2) Structural information

LiDAR technology can accurately obtain three-dimensional information about objects, enabling the precise segmentation of crops and associated shadows and vegetation overlap within crops. LiDAR information often complements spectral data by addressing the issue of spectral confusion (spectral confusion arises when different materials or objects exhibit similar spectral characteristics, making it difficult to differentiate between them based solely on spectral information). By providing precise distance measurements and detailed 3D point cloud information, LiDAR assists in overcoming spectral confusion and enables better discrimination and identification of objects. Many studies have investigated the static and dynamic changes of structural and functional phenotypes in agriculture using LiDAR technology (Jin et al., 2021a). For example, LiDAR data have been used to segment individual trees in data preprocessing to improve the accuracy of monitoring diseases with narrow-band spectral information (Zhou et al., 2022). LiDAR metrics, such as crown volume, crown

area, the coefficient of variation of crown-return intensity, the 25th cumulative percentile of crown-return intensity, and the kurtosis of crown-return intensity, have been used in models of disease classification (Yu et al., 2021a). Spatially aligning LiDAR and spectral data, however, remains a considerable challenge due to geometric and radiometric distortions (Maschler et al., 2018).

2.3.6 Temporal information

Temporal information, which involves knowledge derived from sequences of hyperspectral images or multimodal remote sensing data over time, can significantly enhance the accuracy of crop disease monitoring. Such temporal data allow for the identification of trends throughout the stages of crop growth. For example, Anderegg et al. (2019) demonstrated that temporal changes in canopy spectral reflectance allowed the specific monitoring and quantification of *Septoria tritici* blotch in various wheat germplasms, minimizing the confounding effects of genotype and environment. Compared to reflectance spectra obtained at individual time points, time-integrated information offers improved specificity and robustness in assessing crop diseases. Spectral-temporal features can also aid in distinguishing diseases from physiological aging. Despite these advantages, only a few studies have investigated the use of hyperspectral temporal information from multi-period images for monitoring crop disease. The increased workload and cost associated with data acquisition and analysis are the primary challenges in using time-series data for monitoring diseases.

2.3.7 Four criteria for selecting features

The essence of remote sensing feature selection corresponds to feature engineering in computer science. Feature engineering refers to selecting, creating, and transforming features or variables from raw data to improve the performance of ML models or other computational algorithms. Effective feature engineering is crucial in ML tasks, as it can greatly impact models' performance and generalization ability (Li et al., 2011). This paper identifies four simple criteria for feature selection, including diversity, robustness, relevance, and parsimony.

Diversity: Obtaining multiple and independent crop features, rather than only one, is essential for accurately identifying crop diseases. Multiple spectral domains or sensor modalities can provide a comprehensive understanding of complex interactions between diseases and crops (as discussed in Section 2.3.6).

Robustness: The radiance received by hyperspectral sensors is often decreased by atmospheric influences and environmental disturbances. Features should be robust to variations in geometry, illumination, canopy structure, and soil, which ensures a model's generalization to different spatiotemporal scales.

Relevance: Features must be relevant to the target disease, as this helps models better simulate the relationship between remote sensing features and diseases, leading to more accurate monitoring. Features should also be pertinent to the stage of the disease, as different stages trigger physiological responses associated with distinct features. Additionally, features should align with the properties of the sensors. An overview of widely used spectral indices can be found in an online database

(www.indexdatabase.de).

Parsimony: Reducing feature dimensionality can improve model efficiency and generalization and decrease computational costs. But the number of features should be kept still uncertain. For example, two to four disease-specific spectral features were sufficient to identify rice leaf blast (Tian et al., 2021), but eight spectral bands to monitor tomato spotted wilt achieved the best classification accuracy (Wang et al., 2019).

The relevance of the four criteria for feature selection can be observed in studies that aim to detect and differentiate infection sources and distinguish between biotic and abiotic sources. Notably, different diseases or stages of infection may yield different feature selection outcomes. In summary, no single feature is best. To monitor diseases more accurately, we recommend considering instrument attributes and disease characteristics and focusing on extracting appropriate features.

2.4 Algorithms for modeling crop disease

The methods used to monitor crop diseases can be broadly categorized into three groups: (i) traditional statistical methods, (ii) machine learning-based methods, and (iii) physically-based approaches that integrate RTMs with machine learning algorithms. Each of these methods has unique strengths, but they also come with inherent limitations, as detailed in Table 2.2. These algorithms have shown varying levels of accuracy when applied to specific crops and diseases, as detailed in Table 2.3.

2.4.1 Traditional statistical methods

Over the last few decades, scientists have attempted to use single or combinations of multiple indicators to estimate the extent of disease occurrence. Univariate and multivariate regression-based algorithms have been extensively used to monitor crop diseases using hyperspectral signatures. For example, PRI exhibited a negative linear relationship with the disease index of wheat yellow rust (Huang et al., 2007). A single index lacks specificity for identifying and differentiating diseases, but combining two or three spectral vegetation indices can improve disease retrievals (Hillnhuetter et al., 2012; Mahlein et al., 2010). Multivariate regression models such as multinomial logistic regression (MLR) and partial least squares regression (PLSR) have subsequently been used for monitoring diseases (Prabhakar et al., 2013; Zhang et al., 2014). These methods are quick for building linear relationships between spectral bands and disease severity. However, they tend to oversimplify complex, nonlinear interactions, which can limit their effectiveness for detecting early-stage or subtle disease symptoms.

Table 2.2 Comparative analysis of various algorithms

Algorithms	Advantages	Disadvantages	Exemplary studies
Univariate linear regression	Simple and easy to understand Suitable for selecting features	Limited to linear relationships Does not consider interactions among features Limited areas of application	(Huang et al., 2007)

Multiple linear regression	Considers multiple features	Limited areas of application	(Prabhakar et al., 2013; Zhang et al., 2014)
Statistical analysis	Considers multiple source features Computationally efficient	Sensitive to noise Performs poorly for weak spectral responses	(Hillnhuetter et al., 2012; Li et al., 2012)
Traditional machine learning	Suitable for modeling complex relationships	Requires feature selection Difficult to interpret	(Alisaac et al., 2018; Iordache et al., 2020)
Deep learning	The end-to-end model Suitable for modeling complex relationships	Difficult to interpret	(Wang et al., 2019; Yu et al., 2021b)
RTM + ML	Leverages available physical understanding	Model errors due to simplification of reality Accumulation of model errors	(Hornero et al., 2021; Poblete et al., 2023a)

A set of classical supervised classification algorithms based on statistical analysis, such as minimum distance, which uses Euclidean or Mahalanobis distances between pixel values and the centroid value of the sample class, have been used (Bagheri et al., 2018; Li et al., 2012; Zhang et al., 2011). The spectral angle mapper (SAM) has been a promising tool for hyperspectral classification, wherein each spectrum is classified based on its angular similarity to the spectra of the endmember. This method indicated an overall accuracy of 79.4% in discriminating symptoms (healthy 2 diseases alone or in combination) on sugar beet (Hillnhuetter et al., 2012). These methods are useful for hyperspectral classification, particularly in well-defined cases. However, in complex or heterogeneous canopies, where disease symptoms overlap with healthy plant features, these methods can struggle to differentiate between classes.

In the future, traditional statistical methods should incorporate more advanced preprocessing steps to handle noise and spectral overlaps better. For example, incorporating machine learning feature selection or dimensionality reduction techniques may improve the robustness of these methods.

Table 2.3 Summary of algorithms for monitoring plant disease using hyperspectral feature

Crop	Diseases	Equipment type	Features	Method	Best accuracy	Reference
Empirical methods						
Sugar beet	Leaf spot, rust, and powdery mildew	Leaf clip	Spectral	RELIEF-F	92, 87, and 85%, respectively	(Mahlein et al., 2013)
Wheat	yellow rust	Proximal, airborne	Spectral	RE	--	(Huang et al., 2007)
Sugar beet	Leaf spot, powdery mildew, and rust	Leaf clip	Spectral	COC	--	(Mahlein et al., 2010)
Supervised classification methods						
Wheat	Powdery mildew	Proximal	Spectral, textural	PLSDA, SAM	91.4%	(Xuan et al., 2022)
Rice	Rice blast	Proximal	Spectral	ML-SFFS (ML: LDA, KNN, SVM)	Asymptomatic: 69.58% Early: 95.77% Mild: 98.65%	(Tian et al., 2021)
Wheat	*Septoria tritici* blotch	Proximal	Spectral, temporal	PLSDA	86%	(Anderegg et al., 2019)
Wheat	Fusarium head blight	Proximal	Spectral, SIF, multimodal	SVM	89%	(Mahlein et al., 2019)
Tomato	Spotted wilt virus	Proximal	Spectral	GAN	96.25%	(Wang et al., 2019)
Pine forests	Pine wilt disease	UAV	Spectral	3D-Res CNN	Early: 72.86% 88.11%	(Yu et al., 2021b)
Physical-based approaches						
Holm oak	*Phytophthora*-induced symptoms	Airborne	Spectral, pigment concentration, SIF, multimodal	3D RTM, SVM, RF	71–82%	(Hornero et al., 2021)
Olive	*Xylella fastidiosa*	Airborne	Spectral, pigment concentration, SIF, multimodal	3D RTM, SVM, NNE, LDA	80.9%	(Zarco-Tejada et al., 2018)
Olive, Almond	*Xylella fastidiosa and Verticilliu m dahliae*	Airborne	Spectral, pigment content, structural properties, CWSI, SIF	PRO4SAIL, SVM, RF, spectral clusering, multi-stage classificatio	92%-94%	(Zarco-Tejada et al., 2018)

				n		
Olive	*Xylella fastidiosa and Verticilliu m dahliae*	Airborne	Spectral, pigment content, structural properties, CWSI, SIF	PRO4SAIL, SVM, RF, spectral clusering, multi-stage classificatio n	92%, 98%	(Poblete et al., 2021)
Grape	Yellownes s and esca	Leaf clip	Spectral, pigment concentrat ion, textural	PROSPECT -D, BPNN	99%	(Al-Saddik et al., 2018)

Note: UAV, unmanned aerial vehicle; RE, regression equation; COC, coefficient of correlation; PLSDA, partial least squares discriminant analysis; SAM, spectral-angle mapper; ML-SFFS, machine-learning-based sequential floating forward selection; LDA, linear discriminant analysis; KNN, K-nearest neighbor; SVM, support-vector machine; GAN, generative adversarial nets; 3D-Res CNN, three-dimensional convolutional neural network; RTM, radiative-transfer model; 3D RTM, three-dimensional RTM; RF, random forest; NNE, neural network ensemble; BPNN, back-propagation neural network.

2.4.2 Machine learning-based methods

Algorithms for supervised ML classification have become highly effective tools for accurately identifying and quantifying crop diseases. Popular algorithms, including linear discriminant analysis, random forest, support vector machines, stepwise discriminant analysis, multilayer perceptron, radial basis function, decision trees, and K-nearest neighbor, have all been widely used (Alisaac et al., 2018; Calderon et al., 2015; Fernandez et al., 2020; Huang et al., 2020; Iordache et al., 2020; Meng et al., 2020; Zhang et al., 2012a). These traditional ML algorithms can model complex relationships, but careful engineering and selection of features are required before modeling.

Deep learning (DL) has become a powerful tool for processing hyperspectral data, with applications in the monitoring and diagnosis of diseases (Loey et al., 2020). Convolutional neural networks (CNNs) are particularly effective for these tasks because CNNs can extract highly discriminatory features and leverage the spatial-contextual and spectral information contained in cubes of hyperspectral imagery data. For instance, 1D-CNNs have demonstrated a high average accuracy of 97.72% in identifying disease spots on potato leaves using hyperspectral imagery, offering faster and more accurate results (Liu and Xiao, 2020). Similarly, 2D-CNNs achieved an F1 score of 0.75 and an accuracy of 74.3% when classifying hyperspectral pixels of healthy wheat heads versus those affected by fusarium head blight in field conditions (Jin et al., 2018). Furthermore, 3D-CNNs can outperform 2D-CNNs because they take advantage of the spectral dimension in hyperspectral data cubes, enabling the model to capture both spatial and spectral relationships (Nguyen et al., 2021). Notably, 3D-Res CNNs achieved an overall accuracy of 88.11% in identifying pine trees infected with pine wilt disease (PWD) from hyperspectral images, with an accuracy of 72.86% for detecting

early-stage infections (Yu et al., 2021b). Although CNNs and 3D-CNNs can deliver high accuracy, their performance is heavily dependent on large, labeled training datasets. In agricultural remote sensing, such datasets are often limited, especially for diseases that are rare or poorly represented in existing datasets. Data augmentation or transfer learning might be necessary to overcome this limitation.

2.4.5 Physical-based Methods

Physically-based methods, also known as RTM methods, consider the radiative transfer processes involved in remote sensing. RTMs have been developed to simulate the interaction of electromagnetic radiation with canopy elements (such as leaves and soil) while also representing the architecture of the canopy and the structural and biochemical properties of its constituents. Although crop diseases are often considered secondary variables that cannot be directly associated with the mechanisms of radiative transfer observed in remote sensing (Weiss et al., 2020), they are closely linked to primary variables (e.g., pigment concentrations and leaf area index) that are directly involved in radiative transfer. This relationship has led to combining RTMs with ML methods, resulting in accurate and efficient hybrid models.

The hybrid approach is a powerful tool for estimating biophysical and biochemical variables without the need for in situ reference data. For example, Camino et al. (2021) combined the PROSAIL model with Random Forest (RF) to monitor infections, using chlorophyll and anthocyanin concentrations derived from PROSAIL as inputs to RF, thereby improving monitoring accuracy. Similarly, Hornero et al. (2021) employed additional RTMs, including FLIGHT+FLUSPECT and FLIGHT+PROSPECT, to invert a broader range of crop functional traits related to crop health, such as water content, chlorophyll, carotenoid, anthocyanin levels, fluorescence, leaf area index, and increases in crown temperature and dry matter content.

In these studies, RTMs provide valuable physical constraints and domain knowledge, but they also have limitations in representing complex disease processes. However, when combined with ML, they offer an effective way to improve disease monitoring accuracy by incorporating both physical and data-driven approaches. Further research is needed to explore more flexible and advanced approaches for combining RTMs with ML to improve the are liability and accuracy of disease monitoring under diverse conditions.

2.5 Areas of application

Research utilizing hyperspectral sensing for crop diseases can be categorized into four applications: 1) assessment of disease incidence and severity, 2) discriminating among stressors, 3) monitoring disease symptoms at the early stage, 4) discriminating crop resistance in breeding, and 5) monitoring disease in a large scale. The concepts of these four categories are illustrated in Fig. 2.2. The first category serves as the fundamental task in monitoring crop diseases. In contrast, the remaining categories present an array of challenges. This section will overview the research advancements made in categories 2 to 5.

2.5.1 Stresses discrimination

Crops are constantly exposed to various stress factors, including biotic and abiotic stress, which can affect their growth, development, and productivity. Accurate and timely monitoring of stress is essential for effectively managing crops. Hyperspectral remote sensing has been used to discriminate differences between symptoms induced by pathogens (Poblete et al., 2021) and different types of stress in crops, including water-induced stress (Zarco-Tejada et al., 2021; Zibrat et al., 2019), nutrient deficiency (Abdulridha et al., 2018; Reisig and Godfrey, 2010; Zhang et al., 2012b; Zhang et al., 2012d), pest and disease infestation (Liu et al., 2018), extreme weather (Lacoste et al., 2015), and heavy-metal toxicity (Fu et al., 2020; Li et al., 2021; Xia et al., 2022). Different types of stresses can be identified based on the unique spectral signatures they produce. For example, nutrient deficiency due to yellow rust can be identified by changes in PRI (Zhang et al., 2012b), and drought stress and infestation have different patterns of change in reflectance in NIR and SWIR (Zibrat et al., 2019). A phylodynamic approach with multi-stage classificatory methodology has been used for identifying diseases (Poblete et al., 2021), and uncoupling biotic-abiotic spectral dynamics has been used to reduce uncertainty (Zarco-Tejada et al., 2021). Furthermore, the occurrence of diseases has been linked to prior knowledge, such as climate and the history of crop growth (Chakraborty and Newton, 2011b). While prior knowledge is indeed important, the challenge lies in integrating these data sources with hyperspectral imagery to improve model accuracy. A better approach may involve the dynamic integration of remote sensing data with real-time environmental factors.

2.5.2 Early symptom monitoring

The accurate monitoring and diagnosis of the symptoms at the early stage of disease are crucial for minimizing crop yield losses and monitoring the spread of diseases. Researchers have recently explored the potential of using remote sensing features and spectral crop trait analysis to monitor pre-visual symptoms of disease infection. Tian et al. (2021) showed promising results in the pre-visual monitoring of infection with rice leaf blast infection. Also, they designed indices that could quantify a disease index and track dispersal at multiple spatial scales (Tian et al., 2023). A practical framework using high-resolution hyperspectral images, thermal data, and radiative-transfer modeling has also been developed to evaluate the efficacy of monitoring pre-visual *Xylella fastidiosa* infection (Zarco-Tejada et al., 2018). Camino et al. (2021) developed a method for predicting diseases that combined spatial epidemiological models and remote sensing to accurately predict the spatial distribution of *Xylella fastidiosa* in almond orchards. These achievements represent a major step forward in monitoring vegetative health and its potential application at airborne canopy scales. To make early disease detection more practical, the integration of temporal spectral data and real-time environmental data (e.g., temperature, humidity, soil moisture) is crucial. Future work should focus on developing algorithms that combine hyperspectral, thermal, and environmental datasets to track disease spread across diverse environments.

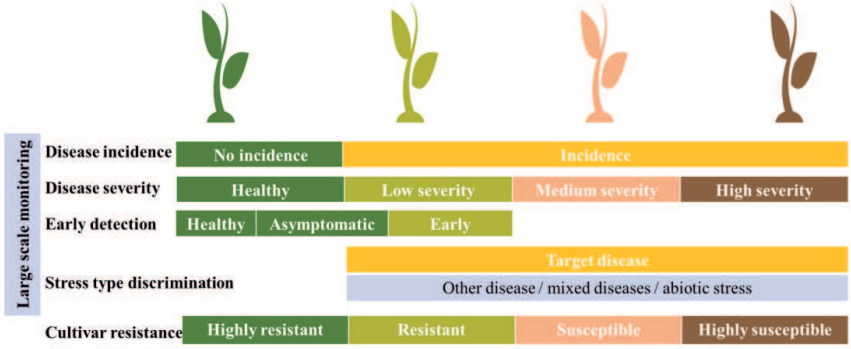


Fig. 2.2. *Areas of application of hyperspectral sensing of disease. Green, cyan, pink, and brown colors serve as indicators of an increase in the severity of disease. Gray indicates stress factors other than the disease, and the hatching represents crop genotypes with various phenotypes.*

2.5.3 Breeding resistance

The development of resistant cultivars is a key strategy for controlling pathogen infection. Phenotyping is a vital step in breeding programs because it involves a qualitative characterization of the genomic expression of crop function in an environment (Fiorani et al., 2013; Reynolds et al., 2019). Phenotypes have traditionally been visually estimated, which is laborious, time-consuming, and can be subjective depending on the breeder's expertise. Image-based phenotyping offers a promising solution to these problems because it can help the breeder to objectively quantify resistance and reduce the subjectivity in selecting potential genotypes (Gold et al., 2020b; Joalland et al., 2018; Marzougui et al., 2019; Yu et al., 2018). However, genotypic diversity and contrasting environmental conditions are major challenges for evaluating crop resistance using hyperspectral sensors. Anderegg et al. (2019) devised a spectral-temporal feature method that relies on relative changes in spectral reflectance over time. Researchers employed two types of dynamic parameters. The first type, "key time-points", corresponded to specific moments when predetermined criteria, such as a threshold, were met. The second type, called "change parameters", represented either the rate or duration of a particular process. Their findings highlighted the absence of specificity and robustness in evaluating diseases based only on reflectance spectra at individual time points. Focusing on temporal changes in canopy reflectance during pathogenesis may enable the specific monitoring and quantification of crop diseases while reducing the confounding effects of genotype and environment. This study initially succeeded in proximal canopy using a handheld non-imaging spectroradiometer. However, there is still a lack of research on hyperspectral sensing in breeding resistance. future research could explore the integration of hyperspectral data with genomic data to develop better genotype-environment interaction models.

2.5.4 Large scale monitoring

Large-scale monitoring refers to the observation and analysis of extensive

geographic areas, which is crucial for understanding and managing widespread crop disease challenges. A review of the literature identified only two relevant studies that employed satellite-based hyperspectral data for monitoring crop diseases. One study by Apan et al. (2004) assessed several narrow-band indices derived from EO-1 Hyperion imagery to identify sugarcane areas affected by "orange rust". Another study by Dutta et al. (2024) developed an integrated two-step wilt detection approach and a disease-specific spectral index for *Cajanus cajan* using the ASI-PRISMA hyperspectral dataset. Their method enabled the detection of wilt in *Cajanus cajan* plants at least 2–3 weeks earlier than conventional multispectral satellite imagery.

While significant progress has been made in hyperspectral disease monitoring at the leaf and near-ground scales, applying these methods at larger scales presents both opportunities and challenges. Since 2000, seven satellites equipped with hyperspectral sensors have been launched, including EO-1 Hyperion, PROBA-CHRIS, HyspIRI, HJ-1A, PRISMA, EnMAP, and PACE (see Table S2.2 for details). These satellites offer valuable spectral data, providing powerful tools for monitoring plant diseases over large regions. However, limitations such as lower spatial resolution and environmental factors like cloud cover can reduce the effectiveness of satellite-based disease monitoring. In contrast, ground-based and UAV-based hyperspectral imaging systems have demonstrated higher accuracy in crop disease detection due to their superior spatial resolution and greater operational flexibility. As a result, the future of large-scale plant disease monitoring will likely involve integrating ground-based, airborne, and satellite-based hyperspectral technologies to leverage the complementary strengths of each. While multispectral satellite data, such as those from Sentinel and Landsat, often offer better spatial resolution than hyperspectral data, the finer spectral detail provided by hyperspectral data can complement multispectral data. Integrating multispectral and hyperspectral data sources holds significant potential to enhance the accuracy of large-scale disease monitoring. This multi-source data fusion approach could address the current limitations and greatly improve the precision and reliability of disease monitoring across expansive agricultural regions.

2.6 Challenges and future perspective

2.6.1 Literature review

The primary objective of this systematic review was to understand the advances in the hyperspectral monitoring of diseases and to analyze the research challenges and trends. We adopted the method of gathering literature proposed by Cronin et al. (2008) to obtain all relevant studies. The analysis of the literature consisted of four main steps. Firstly, the keyword combination "remote sensing & hyperspect* & (crop disease OR biotic) & (agriculture OR crops)" was selected to search for studies in the Web of Science database published before 31 July 2024. This processing yielded a large pool of records. This identification step involved an initial check to remove duplicates, producing approximately 500 studies eligible for further investigation. Secondly, we considered records that were not peer-reviewed as irrelevant (e.g., conference

proceedings or reports). After examining the titles and abstracts, we also excluded review studies and records that focused on topics other than crop diseases. The screening step led to a total of 192 studies. Finally, we carefully read and analyzed these studies and categorized them based on research methods and application scenarios, aiming to gain insights into the progress and challenges in studies of hyperspectral monitoring crop diseases using this review.

2.6.3 Keywords trends analysis

1) "Burstiness" analysis of keywords

To investigate the main research foci in monitoring crop diseases using hyperspectral remote sensing for 2006–2024, we used a burstiness analysis in CiteSpace (Chen and Song, 2019) to identify the ten most prominent keywords. The burstiness analysis enables the evaluation of frequently cited keywords and their corresponding periods of significance. The burst strength in CiteSpace characterizes these keywords, with higher burst strength indicating a greater frequency of citation over a specific period. A burst signifies a sudden surge in the frequency of a particular keyword. We adopted a broad perspective, incorporating all the keywords from the titles, abstracts, keywords provided by the authors, and keywords extracted from the titles of the references cited (Fig. 2.4).

The most prominent keyword (based on strength) in 2020 was machine learning, followed by deep learning, bacterial wilt, and yellow rust. The research foci of hyperspectral remote sensing for crop disease monitoring can be broadly categorized into two periods, based on evolving research trends and keyword bursts: 2006–2012, focused on equipment, algorithms, and applications; and 2012 to the present, with an increased focus on advanced algorithms like machine learning and specific disease applications. For equipment, the burst of handheld radiometry began in 2006 and gradually weakened after 2012 due to the development of imaging hyperspectral technology and other platforms, such as drones and airborne platforms. For algorithms, researchers constructed disease index models for simulating diseases before 2012. For applications, sugar beet was a focal research species.

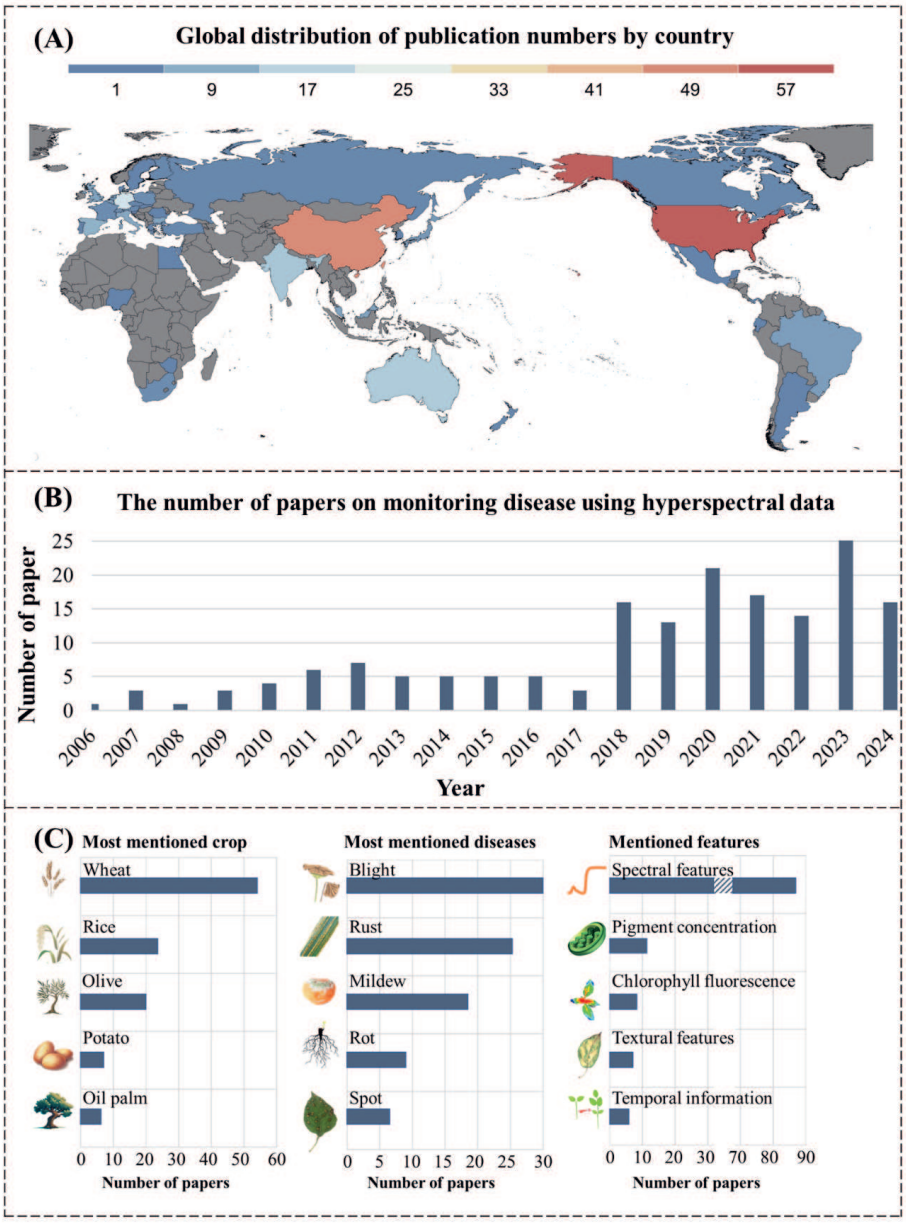


Fig. 2.3. *Status of global monitoring of crop disease using hyperspectral remote sensing. (A) The distribution of related publications around the world. Gray indicates no publications from the country. (B) The number of papers on the monitoring of disease using hyperspectral data from 2004 to 2022. (C) Summary of crops, types of disease, and hyperspectral-based features for 2006–2024.*

The research foci from 2012 to the present have focused on algorithms and

applications. For algorithms, the burst intensity of machine learning and deep learning remained high due to the rapid development of advanced artificial intelligence technologies. More remote sensing features were simultaneously used to monitor diseases, such as the wage index and the leaf area index. For applications, yellow rust and bacterial wilt received considerable attention. Drought stress has been continuously monitored since 2006 with weak intensity, but distinguishing between drought stress and diseases has remained a research challenge because drought stress and diseases have similar symptoms such as wilting and changes in transpiration.

2) A time zone of keywords

We analyzed temporal zones using CiteSpace to research deeper into the evolving landscape of research foci in monitoring diseases using hyperspectral remote sensing for 2006–2024 (Fig. 2.5). Please note that we only included keywords from titles and those provided by the authors to represent the evolution of our research topic better. While this approach limits the analysis to keywords found in titles and abstracts, which may exclude some relevant terms not explicitly mentioned by the authors, we believe it provides a focused view of the main research trends.

The keywords can be divided into six categories: type of disease, species; features; algorithms; aspects of sensors, platforms, and scales; and an "others" category. The "others" category includes broad keywords that cannot be allocated to the other four categories, such as remote sensing and disease. Biological stress was notably continuously mentioned from 2020 to 2024.

The UAV has frequently appeared in the category containing "sensors, platforms, and scales" since 2020, and the multimodal fusion technology of hyperspectral sensors and thermal infrared sensors attracted attention in 2022. Machine learning and artificial intelligence in the algorithm category, consistent with the results of keyword burstiness analysis. Spectral features in the "features" category such as reflectance, vegetation index, and wavelet transform-based features were the main terms identified. Biochemical-parameter features (e.g., nitrogen and anthocyanin concentrations) and physiological parameters (e.g., fluorescence) were also mentioned.

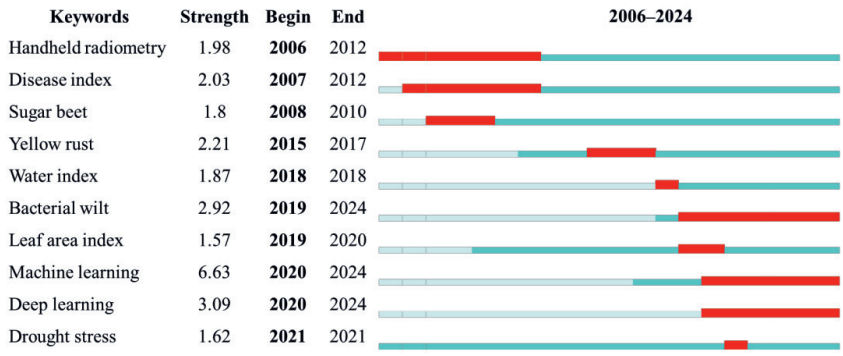


Fig. 2.4. *Top 10 keywords with the strongest citation bursts of hyperspectral remote sensing for crop disease monitoring*

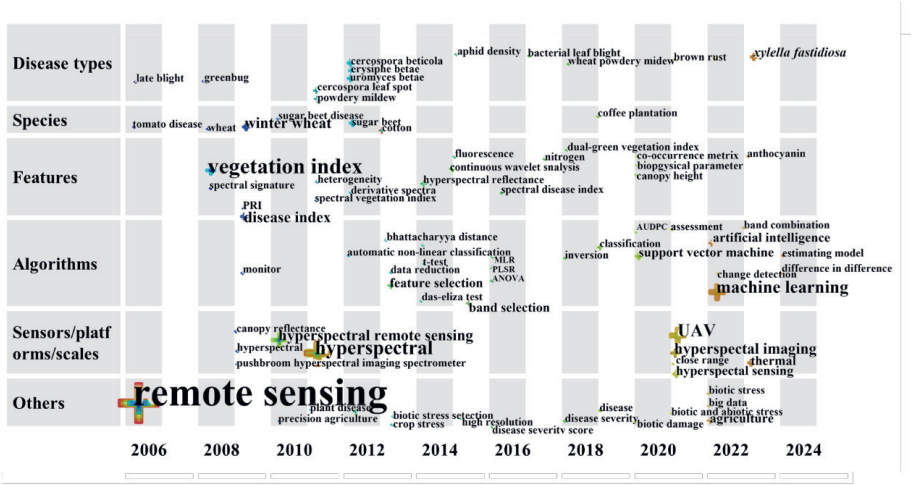


Fig. 2.5. *Keyword time zone view. A cross represents each keyword, and the vertical position of the keyword's first letter corresponds to the year of its first appearance. Arms around the crosses depict subsequent years, with the thickness of each arm indicating the keyword's frequency for that year. Note: PRI, photochemical reflectance index; MLR, multivariate linear regression; ANOVA, partial least square regression; AUDPC, under disease progress curve; UAV, unmanned aerial vehicle.*

2.6.4 Future perspectives

Based on the above-presented research, we can identify emerging trends and future research directions in hyperspectral remote sensing for monitoring crop diseases. The main challenges and trends have been illustrated in Fig. 2.6.

Relationship between foliar and canopy scales. Observation platforms have shifted over time from handheld devices to airborne platforms, including piloted aircraft and drones, and the scale of observation has expanded from individual leaves to crops and even entire ecosystems. While this approach limits the analysis to keywords found in titles and abstracts, which may exclude some relevant terms not explicitly mentioned by the authors, we believe it provides a focused view of the main research trends (Yang, 2022). To address this issue, future research should explore the factors causing a disconnect between canopy and foliar remote sensing. This includes examining structural and angular dependencies that might influence the data, potentially with the physically-based RTMs. By understanding the invariants and establishing a more seamless link between leaf-level and canopy-level information, we can enhance the robustness and capability of remote sensing algorithms.

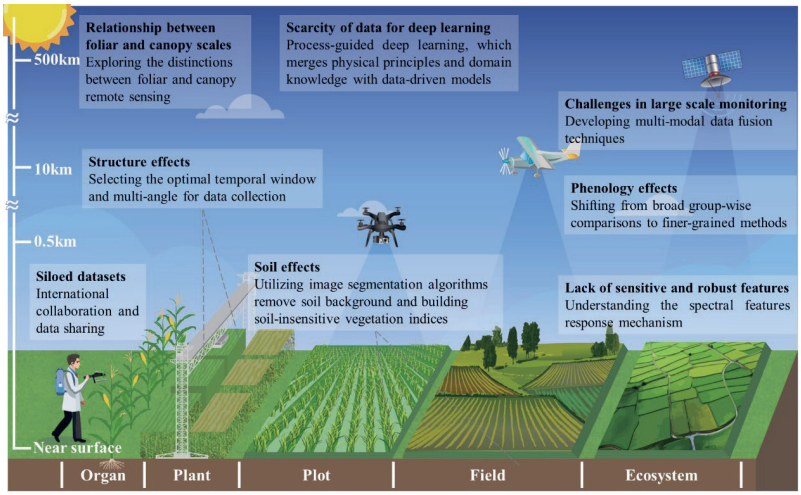


Fig. 2.6. *A summary of challenges and trends*

Soil, crop structure and phenology effects. Remote sensing captures a wide range of surface information, encompassing not only vegetation and diseases but also elements like soil, crop structure, and phenology (Weiss et al., 2020). For instance, the spectral response curves of soil and crop lesions can easily overlap, particularly in the visible light spectrum (Fig. 2.1B). This overlap necessitates careful data preprocessing, including soil segmentation, before developing any monitoring models. Furthermore, selecting or developing spectral features minimally affected by soil background variations is crucial.

The structure of the crop, specifically in the canopy scale, can significantly impact spectral responses. This effect is most evident in metrics like the LAI and vegetation cover fraction. For instance, in dense canopies (LAI > 4), studies have suggested that structural variations less influence PRI, although this effect may vary across different crops and environmental conditions (Yang, 2022). Therefore, choosing the appropriate temporal window for data collection can mitigate the influence of such structural disparities. Additionally, by collecting data from various angles, multi-angle remote sensing can provide accurate information on crop structure and potentially mitigate structural variations issues (Yan et al., 2019).

Phenological changes, such as leaf senescence, can also mimic the spectral features of diseases (Ouyang et al., 2013). There is an emerging need to transition from general group-wise comparisons to more sensitive methods capable of detecting deviations in individual crop or plot diseases. One promising approach is to employ time-series analysis of hyperspectral data. This could differentiate between typical seasonal changes and actual disease-related anomalies, enabling early disease detection at the individual level.

Lack of sensitive and robust features. Traditional machine learning (ML) methods have remained the most commonly used approach for hyperspectral disease monitoring in recent years. One of the key challenges in building traditional ML models is

identifying appropriate input features (Li et al., 2017). Researchers typically rely on their expertise to select spectral, textural, structural, thermal, pigment, and solar-induced fluorescence (SIF) features. However, the way these features respond to diseases remains largely unknown. Understanding the feature response mechanisms and identifying features with high sensitivity and robustness are crucial for advancing future model development and improving monitoring accuracy.

Challenges in large scale monitoring. Several hyperspectral satellite missions focused on vegetation monitoring are currently underway. These missions, which provide rich spectral information, hold significant potential for large scale crop disease monitoring. However, spatial and temporal resolution remain key limitations for large scale applications. To make hyperspectral data suitable for agricultural applications, additional downscaling techniques are required. For example, multispectral satellites offer higher spatial resolution, while UAV platforms provide greater flexibility, particularly in terms of revisit frequency. Furthermore, the integration of ancillary data, such as climate information (temperature, humidity, precipitation), can significantly influence the occurrence, spread, and severity of crop diseases. Overall, the use of multi-modal data fusion techniques can enhance the accuracy and effectiveness of crop disease monitoring at larger scales.

Scarcity of data for deep learning. Although DL has significant potential for hyperspectral disease monitoring, its application has been limited due to challenges such as small, imbalanced datasets, high computational costs, and the difficulty of obtaining diverse, high-quality labeled data for training DL models (Ma et al., 2019). A new paradigm called process-guided deep learning (PGDL) has begun to overcome these challenges (Karniadakis et al., 2021). PGDL integrates domain-specific knowledge and physical models into deep learning approaches, which can help overcome some challenges in hyperspectral disease monitoring, such as the difficulty of solving inverse problems or modeling complex physical processes. This approach has been evaluated for quantifying the biomass and nitrogen concentration of cover crops from hyperspectral remotely sensed imagery (Wang et al., 2023b). PGML, however, has rarely been tested in remote sensing for monitoring diseases because diseases cannot be directly inferred using RTMs. Two potential solutions could resolve this issue: first, from a mechanistic perspective, developing RTMs that consider disease parameters, and second, from an empirical perspective, using measured foliar spectral information for diseases with different severities to simulate canopy data using canopy RTMs. In summary, combining RTMs with ML is a promising solution for exploring hyperspectral data for crop diseases, as demonstrated in recent publications (Hornero et al., 2020; Poblete et al., 2020; Zarco-Tejada et al., 2018). However, the way to combine RTMs with DL requires further exploration and research.

Siloed datasets. In contrast to digital RGB images, obtaining high-dimensional spectral datasets (especially hyperspectral data) is costly due to the specialized equipment required and the time-intensive nature of fieldwork and data processing, which in turn hinders the transferability and validation of monitoring algorithms. A

comprehensive study that includes different scales, regions, and diseases requires collaboration among international researchers. For example, the rice blast index (RIBI) development relied on a vast data set of foliar- and canopy-scale reflectance spectra and satellite imagery gathered over seven independent campaigns in four years (Tian et al., 2023). The specificity of RIBI was assessed using independent hyperspectral data sets containing healthy leaves and leaves infected with sugar beet rust, powdery mildew, and *Cercospora* leaf spot (Mahlein et al., 2010). Sharing data sets of crop diseases plays a crucial role in assessing model evaluation and transferability by providing a standardized benchmark for fair comparisons, ensuring reproducibility, enabling the assessment of transferability, fostering collaboration, and accelerating progress in this field. We, therefore, stress the importance of international collaboration, open-source initiatives, and big data in advancing research and practical applications in the hyperspectral monitoring of crop diseases. By embracing these strategies, we can collectively work towards the sustainable management of crop diseases, ensuring global food security and agricultural resilience.

2.7 Conclusion

Effective and timely monitoring of crop diseases is critical for field management, food security, and crop breeding. Recent advancements in hyperspectral sensor technologies and data analysis techniques have provided powerful tools for monitoring crop diseases at both high spatial and temporal resolutions. This review offers a comprehensive overview of the key aspects involved in hyperspectral remote sensing for crop disease monitoring. We began by defining common crop diseases and their symptoms, then explored hyperspectral-derived features used in disease monitoring. We also introduced a set of four criteria for selecting relevant features. Additionally, we reviewed the range of algorithms currently used in crop disease detection, highlighting their advantages and limitations. This analysis identified several key application areas and associated challenges in the field. Looking ahead, the potential of hyperspectral remote sensing for crop disease monitoring remains vast. Advancements in image processing and data analysis, along with the development of new sensors with sub-nanometer spectral resolution, will significantly enhance the accuracy and scalability of disease monitoring. Improvements in spatial resolution and reductions in the cost of hyperspectral instruments will further drive the adoption of these technologies. By overcoming current barriers, these innovations will lead to more effective, timely disease management and improved agricultural practices, ultimately supporting global food security and crop resilience.

2.8 Supplementary information

Additional tables and figures supporting this chapter are available online. They can be accessed via the QR code or at the following URL: PhD-thesis/Chapter2_supplymentary.pdf at main · Briya1990/PhD-thesis

3

A novel disease sensitive index (DSI) for monitoring early maize leaf disease using PROSPECT-D and LESS models

This chapter is based on:
Bai, Y., et al. (2025) A novel disease sensitive index (DSI) for monitoring early maize leaf disease using PROSPECT-D and LESS models. Smart Agricultural Technology (Under review).

Abstract

Monitoring crop diseases on a large scale with non-destructive remote sensing technology is a promising approach to mitigating their impacts. However, monitoring early maize leaf diseases at canopy scales is still challenging. In this study, we introduce the Disease Sensitive Index (DSI), a novel disease index specifically designed to monitor early maize leaf diseases at the canopy scale. Early leaf diseases predominantly cause changes in leaf pigments associated with photosynthesis, with a minimal impact on plant structure. Here, we analyzed the effects of leaf pigments and plant spacing (PS) on canopy spectral reflectance using PROSPECT-D and LESS models and found that the red-edge band (717 ± 5 nm) and green band (560 ± 10 nm) were more sensitive to leaf pigments than to PS. To better monitor early maize leaf diseases, we presented the DSI, which showed a high sensitivity to changes in leaf pigments, especially chlorophyll content, but a low sensitivity to PS. Our results demonstrated that the DSI was extremely statistically significant in differentiating rust severity, especially between low disease severity ($p < 0.001$). Furthermore, the DSI showed improved performance when quantifying the disease index (DI) across different years and sites ($R^2 = 0.69$ in 2021; $R^2 = 0.62$ in 2022). The time-series response patterns of vegetation indices (VIs) indicated that the DSI can detect disease onset as early as 10 days after infection (DAI 10). Our findings highlight the potential of the DSI for monitoring early maize disease in precision agriculture.

3.1 Introduction

Maize serves as a significant staple crop, livestock feed, and ethanol fuel source worldwide (Ranum et al., 2014). However, the increased frequency of disease outbreaks in maize is a crucial reason for the reductions both in crop yield and quality (Chakraborty and Newton, 2011a). Common leaf diseases in maize include maize rust and leaf spot. Infected leaves appear as small yellow spots at first, and then the spots gradually rise to form spore piles. These spore piles are mainly round or oval, golden or light brown in color, and scattered on the leaves' upper surface. As the disease becomes more serious, plant leaves fade from green to yellow and appear to senesce early (Sun et al., 2021b). Pathogen-infected crops show more changes in functional characteristics, such as biochemical composition and physical structure, than healthy plants (Ahrens et al., 2020; Zarco-Tejada et al., 2018). Among these, leaves' anthocyanin (Anth), chlorophyll (C_{ab}), and carotenoid (C_{ar}) content are effective indicators for disease monitoring (Hernandez-Clemente et al., 2019).

Traditional methods for monitoring maize disease rely on field visual inspection, which is laborious and limited by subjective experience (Berger et al., 2022). Therefore, developing an objective and accurate approach to monitoring maize diseases at canopy scales is critical. In previous studies, remote sensing techniques have been widely used in monitoring plant diseases due to their advantages of non-destructive, rapid, and large-scale monitoring (Poblete et al., 2020; Tian et al., 2023; Zarco-Tejada et al., 2018). Remote sensing data obtained from different platforms at different scales is used to monitor plant diseases such as oil red ring and bud rot (Viera-Torres et al., 2020), coffee leaf rust (Chemura et al., 2017), wheat yellow rust (Ren et al., 2021a), and wheat powdery mildew (He et al., 2021; Yuan et al., 2016). There are three critical components in plant disease monitoring using remote sensing technology: selecting disease-sensitive features, establishing disease monitoring models, and evaluating the results' accuracy (Zhang et al., 2019a). In these three components, feature selection directly determines the accuracy of disease monitoring models (Hornero et al., 2021; Tian et al., 2021). Various vegetation indices (VIs) are common remote sensing features used in monitoring plant disease. For instance, the chlorophyll/carotenoid index (CCI), simple ratio pigment index (SRPI), and health-index (HI) have been identified as sensitive features for distinguishing between rice leaf blast and healthy leaves across different years (Tian et al., 2021). Additionally, the normalized difference vegetation index (NDVI) has been extensively utilized in identifying diseases (Abdulridha et al., 2020; Calderon et al., 2013). However, due to limitations in disease specificity identification of these common VIs (Huang et al., 2014; Liu et al., 2020b; Mahlein et al., 2013), there has been a pressing need to propose VIs based on disease-specific spectral information.

Disease-specific VIs are often proposed following a spectral response analysis of specific disease lesions. For example, Ren et al. (2021b) developed the yellow rust spore index (YRSI) using fungal spore information on leaves to identify yellow rust. The powdery mildew-index, yellow rust-index, and aphids-index were developed by

Huang et al. (2014) to identify and monitor different winter wheat diseases. Mahlein et al. (2013) identified disease specific single wavelengths from sugar beet leaves and developed the leaf spot index, sugar beet rust index, and powdery mildew index to monitor and identify sugar beet diseases. However, these VIs are calculated based on hyperspectral data's narrow spectral reflectance and are less effective for low-cost multispectral data (Marshall et al., 2016). Additionally, these specific disease indices, which are derived from leaf spectral data, do not consider the structural parameters of plants, leading to a decrease in accuracy during canopy monitoring tasks (Asner and Martin, 2008). Furthermore, different pathogens exhibit unique interactions with their host plants, and stressed tissues vary across various stages, which results in different sensitive spectral wavebands and indices (Terentev et al., 2022b; Zhang et al., 2020).

Previous studies highlighted that photosynthetic pigments, detectable through remote sensing techniques, act as physiological indicators for monitoring the early responses of plants to various stressors, as reviewed by Hernandez-Clemente et al. (2019). Among these pigments, chlorophyll is the primary pigment group. Building on this foundation, we hypothesize that an index sensitive to chlorophyll variations yet robust against changes in plant structure will be effective for the early detection of plant diseases. To test this hypothesis, our research employed simulations derived from radiative transfer models to replicate changes in pigment and structural parameters triggered by maize leaf diseases. The simulations used the latest version of the PROSPECT model, PROSPECT-D (Féret et al., 2017), and the large-scale remote sensing data and image simulation framework, LESS (Qi et al., 2019). PROSPECT-D generates leaf spectra by considering various biochemical components, while LESS incorporates these leaf spectra into different maize planting scenarios to generate simulated canopy spectra. Pigment content is directly integrated into PROSPECT-D, while plant structural information is depicted in LESS through variations in plant spacing (PS). Therefore, the objectives of this study were to (i) understand responses of spectral reflectance and VIs to changes in biochemical and PS through radiative transfer modeling; (ii) develop a multispectral index (i.e., DSI developed in this study) that is sensitive to chlorophyll changes but resistant to PS; and (iii) validate the performance of the proposed DSI for maize disease monitoring in various application scenarios.

3.2 Materials

3.2.1 Experimental site

Our study sites located in Xinxiang City, China, are characterized by a warm temperate continental monsoon climate with hot summers and cold winters (113°47'E, 35°10'N, ***Fig. 3.2***). This region is predominantly a maize-growing area of China, typically cultivated in May and harvested in October. To assess the applicability of the methods described in this paper, four sites in diverse locations and years were chosen for maize disease monitoring, named sites A, B, C, and D.

Sites A and B were planted in Xinxiang on May 30, 2021. Site A was segmented into 492 plots with a planting density of 90,000 plants per hectare. Each plot (1.25 m × 1.80

m) was dedicated to a single maize genotype. This site underwent treatment with a leaf spot bacterial solution on the evening of August 2, 2021. Site B with 56 plots was organized into four sections, each measuring 2475.2 m² and hosting a different planting density: 45000, 60000, 75000, and 90000 plants per hectare. Each section was further divided into 14 plots, each plot hosting a different maize variety. These varieties exhibited varying levels of resistance to maize rust, introducing different disease severities across the study site. Given that maize rust is a recurring disease in the study region, the rust naturally occurred.

Sites C and D, located in Yuanyang, had a planting density of 90,000 plants per hectare and were planted on May 30, 2022. Site C was organized into 120 rows of 3 meters, with every 20rows forming a plot containing a unique genotype. A subset of these plots was selected as infected areas that received treatment with the leaf spot bacterial solution on August 2, 2022marked in red on the overview map of site C. We identified healthy areas (uninfected areas, yellow masked areas), which are equal in number and size to the infected areas. These, infected and healthy areas were intermingled and distributed at intervals to minimize the impact of pathogen transmission. Site D had 1031 rows of 3 meters, each considered an individual plot. All plots received treatment with the leaf spot bacterial solution on August 2, 2022.In managing fields, we adhered to fertilizer application and irrigation practices guided by the expertise of local agricultural professionals and established standards. This approach aimed to maintain a balanced supply of water and nutrients, minimizing their potential influence on the prevalence of maize diseases.

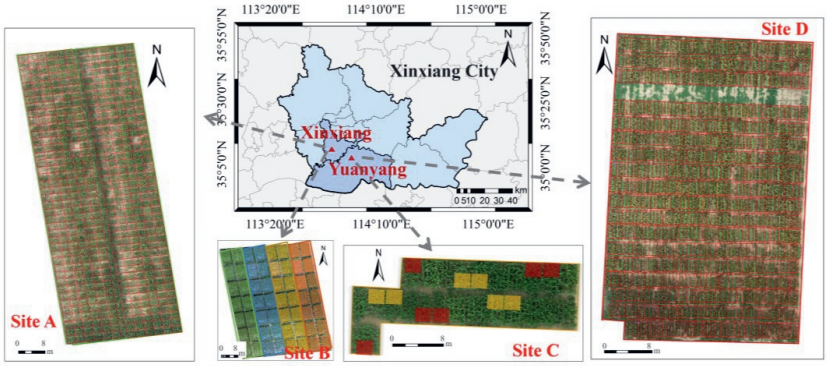


Fig. 3.2. *Layout of field experiments at two locations (Xinxiang and Yuanyang) in 2021 and 2022. The upper center figure shows the geographic location of experimental sites. Site A (left) and B (lower left) in Xinxiang in 2021. Green, blue, yellow, and orange in site B represent planting densities of 45000, 60000, 75000, and 90000 plants per hectare. Site C (lower right) and D in Yuanyang in 2022. The red mask in site C presents infected areas, and the yellow mask shows healthy areas.*

3.2.2 Field survey

Our field surveys adhered to the survey standard of maize rust by China's Ministry

of Agriculture (NY/T 1248.14-2021) and China's national standard (NY/T 1248.1-2006), titled technical specification for identification of maize resistance to leaf spot disease. This approach is organized into two primary segments: leaf-level assessment and canopy-level assessment. Initially, it involves quantifying the leaf disease (n) level based on the area of a leaf affected by the target disease. Subsequently, a canopy disease index (DI) is computed, incorporating the disease levels of leaves from all randomly sampled plants.

The practical procedure was divided into four main stages: sample collection, expert analysis, DI calculation, and resistance/disease severity assessment (***Fig. 3.3***). Initially, we documented images of maize leaves above, at, and below ear level. Following this, a team of experts categorized each leaf into a class based on coverage of disease spots through visual assessments. After the classification, the DI for each plot was calculated following the method established by Huang et al. (2007). Finally, we assessed resistance or disease severity based on various application scenarios. We classified maize resistance into two categories: resistant (DI ranging from 0–30%) and susceptible (DI ranging from 31–100%) according to maize breeding program. Similarly, we categorized the disease severity in maize plots into three levels: low (DS 1, DI of 0–30%), medium (DS 2, DI of 31–60%), and high (DS 3, DI of 61–100%).

At sites A and D, genotype resistance to leaf spot was assessed. Field surveys at these sites were conducted on August 21, 2021, and August 24, 2022, respectively. Site A hosted 492 genotypes, comprising 311 susceptible and 181 resistant genotypes. Conversely, site D hosted 1,013 genotypes, including 483 susceptible and 530 resistant genotypes. At site B, the disease severity of maize rust was evaluated. Field surveys were conducted on August 27, September 3, and September 8, 2021. A total of 168 samples (56 plots × 3 surveys) were included in this study, among which there were 12 for DS 1, 31 for DS 2, and 125 for DS 3. Since each plot contains numerous homogenous observations (pixels), we subdivided DS 1 plots into twelve equal parts and DS 2 plots into four equal parts, inspired by the data processing methodologies described by Damm et al. (2022). This approach was aimed at enriching and balancing the sample data. As a result, the final sample distribution for this study was adjusted to 120 samples for DS 1, 124 samples for DS 2, and 125 samples for DS 3. In site C, visual inspections were conducted every two days after the onset of the disease infection. These visual inspections revealed that areas of the disease lesions continued to expand in infected areas and remained unaffected by the disease in healthy areas.

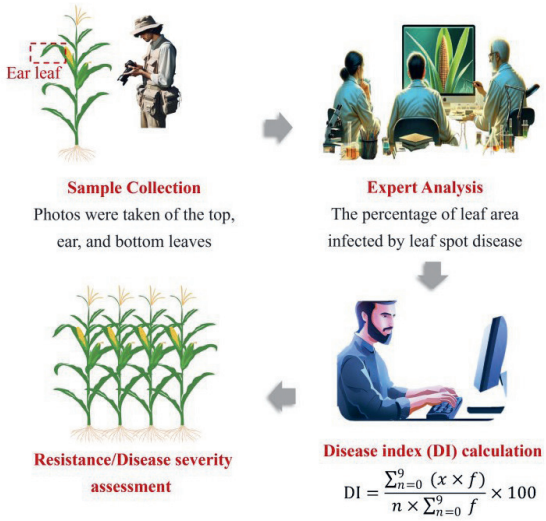


Fig. 3.3. *Flow chart of maize field leaf disease survey. x is the class determined by the proportion of a leaf affected by disease spots. The values for x are defined as 0, 1, 3, 5, 7, and 9, representing respective disease areas of 0%, 0%–5%, 6%–25%, 26%–50%, 51%–75%, and 76%–100% on a leaf; f is the total number of leaves of each class; n refers to the highest leaf disease severity (in this paper, n = 9). The resistance or disease severity can be assessed in various application scenarios based on the disease index (DI).*

3.2.3 Multispectral imagery

The details of our multispectral images obtained from flight missions are presented in Table 3.1. For sites B and D, the image capture time coincided with the field survey dates. For sites A and C, images were collected sequentially, allowing for a time-lapse view of disease progression.

High-resolution multispectral images were taken under clear skies using a RedEdge-MX mounted on a multi-rotor UAV (DJI-M600Pro, SZ DJI Technology Co., Ltd., Shenzhen, China) at the height of 30 m above ground during the local time window of 10:00-14:00. Both lateral and forward overlaps were set at 80%. The RedEdge-MX is a 5-band multispectral camera, including blue band (B: 465–485 nm), green band (G: 550–570 nm), red band (R: 663–673 nm), red-edge band (Re: 712–722 nm), and near-infrared band (NIR: 820–860 nm). A standard Micasense panel, captured at the beginning and end of each flight, was used to convert raw images into reflectance images.

Table 3.1 Overview of research sites and data collection schedule

Site	Location	Disease Type	Study Year	Survey Timing	Survey Outputs	Image Collection Schedule
A	Xinxiang	Leaf spot	2021	Aug. 21	Resistance	July 31, Aug. 4, Aug. 14, Aug. 21, Sep. 1
B	Xinxiang	Rust	2021	Aug. 2, Sep. 3, Sep. 8	DI/DS	Aug. 27, Sep. 3 , Sep. 8
C	Yuanyang	Leaf spot	2022	N/A	N/A	Aug. 2, Aug. 4, Aug. 6, Aug. 8, Aug. 10, Aug. 12, Aug. 14, Aug. 17, Aug. 24, Aug. 26, Sep. 1 (DAI 0, 2, 4, 6, 8, 10, 12, 15, 22, 24, 30)
D	Yuanyang	Leaf spot	2022	Aug. 24	DI/Resistance	Aug. 24

DI: disease index; DS: disease severity; DAI: day after infections; N/A: not applicable. Each site or output serves as an independent dataset for evaluating the performance of the DSI across various scenarios.

3.2.4 Simulation data

This paper used radiative transfer models to estimate the effects of structural parameters and leaf pigment contents on spectral reflectance and VIs. The application of radiative transfer models aimed to understand the responses of spectral reflectance and VIs to biochemical and structural changes (Kattenborn et al., 2019). Understanding these responses is crucial for developing a new canopy index sensitive to target biochemical changes during early maize leaf disease occurrence.

The canopy reflectance of a maize field was simulated by coupling the leaf-level PROSPECT-D (Féret et al., 2017) model with the canopy-level LESS model (Qi et al., 2019). PROSPECT-D is a radiative transfer model for broadleaf crops that can simulate the reflectance of leaves based on information on leaf pigments such as Anth, C_{ab}, and C_{ar} (Féret et al., 2017). The LESS model is a realistic three-dimensional (3D) canopy radiation transfer model based on a ray tracing algorithm that accurately describes interactions between solar radiation and heterogeneous surfaces (Qi et al., 2019). In LESS, crop planting scenes can be described by adjusting different planting distances to describe various planting densities in a realistic maize field (***Fig. 3.4***). The combination of PROSPECT-D and LESS model was used to evaluate the effects of PS and leaf biochemical parameters (C_{ab}, C_{ar}, and Anth) on spectral reflectance and VIs. The inputs of the PROSPECT-D and LESS models used in this study are shown in Table 3.2. These different parameters were used to construct synthetic images. The mean

reflectance of these images was used to analyze responses of spectral reflectance to the changes in biochemical and structural parameters.

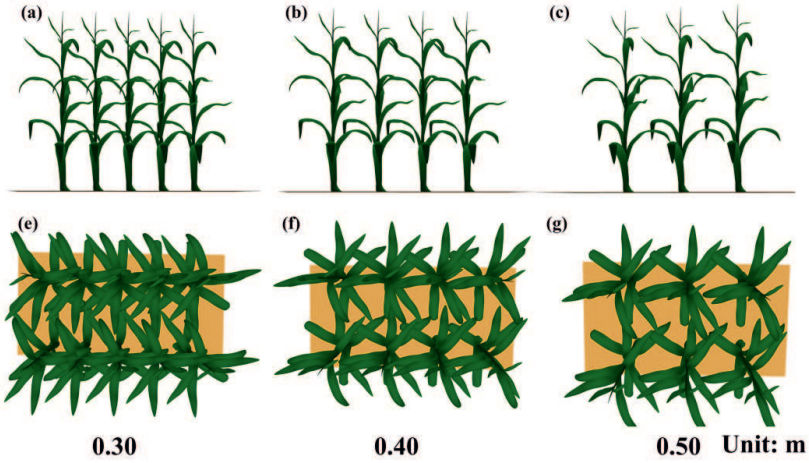


Fig. 3.4. *3D scenes generated with LESS to simulate variations in plant spacing (PS). The top row corresponds to a horizontal view, while the bottom row corresponds to a top view. (a) and (e) depict a planting spacing of 0.30 m, (b) and (f) illustrate a spacing of 0.40 m, as well as (c) and (g) show a spacing of 0.50 m.*

Table 3.2 The inputs of PROSPECT-D and LESS

Variable	Units	Acronym	Values	Steps
PROSPECT-D				
Leaf structural parameter	-	N	1.5	-
Dry matter content	g/cm²	C_m	0.012	-
Brown pigment content	-	-	0	-
Carotenoids content	µg/cm²	C_{ar}	0–60	10
Chlorophyll content	µg/cm²	C_{ab}	15–70	5
Anthocyanin content	µg/cm²	Anth	0–5	1
Water equivalent thickness	cm	C_w	0.015	-
LESS				
Plant spacing	m	PS	0.2–0.55	0.05

Note: Other inputs in the LESS model are shown in Table S3.1 in the supplemental information.

3.3 Methods

The methodology framework of this paper is shown in ***Fig. 3.5***. The framework including four key processing: developing simulation data using PROSPECT-D and LESS, establishing the DSI and evaluating the performance of DSI using both simulation data and UAV-collected images.

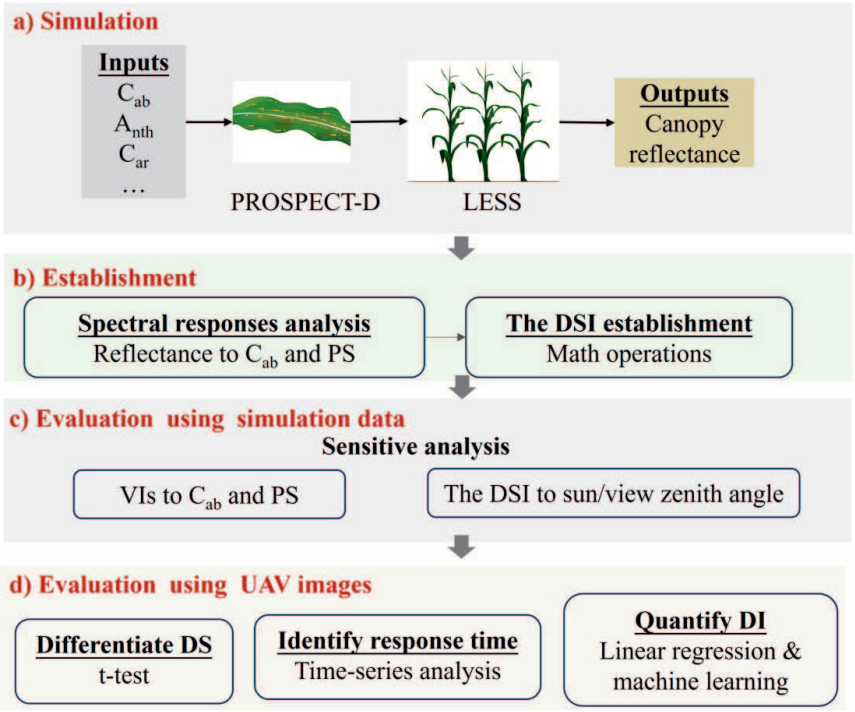


Fig. 3.5. *Flowchart of monitoring early maize leaf disease using PROSPECT-D and LESS models.*

3.3.1 Analysis of spectral and pigment dynamics after disease infection

This section aims to analyze the dynamics of spectral and pigment changes following disease infection in maize leaves, focusing on early detection and monitoring. Disease in the early stage typically exhibits constitutive changes among leaf photosynthetic pigment pools (Osdaghi et al., 2020; Zarco-Tejada et al., 2018), with increasing disease severity over time causing variations in plant structure (Berger et al., 2022). However, in the practical field, plant structures are inconsistent due to variations in PS and cultivars (Kuai et al., 2016). Therefore, features sensitive to pigments but insensitive to PS have the potential for early disease monitoring (Zhang et al., 2012c).

To validate this viewpoint, we collected time series leaf spectral data after maize leaf spot infection. An ASD Field Spec PRO 4 (Analytical spectral devices, Inc., boulder, colorado, U.S.) was equipped with a leaf clip to measure the leaf reflectance. We identified and marked 84 infected leaves for spectral measurements. We obtained reflectance spectra for each leaf at three different points on the adaxial surface (1/3, 1/2, and 2/3 of the distance from the base, respectively). An average reflectance was calculated by the spectra collected from each leaf to minimize random measurement errors. It should be noted that we only utilized 20 leaves of all the measured leaves for further analysis. That is because these leaves demonstrated a consistent increase in the

infected area and consequently showed a rise in disease severity.

The pigment was quantified by inverting the PROSPECT-D model. The C_{ab} was specifically analyzed due to its obvious response in the multispectral sensors used in this study, as compared to C_{ar} and Anth. The input variables for this model were estimated based on datasets about leaf optical properties (Rocha et al., 2019) and prior studies (Nie et al., 2023). We utilized the iterative optimization method, the fminsearch function in Matlab, to invert the PROSPECT-D model. This method was employed to pinpoint the best-simulated spectra from each model, identified as those with the lowest root mean square error (RMSE) value, following the approach of previous research (Botha et al., 2010).

The collected leaf spectra showed an obvious pattern in infected leaves on various days after infection (Fig. 3.6a, taking a selected leaf as an example). At the early stage of the disease, significant spectral alterations mainly occur in the visible region, especially the primary absorption band for pigments (Blackburn, 1999). Additionally, as disease severity increases, C_{ab} retrieved by PROSPECT-D revealed a consistent reduction (Fig. 3.6b). This finding confirmed that PROSPECT-D model-based C_{ab} is consistent with the process of disease infection.

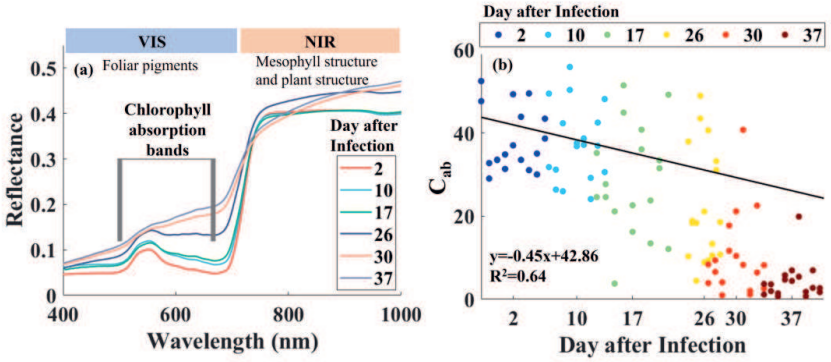


Fig. 3.6. *Changes of measured spectrum (a) and model-based chlorophyll content (b) (C_{ab} [μg/cm²]) from an infected leaf on various days after infection.*

3.3.2 Responses of spectral reflectance to pigments content and PS

The average reflectance of images simulated by the radiative transfer model demonstrated responses of multispectral reflectance to pigments content and PS (Fig. 3.7). The reflectance of band B is lightly affected by PS. The G varies with different levels of C_{ab} and Anth. The R is primarily influenced by PS, with a slight sensitivity to C_{ab}. The Re is primarily influenced by C_{ab} and has a minor sensitivity to PS. The NIR varies with different levels of PS. Therefore, the Re and G are selected to be combined with other bands to create a new index that is sensitive to pigments but not to PS.

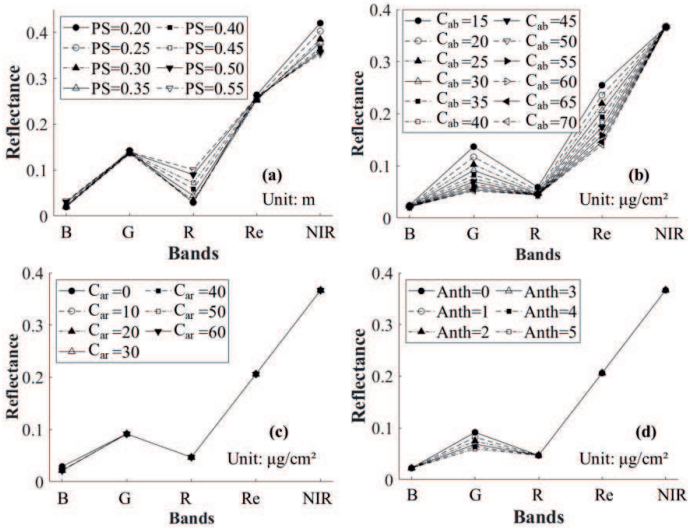


Fig. 3.7. *Simulations by coupling PROSPECT-D and LESS model to evaluate the effects of plant spacing (PS), chlorophyll content (C_{ab}), carotenoids content (C_{ar}), and anthocyanin content (Anth) on the reflectance used in this study. B, G, R, Re, and NIR are blue band (465–485 nm), green band (550–570 nm), red band (663–673 nm), red-edge band (712–722 nm), and near-infrared band (820–860 nm), respectively.*

3.3.3 Establishment of the DSI

Building upon our spectral response analysis in section 3.3.2, we identified Re and G reflectance as being particularly sensitive to variations in C_{ab} and Anth while exhibiting minimal sensitivity to PS. These findings facilitated the creation of the DSI. The DSI encompasses the following three critical components:

(1) Normalized pigment sensitivity component. We crafted a normalized index using Re plus G with NIR. The NIR is known for distinguishing between vegetative and non-vegetative surfaces (Brest and Goward, 1987; Zhan et al., 2007). Normalization mitigates radiometric differences across remote sensing images, rendering data from diverse temporal and sensor sources comparable for analysis (Chen et al., 2005; Leach et al., 2019). Since NIR is sensitive to PS, the normalized component simultaneously accounts for pigment and PS variations.

(2) PS sensitivity reduction component. To mitigate the DSI's sensitivity to PS, we included the B, which has demonstrated a similar range sensitivity to PS as the Re. These spectral characteristics lead to the ratio formulation $R_B / (R_G + R_{Re})$, where the similar trends in both the numerator (B) and denominator (Re) could approximately cancel out during calculation, thus reducing the influence of PS. Due to the saturation resistance of Re and G, this formulation has a wider C_{ab} sensitivity range (Zhang et al., 2022).

(3) Gain factor (K). To normalize the DSI values within a practical range, primarily

between 0 and 1 for vegetative areas, we introduced a gain factor, K. Based on the range of simulation results, we set K = 10 for our study. This scaling ensures the DSI is dimensionless and comparable across different datasets.

The DSI is constructed as follows:

$$DSI = K \times \frac{R_{NIR} - R_G - R_{Re}}{R_{NIR} + R_G + R_{Re}} \times \frac{R_B}{R_G + R_{Re}} \quad (1)$$

3.3.4 Evaluations of VIs in various disease monitoring scenarios

To evaluate the performance of the DSI in maize disease monitoring, we compared it to VIs sensitive to C_{ab} and those used in previous plant disease monitoring studies (Table 3.3). Our comparison focused on three aspects: the ability of these indices to differentiate between different rust severity, the correlation with DI, and the response time after disease infection (Table 3.4).

In the first aspect, the t-test with the *p*-value was used to determine significant differences between different maize rust severity, including not considered statistically significant ($p > 0.05$, ns), statistically significant ($p < 0.05$, *), very statistically significant ($p < 0.01$, **), and extremely statistically significant ($p < 0.001$, ***).

In the second aspect, simple linear regression models were employed to evaluate the performances of VIs in quantifying DI in maize leaf diseases. The dataset was initially divided into a training set (80%) and a testing set (20%). We determined the linear equations for each VI and DI pair within the training set. The significance of the regression variables was interpreted by *p*-values. The performances of these linear equations were then assessed using three metrics in the testing set: coefficient of determination (R^2), root mean square error (RMSE), and relative root mean square error (rRMSE) (Wilson and Sagan, 1995).

In the third aspect, time-series analysis was used to evaluate the response time of VIs to maize diseases. This involved a normalization approach that accounted for canopy structure effects on the hyperspectral features. We calculated the difference between feature values on the day after infection and the day before infection. The time series changes in each feature were then analyzed. To determine the impact of leaf disease on maize plants, we utilized statistical measures: 95% confidence intervals based on a z-distribution and effect size using Cohen's d. An effect size larger than 0.8 (Charach et al. 2011) indicates a substantial difference between healthy and infected plants. The start of consecutive substantial differences (|effect sizes| ≥ 0.8) marks the VI's initial response to the disease.

Table 3.3 Vegetation indices (VIs) used in this paper

VIs	Abbreviation	Equal	Reference
VIs sensitive to C_{ab}			
Disease sensitive index	DSI	$10[(R_{NIR}-R_G-R_{Re})/(R_{NIR}+R_G+R_{Re})][R_B/(R_G+R_{Re})]$	This paper-
Red-edge normalized difference vegetation index	$NDVI_{re}$	$R_{NIR}-[R_{Re}/(R_{NIR}+R_{Re})]$	(Gitelson and Merzlyak, 1994)
Red-edge chlorophyll index	CI_{re}	$R_{NIR}/R_{Re}-1$	(Gitelson et al., 2005)
MERIS terrestrial chlorophyll index	MTCI	$(R_{NIR}-R_{Re})/(R_{Re}-R_R)$	(Dash and Curran, 2004)
Transformed chlorophyll absorption in reflectance index	TCARI	$3[(R_{Re}-R_R)-0.2(R_{Re}-R_G)/(R_{Re}/R_R)]$	(Haboudane et al., 2002)
Datt 99	Datt99	$(R_{NIR}-R_{Re})/(R_{NIR}-R_R)$	(Datt, 1999)
TCARI/optimized soil-adjusted vegetation index	TCARI/OSAVI	$TCARI/[(1+0.16)(R_{NIR}-R_R)/(R_{NIR}+R_R+0.16)]$	(Wu et al., 2008)
Red reflectance of the vegetation	RED_V	$R_R\times[(R_{NIR}-R_R)/(R_{NIR}+R_R)]^2$	(Liu et al., 2020d)
VIs used for monitoring plant disease in previous papers			
Chlorophyll/carotenoid index	CCI	$(R_G-R_R)/(R_G+R_R)$	(Gamon et al., 2016)
Simple ratio pigment index	SRPI	R_B/R_R	(Penuelas et al., 1995)
Health-index	HI	$(R_G-R_{Re})/(R_G+R_{Re})-(0.5\times R_{Re})$	(Mahlein et al., 2013)
Normalized difference vegetation index	NDVI	$(R_{NIR}-R_R)/(R_{NIR}+R_R)$	(Rouse et al., 1974)

Table 3.4 Summary of statistical methods and outcomes

Aim	Statistical Methods	Description	Outcome/Metric
Differentiation of rust severity	t-test	Used to determine significant differences in maize rust severity	- not considered statistically significant (ns): $p > 0.05$ - statistically significant (*): $p < 0.05$ - very statistically significant (**): $p < 0.01$ - extremely statistically significant (***): $p < 0.001$
Quantifying DI in maize leaf diseases	Simple linear regression	Evaluated the performance of VIs in quantifying DI	- Linear equations for each VI and DI pair - Significance of regression variables: *p*-values - Coefficient of determination: R^2 - Root mean square error: RMSE - Relative root mean square error: rRMSE
Response time to disease infection	Time-series analysis	Assessed the response time of VIs to maize leaf diseases	- 95% confidence intervals: z-distribution - Effect size: Cohen's d

3.4 Results

3.4.1 Sensitive analysis of VIs using simulated data

3.4.1.1 Sensitivity of VIs to C_{ab} and PS

The VIs calculated from the average reflectance of synthetic images displayed the response of these indices to C_{ab} and PS (Fig. 3.8). For indices sensitive to C_{ab}, the DSI, MTCI, and Datt99 showed a strong correlation with C_{ab}, while their sensitivity to PS alterations was notably subdued. In contrast, $NDVI_{re}$, CI_{re}, TCARI, TCARI/OSAVI, and RED_v responded to both PS and C_{ab}. Meanwhile, VIs used in previous plant disease monitoring studies, such as CCI, SRPI, and NDVI, were responsive to both PS and C_{ab}, while HI displayed insensitivity to PS at C_{ab} levels under 35 μg/cm².

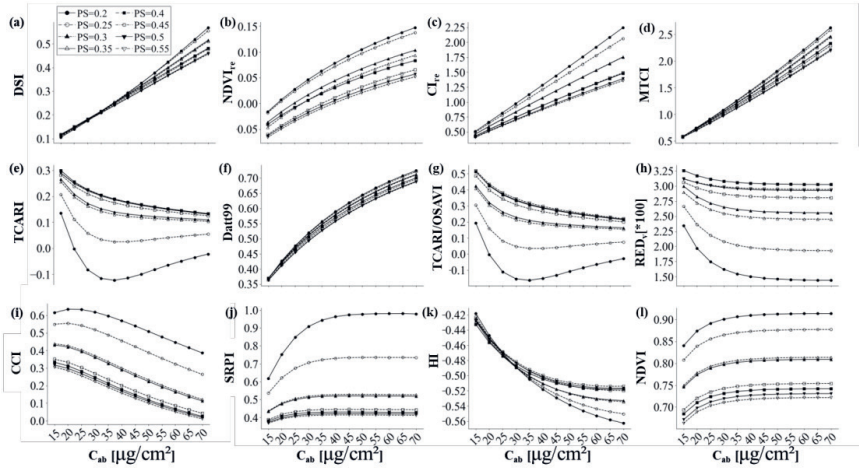


Fig. 3.8. *Sensitivity of vegetation indices (VIs) to plant spacing (PS) and Chlorophyll content (C_{ab}) using simulations based on PROSPECT-D and LESS model. (a)–(h) represent VIs sensitivities to C_{ab}, including DSI, $NDVI_{re}$, CI_{re}, MTCI, TCARI, Datt99, TCARI/OSAVI, and RED_v. (i)–(l) show VIs used in previous plant disease monitoring studies, including CCI, SRPI, HI, and NDVI.*

3.4.1.2 Sensitivity of the DSI to sun/view zenith angle

The changes of solar zenith angle (SZA) and view zenith angle (VZA) induce little difference in the DSI, as shown in Fig. 3.9. The curves for VZA and SZA were relatively flat, indicating that the changes in these parameters have a minor impact on the DSI. In contrast, the curve for C_{ab} showed a more pronounced trend, signifying a higher sensitivity of the DSI to the change of C_{ab}.

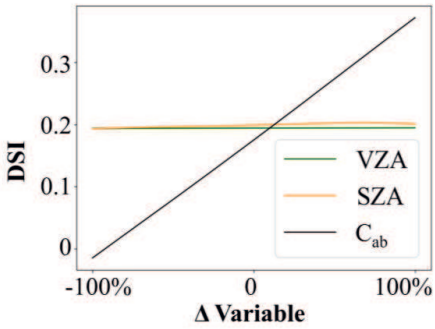


Fig. 3.9. *Sensitivity of the DSI to variations in different parameters. View zenith angle (VZA) variation range: 0°–20°, reference value: 10°; solar zenith angle (SZA) variation range: 20°–60°, reference value: 40°; Chlorophyll content (C_{ab}) variation range: 10–70 μg/cm², reference value: 35 μg/cm².*

3.4.2 Performances of VIs in differentiating DS

The ability of VIs to differentiate disease severity was scrutinized using a t-test (***Fig.***

3.10). All chlorophyll-sensitive VIs showed an extremely significant capacity to identify high disease severity when comparing DS 1 to DS 3 and DS 2 to DS 3. However, these VIs showed different patterns in discerning between DS 1 and DS 2. Specifically, $NDVI_{re}$ and TCARI/OSAVI did not show a significant difference with a *p*-value greater than 0.05, TCARI and RED_v were statistically significant ($p < 0.05$), and the DSI, CI_{re}, MTCI, and Datt99 were found to be extremely statistically significant ($p < 0.001$). Contrastingly, VIs previously validated as sensitive to other diseases manifested varying capacities in distinguishing the severity of rust disease. These VIs showed an extremely significant capacity to identify DS 2 when compared with DS 1 and DS 3. However, these VIs showed different patterns in discerning between DS 1 and DS 2. In specific, NDVI did not show a significant difference; CCI was statistically significant ($p < 0.05$), and SRPI and HI were found to be extremely statistically significant ($p < 0.001$).

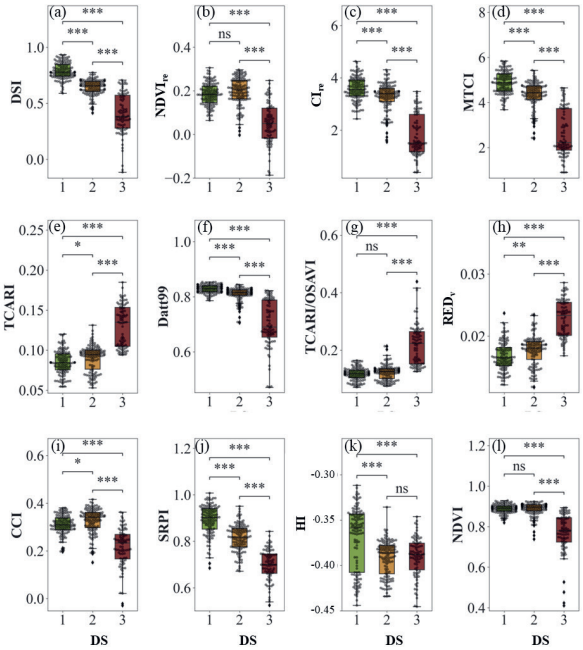


Fig. 3.10. *Significant differences in vegetation indices (VIs) across various rust disease severity (DS): low (DS 1), medium (DS 2), and high (DS 3). (a)–(h): VIs sensitive to C_{ab}, including DSI, $NDVI_{re}$, CI_{re}, MTCI, TCARI, Datt99, TCARI/OSAVI, and RED_v. (i)–(l): VIs were used in previous plant disease monitoring studies, including CCI, SRPI, HI, and NDVI. Distinctions were made based on the p-value: not considered statistically significant ($p > 0.05$, ns), statistically significant ($p < 0.05$, *), very statistically significant ($p < 0.01$, **), and extremely statistically significant ($p < 0.001$, ***).*

3.4.3 Performances of VIs in quantifying DI

The relationships between VIs and DI in maize fields infected with rust are shown in

Fig. 3.11. The performances of chlorophyll-related VIs outperformed other indices used in previous disease monitoring studies. The R^2 for chlorophyll-related VIs ranged between 0.38 and 0.69, with RMSE values from 0.13 to 0.22. In contrast, indices validated for sensitivity to other diseases showed a broader range of R^2 from 0.11 to 0.63, with RMSE values stretching from 0.16 to 0.24. DSI, MTCI, and SRPI demonstrated superior performance with lower RMSE and rRMSE alongside higher R^2 values among the tested indices. Specifically, DSI achieved the highest accuracy (R^2=0.69, RMSE=0.13).

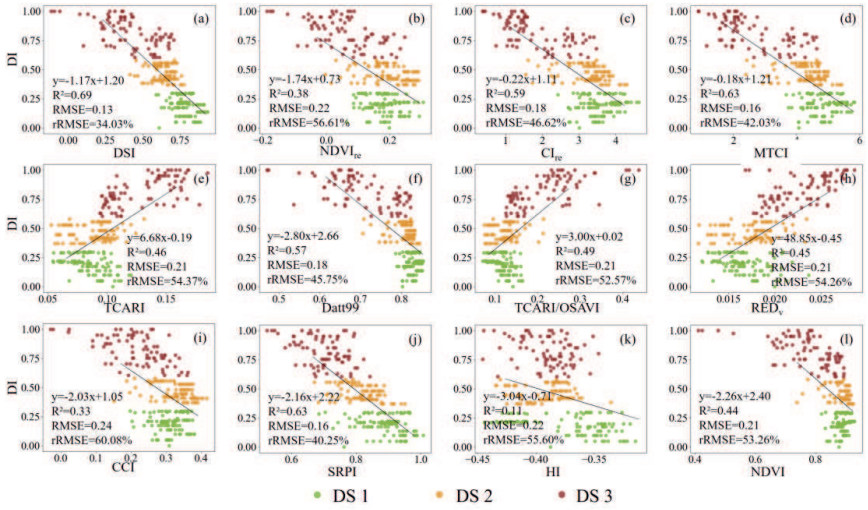


Fig. 3.11. *Relationships between vegetation indices (VIs) and disease index (DI) in maize rust infected fields. The low (DS 1), medium (DS 2), and high (DS 3) severity of disease were represented in colors of green, yellow, and red, respectively. All regressions were statistically significant ($p < 0.05$).*

The relationships between VIs and DI in fields infected with maize leaf spot were presented in Fig. 3.12. Similar to the findings in rust infection fields, chlorophyll-related VIs were more effective than disease sensitive indices used in previous studies. The R^2 values for chlorophyll-related VIs ranged from 0.25 to 0.62. Other disease sensitive indices ranged more variably in effectiveness, with R^2 values from 0.07 to 0.58. Among them, the DSI attained the highest accuracy with the highest R^2 value (R^2=0.62), followed by SRPI (R^2=0.58).

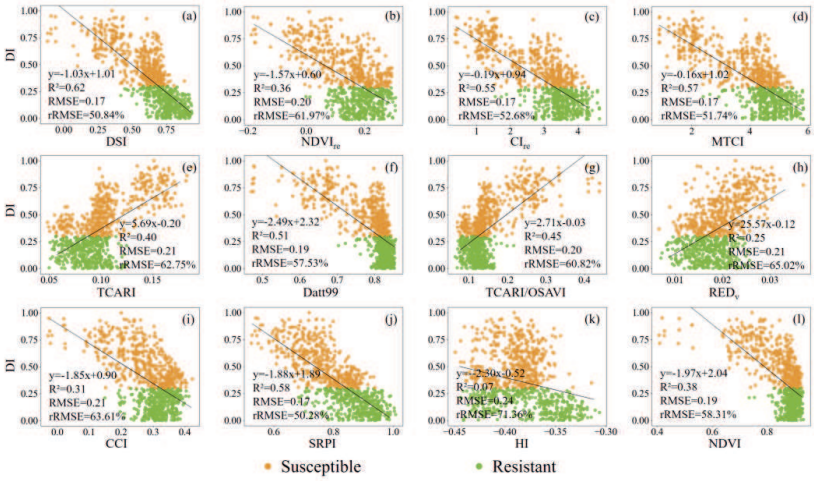


Fig. 3.12. *Relationships between vegetation indices (VIs) and disease index (DI) in maize leaf spot infected fields. The resistant and susceptible genotypes were represented in green and yellow colors. All regressions were statistically significant ($p < 0.05$).*

2.6.2 Current status and focus

The number of studies monitoring crop diseases using hyperspectral techniques increased sharply from 2006 to 2024 (Fig. 2.3B). Most publications were from The United States of America, followed by China, France, Australia, India, Spain, and Italy (Fig. 2.3A). The compilation identifying the most frequently mentioned species, types of diseases, and features are presented in Fig. 2.3C. Wheat, rice, olive, potato, and oil palm, respectively were the crops most studied in the papers selected. Blight, rust (stripe and yellow rusts), mildew (powdery and downy mildews), rot (stem and root rots), and spot (target, bacterial, and leaf spots) were the five most common types of diseases investigated in the studies. Blights, including fusarium head, fire, leaf, and late blights, were particularly prevalent. Research on each type of hyperspectral feature indicated that spectral features were most used. Attention has also recently been given to pigment concentration and solar-induced chlorophyll fluorescence based on physical models and hyperspectral-data inversion.

3.4.4 Response time of VIs to maize leaf disease

The analysis of temporal multispectral imagery to differentiate resistance and susceptibility of leaf spot disease in site A revealed distinct patterns (Fig. 3.13). Only the DSI demonstrated a consistently substantial difference (|effect sizes| ≥ 0.8) from DAI 12. TCARI, RED_v, CCI, and NDVI showed a consistent substantial difference from DAI 19. Datt99, and SRPI exhibited substantial differences only on individual days, failing to show a continuous trend. Other indices did not show substantial differences in the period of observation.

The analysis of temporal multispectral imagery to differentiate infected and healthy areas to leaf spot disease in site C was shown in ***Fig. 3.14***. DSI, TCARI, CCI, SRPI,

and NDVI presented substantial differences over three or more consecutive time points. The DSI exhibited the earliest response to infection from DAI 10, followed by CCI from DAI 12, and NDVI from DAI 15. TCARI began to respond to infection from DAI 22, while SRPI responded from DAI 24. Other indices did not show continuously substantial differences within the period of observations.

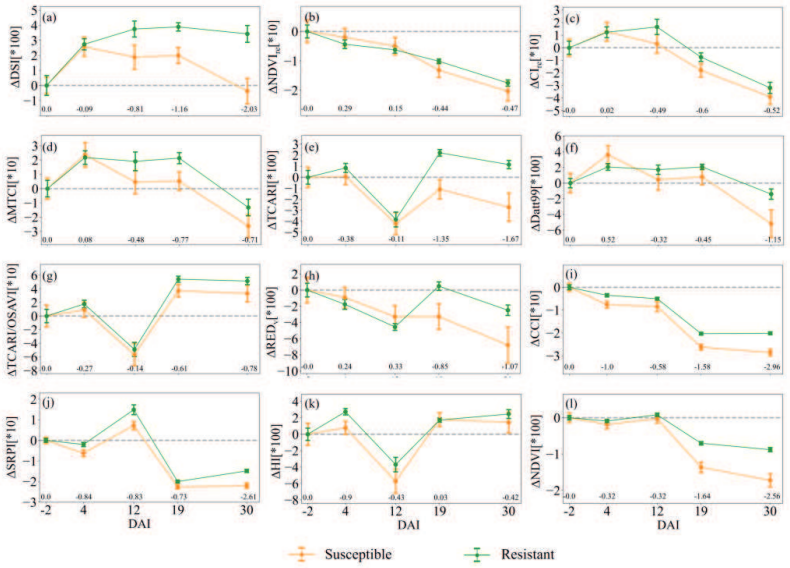


Fig. 3.13. *Changes of vegetation indices (VIs) on different days after infection (DAIs) in maize leaf spot infected fields in 2021 (site A). Error bars represent the 95% confidence interval, and values represent the effect size using Cohen's d.*

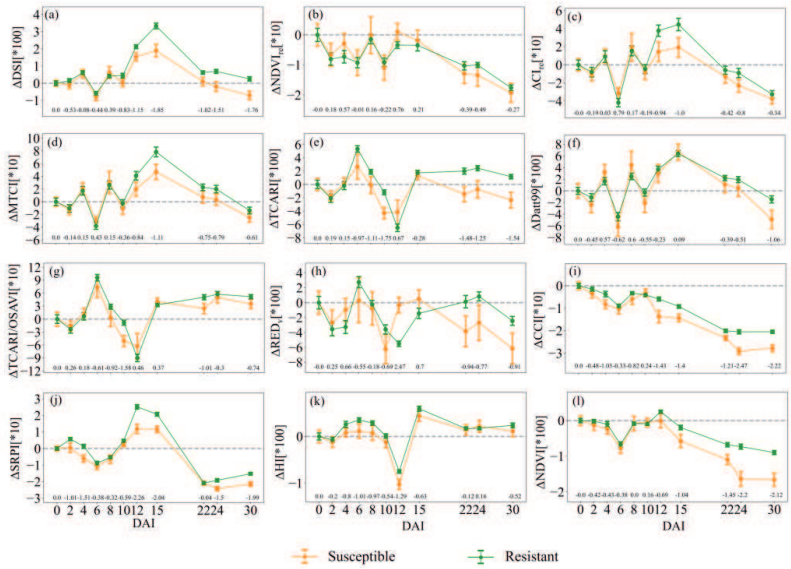


Fig. 3.14. *Changes of vegetation indices (VIs) on different days after infection (DAIs) in maize leaf spot infected fields in 2022 (site C). Error bars represent the 95% confidence interval, and values represent the effect size using Cohen's d.*

3.5 Discussion

3.5.1 Consistency of measured and simulated reflectance

The reflectance of soil, healthy canopy, low leaf disease severity canopy, and high leaf disease severity canopy from remote sensing imagery was visually interpreted (Fig. S3.1). The canopy reflectance of low and high disease severity at G, R, and Re ranges was higher than that of a healthy maize canopy, and this symptom was attributed to the degradation of C_{ab} caused by maize leaf disease. This characteristic is also generally presented at an early stage of other diseases, such as rust in sugar beet (Mahlein et al., 2013), laurel wilt disease in avocado (De Castro et al., 2015), and *Xylella fastidiosa* infection in olive (Zarco-Tejada et al., 2018). At the NIR region, the canopy reflectance of the high severity canopy was slightly lower than that of the healthy and low severity canopies due to the significant reduction of green leaves. This characteristic was also observed in the canopy of rice blast (Tian et al., 2023) and *Xylella fastidiosa* infection in olive orchards (Hornero et al., 2020). These trends of spectral response were consistent with our simulated spectra and our hypothesis that the pigment changes happened in an early disease stage. As the disease progresses, the structural parameters of the crop begin to change. These results suggest that simulated spectra caused by pigment content variations can represent spectral changes caused by maize leaf disease, and it is feasible to construct a vegetation index using simulated spectra.

3.5.2 Interpretability of remote sensing features to biochemical and structural characteristics

To understand the way spectral reflectance and VIs respond to biochemical and structural characteristics, the performances of these remote sensing features were evaluated within the simulation dataset. This dataset was constructed by coupling PROSPECT-D and LESS models. Multispectral imagery with broadband has demonstrated an apparent capacity to reflect changes in C_{ab} and plant structure (i.e., modifications in leaf area index and fractional vegetation cover induced by variations in PS). Nevertheless, these reflectance measurements exhibit a weak sensitivity to changes in Anth and are insensitive to variations in C_{ar} levels. VIs developed for monitoring C_{ab} exhibited variability patterns upon various C_{ab} and PS. The DSI, in line with MTCI, and Datt99, has shown a pronounced sensitivity to C_{ab} while remaining relatively unaffected by alterations in PS. Additionally, the DSI was slightly affected by sun/view zenith angel compared to C_{ab}.

The degradation of plant pigments due to biotic stresses can cause green leaves to yellow and fade, and even result in the death of the entire plant when the leaf disease becomes high severity level. Simultaneously, various planting conditions and cultivars can also lead to differences in crop morphology and fractional vegetation cover. Therefore, it is crucial to identify features sensitive to pigments but not structure in monitoring early disease.

3.5.3 Performance of the DSI in monitoring maize leaf disease

Based on data gathered from four distinct experimental sites in two consecutive years (2021, 2022), our investigations into the performances of the DSI in monitoring maize leaf disease have yielded significant insights. Notably, the DSI has emerged as the most accurate tool in quantifying DI, showing the earliest substantial response to disease infection, appearing as early as DAI 12 in 2021 and DAI 10 in 2022. These findings strongly indicate the scalability and adaptability of the DSI across diverse environments, highlighting its potential for early-stage maize leaf disease monitoring.

Furthermore, our study has revealed promising results with DSI-like indices such as MTCI and Datt99, which show promising results in different disease monitoring scenarios. This effectiveness further solidifies that plant disease at an early stage is primarily marked by changes in C_{ab} levels. Meanwhile, chlorophyll-sensitive VIs show superior capability in disease monitoring applications compared to indices previously used for other disease monitoring. These findings underscore the potential of specific chlorophyll-related VIs for precise and reliable monitoring of maize leaf diseases at an early stage. Therefore, developing and utilizing an index sensitive to C_{ab} changes is advantageous for the early monitoring maize leaf disease.

The sensitive indices identified in previous disease monitoring studies showed poor sensitivity to maize leaf diseases in this study. These indices are usually derived from specific diseases in specific scenarios. The mechanisms of disease onset vary among different diseases, leading to poor transferability of indices between different diseases (Terentev et al., 2022a; Zhang et al., 2020).

Our findings suggest that the DSI could serve as a stable and suitable solution for early maize rust and leaf spot monitoring. The DSI enhances its correlation with C_{ab} by

utilizing Re reflectance in conjunction with G. This enhancement is crucial as C_{ab} is a key indicator of disease onset. Additionally, the negative correlation between G reflectance and Anth further augments the DSI's sensitivity to Anth. Anth has been widely acknowledged for revealing disease occurrence, even in its early or asymptomatic stages (Calderon et al., 2013; Hornero et al., 2021; Zarco-Tejada et al., 2018). Therefore, leveraging these relationships makes the DSI an effective tool for pigment and disease detection.

3.5.4 Limitations and future work

The DSI is developed using commonly available broad-band multispectral sensors, offering a cost-effective and simple solution for data acquisition and analysis in practical agricultural production. The ability of the DSI in monitoring early disease could guide precise pesticide application, reduce pesticide usage and enhance food quality. Additionally, distinguishing maize resistance can aid breeders in rapidly selecting target genotypes. However, this study has only tested the DSI in two mainstream maize diseases: rust and leaf spot. The feasibility of the DSI in other maize leaf diseases and crops remains unknown. For broader agricultural uses, the robustness of the DSI should be validated under different stress (such as water and nitrogen deficit) conditions across a wider range of crops and diseases in the future. Moreover, the DSI's sensitivity to pigments changes caused by early-stage leaf disease means it lacks disease specificity and cannot differentiate between diseases that cause similar pigment changes. Its broad-band properties also challenge capturing more spectral details, such as carotenoid changes, which provide chemical defenses against biological stress (Jomova and Valko, 2013). Although experimental fields in 2021 and 2022 have been utilized to ascertain the DSI's performance, future endeavors must thoroughly evaluate the DSI's performance under a spectrum of environmental conditions.

3.6 Conclusion

This study highlights the effectiveness of a chlorophyll-sensitive index in monitoring maize leaf diseases. The changes in spectral reflectance and VIs under varying pigment content and PS were successfully simulated by coupling PROSPECT-D and LESS models. The results show that Re and G bands were slightly affected by PS but were sensitive to leaf pigments. Therefore, the DSI was proposed, showing higher sensitivity to changing C_{ab} while less affected by alterations in PS and solar/view zenith angles within our simulated dataset. Further empirical evaluation of the DSI has been tailored for diverse disease monitoring scenarios. Statistically robust evidence ($p < 0.001$) supports the DSI's discriminative capability in distinguishing between low maize rust severity and medium. Compared with other VIs, the proposed DSI has shown stronger relationship with the DI for rust infected field ($R^2 = 0.69$) and leaf spot infected field ($R^2 = 0.62$). Temporal analysis of multispectral imagery using the DSI consistently revealed significant differences at DAI 12 in differentiating resistant/susceptible and DAI 10 in differentiating infected/healthy areas in leaf spot disease infected field. These results support the use of DSI and canopy imagery for monitoring the onset of disease

infection, and for facilitating decision-making about disease identification in breeding experiments and control measures on farms.

3.7 Supplementary information

Additional tables and figures supporting this chapter are available online. They can be accessed via the QR code or at the following URL: PhD-thesis/chapter3_DSI-supplymentary.pdf at main · Briya1990/PhD-thesis

4

Comprehensive analysis of hyperspectral features for monitoring canopy maize leaf spot disease

This chapter is based on:
Bai, Y., Nie, C., Yu, X., Gou, M., Liu, S., Zhu, Y., Jiang, T., Jia, X., Liu, Y., Nan, F., Li, L., Tekinerdogan, B., Song, Y., Liu, Q., & Jin, X. (2024). Comprehensive analysis of hyperspectral features for monitoring canopy maize leaf spot disease. Computers and Electronics in Agriculture, 225, 109350

Abstract

Accurate quantification of hyperspectral features altered by plant disease infection is pivotal for effective disease management. However, the sensitivity of hyperspectral features to plant disease progression remains elusive, primarily because these features are often influenced by plant growth and environmental factors in addition to the specific disease. This study explores the sensitivity of biophysical and spectral features as indicators for maize adaptation to leaf spot disease. Using high-resolution UAV hyperspectral imaging, we captured maize adaptation dynamics over 30 days post-infection. We evaluated the sensitivity and importance of hyperspectral features for disease monitoring, including biophysical parameters retrieved by the PROSAIL model, and spectral features, including spectral reflectance, vegetation indices (VIs), and wavelet features (WFs). Our findings reveal that WFs first indicate disease response as early as 6 days after infection (DAI), followed by VIs at DAI 8, and variations in chlorophyll content (C_{ab}) become apparent by DAI 10. The C_{ab}, plant senescence reflectance index (PSRI), and normalized photosynthetic reflectance index (NPRI) are determined to be important features at the early stage of the disease. Our experimental results show that the different feature sets are complementary at the early and severe stages of the disease. Our classification models integrating C_{ab}, VIs, and WFs showed higher overall accuracy than models using only spectral features or VIs, with a maximum improvement of 9.36%. However, these feature sets are redundant in the mild and initial severe disease stages, where models using only spectral features achieve the highest overall accuracy of 86.21%. This study underscores the novel insights by offering an understanding of plant responses to disease infection and enhancing early detection strategies.

4.1 Introduction

Maize (corn, *Zea mays L.*) is one of the most widely demanded and rapidly growing grains globally (Martinez and Fernandez, 2019; Yan and Tan, 2019). It is susceptible to numerous plant diseases, with as many as 112 reported worldwide (Kumar et al., 2014). Leaf spot, a prevalent disease across different regions, has led to significant yield losses in vulnerable maize germplasm (Dhami et al., 2015a; Gonçalves et al., 2013). Traditional methods for monitoring leaf spot rely on visual inspection by experts in the field, which is time-consuming, labor-intensive, and challenging to implement on a large scale.

With the advent of remote sensing technology, particularly hyperspectral imaging, a powerful tool has emerged that is capable of non-invasive, large-scale monitoring of plant disease (Chen et al., 2017; Hornero et al., 2020). Hyperspectral imaging's fine spectral resolution holds the promise of monitoring and diagnosing plant diseases (Mahlein et al., 2018; Thenkabail et al., 2004). This technology captures a broad spectrum of information, potentially revealing intricate details about plant physiology and health that are invisible to the naked eye or through traditional multispectral imaging (Mahlein et al., 2013; Tian et al., 2021). Recent research in hyperspectral disease detection has predominantly focused on constructing machine learning models using hyperspectral features. For instance, Huang et al. (2022) underscored the necessity of choosing suitable machine learning methods and feature selection algorithms to enhance the accuracy of early and mid-term remote sensing monitoring of wheat stripe rust. Tian et al. (2021) demonstrated that a limited yet carefully chosen set of spectral features, identified through the machine learning based sequential floating forward selection (ML-SFFS) algorithm, effectively distinguishing rice leaves infected with leaf blast. Similarly, Luo et al. (2021) evidenced that machine learning models based on vegetation indices are highly promising for surveilling maize dwarf mosaic virus infections. However, remote sensing captures a multifaceted array of surface information, extending beyond vegetation and diseases to include elements like plant growth, environmental conditions, and so on (Weiss et al., 2020). These additional factors add complexity when interpreting hyperspectral features for disease monitoring and model transferability in canopy scales.

Hyperspectral features widely used in plant disease tasks primarily include biophysical parameters and spectral features (Hernandez-Clemente et al., 2019). Biophysical parameters such as leaf pigment content, derived from radiative transfer models, have been used as an indicator of vegetation health (Hornero et al., 2021; Tian et al., 2021; Zarco-Tejada et al., 2018). Increasing disease severity over time can ultimately cause variations among leaf photosynthetic pigment pools, known as constitutive changes (Hernandez-Clemente et al., 2019). Additionally, spectral features like spectral reflectance, vegetation indices (VIs), and wavelet features (WFs) have proven effective for plant disease monitoring (Camino et al., 2021; Tian et al., 2021). Nonetheless, their interpretation is challenged by illumination, structural, and

influenced by different crop varieties and growth stages (Barton and North, 2001; Damm et al., 2015; Myneni et al., 1995). Furthermore, knowledge of causal relations between dynamics in plant response to leaf spot and required sensitivity of hyperspectral features is not fully exploited yet. Therefore, it is urgent to comprehend the sensitivity of different hyperspectral features for monitoring plant disease in canopy scales.

In this study, we hypothesize that the complexity of observations in plant disease monitoring obscures the inherent sensitivity of these observations for plant-pathogen relationships during leaf spot infection. Therefore, it is crucial to disentangle unwanted sensitivities from the targeted features for remote sensing-based classification in monitoring disease. We designed leaf spot infection experiments in three maize fields. The objectives are to (i) unravel the temporal sensitivity of various hyperspectral features as disease severity increased using a time series analysis approach, (ii) analyze the importance of hyperspectral features (biophysical parameters and spectral features) in response to leaf spot infection, (iii) build classification models for assessing maize resistance to leaf spot disease based on the selected features.

4.2 Materials and methods

4.2.1 Experimental design

The study area was in Xinxiang City, China, a warm temperate continental monsoon climate characterized by hot and rainy and breed disease in summer. This region belongs to North Henan Plain (Yubei Plain), with maize as the main crop. Three sites were selected in this study: sites A, B, and C (Fig. 4.1).

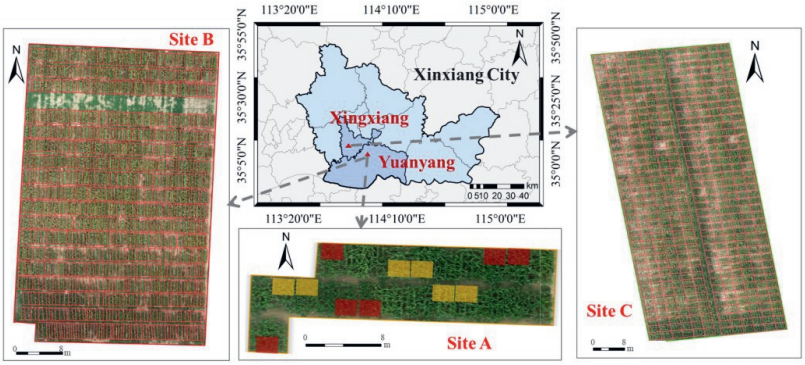


Fig. 4.1. *Overview of field experiments at two locations (Xinxiang and Yuanyang) in 2021 and 2022. The upper center figure shows the geographic location of the experimental area. Site A (lower center) and B (left) in Yuanyang in 2022. The red mask in site A presented infected areas, and the yellow mask showed healthy areas. The site C (right) in Xinxiang in 2021.*

Site A and B were in Yuanyang (35.15° N, 113.97° E). Both sites A and B were maize breeding fields with a planting density of 90,000 plants/ha planted on May 30, 2022.

Site A consists of 120 rows, each 3 meters, and site B consists of 1031 rows, each 3 meters. In site A, 20 rows were considered as a genotype plot, with a total of 6 genotype plots. In each plot, 3 rows *5 plants were selected and treated with the leaf spot bacterial solution on the evening of August 2, 2022. The inoculation of maize with the bacterial leaf spot pathogen adhered to the technical specification for the identification of maize disease and pest resistance of China (NY/T 1248.10-2016). A water-dispersible granule formulation of *Cercospora zeina* bacterial solution was prepared at a concentration ranging from 1 $\times 10^5$ to 1×10^6 pores per milliliter. The bacterial leaf spot solution was dispensed using a sprayer to ensure thorough coverage. The infected areas (6 areas) are shown in Fig. 4.1 using a red mask. The healthy areas (uninfected areas, yellow masked plots) were selected in equal numbers and sizes to the infected areas. When choosing these areas, we aimed to minimize the impact of pathogen transmission. The two adjacent plots' infection and healthy areas were connected separately, and the infected and healthy areas were distributed at intervals. In site B, each row was considered a plot with a genotype. Totally site B contained 1013 genotypes including 483 susceptibility genotypes and 530 resistant genotypes. This entire site was simultaneously treated with the leaf spot bacterial solution, paralleling the treatment applied to site A.

Site C, located in Xinxiang (35.30° N, 113.93° E), consists of 492 plots, each with a single genotype measuring 1.25 x 1.8 meters. Site C contained 492 genotypes, including 311 susceptible and 181 resistant genotypes. This site, with a planting density of 90,000 plants/ha, was planted on May 30, 2021. Each plot of this site was treated with the leaf spot bacterial solution on the evening of 2 August 2021.

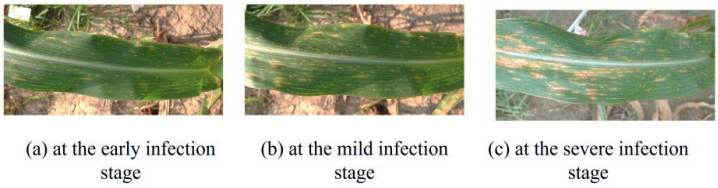
Overall, all the infection processes occurred during the trumpet stage of maize growth. In managing the fields, we adhered to fertilizer application and irrigation practices guided by the expertise of local agricultural professionals. This approach aimed to provide a consistent balance of water and nutrients to reduce their potential impact on disease occurrence in the maize plants.

4.2.2 Field surveys

In field surveys, two different disease severity assessment methods were used. In site A, a temporal ground survey was employed to analyze the response time of remote sensing features to the disease (Fig. 4.2). In sites B and C, the resistance to leaf spot in genotypes was evaluated (Fig. 4.3) to verify the performance of hyperspectral features in disease monitoring tasks. In all field surveys, 3 maize plants were randomly selected from each area/plot. From each plant, 3 leaves were collected: the leaf above the ear, the ear leaf, and the leaf below the ear. There was a total of 9 leaves per area/plot.

In site A, field surveys were conducted simultaneously with hyperspectral data acquisition after the onset of the disease infection (Table 4.1). Following the disease severity grading method from Tian et al. (2021), disease severity was classified into different developmental stages. Though infections varied among leaves, visual inspections helped broadly categorize the infection processes. Disease severity was assessed in three levels based on lesion size and condition (Fig. 4.2). Specifically, early infection, from initial infection to scattered lesions on leaves, occurred between 2 and

10 days after infection (DAI); mild infection, with two or more connected linear lesions, was at DAI 12 and 15; severe infection, with three or more connected planar lesions, occurred at DAI 22, 24, and 30.



(a) at the early infection stage (b) at the mild infection stage (c) at the severe infection stage

Fig. 4.2. *RGB images of maize leaves under different leaf spot disease infection stages.*

In sites B and C, the field surveys were conducted on August 26, 2022 (DAI 24) and September 2, 2021 (DAI 30), respectively (Table 4.1). The images of the selected leaves were documented. Subsequently, multiple experts collaboratively interpreted the proportion of leaf spots presented. Based on visual inspections, leaves were classified into one of six categories depending on the percentage of leaf spot coverage. Following this classification, the disease index (DI) for every plot was computed using the methodology of Huang et al. (2007). The resistance of maize was then determined by referencing the DI values. Maize resistance was classified into two groups, resistant (DI: 0–30%) and susceptible (DI: 31%–100%), following the China national standard (NY/T 1248.1-2006), titled technical specification for identification of maize resistance to leaf spot disease.

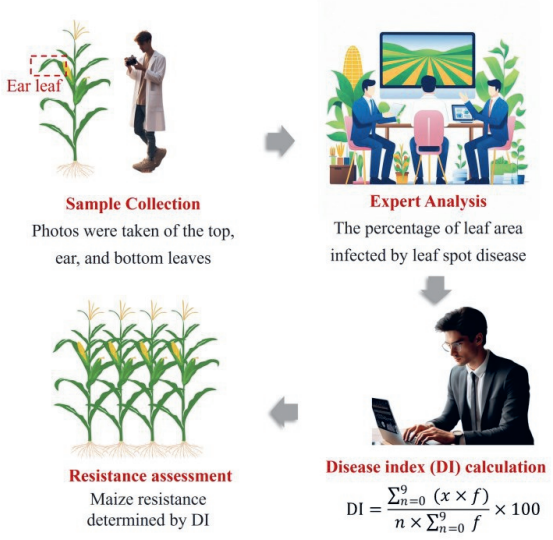


Fig. 4.3. *Flowchart of maize resistance assessment. x is defined as 0, 1, 3, 5, 7, 9, representing respective disease coverage of 0%, 0%–5%, 6%–25%, 26%–50%, 76%–100% on the leaf surface;* f *is the total number of leaves of each class;* n *is the highest degree of disease severity (in this paper,* $n = 9$*). The resistance of maize genotypes was*

categorized as resistant and susceptible, corresponding to DI value ranges of 0–30% and 31–100%, respectively.

4.2.3 Hyperspectral images collection and preprocessing

Hyperspectral images were obtained from the study site using a Pika L hyperspectral camera (Resonon, Bozeman, MT, USA) mounted on an unmanned aerial vehicle (UAV) (Matrice 600 Pro Hexacopter, DJI, Shenzhen, China). The images were taken at 50 m above the ground, flying at a speed of 1.5 m/s. All flights took place between 10:00 and 14:00 to minimize the effects of sun angle. The DJI M600 Pro UAV had a maximum payload capacity of 6 kg and a 30-minute endurance. It was equipped with an onboard RTK-GNSS (real-time kinematic global navigation satellite system) unit for centimeter-level navigation. The Pika L camera featured 150 bands ranging from 400 to 1000 nm with a 2.1 nm spectral resolution and a 3.3 nm FWHM. The hyperspectral sensor's 17 mm optical focal length provided an instantaneous field of view (IFOV) of 1.47 mrad and an angular field of view (FOV) of 30.8°. The image acquisition time is shown in Table 4.1.

Table 4.1. Field surveys and hyperspectral images acquisition time

Site	Year	Field surveys time	Hyperspectral images acquisition time
A	2022	Simultaneous with hyperspectral data acquisition	DAI 0, DAI 2, DAI 4, DAI 6, DAI 8, DAI 10, DAI 12, DAI 15, DAI 22, DAI 24, DAI 30
B	2022	DAI 24	DAI 12, DAI 15, DAI 22, DAI 30, DAI 37
C	2021	DAI 30	DAI 18, DAI 25, DAI 31, DAI 37

DAI: days after infection.

The raw hyperspectral cubes were converted to radiance using the instrument's radiometric calibration file. Cubes on the same flight path were combined into a linear cube. The linear cubes were georeferenced, based on high-resolution RGB images collected simultaneously and the ground control points, using ArcGIS 10.2 (Esri, Redlands, CA, USA). Radiometric calibration was performed with a 60% reflectance gray cloth with known reflectance collected at the same time as hyperspectral data in ENVI 5.3 (ITT Visual Information Solutions, Boulder, United States). Then, a seamless mosaic for the research site was created using all the linear cubes. Finally, zonal statistics were performed on the vector boundaries of each plot. This step was completed using the zonal statistics as a table plugin in ENVI 5.3.

4.2.4 Feature extraction

This study investigated hyperspectral features comprising biophysical parameters and spectral features. Biophysical parameters derived from radiative transfer models (RTM) are considered, leveraging the comprehensive data captured by hyperspectral systems across an array of continuous narrow bands (Kokaly and Clark, 1999). Simultaneously, spectral features based on one or more spectral reflectance exhibited

empirical relationships with plant information.

4.2.4.1 Spectral features

Mean reflectance values at the canopy scale for each plot were utilized to calculate various narrow-band spectral features. These features include spectral reflectance, VIs, and WFs. Spectral reflectance within the wavelength range of 400 nm to 900 nm, comprising 117 bands, was chosen to avoid the lower signal-to-noise ratio typically observed at the edges of the sensor's spectral range. VIs (Table S4.1) gathered from the literature were computed for spectral feature analysis. WFs were derived from the spectral data using the continuous wavelet transform (CWT), leveraging the PyWavelets library's pywt (Python 3.7). The CWT was executed on the reflectance spectra to obtain wavelet coefficients, which encapsulate the spectral information at various scales. Specifically, for each reflectance spectrum within the dataset, the transformation was conducted over scales 3 to 8 and applied the Mexican Hat wavelet as the mother wavelet basis, following the methodology outlined by Cheng et al. (2010).

4.2.4.2 Biophysical parameters

Biophysical parameters, including chlorophyll content (C_{ab}), carotenoid content (C_{ar}), equivalent water thickness (C_w), dry matter content (C_m), and anthocyanin content (A_{nth}), were quantified by inverting the PROSAIL model, using the mean reflectance values of each plot (Fig. 4.4). The PROSAIL model couples the PROSPECT-D leaf reflectance model with the SAIL canopy model. PROSPECT-D accounts for the biophysical parameters in the leaf, while SAIL considers the properties of the canopy structure. We chose this model because, at the time of this study, the study plots had reached canopy closure and could be considered a uniform chaotic medium.

Initially, a simulation dataset containing 79.872 million measures was generated with the PROSAIL model. The input variables for the model were estimated based on leaf optical property datasets and prior studies (Nie et al., 2023), aiming to encompass the range of variability in the practical maize field (Table 4.2). The output spectra were weighted average according to the spectral response function of the PikaL sensor, ensuring uniform and comparable spectral resolution across different spectra.

A multilayer perceptron (MLP) model was trained on the simulated dataset to establish the relationship between the simulated spectra and biophysical parameters. The leaf area index (LAI) was obtained using actual values measured in the field with a SUNSCAN instrument (Delta-T Devices， Cambridge， UK) to address the ill inversion issue. The MLP network was designed with an input layer with the same number of nodes as the number of the PikaL bands plus one (LAI). The inner layers successively applied a compression ratio of two, reducing the number of nodes by half. The output layer had the same number of nodes as the biophysical parameters. The network employed dropout regularization to prevent overfitting with a probability of 0.2. The ReLU activation function was applied throughout the network. Finally, the inversed C_{ab} and A_{nth} were evaluated using the coefficient of determination (R^2) and root mean square error (RMSE) based on the field measured C_{ab} and A_{nth} at site A (**Fig.**

S4.1). The C_{ab} and A_{nth} were measured with Dualex Scientific+ (Force-A, Orsay, France) following the measurements described by Zhou et al. (2023)

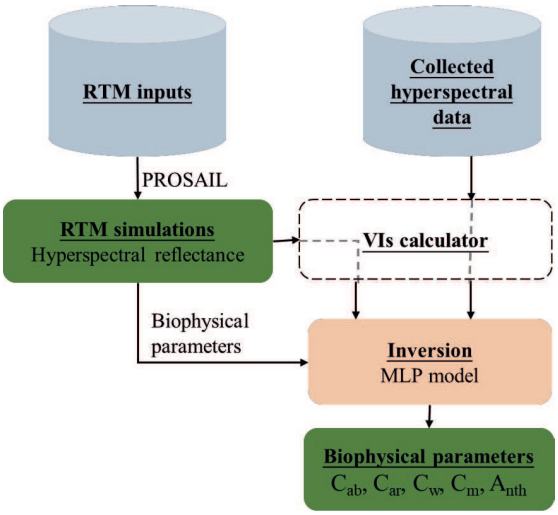


Fig. 4.4. *Flowchart of PROSAIL simulation and retrieval. C_{ab}: chlorophyll content, C_{ar}: carotenoid content, C_w: equivalent water thickness, C_m: dry matter content, A_{nth}: anthocyanin content, VIs: vegetation indices, MLP: multilayer perceptron.*

. These measurements were conducted simultaneously with field surveys.

Table 4.2 Inputs for PROSAIL simulation

Model	Variable	Acronym	Range	Steps	Units
PROSPECT-D (leaf level)	Chlorophyll content	C_{ab}	1-100	5	μg/cm^2
	Carotenoid content	C_{ar}	0-26	1	μg/cm^2
	Anthocyanin content	A_{nth}	0-20	1	μg/cm^2
	Brown pigment content	C_{brown}	0.2	*N/A*	*N/A*
	Equivalent water thickness	C_w	0-0.08	0.01	cm
	Dry matter content	C_m	0-0.04	0.01	g/cm^2
	Leaf structure parameter	N	1-1.5	0.1	*N/A*
SAIL (canopy level)	Leaf area index	LAI	1-5	0.3	*N/A*
	Hot-spot size parameter	Hspot	0.25	*N/A*	mm^{-1}
	Solar zenith angle	SZA	65	*N/A*	Degree
	Observed zenith angle	OZA	0	*N/A*	Degree
	Relative azimuth angle	RAA	0	*N/A*	Degree
	Average leaf inclination angle	ALA	30-50	10	Degree

Note: The 'Range' column indicates the variation interval for each parameter, and 'Steps' describes the quantification intervals within this range. For example, C_{ab} quantified within a range of 1 to 100 μg/cm², with 5 μg/cm² increments. *N/A*: not applicable.

4.2.5 Feature analysis

We proposed a comprehensive feature analysis method to identify sensitive features, as illustrated in Fig. 4.5. This process begins by utilizing all hyperspectral features retrieved from infected and healthy plots at site A. Given that each plot consists of numerous observations (pixels), we subdivided each plot into twelve equal parts, enriching the hyperspectral data for analysis. In total, both infected and healthy areas had 72 samples. We applied time series analysis to unravel the temporal sensitivity of various hyperspectral features to increase leaf spot severity **(Section 4.2.5.1)**, considering the effect size using Cohen's d. Subsequently, we trained an intelligent agent capable of automatically learning policies to select an optimal feature subset to address multicollinearity and select-rich information features. These features are named as 'parsimony features' **(Section 4.2.5.2)**.

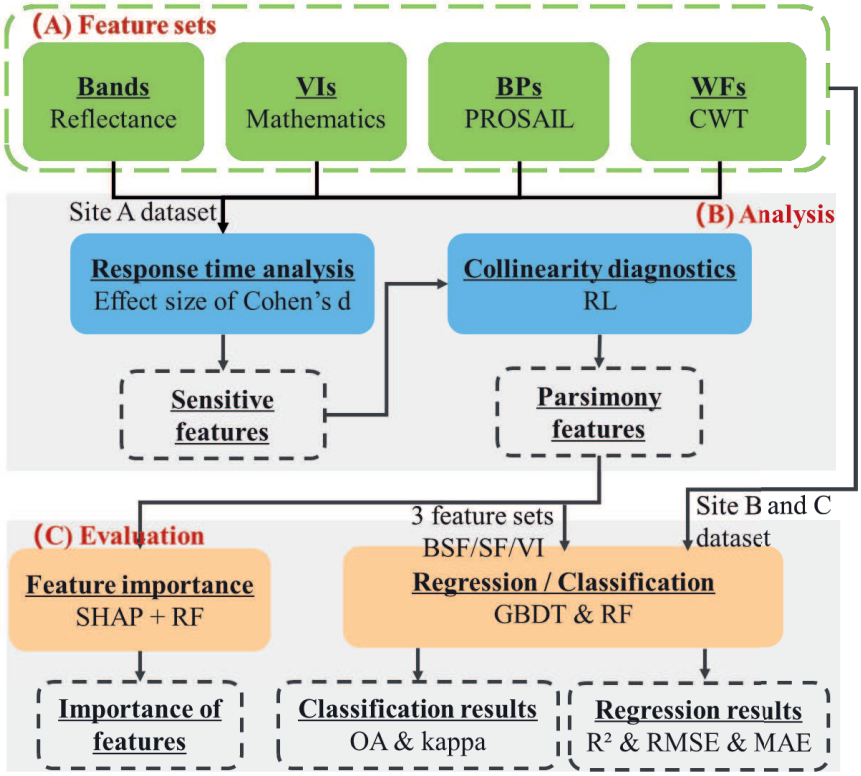


Fig. 4.5. *Overview of the methodology used for feature analysis and classification. Note: VIs: vegetation indices, BPs: biophysical parameters, WFs: wavelet features, CWT: continuous wavelet transform, RL: reinforcement learning, SHAP: Shapley additive explanations, GBDT: gradient-boosting decision tree, RF: random forest, OA: overall accuracy; 3 feature sets include biophysical parameters in combination with spectral features (BSF), spectral features alone (SF), and vegetation indices alone (VI).*

4.2.5.1 Response time analysis

The response time analysis is crucial for understanding and quantifying the temporal

dynamics of hyperspectral features in response to the vegetation stress process (Behmann et al., 2014; Langenkämper et al., 2022). To accurately focus on the target disease, a time-based normalization approach was employed to account for canopy structural influences that frequently overlay dynamics in hyperspectral features. This normalization strategy is essential to avoid misinterpretation of data and has been proven to compensate for most of the remote sensing parameter variation caused by illumination effects and canopy structure (Damm et al., 2022; Zarco-Tejada et al., 2012). This approach calculated the difference between the hyperspectral feature values observed at a given time (denoted as F_t) and the average of these features recorded before the infection event on August 2nd (denoted as F_t'). We use ΔF to represent the time series of change in each hyperspectral feature, which is calculated by

$$\Delta F = F_t - F_t' \quad (1)$$

The resulting time series represents the increment of individual hyperspectral features considering the first observations (DAI 0) in physical units. To assess the impact and reliability of leaf spot infection on plant responses as estimated by various hyperspectral features, we employed two statistical measures: (1) 95% confidence intervals based on a z-distribution; (2) effect size using Cohen's d, which accounts for the standard deviation of the healthy canopy.

We define a threshold effect size Z to represent the substantial difference between the healthy and infected observations. Based on our comprehensive testing and previous study (Charach et al., 2011), Z = 0.8 is the most effective value and, therefore, chosen for the implementations. In this step, we established a sensitive feature selection criterion: the start time of consecutive substantial difference with the same sign is determined as when the hyperspectral feature begins to respond to the leaf spot disease. In addition, only features that showed a response before DAI 15 were selected for further analysis in the following stages. These were observed at more than three-time points, demonstrating the substantial differences between the healthy and infected observations.

4.2.5.2 Collinearity diagnostics

Following sensitivity analysis in Section 4.2.5.1, we identified several sensitive features, some exhibiting multicollinearity and redundancy. These sensitive features will now be subjected to an in-depth collinearity assessment to refine our feature selection for the classification model. We modeled the task of collinearity diagnostics as a Markov decision process (MDP) from Mou et al. (2022). Consequently, RL was adopted as the strategy of choice for formulating a sophisticated collinearity diagnostics methodology (Fig. 4.6). Compared with traditional approaches, RL allows for continuous learning and adjustment, a critical advantage in environments where the features change over time (Mou et al., 2022). In addition, RL can efficiently manage the complex, high-dimensional spaces typical of hyperspectral images (Feng et al., 2022a).

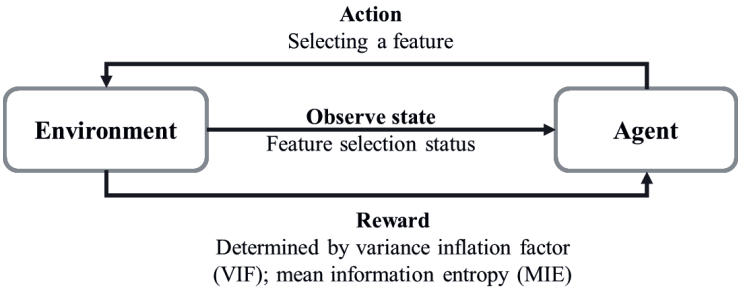


Fig. 4.6. *Overview of reinforcement learning strategy*

In this MDP, we define the action, state, and reward. Let F denote the set of all the sensitive features, representing the total count of these features, and let f_i represent an individual feature within F. The RL model's state, action, and reward are defined as follows.

State: The state (s) is a subset of F, with the state space being the power set of F. Each state is uniquely depicted by a feature encoding—a vector of length n. If a feature is selected, its corresponding element is set to 1; otherwise, it remains 0.

Action: The agent's primary objective is to select a feature from F at each iteration. Action refers to the position of a feature in a list, where the chosen position's value changes from 0 to 1. This selection process continues until the predefined number of features is reached; *x* features were optimal for ensuing classification models.

The transition function defines how the system moves from one state to another based on an action taken. Specifically, if an action is taken to select a feature already chosen within the current episode, the state s_t remains unaltered in the succeeding step. If the chosen feature f_i has not been selected in the current episode, then the state s_t evolves to a new state s_{t+1}, where the corresponding element of f_i is set to 1 in the feature encoding. When the count of chosen features matches the predefined threshold, the state transitions to a "Terminal" state, signifying the end of the episode.

Mathematically, the transition function can be described as:

$$s_{t+1} = \begin{cases} \text{Terminal} & \text{if reaching the preset number} \\ s_t & \text{if } a_t = \text{ select a feature } f_i \text{ already in } s_t \\ s_t + f_i & \text{if } a_t = \text{ select a new feature } f_i \end{cases} \quad (2)$$

in which s_t is the current state, s_{t+1} is the next state, f_i is the selected feature, and a_t is the current action.

Reward: The agent is rewarded based on the efficacy of its feature selection. A penalty of -1 is applied if a repeated feature is chosen. Conversely, a reward of 1 is granted when a non-collinear feature is selected. To determine collinearity, we employ the variance inflation factor (VIF), a metric introduced by Gareth et al. (2013), to measure the variance increase of a regression coefficient due to collinearity. A VIF below 10 suggests that the chosen feature is not collinear with previously selected ones. However, if collinearity is selected (VIF > 10), the information entropy, gauging the richness of spectral information, is used. The reward difference between states and s_{t+1}

is governed by the disparity in information entropy. Specifically, the average information entropy of the selected features was measured as Equation (3), in which A represents a set of previously executed actions, N designates the total count of chosen features, and P stands for the probability mass function.

$$\mathrm{MIE}(s) = -\frac{1}{|\mathcal{A}|}\sum_{i\in\mathcal{A}}\sum_{n=1}^{N} P\left(f_i^n\right)\log_2 P\left(f_i^n\right) \tag{3}$$

Subsequently, the reward function is mathematically structured as:

$$r_t = \begin{cases} -1 & \text{if } a_t = \text{ select a feature } f_i \text{ already in } s_t \\ 1 & \text{if } a_t = \text{ select a feature } f_i \text{ noncollinearity with features already in } s_t \\ \mathrm{MIE}(s_{t+1}) - \mathrm{MIE}(s_t) & \text{if } a_t = \text{ select a feature } f_i \text{ collinearity with features already in } s_t \end{cases} \tag{4}$$

, in which s_t is the current state, s_{t+1} is the next state, f_i is the selected feature, a_t is the current action, and r_t is the current reward.

To implement this strategy, we adapted our approach to incorporate the proximal policy optimization (PPO) algorithm. This training process was facilitated by the Ray framework. The tune library was used to search for the optimal model hyperparameters. Detailed settings of each parameter are provided in Table 4.3.

Table 4.3 Parameters for PPO in Ray

Parameter	Value	Parameter	Value
lr	5e-3	num_workers	6
train_batch_size	256	num_envs_per_worker	1
sgd_minibatch_size	128	rollout_fragment_length	10
num_sgd_iter	10	entropy_coeff	0.01
gamma	0.8	vf_loss_coeff	1.0
lambda	0.95	vf_clip_param	10.0
clip_param	0.3	use_gae	True
kl_coeff	0.2		

4.2.6 Feature evaluation

To validate the selected features, we assessed the importance of the parsimony features **(Section 4.2.6.1)** and demonstrated the effectiveness of these features for machine learning models across different sites and times (**Section 4.2.6.2)**.

4.2.6.1 Feature importance

We utilized the Shapley additive explanations (SHAP) method (Lundberg and Lee, 2017) for model feature interpretation in this evaluation. We generated SHAP summary plots based on random forest (RF) models to visualize the significance of each feature. The performances of the models are shown in Table S4.2.

The feature importance analysis process consisted of two main parts. Firstly, we conducted a SHAP summary using the infected areas. We utilized hyperspectral features that were calculated throughout the entire experimental period and compared

them to DAI, which increases with leaf spot severity. This phase aimed to gain insights into the relationship between hyperspectral features and disease severity. Secondly, we compared the hyperspectral features obtained from the infected and healthy areas at early, mild, and severe infection stages. This comparison sought to identify the contribution of features in distinguishing between infected and healthy plots at different disease stages.

4.2.6.2 Machine learning models

We employed two regression machine learning algorithms to estimate the DI for each plot on the survey dates: RF and gradient-boosting decision tree (GBDT). Similarly, we applied the same machine learning algorithms in a classification context to categorize maize genotypes as disease-resistant or susceptible.

In this study, we conducted 100 iterations of data division into two samples, namely the training and testing samples, by randomly selecting 80% (n = 810 for 2022; n = 394 for 2021) and 20% (n = 203 for 2022; n = 98 for 2021) of the dataset, respectively. The validation process involved k-fold cross-validation, wherein the original sample was partitioned randomly into 10 subsamples of equal size and repeated five times. Optimal hyperparameters for the models were identified by grid search and are presented in Table 4.4. Model performance was quantified by calculating R^2, RMSE, and mean absolute error (MAE) for regression accuracy. We analyzed the confusion matrix, overall accuracy (OA), and Cohen's kappa coefficient (kappa) for classification accuracy. In the development of the regression and classification models, we utilized Python 3.7 and the scikit-learn library. For GBDT models, we employed the GradientBoostingRegressor and GradientBoostingClassifier from the ensemble module. Similarly, we used the RandomForestRegressor and RandomForestClassifier from the same module for RF models.

To compare the effectiveness of different feature sets in classification models, we evaluated the classification accuracies of three distinct sets of hyperspectral features: (1) biophysical parameters in combination with spectral features (BSF), (2) spectral features alone (SF), and (3) vegetation indices alone (VI).

Table 4.4 Hyperparameters for each machine learning models

Hyperparameter	Search space	Regression	Classification
Gradient-boosting decision tree (GBDT**)**			
n_estimators	10–100	80	50
learning_rate	0.1–0.5	0.1	0.3
max_depth	2–15	5	5
min_samples_leaf	2–15	5	5
Random forest (RF)			
Number of trees	10–50	40	30
Maximum depth	20–100	50	50

4.3 Results

4.3.1 Temporal response of features after leaf spot infection

This section explores the temporal dynamics of hyperspectral features following maize leaf spot infection. The effect sizes quantify the analysis by comparing these features between infected and healthy areas to pinpoint the onset and progression of the disease's impact (detailed in Supplementary Table S4.3–S3.5).

4.3.1.1 Biophysical parameters

Compared to the DAI 0 measurements (Fig. 4.7), the change in C_{ab} (ΔC_{ab}) exhibited an initial increase followed by a gradual decrease, with the accumulation of C_{ab} in infected areas consistently lagging that in the healthy areas. Starting from DAI 10, a substantial difference in the C_{ab} change rate between infected and healthy areas was observed, substantiating the effect of leaf spot disease on chlorophyll dynamics.

Variations in ΔA_{nth}, ΔC_w, ΔC_m, and ΔC_{ar} did not show consistently substantial differences between infected and healthy areas. These measurements revealed a noisy nature, making it challenging to find a clear trend or identify consistently substantial differences between the infected and healthy areas.

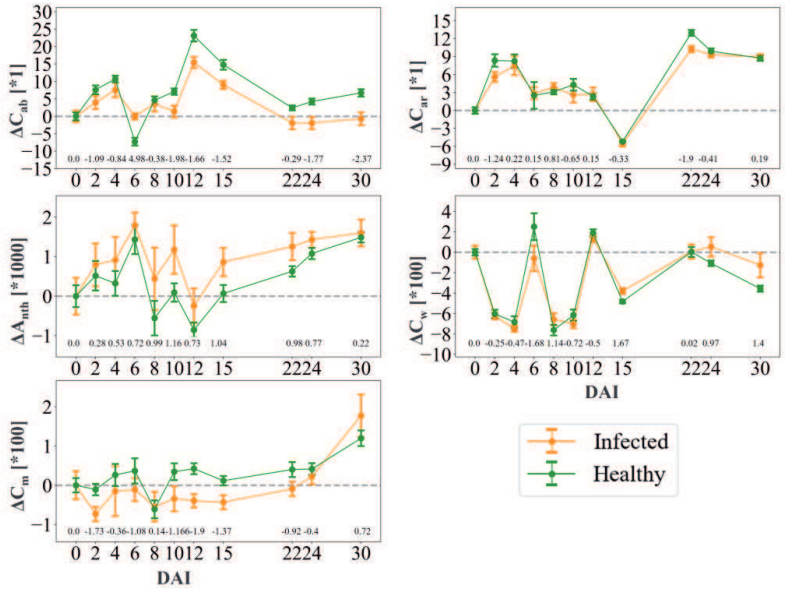


Fig. 4.7. *Changes of biophysical parameters in infected areas (n = 72 samples) and healthy areas (n = 72 samples) on different DAIs. The error bars represent the 95% confidence interval, and the values included represent the effect size, as determined by Cohen's d. Δ: normalized considering the change of the first infection day (2 August); C_{ab}: chlorophyll content; C_{ar}: carotenoid content; C_w: equivalent water thickness; C_m: dry matter content; A_{nth}: anthocyanin content.*

4.3.1.2 Spectral reflectance

Spectral reflectance across the 400–900 nm wavelength range did not meet the sensitivity criteria established for feature analysis as outlined in Section 4.2.5.1 (Fig. 4.8). The lack of consistency and continuity in the data suggests that spectral reflectance is prone to noise, which could complicate disease detection and risk false positives in practical disease monitoring. These findings underscore the limited transferability of models based on spectral reflectance for robust disease monitoring.

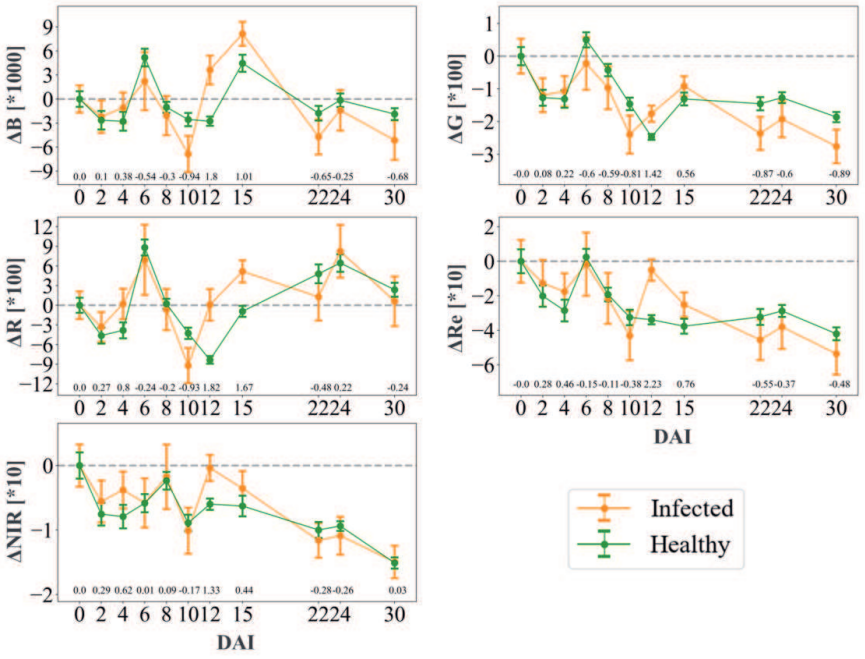


Fig. 4.8. *Changes of spectral reflectance in infected (n = 72 samples) and healthy areas (n = 72 samples) on different DAIs. The red (R), green (G), blue (B), red edge (Re), and near-infrared (NIR) bands were presented by wavelengths of 473 nm, 560 nm, 666 nm, 717 nm, and 843 nm corresponding to the central wavelength positions of the RedEdge-MX multispectral camera (Micasense company, USA), respectively. The error bars represent the 95% confidence interval, and the values included represent the effect size, as determined by Cohen's d.*

4.3.1.3 VIs

The earliest response of VIs to the disease occurred at DAI 8, with the photochemical reflectance index (PRI_n) related to xanthophyll and photosynthetic efficiency continuing to respond to leaf spot disease until DAI 30 (Table 4.5). Subsequently, starting at DAI 12, the responding VIs included five indices associated with carotenoid and chlorophyll (PSRI, B, G, R, and RGI), three indices related to xanthophyll and photosynthetic efficiency (PRI_{515}, PRI_{M3}, and PRI_{M4}), one index related to chlorophyll fluorescence (CUR), and three indices related to anthocyanins (VARI, $VARI_2$, and ARIm). From DAI 15, responding VIs included two related to structural traits (NDVI

and LIC_1) and two to chlorophyll (SIPI and PSND). From DAI 22, responding VIs included the structural-associated OSAVI and chlorophyll-associated TCARI. The response time of VIs highlights a temporal progression in the disease's impact on various physiological and biochemical processes.

Following a multicollinearity diagnosis based on RL, five representative VIs (NDVI, PSRI, PRI_n, RGI, and $VARI_2$) were selected (Fig. 4.9). The change trends in NDVI maintaining a close-to-zero difference between DAI 0–DAI 12 and DAI 0 in both infected and healthy areas, indicate that NDVI does not largely change. After DAI 12, the difference in infected areas compared to DAI 0 was consistently higher than in healthy areas, with the infected areas dropping seriously. VARI followed a similar trend to NDVI but shifted earlier by DAI 10. PSRI's variations were minimal until DAI 15, after which the infected plots increased notably. RGI mirrored PSRI's changes but began at DAI 8. Meanwhile, PRI_n, maintaining a close-to-zero difference with DAI 0 in healthy areas, experienced a sharp increase after DAI 15 in the infected areas. Compared to raw spectral reflectance, these VIs provide a relatively stable indication of vegetation status.

Table 4.5 *Response time of vegetation indices (VIs)*

Response time	VIs
DAI 2	--
DAI 4	--
DAI 6	--
DAI 8	PRI_n
DAI 10	--
DAI 12	PSRI, PRI_{515}, PRI_{M3}, PRI_{M4}, B, G, R, RGI, CUR, VARI, $VARI_2$, ARIm
DAI 15	NDVI, LIC_1, SIPI, PSND
DAI 22	OSAVI, TCARI
DAI 24	SPRI, NPQI, NPCI, CTRI, PRI, PRI_{M1}, PRI_{M2}, BRI_1, BRI_2, LIC_2, HI

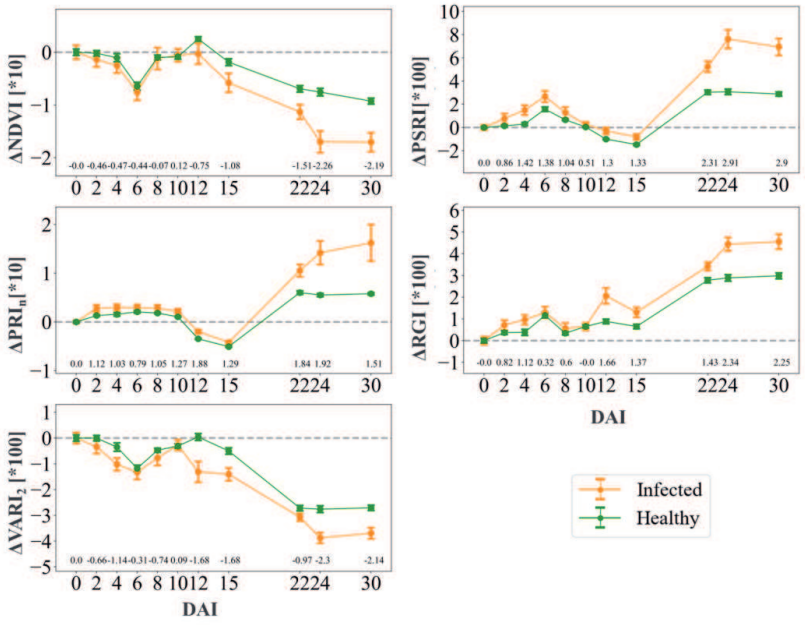


Fig. 4.9. *Changes of selected vegetation indices (VIs) in infected (n = 72 samples) and healthy areas (n = 72 samples) on different DAIs. The error bars represent the 95% confidence interval, and the values included represent the effect size, as determined by Cohen's d.*

4.3.1.4 WFs

From the early to mild infection stages, the WFs are sensitive to leaf spot infection, predominantly spanning the 450–750 nm range, encompassing scales of 3 to 8 (Table 4.6). Notably, the earliest response of WFs to the disease was observed at DAI 6, specifically with $WF_{586,6}$, $WF_{590,7}$, and $WF_{590–598,8}$, located within the yellow edge region (550–650 nm). This region is primarily characterized by the overlapping absorption of various pigments, particularly chlorophyll and anthocyanin, indicating pigment dynamics associated with early disease response.

Starting from DAI 12, responding WFs included $WF_{469–473,3}$, $WF_{465–469,4}$, $WF_{461–469,6}$, $WF_{461–469,7}$, $WF_{461–477,8}$, and $WF_{506–510,8}$, located in the blue region (450–550 nm), primarily governed by chlorophyll absorption. Furthermore, the $WF_{735,3}$, $WF_{735,4,}$ and $WF_{735,5}$ were located in the red edge region (700–750 nm), demonstrating sensitivity to rapid photosynthetic rate changes. From DAI 15, the $WF_{821,5}$, positioned in the near-infrared region and indicative of sensitive plant structure, began to show a significant difference between the infected and healthy areas. These findings imply a broader impact of the disease, associated with progressive changes in chlorophyll content, photosynthetic efficiency, and plant structural integrity.

After conducting a multicollinearity diagnosis using RL, five representative wavelet features ($WF_{494,5}$, $WF_{461,6}$, $WF_{469,7}$, $WF_{548,8}$, and $WF_{590,8}$) were selected (Fig. 4.10). The

trends exhibited by $WF_{494,4}$, $WF_{461,6}$ and $WF_{469,7}$ were consistent, displaying a steady increase from DAI 0 to DAI 30 in both infected and healthy areas, with the changes in the infected plots consistently occurring at a faster rate. Conversely, the changes of $WF_{548,8}$ and $WF_{590,8}$ in infected areas consistently preceded those in the healthy areas. The observed trends in WFs displayed noisy and discontinuous patterns, particularly in the early stages of disease development. This suggests that while WFs responded rapidly to the onset of disease, their stability remains uncertain during the early stage of infection.

Table 4.6 Response time of wavelet features (WFs)

Response time	WFs
DAI 4	--
DAI 6	$WF_{586,6}$, $WF_{590,7}$, $WF_{590–598,8}$
DAI 8	--
DAI 10	--
DAI 12	$WF_{469–473,3}$, $WF_{735,3}$, $WF_{465–469,4}$, $WF_{735,4}$, $WF_{465,5}$, $WF_{735,5}$, $WF_{461–469,6}$, $WF_{461–469,7}$, $WF_{461–477,8}$, $WF_{506–510,8}$
DAI 15	$WF_{477–486,3}$, $WF_{473–486,4}$, $WF_{469–481,5}$, $WF_{821,5}$, $WF_{473,6}$, $WF_{510–515,6}$, $WF_{502–510,7}$, $WF_{481–502,8}$

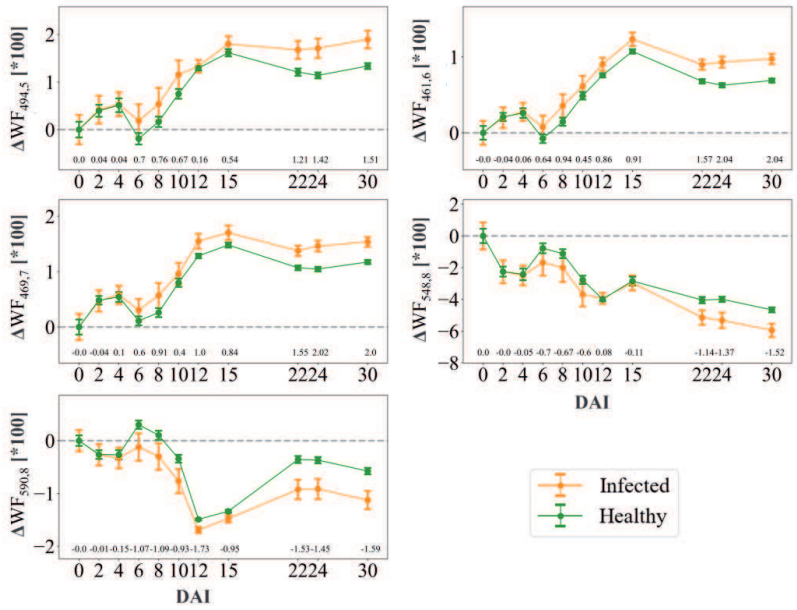


Fig. 4.10. *Changes of selected wavelet features (WFs) in infected (n = 72 samples) and healthy areas (n = 72 samples) on different DAIs. The error bars represent the 95% confidence interval, and the values included represent the effect size, as determined by Cohen's d.*

4.3.2 Importance of identified features

According to our experimental trials, we identified 11 key features characterized by high information entropy and low collinearity. Our RL agent meticulously selected these features, ensuring an optimal balance between information richness and feature independence. These included 10 spectral-based features, 5 VIs and 5 WFs, and a biophysical parameter, namely, C_{ab}. These selected features were utilized as predictors in the final classification model for maize resistance.

The importance of the chosen features in identifying infected and healthy areas during various disease stages is shown in Fig. 4.11a–c. At the early disease stage, C_{ab} emerged as the feature with the highest importance scores in models discriminating between infected and healthy areas, followed by PRI_n and PRSI. These features also showed high importance at the mild and severe disease stages. $VARI_2$, PRSI, and PRI_n demonstrated the highest importance scores in models regressing different levels of severity, as illustrated in Fig. 4.11d. Notably, $VARI_2$ displayed a negative relationship with disease severity. At the same time, PRSI and PRI_n exhibited a positive correlation.

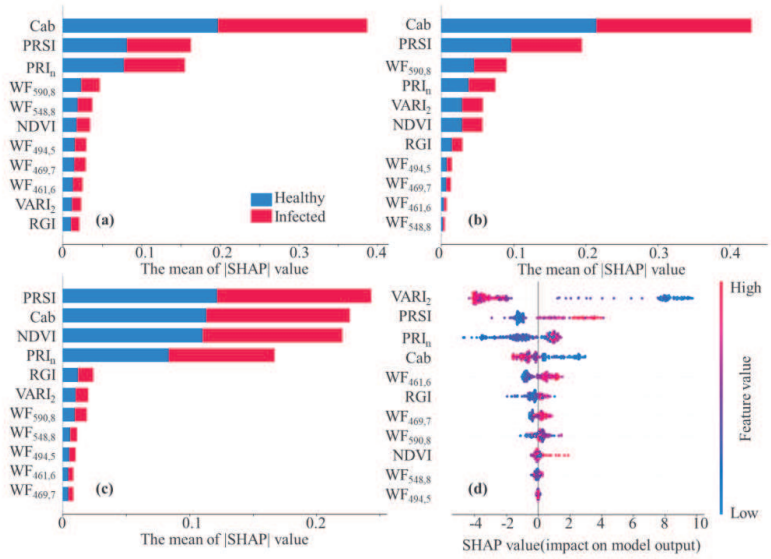


Fig. 4.11. *Feature importance ranking by SHAP value. (a)–(c) represents SHAP value when classifying infected and healthy areas at each leaf spot disease stage: (a) early infection, (b) mild infection, and (c) severe infection. (d) depicts SHAP value when regressing infected plots from DAI 0 to DAI 30 with increasing maize leaf spot disease. The feature importance is ordered along the y-axis, and the contributions of features (SHAP value) to the model are on the x-axis. Positive SHAP values refer to a more severe leaf spot disease.*

4.3.3 Regression models for quantifying DI

The performances of RF and GBDT regression algorithms for estimating the DI of

maize leaf spot, utilizing hyperspectral features in 2022 (DAI 30) and 2021 (DAI 31), are presented in Fig. 4.12 and Fig. 4.13, respectively. In 2022, the RF model exhibited an R^2 ranging from 0.51 to 0.62. The GBDT algorithm displayed comparable performance, with an R^2 between 0.71 and 0.79. For the GBDT model, RMSE values ranged from 0.12 to 0.15, and MAE values varied from 0.10 to 0.12. In contrast, the RF model with R^2 values from 0.59 to 0.63 in 2021, while the GBDT model's R^2 spanned from 0.67 to 0.74. The RF model reported RMSE and MAE values from 0.12 to 0.17 and 0.10 to 0.14, respectively, whereas the GBDT model exhibited RMSE values between 0.08 and 0.12 and MAE from 0.07 to 0.10. Optimal performance in both models and years was achieved using spectral features. These results demonstrate a redundancy in integrating biophysical parameters and spectral features for monitoring disease at the initial severe stages.

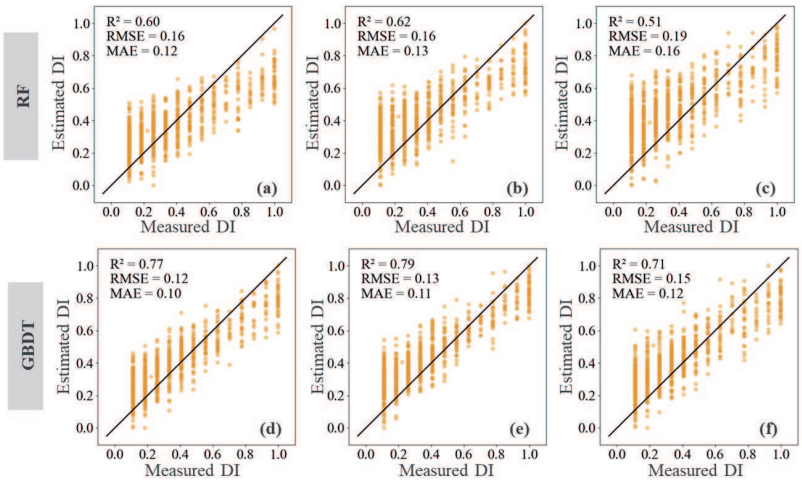


Fig. 4.12. *Scatter plots between the measured DIs and the best estimated DIs by RF (upper) and GBDT (bottom) in 2022. The models were trained on different sets of features: (a) and (d) utilize biophysical parameters in combination with spectral features (BSF), (b) and (e) rely on spectral features, including wavelet features and vegetation indices (SF), and (c) and (f) focus on vegetation indices alone (VI), respectively.*

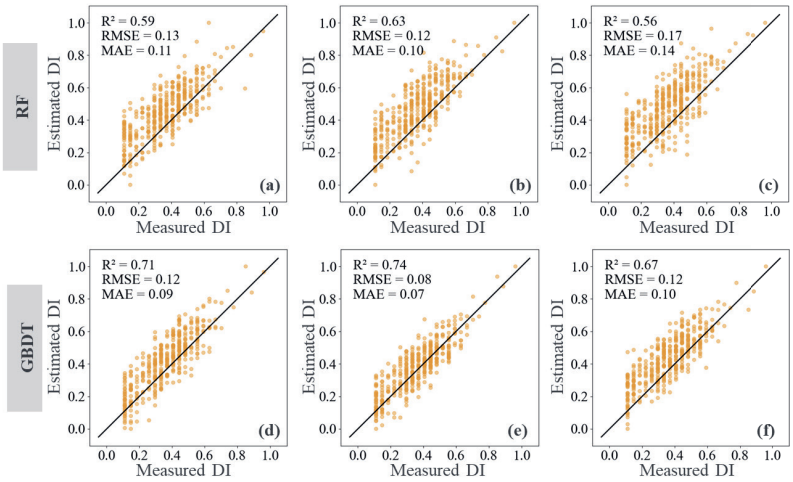


Fig. 4.13. *Scatter plots between the measured DIs and the best estimated DIs by RF (upper) and GBDT (bottom) in 2021. The models were trained on different sets of features: (a) and (d) utilize biophysical parameters in combination with spectral features (BSF), (b) and (e) rely on spectral features, including wavelet features and vegetation indices (SF), and (c) and (f) focus on vegetation indices alone (VI), respectively.*

4.3.4 Classification models for assessing maize resistance

The resistant and susceptible classification models using hyperspectral imagery from different time points in 2022 demonstrated varying levels of OA and kappa (Fig. 4.14; Table S4.6–S3.7). OA ranged from 56.16% to 86.21%, and kappa values ranged from 0.39 to 0.76. The models exhibited varying accuracy patterns based on three distinct sets of hyperspectral features. DAI 12 and 37 notably enhanced OA and kappa when integrating biophysical parameters with WFs and VIs. Omitting the C_{ab} decreased OA by up to 3.45% and 2.96%, respectively. Furthermore, removing C_{ab} and WFs led to additional reductions in OA by up to 9.36% and 8.87%, respectively. A decline in this trend was observed at DAI 15. At DAI 22 and 30, the classification models using different feature sets achieved a balanced and best performance, with no significant differences observed among the three cases of features used, with the best precision obtained by combining WFs and VIs.

The 2021 data presented an OA range of 65.31% to 85.71% and kappa values from 0.42 to 0.74 (Fig. 4.15; Table S4.8–S3.9). DAI 31 achieved the peak level of accuracy in the study. Paralleling the 2022 findings, DAI 37 of 2021 also exhibited superior OA and kappa when using BSF. The exclusion of the C_{ab} feature led to a 5.10% reduction in OA, while excluding both the C_{ab} and WFs resulted in further OA drops of a maximum of 7.14%. By DAI 18, the once pronounced complementary strengths of the three feature types began to moderate, and by DAI 25 and DAI 31, this trend disappeared entirely.

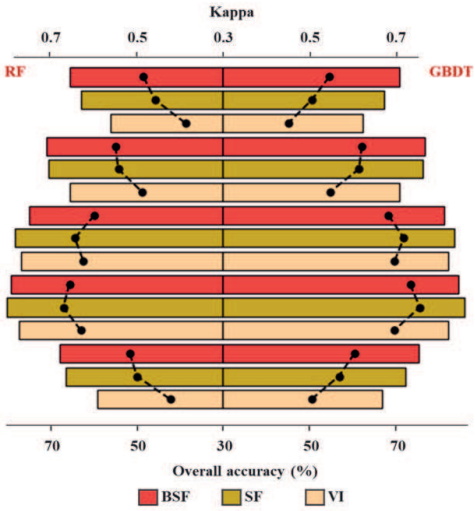


Fig. 4.14. *Performances of classification models in 2022. Overall accuracy (bars) and Kappa (bullets) metrics of RF and GBDT algorithms classifying maize plants resistant to leaf spot disease from susceptible. The models were trained using biophysical parameters in combination with spectral features (BSF), spectral features including wavelet features and vegetation indices (SF), and vegetation indices alone (VI), respectively. The models used hyperspectral imageries from DAI 12, DAI 15, DAI 22, DAI 30, and DAI 37, 2022, respectively.*

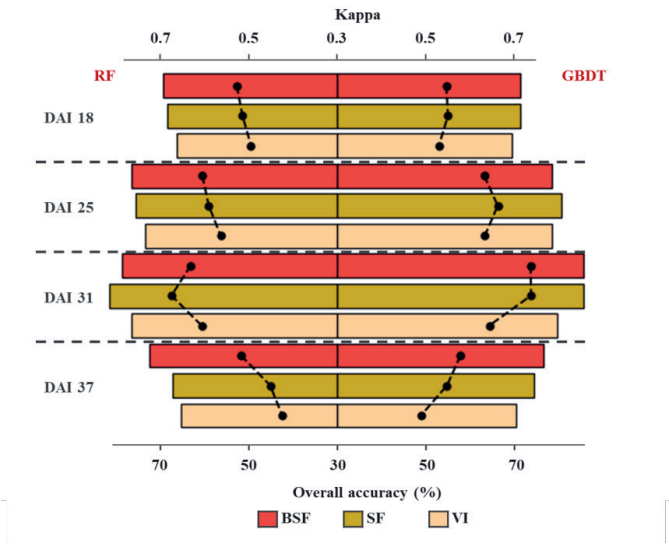


Fig. 4.15. *Performances of classification models performance in 2021. Overall accuracy (bars) and Kappa (bullets) metrics of RF and GBDT algorithms classifying maize plants resistant to leaf spot disease from susceptible. The models were trained*

using biophysical parameters in combination with spectral features (BSF), spectral features including wavelet features and vegetation indices (SF), and vegetation indices alone (VI), respectively. The models used hyperspectral imageries from DAI 12, DAI 15, DAI 22, DAI 30, and DAI 37, 2021, respectively.

4.4 Discussion

4.4.1 Sensitivity of normalized features for plant-pathogen interaction

Our results revealed that the normalized features response to leaf spot disease infection display varying temporal dynamics and amplitude. This expected behavior can be attributed to the sensitivity of individual features to specific plant adaptation mechanisms, including functional, biochemical, or structural changes brought on by disease infection refer to a review on this topic (Hernandez-Clemente et al., 2019). Notably, we observed a dual response from ΔC_{ab}. An initial slow, short-term increase was observed in response to maize growth and exacerbation of leaf spot disease, followed by a longer-term decrease under sustained leaf spot disease infection. Conversely, the ΔPRI_n exhibited an immediate increase but did not decrease over time. This complex interplay of features responses to leaf spot disease at canopy scales, operating at different time scales, is why models struggle with cross-temporal application.

In fact, from DAI 6 to DAI 10, scattered lesions were already visible to the naked eye while maize was still at the growth stage (tassel). Our results showed that the C_{ab}, retrieved by the radiative transfer model, indicates a slight separation of infected and healthy canopies. It suggests slightly slower chlorophyll accumulation and limited growth rates in the infected areas. In addition, an increase of PRI_n in the infected area could be driven by physiological changes, likely signifying a slight reduction of stomatal aperture compared to the healthy area. The yellow edge region wavelet features ($WF_{586,6}$, $WF_{590,7}$, and $WF_{590–598,8}$) as remote sensing proxy sensitive to various pigment variations like C_{ab} and Anth. Notably, the $\Delta WF_{598,8}$ time series showed differences in DAI 6 between infected and healthy areas, indicating pigment dynamics due to plant response to leaf spot disease. These dynamics of features support the idea that plants could have reacted physiologically and biochemically to the evolving leaf spot infection at the early stages.

From DAI 12, scattered lesions began extending into contiguous ones as the maize entered the reproductive stage (silking). More features began responding to the leaf spot disease infection. For instance, the PRI_{M4}, a proxy for short-term changes in photosynthetic activity and less sensitivity to structural effects, showed a larger reduction in infected than healthy areas. Higher changes of CUR in infected areas than in healthy areas could be due to the physiological impacts and changes in chlorophyll fluorescence. The PSDN showed a decline in both infected and healthy areas but a more pronounced decrease in the infected area, indicating a quicker rate of plant senescence. Additionally, blue region wavelet features and red edge region wavelet features ($WF_{735,3}$, $WF_{735,4}$, and $WF_{735,5}$) showed notable differences between leaf spot infected

and healthy canopies. The blue region is related to pigment degradation, while the red edge region is sensitive to chlorophyll concentration and quick photosynthetic rate changes (Carter and Knapp, 2001; Hernández-Clemente et al., 2016).

Contrasting with prior research, our findings provide analytical insight into the biophysical and spectral feature responses throughout the progression of leaf spot infection. While several of our observations align with prior studies, some findings diverge. Interestingly, none of the spectral reflectance features demonstrated significant continuous changes in response to the disease over the observation period. However, several studies have identified the green, red, and near-infrared spectral regions as sensitive to various plant diseases (Bauriegel et al., 2011; Garcia-Ruiz et al., 2013; Huang et al., 2012a). Both results seem to contradict but can be explained by the susceptibility and instability of spectral reflectance to environmental factors at different time scales. To our knowledge, this is the first time that the stability of spectral reflectance in disease monitoring under natural conditions has been experimentally verified using canopy time-series data.

Displaying the changes in biophysical parameters, spectral reflectance, VIs, and WFs is crucial for understanding the disease dynamics comprehensively. This comprehensive understanding is fundamental for improving disease monitoring strategies. In practical terms, it is essential to select features that show a consistent response to disease for effective monitoring tasks. Specifically, for early-stage disease monitoring, features that respond before DAI 10 should be prioritized. For mild-stage monitoring, features that respond before DAI 15 should be selected. For severe stage monitoring, choosing features that exhibit continuous and stable responses is important.

4.4.2 Performance of hyperspectral features

The ranking of feature importance provides insights into the ability of each feature to distinguish between healthy and infected areas. The C_{ab} and PRSI consistently stand out as the most influential features throughout every stage of infection. Their prominent SHAP values underscore their essential role in differentiating between healthy and infected maize areas. As infection severity escalates, there is a notable reduction in chlorophyll concentration, aligning with patterns of decline observed in other stress experiments conducted under controlled conditions (Damm et al., 2022; Hornero et al., 2021) and field surveys (Camarero et al., 2012). Notable, the importance of PRSI even exceeded C_{ab}, reinforcing its utility as a sensitive index to variations in pigment composition, including C_{ab} and C_{ar}. Additionally, VIs such as NDVI, PRI_n, RGI, and $VARI_2$ gain increased importance in severe infection, indicating their potential to reflect compounded stress impacts on plant physiology as the disease advances.

The performances of our maize resistance classification models demonstrated both complementarity and redundancy among the biophysical parameters and spectral features. These diverse spectral features exhibited complementary information at the early stages of disease infection, improving accuracy when integrated. Specifically, models incorporating C_{ab}, VIs, and WFs outperformed models that solely relied on spectral features or VIs, with a maximum OA difference of 9.36%. This finding

highlighted the added value of integrating different types of features during the early disease stages (Poblete et al., 2021; Zarco-Tejada et al., 2018). However, as the disease progressed, the complementarity of these features gradually diminished, indicating a redundancy of information at the mild and initial severe disease stages. This observation aligns with previous studies that have reported that a reduced set of selected features can achieve optimal results in disease classification models (Poblete et al., 2020; Wang et al., 2019).

Our study provided a novel explanation for this contradiction. The complementary advantages of multiple features are effective for monitoring challenges during the early stages of disease classification and the latter part of the severe stage when disease intersects with crop senescence. As the disease becomes more distinguishable at the mild and initial severe stages, the classification difficulty decreases, leading to the emergence of redundant properties among the different features. This understanding of the contradictory nature of the influence of multiple features on disease classification models contributes to further research.

In addition, the performance of classification models showed inconsistency. At the early stages of the disease (DAI 12), the models performed very well in identifying the resistant genotypes, but they struggled to correctly identify susceptible genotypes, resulting in high precision and lower recall. This is because the susceptible genotype showed weak symptoms, making it easy to misclassify as resistant. Conversely, in the severe stages of the disease (DAI 37), the models exhibited high recall but lower precision. This indicates that while the models could successfully identify susceptible genotypes, they mistakenly classified some resistant genotypes as susceptible. This is because the susceptible genotype undergoes accelerated senescence as maize was in the mid-milk stage, making it easier to identify with high recall. Meanwhile, resistant genotypes also showed signs of senescence and were easily misclassified as susceptible, leading to lower precision.

4.4.3 Limitations of this study

The findings of this study, substantiated by numerous field experiments, leave open questions regarding their applicability to other maize leaf diseases. However, maize is also susceptible to other foliar diseases such as rust, blight, and anthracnose. The potential applicability of our findings to these additional diseases has not been studied and necessitates further research. Additionally, the specificity of the identified features in distinguishing between different diseases must be confirmed in future studies.

The mismatch between field survey data and remote sensing data has always been a source of uncertainty in disease monitoring. To address this, multi-scale analysis should be employed to analyze the disconnect between various scales and explore the factors causing this disconnect. Moreover, the current methodology of evaluating maize resistance through subjective assessment by researchers introduces potential biases. To address this, future work should consider the adoption of automated image analysis algorithms. Such technological advancements promise a more objective and practical approach to quantifying disease impact on leaf tissue, substantially diminishing

subjectivity and bolstering the efficacy of monitoring processes for crop resistance.

4.5 Conclusion

Hyperspectral technology provides diverse avenues to explore plant-pathogen relationships on large scales, yet the complexity of leaf spot-associated plant responses remains a significant problem. This study develops a systematic approach for identifying hyperspectral features sensitive to leaf spot disease. Our experimental results illustrate that temporal response analysis enables the analysis of inherent spectral characteristics of plants and pathogens. We conclude that canopy-derived C_{ab}, PRI_n, and PRSI are significant features at all leaf spot disease infection stages. The effectiveness of our classification models highlights the complementary information from biophysical and spectral-based features during the early and severe disease infection stages, suggesting the information redundancy at the mild and initial severe stages of disease infection. This conflict was confirmed for the first time through continuous observation data collection. Our research methodology and the important features derived from this study could guide other disease monitoring research.

4.6 Supplementary information

Additional tables and figures supporting this chapter are available online. They can be accessed via the QR code or at the following URL: PhD-thesis/chapter4-CEA-Supplymentary.pdf at main · Briya1990/PhD-thesis

5

Physical model-guided deep learning (PGDL) for enhanced monitoring of maize leaf spot disease

This chapter is based on:
Bai, Y., Kooistra, L., Liu, Q., Yu, X., Jia, T., Zhu, Y., Jiang, T., Jiang, T., Li, S., Tekinerdogan, B., Duan, C., Jin, X. (2025). Physical model-guided deep learning for enhanced monitoring maize leaf spot. IEEE Transactions on Geoscience and Remote Sensing (Under review)

Abstract

Accurate and efficient monitoring of crop diseases, such as maize leaf spot, is crucial for both maize breeding and precision agriculture. While UAV-based hyperspectral sensors and advanced machine learning models offer high-throughput solutions, these models often suffer from limited generalizability in practical applications. To overcome this challenge, we propose a novel approach—physical model-guided deep learning (PGDL)—which leverages the knowledge gained from radiative transfer model simulations and improves the generalization of monitoring maize leaf spot from UAV-collected hyperspectral data. We tested three simulation methods: canopy spectrum simulations with evenly spaced chlorophyll contents (SIM #1), measured leaf disease spectra (SIM #2), and mixed endmember spectra (SIM #3). The results showed that SIM #2 and SIM #3, which combine real leaf disease spectral data, achieved better performance (R^2 = 0.99 for SIM #2, R^2 values range from 0.97 to 0.98 for SIM #3) across all disease infection levels in the consistency analysis between simulated and UAV spectra. Correlation analysis further supported this consistency, showing that both SIM #2 and SIM #3 aligned with UAV spectra in the visible wavelength range (400–700 nm) and demonstrated a positive correlation ($r > 0$) with DI. We then tested PGDL, physically based methods (using SIM #2 and SIM #3), and data-driven models for DI retrieval across four disease stages: early, mild, moderate, and severe. While all models performed worst in the early disease stage, the PGDL approach demonstrated superior and more stable accuracy in that stage. Models pre-trained on SIM #2 achieved the highest performance in the early stage (R^2 = 0.76 for 2021; R^2 = 0.70 for 2023), followed by SIM #3 (R^2 = 0.73 for 2021; R^2 = 0.63 for 2023). This study highlights the potential of integrating multi-source spectral data into PGDL models, offering a promising approach for disease monitoring and improving early disease detection capabilities.

5.1 Introduction

Maize leaf spot disease poses significant threats to maize yield and quality, making effective monitoring crucial for sustainable agriculture (Dhami et al., 2015b). Accurate assessment of disease severity is essential for timely intervention, which is critical for managing disease outbreaks. Traditionally, disease severity is quantified using a metric known as the disease index (DI), which reflects the percentage of symptomatic area on a leaf or plant and is commonly assessed through expert visual inspection (Bock et al., 2010). However, this method is labor-intensive, subjective, and difficult to scale. These limitations highlight the need for more advanced, scalable solutions, such as remote sensing technologies (Zarco-Tejada et al., 2018).

Hyperspectral imaging, a key remote sensing technique, offers a promising alternative for crop disease monitoring. Hyperspectral sensors capture a broad spectrum of electromagnetic wavelengths, providing detailed information that can distinguish healthy from diseased plant tissues (Bai and Jin, 2024). For instance, hyperspectral data has been used to detect subtle physiological changes that precede visible disease symptoms (Zarco-Tejada et al., 2018) and uncouple biotic/abiotic-induced symptoms (Zarco-Tejada et al., 2021). The rich spectral information from these sensors can effectively reveal pathogen-induced physiological alterations, which are often undetectable through traditional visual inspection.

Traditional machine learning (ML) algorithms, such as support vector machines (SVM) and random forests (RF), have been widely used for hyperspectral disease classification. These methods have shown success in identifying diseases like wheat powdery mildew (Feng et al., 2022b), rice leaf blast (Tian et al., 2021), and corn rust (Meng et al., 2020). However, these traditional ML approaches rely heavily on hand-crafted features such as vegetation indices, wavelet features, and texture features (Poblete et al., 2020; Tian et al., 2021; Xuan et al., 2022). While these features are interpretable, their development is time-consuming, and they may not fully capture the complexity of the original hyperspectral data (Reichstein et al., 2019).

Deep learning (DL) has emerged as a more powerful alternative, capable of automatically extracting both spatial and spectral features for disease monitoring. For example, Guo et al. (2024) developed a dual-branch selective attention capsule network that separately extracts spectral and spatial features to classify kiwifruit soft rot. Using data acquired in a controlled laboratory setting, the model achieved an overall accuracy of 97.08%. Nguyen et al. (2021) used a 3D convolutional neural network (3D-CNN) to exploit joint spatial-spectral features for early detection of grapevine viral disease at the plant level. While DL models can effectively extract features, they often struggle to generalize across different crops or environmental conditions (Osco et al., 2021; Sun et al., 2021a). This lack of generalization hampers their large-scale adoption, as models trained on one crop or in a specific environment may fail to maintain similar accuracy elsewhere.

A promising new approach, combining physical process-based models with DL, has

recently been proposed. This method leverages knowledge from physical models to enhance DL's ability to solve target tasks (Reichstein et al., 2019). The process involves three main steps: (1) generating a high-quality simulation dataset using physical models—such as radiative transfer models (RTMs)—to capture essential spectral–physiological relationships; (2) pre-training a DL model on these simulations so that it learns fundamental patterns derived from physically consistent data; and (3) transferring this pre-trained model to real-world field data, allowing it to adapt and improve its performance under actual conditions. This method has been successfully applied in estimating various agricultural variables, such as nitrogen content (Wang et al., 2023b), fractional vegetation cover (Yu et al., 2022), leaf area index (Sun et al., 2021a), and leaf chlorophyll content (C_{ab}) (Bhadra et al., 2024; Chen et al., 2022b), which are directly involved in the RTMs. However, directly applying this strategy to disease monitoring remains difficult because leaf diseases lead to complex changes in multiple variables, such as C_{ab}, nitrogen content, and leaf area index, making it challenging to simulate different disease severities using RTMs alone.

To address this challenge, this study aims to develop an effective simulation method based on RTMs and use them to drive a physical model-guided deep learning (PGDL) approach for monitoring maize leaf spot. Specifically, the objectives of this study are to: (1) develop spectrum simulation methods and evaluate their accuracy by comparing simulated spectra with those collected from UAV hyperspectral data; (2) compare the performance of different models, including physically-based methods, data-driven methods, and PGDL, in regressing DI across different datasets; and (3) interpret the hyperspectral features that contribute to accurate DI quantification for maize leaf spot monitoring.

5.2 Materials and methods

5.2.1 Study area and data collection

5.2.1.1 Experimental design

This study was conducted in Xinxiang City (35.30° N, 113.93° E), Henan Province on the North Henan Plain (Yubei Plain) of China. Maize is the primary crop cultivated in this region. The region experiences a warm temperate continental monsoon climate. This climate is marked by hot, rainy summers that create favorable conditions for maize leaf spot occurrence and diffusion.

The experiments were carried out in 2021 and 2023 (Fig. 5.1). In 2021, the experimental field had 492 plots in total. Each plot measured 1.25 × 1.8 m and contained a single maize genotype. In each plot, 24 maize plants were planted in 4 rows with 60 cm row spacing and 22.5 cm plant spacing. The maize seeds were sowed on May 30, 2021. A total of 246 genotypes with two pathogen treatments were tested. To promote disease occurrence, plots in treatment 1 were inoculated with *Bipolaris maydis* (cause southern leaf blight), and those in treatment 2 with *Curvularia lunata* (*Curvularia* leaf spot), two widely distributed pathogens in China. The inoculation was

produced on the evening of August 2, during the big trumpet period of maize. The inoculation followed the technical specification on evaluation of maize resistance to pests-part 10: *Curvularia* leaf spot (NY/T 1248.10-2016). A water-dispersible granule formulation was prepared at a concentration of 1×10^5 spores per milliliter and applied using a hand sprayer.

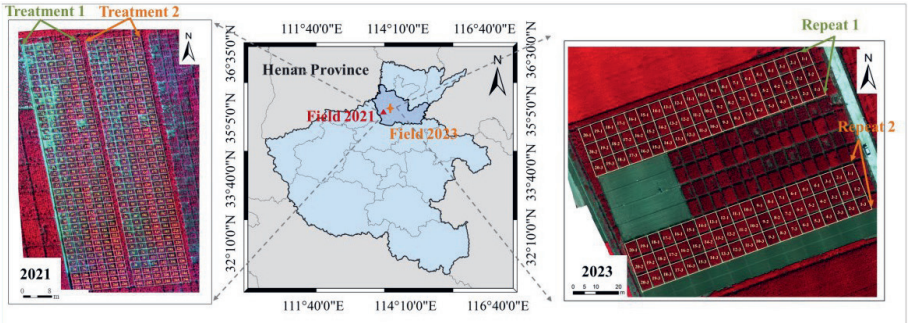


Fig. 5.1. *Overview of field experiments. The experimental field on the left was conducted in 2021, while the one on the right was conducted in 2023. Plot boundaries are outlined with yellow polygons, and the yellow numbers indicate plot identifiers. Below each plot, a false-color composite of the hyperspectral orthomosaic is displayed (red: 852.12 nm; green: 649.01 nm; blue: 552.08 nm), acquired on 27 August 2021 and 29 August 2023, respectively.*

In 2023, two independent repeats (repeat 1 and repeat 2) were arranged, each consisting of three rows of plots containing the same set of 20 maize genotypes. Each plot measured 4 × 4.8 m and contained a single genotype. Plots of the same genotype were labeled with suffixes "–1", "–2", and "–3" to distinguish treatment types (Fig. 5.1). In repeat 1, plots ending with "–1" were inoculated with *Curvularia lunata*, "–2" with *Bipolaris maydis*, and "–3" remained uninoculated. The treatment order was rotated in repeat 2 to minimize cross-contamination ("–3": *Curvularia lunata*; "–2": *Bipolaris maydis*; "–1": uninoculated). The inoculation with the bacterial leaf spot solution followed the same procedure as in 2021, conducted on the evening of August 16, during the big trumpet period of maize.

Both experimental years maintained a consistent planting density at approximately 75,000 plants per hectare. Field management practices, including fertilization and irrigation, were carried out according to recommendations from local agricultural experts to ensure balanced water and nutrient levels (Xu et al., 2017). These practices were designed to minimize potential influences on disease development, ensuring uniformity across both experimental years.

5.2.1.2 Field surveys

Field surveys were conducted following the onset of infection to calculate the DI for each plot and monitor the progression of maize leaf spot (Fig. 5.2). The survey dates are listed in Table 5.1.

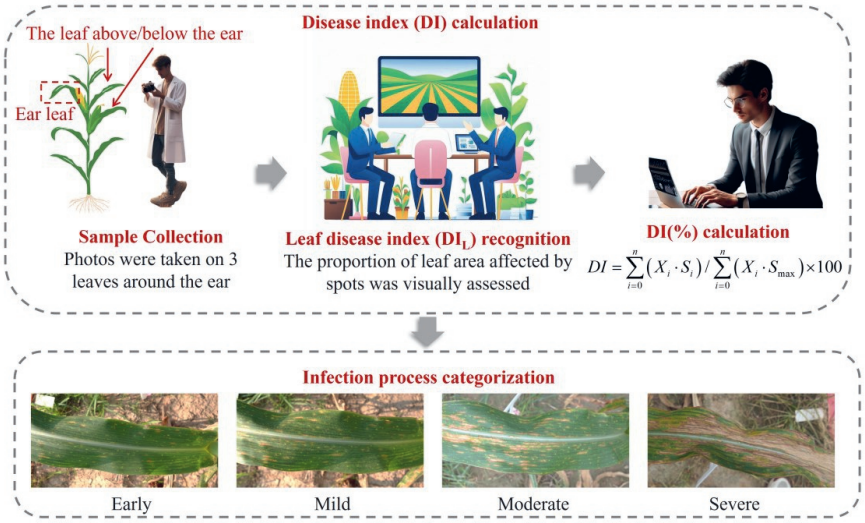


Fig. 5.2. *Flow chart of field survey. Note: S_i = the degree of disease severity (0, 1, 3, 5, 7, 9 for lesion coverage of 0%, 1%–5%, 6%–25%, 26%–50%, 51%–75%, 76%–100%); S_{max} = 9; i = the degree of disease severity; X_i = number of leaves in class i.*

DI reflects the percentage of leaf area affected by leaf spot symptoms and serves as a quantitative measure of disease severity. The DI calculation consisted of three main steps: sample collection, leaf DI (DI_L) assessment, and canopy-level DI estimation. In the sample collection phase, 3 maize plants per plot were randomly selected in 2021, and 5 plants per plot in 2023, due to the larger plot sizes in 2023. From each selected plant, three leaves were collected, specifically the leaf above the ear, the ear leaf, and the leaf below the ear. Leaf images were captured on-site for further analysis. Leaf disease severity was evaluated by three expert assessors, who estimated the proportion of each leaf surface covered by lesions based on the images. This proportion was recorded as the DI_L. Based on the DI_L, the plot-level DI was calculated using (1).

$$DI = \sum_{i=0}^{n}(X_i \cdot S_i) / \sum_{i=0}^{n}(X_i \cdot S_{\max}) \times 100 \quad (1)$$

Where, S_i represents the degree of disease severity, taking values of 0, 1, 3, 5, 7, and 9, which correspond to lesion coverage ranges of 0%, 1%–5%, 6%–25%, 26%–50%, 51%–75%, and 76%–100%, respectively; and S_{max} is the highest degree of disease severity, which in this study is 9; i denotes the degree of disease severity (0–n); X_i is the number of leaves assigned to severity class i.

To evaluate model performance across the disease progression, we categorized the infection process into four stages based on lesion characteristics and the condition of the majority of leaves (more than 50% of leaves per plot). The **early stage** was characterized by scattered small lesions and occurred within 18 days after infection (DAI). The **mild stage** involved the appearance of two or more connected linear lesions, typically between DAI 19 and 26. The **moderate stage** was defined by three or more

connected planar lesions, observed between DAI 27 and 34. Finally, the **severe stage** was identified when more than 50% of the leaf area was affected, generally occurring after DAI 34.

5.2.1.3 Hyperspectral images collection and preprocessing

Hyperspectral imagery was collected on the same dates as the field survey (Table 5.1) to ensure consistency between the imagery and field observations. Hyperspectral images were captured using a Pika L hyperspectral camera (Resonon, Bozeman, MT, USA), mounted on a Matrice 600 Pro Hexacopter UAV (DJI, Shenzhen, China). The UAV was equipped with an onboard RTK-GNSS unit for centimeter-level navigation accuracy. Images were taken at an altitude of 50 m with a speed of 1.5 m/s, and all flights conducted between 10:00 and 14:00 to minimize the influence of sun angle.

The hyperspectral sensor has 150 spectral bands ranging from 400 to 1000 nm, with a spectral resolution of 2.1 nm (with two adjacent bands combined into one) and a full width at half maximum (FWHM) of 3.3 nm. The sensor's 17 mm optical focal length provided an instantaneous field of view (IFOV) of 1.47 mrad and a field of view (FOV) of 30.8°, resulting in a spatial resolution of approximately 0.5 cm.

Raw hyperspectral images were initially converted to radiance by applying the instrument's radiometric calibration file using SpectrononPro (Resonon, Bozeman, MT, USA). This calibration process applied a pixel-specific gain cube and an automatically selected offset (dark noise) cube to correct for instrument response. Specifically, radiometric calibration was performed using (2):

$$Radiance = (RawData - offset) \times gain \quad (2)$$

where the gain and offset were derived from the .icp calibration file provided by the manufacturer.

Data cubes captured along the same flight path were then merged into a single linear cube based on each flight line. These linear cubes were georeferenced in ArcGIS 10.2 (Esri, Redlands, CA, USA) and co-registered using high-resolution RGB images acquired simultaneously, incorporating ground control points to ensure precise spatial alignment. Radiometric calibration was subsequently performed in ENVI 5.3 (ITT Visual Information Solutions, Boulder, USA) using a 60% reflectance gray reference panel placed in the field. The panel was placed on a flat and open surface in the field and included in each flight mission to correct for ambient lighting conditions. The calibrated linear cubes were merged into a seamless mosaic of the study area. Zonal statistics were then extracted for each plot boundary using the "Zonal Statistics as Table" tool within ENVI 5.3, providing plot-level reflectance data.

Table 5.1 Experiment data acquisition time

Year	Infection date	Field survey and hyperspectral image acquisition (days after infection, DAI)
2021	2 August	Early: DAI 18; Mild: DAI 25; Moderate: DAI 31; Severe: DAI 37
2023	16 August	Early: DAI 13, DAI 16; Mild: DAI 20, DAI 24; Moderate: DAI 27, DAI 31; Severe: DAI 37, DAI 40

5.2.2 PGDL framework

Our PGDL framework (Fig. 5.3) consists of three main stages. First, we generated a large synthetic spectral dataset using RTMs by simulating diverse combinations of maize biophysical and biochemical variables, as described in **Section 5.2.3**. Second, we pre-trained a DL model on the simulated data, using spectral features as inputs and either the DI or a closely related biochemical variable (C_{ab}) as the output. This process enabled the model to learn generalizable domain-specific knowledge encoded in the RTM. The structure of the DL model is further detailed in **Section 5.2.4.2**. Finally, we applied transfer learning by fine-tuning the pre-trained model on observed UAV-based hyperspectral data to estimate DI under real-world conditions.

Transfer learning is a ML approach that reuses a model trained on one domain (source) to improve performance on another (target), particularly when labeled data in the target domain is limited (Pan and Yang, 2010). It encompasses several types: inductive, transductive, and unsupervised transfer learning (Zhuang et al., 2020). Inductive transfer uses the pre-trained model as a feature extractor; transductive fine-tunes the model on a small labeled dataset from the target domain; and unsupervised transfer adapts the model without using labeled target data. Our approach follows the transductive transfer learning paradigm. In this case, both the source and target domains—RTM-simulated and UAV-observed hyperspectral data, respectively—share the same spectral feature space. Thus, our transfer learning setup is straightforward and falls under the category of fine-tuning transfer learning [24], where knowledge from the large, labeled simulation dataset is transferred to enhance model performance on the smaller, labeled UAV dataset.

5.2.3 RTM simulation

RTM simulations were employed to support both the physically based DI retrieval and the development of the PGDL framework. Given that UAV hyperspectral data were collected at the canopy scale, the simulations were also designed at this scale to ensure compatibility. To simulate canopy-level reflectance, we combined leaf RTM and canopy RTM. The leaf RTM accounts for chemical and structural characteristics such as pigment concentration and leaf thickness (Stuckens et al., 2009), while the canopy RTM describes how canopy reflectance is influenced by wavelength, leaf and soil optical properties, 3D canopy structure, and illumination and viewing geometry (Qi et al., 2023). Since DI is not a direct input variable in RTMs, we employed two strategies

to simulate canopies at different stages of disease severity. The first strategy replaced DI with biophysical parameters (e.g., C_{ab}) that are directly modeled in RTMs and correlated with disease progression. The second strategy used field-measured leaf spectra corresponding to different DI levels as inputs to the canopy RTM, allowing us to simulate disease-specific canopy reflectance. Specifically, we designed three simulation approaches (Fig. 5.3a, Table 5.2) to span a range of disease conditions: simulations based on evenly spaced C_{ab} (SIM #1), measured leaf disease spectra (SIM #2), and mixed endmember spectra (SIM #3). The simulations utilized two physical models: the leaf RTM, PROSPECT-D (Féret et al., 2017), and the canopy RTM, LESS (Qi et al., 2019). The PROSPECT-D simulates leaf spectral reflectance under varying pigment content, while LESS uses leaf reflectance as input to model canopy spectral reflectance, incorporating factors like planting spacing, 3D plant structure (object properties), solar zenith, and azimuth angles. The model input parameters were estimated using leaf optical property datasets (Peters and Noble, 2024), findings from prior studies (Nie et al., 2023), and the experimental settings of this study, to capture the range of variability observed in real-world maize fields. Model inputs are summarized in Table 5.3, Table S5.1 and Table S5.2.

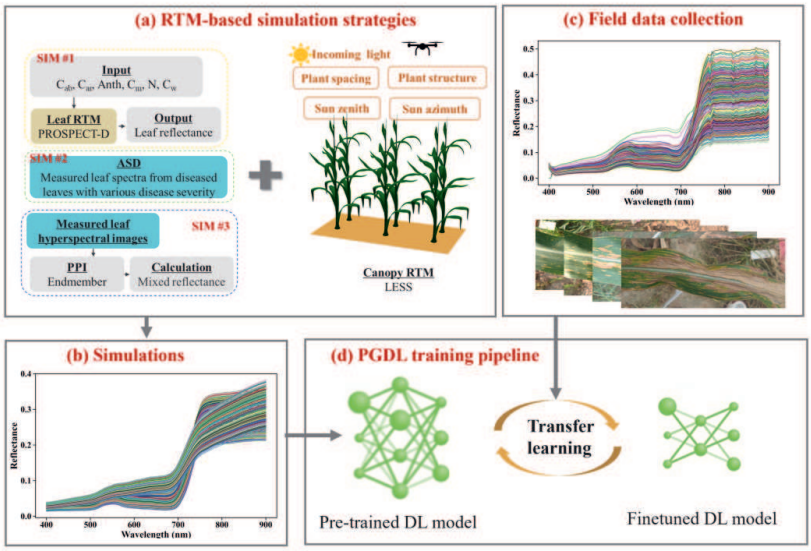


Fig. 5.3. *PGDL framework. (a) Three canopy-scale RTM simulation strategies. (b) Simulated spectral reflectance curves generated using the three RTM strategies. (c) Field-acquired hyperspectral data and corresponding disease severity assessments used to build and validate practical models, and (d) PGDL training pipeline, consisting of two phases: model pre-training using simulations and fine-tuning via transfer learning with field data. Note: RTM: radiative transfer model, C_{ab}: chlorophyll content, C_{ar}: carotenoid content, Anth: anthocyanin content, C_m: dry matter content, N: leaf structural parameter, C_w: equivalent water thickness, PPI: pixel purity index.*

Table 5.2 Details of simulation methods.

Method Name	Input	RTM Model	Output	Advantages	Disadvantages
SIM #1	Leaf chlorophyll content (C_{ab})	PROSPECT -D + LESS	Canopy spectra with varying C_{ab}	No measured data required	Conceptual Bias: $C_{ab} \neq$ disease index (DI)
SIM #2	Measured leaf spectra with varying DI	LESS	Canopy spectra with varying DI	Closer to real data, lower cumulative error	Large data workload
SIM #3	Endmember spectra identified from hyperspectral leaf images	LESS	Canopy spectra with varying DI	Smaller data workload	Overly idealized simulation results

Table 5.3 The inputs of PROSPECT-D and LESS

Model	Variable	Unit	Acronym	Range	Step	Number of Values
PROSPECT-D	Chlorophyll content	μg/cm^2	C_{ab}	15–70	2	28
LESS	Plant spacing	m	PS	0.2–0.55	0.05	8
	Sun Zenith	°	SZ	26–38	2	7
	Sun Azimuth	°	SA	124–253	2	65
	Object	-	-	Two different maize plants	-	2

Note: To eliminate the influence of factors such as observation angle, spectral resolution, and plot size, we fixed other parameters in the PROSPECT-D and LESS models. The fixed inputs are detailed in Table S5.1 and Table S5.2 of the supplemental information.

5.2.3.1 SIM #1: simulations based on C_{ab}

In SIM #1, C_{ab} was used as a proxy for DI, as reduced chlorophyll levels are often associated with crop disease severity (Wang et al., 2023a; Zarco-Tejada et al., 2018). Combining PROSPECT-D and LESS, we simulated canopy reflectance spectra by varying C_{ab}. The other inputs of PROSPECT-D were fixed. The range of PROSPECT-D variables considered for our study was based on the measurements for maize in the literature. The LESS variables were based on observations from Xinxiang on August 1, 2021, between 10:00 and 14:00 and local agricultural practices. The inputs are detailed in Table 5.3. A total of 203,840 canopy-level spectra were generated by combining all parameter permutations: 28 C_{ab} levels, 8 plant spacing configurations, 7 solar zenith angles, 65 solar azimuth angles, and 2 maize plant types.

5.2.3.2 SIM #2: simulations based on measured spectra from diseased leaves

In SIM #2, canopy reflectance was simulated using the LESS model alone, with leaf-level reflectance spectra as inputs. These spectra were collected using an ASD Field Spec PRO 4 (Analytical Spectral Devices, Inc., Boulder, CO, USA) equipped with a leaf clip. Measurements were taken from maize leaves infected with leaf spot disease during the 2021 field experiment at multiple time points (DAI 2, 10, 17, 26, 30, and 37). A fixed leaf was selected for measurement from the second column (counting west to east) of each replicate plot at each time point. In total, 82 infected leaves were sampled, with reflectance measured at three points on the adaxial surface (1/3, 1/2, and 2/3 of the distance from the maize leaf sheath). The average reflectance value from these three measurements was used to minimize the effects of local variability and random measurement errors.

Concurrently, the percentage of the leaf surface covered by leaf spots was recorded as the DI_L following the field survey workflow. To reduce human error in DI_L, we categorized leaf spot severity in 10% increments, resulting in 11 discrete DI_L levels (i.e., 0, 10%, 20%, ..., 100%). For each DI_L category, the averaged spectra were used as input for the LESS model. The other LESS model inputs are consistent with SIM #1. A total of 80,080 canopy reflectance spectra were simulated by combining 11 DI_L levels, 8 plant spacing configurations, 5 solar zenith angles, 44 solar azimuth angles, and 2 maize plant types.

5.2.3.3 SIM #3: simulations based on mixed endmember spectra

In SIM #3, canopy reflectance was again simulated using the LESS model, but with synthetic leaf-level spectra generated through linear mixing of healthy and diseased endmember spectra. To obtain these pure endmembers, hyperspectral images of infected maize leaves were collected under controlled laboratory conditions. The process consisted of three main steps: hyperspectral image collection, endmember extraction, and mixed spectra generation.

Hyperspectral image collection. Hyperspectral images were acquired from maize leaves exhibiting visible leaf spot symptoms during the 2023 field experiment at DAI 31. Three infected leaves were excised in the field and imaged on the same day. Imaging was performed using an indoor hyperspectral imaging system (Pika L, Resonon, Bozeman, USA) and processed with SpectrononPro software (Resonon, Bozeman, USA). The sensor's spectral characteristics matched those of the UAV-mounted sensor. Images were taken at a distance of 0.5 m from the leaf, with a reference panel (100% reflectance) placed nearby for spectrum calibration. The spatial resolution of the images was 0.5 mm per pixel. A halogen lamp illuminated the sample at a 45° incident angle, and a 100% diffuse reflectance reference panel was placed horizontally at the same distance from the sensor to estimate incoming irradiance. Reflectance for each pixel and band was calculated as the ratio of the target signal to that of the reference panel.

Endmember extraction: Endmember extraction was used to isolate spectrally pure pixels representing healthy and diseased tissues. Endmember spectra were extracted

from the collected hyperspectral images using ENVI's Endmember Extraction Tool, applying the pixel purity index (PPI) method (Ex, 2009). The PPI was run with 100 iterations and a threshold factor of 1. Pixels located at the vertices of the spectral data cloud were selected as candidate endmembers, resulting in the identification of approximately six spectral endmembers. These candidates correspond to pixels that may represent healthy and diseased tissues, leaf veins, leaf edges, or other spectral extremes. To determine the healthy and diseased endmembers, we used leaf spectra with DI_L values of 0% and 100% (from SIM #2) as reference spectra. Spectral similarity between the extracted endmembers and the reference spectra was quantified using the spectral angle mapper algorithm (Kruse et al., 1993). The endmembers with the smallest spectral angle relative to the healthy and diseased reference spectra were selected as the final inputs representing healthy and diseased leaf, respectively. The mean spectra from the three sampled leaves were used as the representative healthy and diseased endmember spectra for further calculation.

Mixed spectra generation: Mixed spectra for different DI_L levels were generated by linearly combining the healthy and diseased endmember spectra with (3).

$$R_{mix} = DI_L \times R_d + (1 - DI_L) \times R_h \quad (3)$$

where, R_d and R_h are the endmember spectra for diseased and healthy leaf pixels, respectively. A total of 101 mixed spectra (R_{mix}) were generated, covering DI_L levels from 0% to 100% in 1% increments. Other inputs for the LESS model are consistent with SIM #1. In total, 735,280 canopy reflectance spectra were generated by combining 101 R_{mix} spectra, 8 plant spacing configurations, 5 solar zenith angles, 44 solar azimuth angles, and 2 maize plant types. In these simulations, DI_L corresponds directly to the DI, as each leaf in the maize plant has a consistent DI_L value.

5.2.3.4 Spectral consistency and correlation analysis

To evaluate the feasibility of using simulated reflectance data for maize leaf spot monitoring, we conducted a consistency analysis. Specifically, we compared canopy reflectance spectra generated from the three simulation methods (SIM #1, SIM #2, and SIM #3) with UAV-based hyperspectral observations. The comparison focused on four representative DI levels: 0%, 30%, 50%, and 70%.

For UAV data, canopy reflectance spectra were averaged from field plots with DI values within ±5% of the target levels. Simulated spectra were selected under conditions that closely matched the field experiment setup, including plant spacing (0.20 m), solar zenith angle (29°), and solar azimuth angle (166°). For SIM #1, canopy spectra were simulated using C_{ab} values of 15, 25, 35, and 45 μg/cm², corresponding to the DI levels, following the approach in Wang et al. (2023a).

We then performed linear regression analysis between the simulated and UAV-derived spectra for each DI level. Model performance was evaluated using the coefficient of determination (R^2), root mean square error (RMSE), relative RMSE (rRMSE), slope, and intercept. In this study, rRMSE was defined as RMSE normalized by the mean of the DI values from field survey.

To further evaluate the potential of integrating simulated and UAV spectra for DI monitoring, Pearson's correlation coefficients were computed between reflectance values and corresponding disease indicators. For UAV data, the ground-truth DI from field surveys was used. For SIM #2 and SIM #3, the DI was derived directly from the simulated leaf-level spectral input. In the case of SIM #1, C_{ab} concentration served as a proxy for DI.

5.2.4 Modeling methods for DI retrieval

Three strategies were employed to monitor maize leaf spot: physically-based methods (Section 5.2.4.1), data-driven methods (Section 5.2.4.2), and the PGDL approach (Section 5.2.2). To minimize noise in the raw reflectance data, we selected features sensitive to maize leaf spot as model inputs. These features were identified through a controlled time-series field experiment that characterized the temporal dynamics of spectral responses over a 30-day period following maize leaf spot infection. The selected features consistently responded to infection severity and passed collinearity diagnostics. Detailed methodology and feature selection criteria are described in (Bai et al., 2024a). A list of these features is presented in Table 5.4.

5.2.4.1 Physically-based method

We employed a numerical optimization method to estimate the DI from UAV-based hyperspectral data using features derived from physically simulated spectra. This method follows the workflow described by van der Tol et al. (2016). It works by iteratively adjusting model parameters to minimize a cost function that compares simulated and measured reflectance. Here, we used the Python function least_squares (from scipy.optimize) to minimize the difference between simulated and observed UAV hyperspectral spectra. The optimization process was stopped when the relative change in the cost function fell below 10^{-3} (controlled by the ftol parameter). DI retrieval was performed using the SIM #2 and SIM #3 simulation datasets, as they establish a correspondence between spectral features and DI. To minimize uncertainties in disease monitoring, only simulation data with solar zenith and azimuth angles within 5° of the UAV data were considered. Plant spacing was fixed at 0.20 m, consistent with field experimental conditions. In total, 550 simulated spectra in SIM #2 (11 DI_L levels, 5 solar zenith angles, 5 solar azimuth angles, and 2 maize plant types) and 5050 simulated spectra in SIM #3 (101 R_{mix} spectra, 5 solar zenith angles, 5 solar azimuth angles, and 2 maize plant types) were used.

Table 5.4 Features used in modeling.

Feature	Abbreviation	Formula	Response time to maize leaf spot	Reference
NDVI	Normalized Difference Vegetation Index	$(R_{800}-R_{670})/(R_{800}+R_{670})$	DAI 15	Rouse et al. (1974)
PSRI	Plant Senescence Reflectance Index	$(R_{680}-R_{500})/R_{750}$	DAI 12	Merzlyak et al. (1999)
PRIn	Normalized Photosynthetic Reflectance Index	$PRI_{570}/[RDVI\times(R_{700}/R_{670})]$, Where $RDVI=(R_{800}-R_{670})/(R_{800}+R_{670})^{1/2}$	DAI 8	Zarco-Tejada et al. (2013)
RGI	Relative Greenness Index	R_{690}/R_{550}	DAI 12	Zarco-Tejada et al. (2005)
VARI2	Visible Atmospherically Resistant Index 2	$(R_{560}-R_{668})/(R_{560}+R_{668}-R_{475})$	DAI 12	Gitelson et al. (2001)
$WF_{494,5}$	Wavelet Feature at 494 nm with a Scale of 5	--	DAI 22	Cheng et al. (2010)
$WF_{461,6}$	Wavelet Feature at 461 nm with a Scale of 6	--	DAI 12	Cheng et al. (2010)
$WF_{469,7}$	Wavelet Feature at 469 nm with a Scale of 7	--	DAI 12	Cheng et al. (2010)
$WF_{548,8}$	Wavelet Feature at 548 nm with a Scale of 8	--	DAI 22	Cheng et al. (2010)
$WF_{590,8}$	Wavelet Feature at 590 nm with a Scale of 8	--	DAI 6	Cheng et al. (2010)

5.2.4.2 Data-driven method

For the data-driven method, we tested an ML model—gradient boosting decision trees (GBDT)—as well as three DL architectures: multilayer perceptron (MLP), long short-term memory (LSTM), and gated recurrent unit (GRU) networks.

GBDT is an ensemble learning method that builds a sequence of decision trees, where each successive tree corrects the residual errors of the previous one. This model was selected due to its demonstrated effectiveness in maize leaf spot monitoring, having outperformed RF and support vector regression (SVR) in a previous study by Bai et al. (2024b).

All DL models adopted a shared architecture consisting of three components: a core neural network (MLP, LSTM, or GRU), an attention layer, and a final regression layer. First, normalized hyperspectral features were processed by the core network. The resulting outputs were passed to the attention layer, which computed feature-level attention weights to indicate importance. The outputs from both the core unit and the attention layer were concatenated and input into a fully connected regression layer to predict DI. This architecture was also used in the PGDL framework.

MLP is a basic network composed of multiple layers of artificial neurons. Given that the spectral input data consisted of 10 features, the MLP architecture in this study was

designed with three hidden dense layers containing 10, 40, and 80 neurons, respectively. Each layer employed a Rectified Linear Unit (ReLU) activation function to introduce nonlinearity.

The LSTM unit is capable of learning long-term dependencies by maintaining an internal memory of past inputs, making it well-suited for handling the temporal patterns present in hyperspectral data. An LSTM unit uses three gating mechanisms—input gate, forget gate, and output gate—to regulate the flow of information through the network. These gates determine which information is added to, removed from, or passed through the memory cell at each time step. Specifically: The input gate (i_t) controls how much new information is written to the cell state, the forget gate (f_t) decides how much of the previous cell state should be retained, and the output gate (o_t) determines how much of the cell state is exposed to the output. The LSTM equations governing these gates and the cell state update are defined in (4)-(8):

$$i_t = \sigma\left(W_i \cdot \left[h_{t-1}, x_t\right] + b_i\right) \quad \text{(input gate)} \quad (4)$$

$$f_t = \sigma\left(W_f \cdot \left[h_{t-1}, x_t\right] + b_f\right) \quad \text{(forget gate)} \quad (5)$$

$$o_t = \sigma\left(W_o \left[h_{t-1}, x_t\right] + b_o\right) \quad \text{(output gate)} \quad (6)$$

$$C_t = f_t * C_{t-1} + i_t * \tanh\left(W_C \cdot \left[h_{t-1}, x_t\right] + b_C\right) \quad (7)$$

$$h_t = o_t * \tanh\left(C_t\right) \quad (8)$$

Here, x_t, h_t and c_t represent the input, hidden state, and cell state at time step t, respectively. W and b denote the learnable weights and biases for each gate. The sigmoid (σ) and hyperbolic tangent ($\tanh$) functions introduce nonlinearity and ensure gated control over information flow.

The GRU unit, designed for sequential data, includes an update gate and a reset gate. The update gate focuses on integrating new information into the hidden layer, while the reset gate disregards less important information. The formulas are given as in (9)-(12):

$$z_t = \sigma\left(W_z \cdot \left[h_{t-1}, x_t\right]\right) \quad \text{(Update gate)} \quad (9)$$

$$r_t = \sigma\left(W_r \cdot \left[h_{t-1}, x_t\right]\right) \quad \text{(Reset gate)} \quad (10)$$

$$\tilde{h}_t = \tanh\left(W \cdot \left[r_t * h_{t-1}, x_t\right]\right) \quad \text{(New memory cell)} \quad (11)$$

$$h_t = \left(1 - z_t\right) * h_{t-1} + z_t * \tilde{h}_t \quad (12)$$

where, h_{t-1} represents the output from the previous time step, x_t is the current input, [ ] denotes concatenation, W_z, W_r, and W represent the learning weights for the update gate, reset gate, and new memory cell, respectively, σ and tanh are sigmoid and tanh activation functions, respectively, while $\tilde{h}_t$ represents the output of the new memory cell, and h_t denotes the output at the current time step.

The attention mechanism assigns importance weights to each feature, enhancing the model's ability to focus on relevant spectral features for DI prediction (Vaswani, 2017). The attention weights are computed in (13)-(15):

$$e^j = score(h^j) \tag{13}$$

$$\alpha_j = \frac{\exp\left(e^j\right)}{\sum_{i=1}^{T_x} \exp\left(e^i\right)} \cdot \Leftrightarrow \cdot \alpha = \mathrm{SoftMax}(e) \tag{14}$$

$$C = \sum_{i=1}^{T_x} \alpha_i h^i \tag{15}$$

where, h^i represents the input feature, while e^i and e^j denote the scores for each feature. The mapping function (score) used is a linear function. α represents the attention weight, and e denotes the total feature scores. The SoftMax function is applied, where exp refers to the exponential function. T_x is the total number of features. Finally, C represents the weighted sum of the features.

5.2.4.3 Training and evaluation

The model training scenarios in this study were organized into three categories: ML, DL and PGDL. In this section, we will explain how different models were trained to monitor DI. The modeling datasets include data collected from 2021 and 2023, which were divided into four disease stages: early, mild, moderate, and severe. For each stage dataset, 80% of the data were randomly selected for training, and the remaining 20% for testing. All models were trained on the training set and evaluated on the independent test set.

GBDT. The GBDT model was trained using scikit-learn library (version 1.1.3) in Python 3.7. Hyperparameters were identified using a grid search approach combined with repeated 10-fold cross-validation. Specifically, within each iteration of grid search, a 10-fold cross-validation was performed and repeated five times with different random splits to reduce the impact of data partitioning bias. The average performance across these repetitions was used to determine the optimal hyperparameter configuration. The final parameter settings were: n_estimators = 50, learning_rate = 0.3, max_depth = 5, and min_samples_leaf = 5.

DL. We considered DL models with three different combinations of architectures (i.e., MLP, LSTM, and GRU) to regressing DI. The DL model training and evaluation were performed using Python 3.7, PyTorch 2.4.1. As a regression task, the mean squared error (MSE) was used as the loss function with the Adam optimizer. The learning rate was initialized at 0.01 and decayed exponentially during training. A batch size of 1000 was used. All models were trained for up to 1000 epochs with an early stopping criterion. We divided the training set for the deep learning model into training and validation. The DL model was trained on the training set, and performance was evaluated on the validation set using R^2 and RMSE metrics after each epoch. The early stopping enables the models to automatically stop training when the testing R^2 value does not increase by at least 0.005 over 20 epochs.

PGDL. We considered a variety of PGDL in this study, PGDL with many different combinations of architectures (i.e., MLP, LSTM and GRU) based on three simulation datasets (SIM #1; SIM #2 and SIM #3). The PGDL training process included two stages: pre-training and transfer learning.

During pre-training, each simulation dataset (SIM #1, SIM #2, and SIM #3) was used separately to pre-train a DL model. The same learning rate, batch size, loss function, optimizer, and early stopping criteria as DL training were used. For SIM #1 simulations, C_{ab} was normalized to a range of 0 to 1 to ensure consistency in the range of DI values. In the second phase, transfer learning was applied by fine-tuning the pretrained models using real-world UAV-based observations, maintaining the same training configurations as in DL.

Evaluation. To assess and compare model performance, we employed several metrics: R^2, RMSE, mean absolute error (MAE), and rRMSE. Evaluation was conducted using both 2021 and 2023 datasets, and models were tested across different disease stages (early, mild, moderate, severe) to evaluate their ability to generalize. Additionally, to gain insights into spectral feature relevance, the attention layer in DL models were used to estimate feature importance. The integrated attention mechanism assigned interpretable weights to input features, highlighting their relative contributions to the DI monitoring.

5.3 Results

5.3.1 Consistency analysis between simulated reflectance and UAV spectra

5.3.1.1 Spectral trends

A comparison of reflectance spectra from simulations and UAV measurements under different levels of leaf spot severity is presented in Fig. 5.4. The spectral reflectance curves (Fig. 5.4e–h) show that UAV spectra demonstrated a consistent increase in the visible range, particularly from 550–700 nm, with DI increases. Similar trends were observed for SIM #2 and SIM #3, although with more pronounced variations. In contrast, SIM #1 exhibited an increase in reflectance around 550 nm (±50 nm) as C_{ab} decreased, diverging from the UAV pattern.

Regression results further highlight these differences (Fig. 5.4i–l; Table S5.3). Among the simulations, SIM #2 outperformed the others, achieving the R^2 (0.99) and RMSE (0.01) consistently across all DI levels. It also showed the most stable rRMSE (0.03–0.06), slope (1.24–1.36), and intercept (-0.03–0.00), indicating robust adaptability to varying DI levels. While SIM #3 performed comparably, it was slightly less accurate than SIM #2. In contrast, SIM #1 showed a decline in R^2 (from 0.98 to 0.94) and an increase in rRMSE (from 0.10 to 0.17) as DI increased, reflecting weaker adaptability under higher disease severity.

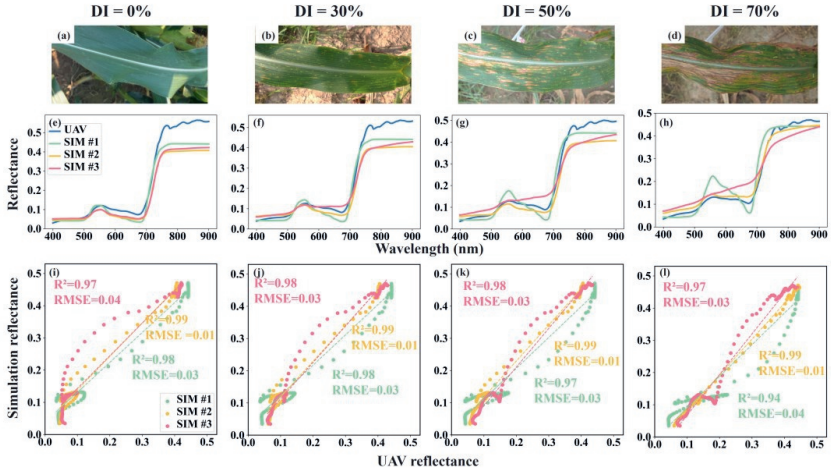


Fig. 5.4. *Comparison of simulated and UAV-measured hyperspectral reflectance under varying maize leaf spot severity levels. Top row (a)–(d): representative maize leaves with different disease index (DI) values. Middle row (e)–(h): spectral reflectance curves from simulations and UAV measurements. Bottom row (i)–(l): regression analysis of simulated vs. UAV reflectance.*

5.3.1.2 Correlation Patterns

The correlation patterns between reflectance and DI revealed that SIM #2, SIM #3, and UAV spectra followed similar trends (Fig. 5.5). However, the magnitude of the correlation coefficients for UAV spectra was consistently lower than those of the simulations. Specifically, in the visible wavelength range (400–700 nm), both SIM #2 and SIM #3 showed a strong positive correlation with DI (r = 0.5 to 1), while UAV spectra exhibited a moderate positive correlation (r = 0.3 to 0.5). In contrast, SIM #1 displayed a negative correlation pattern (r < 0) in this range.

To further explore the relationship between C_{ab} dynamics and DI in maize leaves, C_{ab} values were retrieved from the ASD collected spectra (Section 5.2.3.2) using the PROSPECT-D model inversion (Fig. 5.5b). The inversion process employed an iterative optimization method to identify the optimal simulated spectra with the lowest RMSE, following the approach outlined by Botha et al. (2010). Results showed a significant correlation ($R^2 = 0.45$, RMSE = 11.02, $p < 0.01$) between the retrieved C_{ab} and DI. These results suggest that C_{ab} retrieved by PROSPECT-D reflects disease trends but also has limitations in capturing the full complexity of disease spread progression.

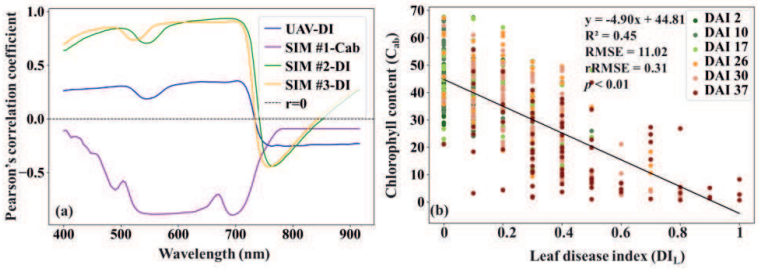


Fig. 5.5 *Correlation patterns. (a): correlation analysis between the spectra and target variables. Blue line: UAV collected wavelength reflectance versus field-surveyed disease index (DI). Purple line: SIM #1 wavelength reflectance versus chlorophyll content (C_{ab}). Green and orange lines: SIM #2 and SIM #3 wavelength reflectance versus DI, respectively. (b): relationship between retrieved C_{ab} and DI_L.*

5.3.2 Model performance in DI regression

5.3.2.1 Performance of pre-trained model on simulations

Table 5.5 summarizes the performance of the pre-trained DL models on the simulation test dataset. The results demonstrated that the DL models achieve state-to-art accuracy across all simulation datasets, which validated the use of the pre-trained DL model as a foundation for developing the transfer learning model.

5.3.2.2 Model performance on field data

The performance of different modeling techniques for monitoring DI from UAV-collected data across two years is presented in Table 5.6, Fig. 5.6 and 5.7, and supplementary Fig. S5.1 and S5.2. Five modeling strategies were compared: physically based models, data-driven models, and three variations of the PGDL framework pretrained using SIM #1, SIM #2, and SIM #3, respectively.

Physically-based models, relying solely on simulations (SIM #2 and SIM #3), exhibited moderate performance, with R^2 values ranging from 0.68 to 0.80, and RMSEs of approximately 0.10–0.11.

Table 5.5 Performance of deep learning models on simulation test sets

Simulations	Model	R^2	RMSE	MAE	rRMSE
SIM #1	MLP	0.95	0.05	0.04	0.11
	LSTM	0.99	0.04	0.02	0.07
	GRU	0.99	0.03	0.01	0.05
SIM #2	MLP	0.93	0.06	0.05	0.15
	LSTM	0.98	0.05	0.04	0.10
	GRU	0.98	0.05	0.03	0.09
SIM #3	MLP	0.99	0.03	0.04	0.12
	LSTM	0.99	0.03	0.04	0.10
	GRU	1.00	0.02	0.01	0.04

Data-driven models trained on field data alone showed improved performance. Among them, the GRU model consistently outperformed others, achieving R^2=0.76 (RMSE = 0.10) in 2021 and R^2=0.84 (RMSE = 0.09) in 2023.

The PGDL strategy showed an improvement in all model performance, highlighting the effectiveness of incorporating prior knowledge from RTM and transfer learning. Specifically, when simulations (SIM #2 and SIM #3) were used to develop pre-trained models with disease-related information, the performance significantly improved. The best performance was achieved with PGDL-GRU using SIM #2 (R^2=0.85 in 2021, R^2=0.93 in 2023). PGDL models based on SIM #3 followed closely, with PGDL-GRU again performing best (R^2=0.82 in 2021, R^2=0.92 in 2023). The lowest RMSE was observed with PGDL using SIM #2 and SIM #3 (RMSE=0.08 in 2021, RMSE=0.06 in 2023). These results indicate prior knowledge combined with measured disease information effectively enhances DI monitoring accuracy. Since the GRU model consistently outperformed the other models, we chose GRU as the basis DL model for the rest of the analysis. Results for other models are provided in the Supplementary Information.

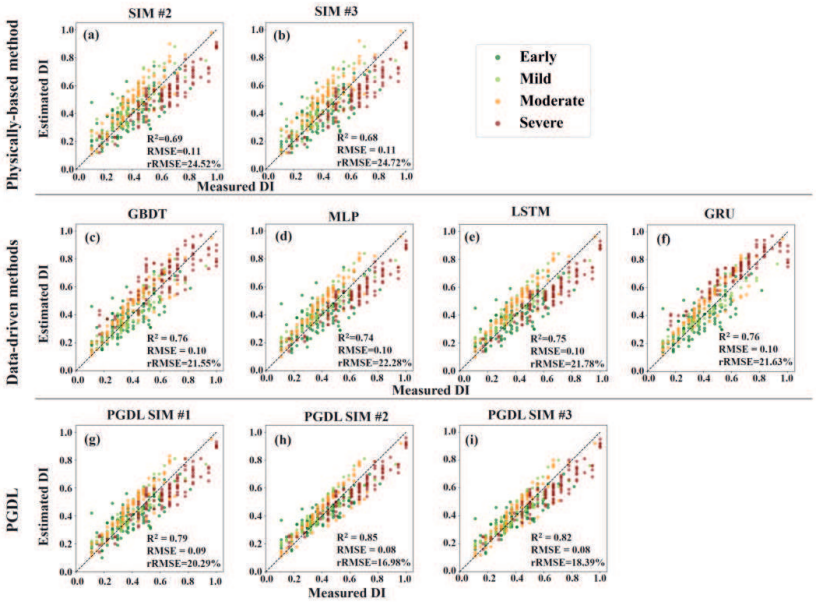


Fig. 5.6 *Model performance for monitoring maize leaf spot disease index (DI) on the 2021 test dataset. All regressions were statistically significant ($p < 0.01$).*

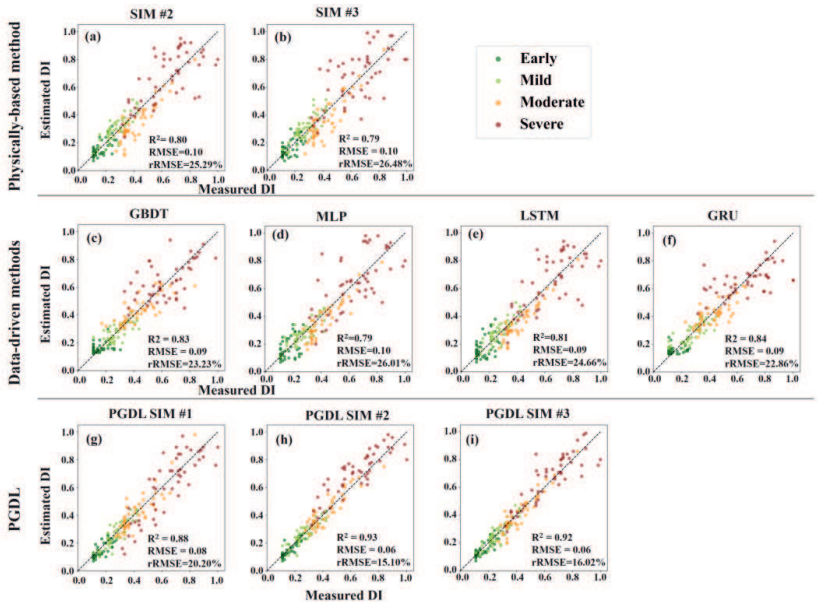


Fig. 5.7 *Model performance for monitoring maize leaf spot disease index (DI) on the 2023 test dataset. All regressions were statistically significant ($p < 0.01$).*

5.3.2.3 Model generalization on time series disease infection

To assess the generalization of our models for monitoring DI over time, we assessed their performance across four stages of maize leaf spot infection (Fig. 5.8, Table 5.7, supplementary Tables S5.4, S5.5, and S5.6). At the Mild and Moderate stages, data-driven models (R^2 ranging from 0.68 to 0.81 in 2021; 0.45 to 0.65 in 2023) showed similar performance to the PGDL approach (R^2 ranging from 0.72 to 0.81 in 2021; 0.68 to 0.81 in 2023). However, at the early stage, data-driven models underperformed (R^2 = 0.55 in 2021; R^2 ranging from -0.07 to -0.05 in 2023), while the PGDL models showed better performance (R^2 ranging from 0.61 to 0.76 in 2021; 0.48 to 0.70 in 2023). Notably, PGDL based on SIM #2 achieved the best performance (R^2 = 0.76 and RMSE = 0.08 in 2021; R^2 = 0.70 and RMSE = 0.03 in 2023), followed by PGDL based on SIM #3 (R^2 = 0.73 and RMSE = 0.08 in 2021; R^2 = 0.63 and RMSE = 0.03 in 2023). Similarly, at the Severe stage, data-driven models showed lower performance (R^2 ranging from 0.60 to 0.63 in 2021; 0.24 to 0.33 in 2023), while the PGDL models performed better (R^2 ranging from 0.68 to 0.80 in 2021; 0.50 to 0.70 in 2023). These results demonstrate that PGDL models, particularly those based on SIM #2 and SIM #3, offer a key advantage in early disease monitoring.

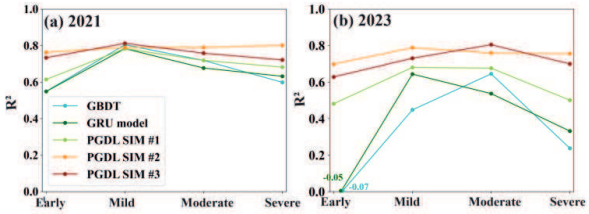


Fig. 5.8 *Model generalization for monitoring maize leaf spot disease index (DI) on time series disease infection*

To further evaluate the performance of PGDL with SIM #2 and SIM #3, we conducted a standardized residual analysis (Fig. 5.9). The residual plots reveal that the residuals are randomly distributed around the baseline (y = 0), suggesting that the PGDL models capture the data's non-linearity. Additionally, the residuals are evenly distributed across different DI values, indicating that the regression model performs consistently well, even at low DI levels.

A spatial map of maize leaf spot disease severity monitored using the PGDL SIM #2 algorithm in 2021 is presented in Fig. 5.10. The results demonstrate balanced performance across the four stages of maize leaf spot infection: Early ($R^2 = 0.76$), Mild ($R^2 = 0.79$), Moderate ($R^2 = 0.79$), and Severe ($R^2 = 0.80$). Through this map and the field evaluations, the differences found can be appreciated, as well as their spatial variability.

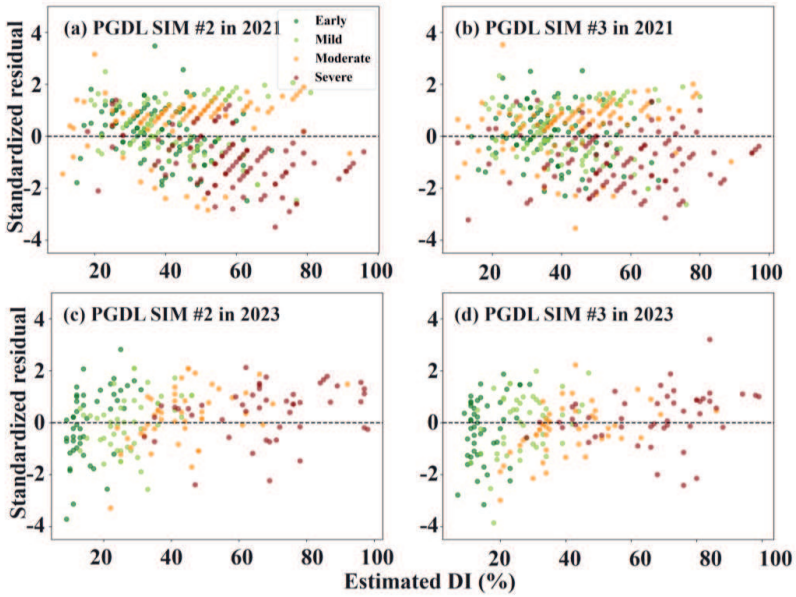


Fig. 5.9 *Standardized residual plot of monitoring maize leaf spot disease index (DI)*

Table 5.6 Model performance for monitoring maize leaf spot disease index (DI) in the 2021 and 2023 test set

Models		2021						2023					
		R^2	**RMSE**	**MAE**	**rRMSE**	**Intercept**	**Slope**	**R^2**	**RMSE**	**MAE**	**rRMSE**	**Intercept**	**Slope**
Physically-based method	Based on SIM #2	0.69	0.11	0.09	24.52%	0.15	0.69	0.80	0.10	0.07	25.29%	0.01	0.96
	Based on SIM #3	0.68	0.11	0.09	24.72%	0.14	0.70	0.79	0.10	0.07	26.48%	0.01	0.96
Data-driven method	GBDT	0.76	0.10	0.08	21.55%	0.10	0.84	0.83	0.09	0.06	23.23%	0.05	0.87
	MLP	0.74	0.10	0.08	22.28%	0.14	0.71	0.79	0.10	0.07	26.01%	0.01	0.94
	LSTM	0.75	0.10	0.08	21.78%	0.14	0.71	0.81	0.09	0.07	24.66%	0.02	0.93
	GRU	0.76	0.10	0.08	21.63%	0.10	0.87	0.84	0.09	0.06	22.86%	0.06	0.83
PGDL SIM #1	MLP	0.77	0.10	0.08	20.83%	0.11	0.74	0.86	0.08	0.06	21.35%	0.01	0.98
	LSTM	0.78	0.09	0.07	20.68%	0.11	0.73	0.87	0.08	0.06	20.38%	0.01	0.99
	GRU	0.79	0.09	0.08	20.29%	0.12	0.74	0.88	0.08	0.06	20.20%	-0.01	0.99
PGDL SIM #2	MLP	0.83	**0.08**	0.07	17.92%	0.11	0.77	0.91	0.07	0.05	17.39%	0.00	0.99
	LSTM	0.83	**0.08**	0.07	18.06%	0.12	0.75	**0.93**	**0.06**	**0.04**	15.28%	0.01	0.96
	GRU	**0.85**	**0.08**	**0.06**	**16.98%**	0.12	0.76	**0.93**	**0.06**	**0.04**	**15.10%**	0.00	1.04
PGDL SIM #3	MLP	0.77	0.10	0.08	20.92%	0.15	0.70	0.91	**0.06**	0.05	16.92%	0.00	1.03
	LSTM	0.81	0.09	0.07	18.84%	0.10	0.75	0.90	0.07	0.05	18.51%	0.01	0.98
	GRU	0.82	**0.08**	0.07	18.39%	0.10	0.77	0.92	**0.06**	**0.04**	16.02%	0.00	1.01

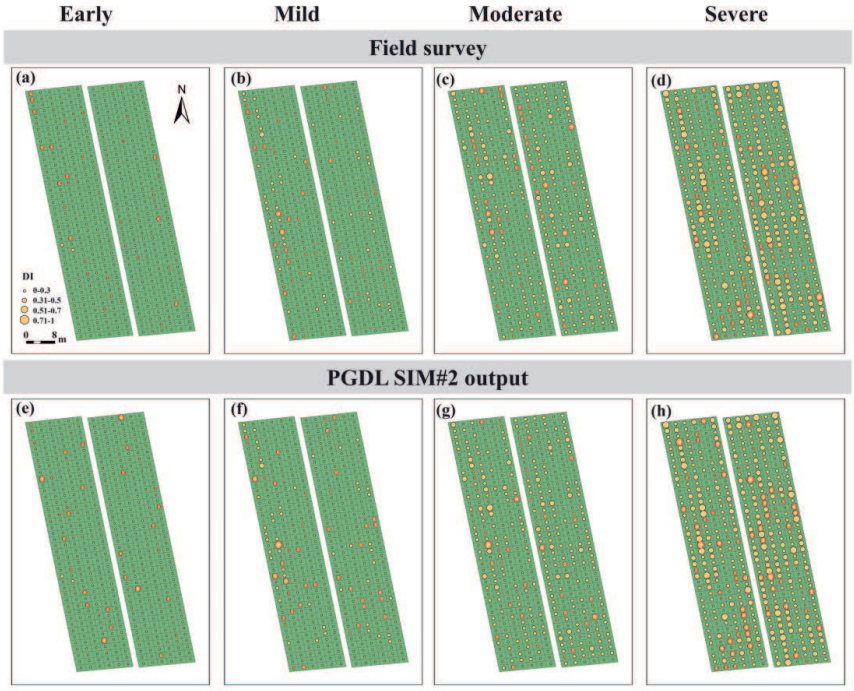


Fig. 5.10 *Spatial maize leaf spot monitoring map from the PGDL SIM #2 output. The top and bottom rows represent field survey and PGDL SIM #2 model outputs, respectively. The size of each circle corresponds to the maize leaf spot disease index (DI), and circles with a red outline indicate discrepancies between the field survey and model output.*

5.3.3 Feature importance and response to DI monitoring

To get a better understanding of how features contribute to model monitoring disease, we evaluated the importance scores of each input feature using attention weights (Fig. 5.11). The results from the pre-trained PGDL SIM #2 and SIM #3 models align with findings from Bai et al. (2024a). The feature with the highest attention score is VARI2, while the lowest is $WF_{494,5}$. VARI2, which is related to anthocyanins, begins to respond to disease from DAI 12. In contrast, $WF_{494,5}$, located in the blue region (450–550 nm), primarily reflects chlorophyll absorption and starts responding to the disease from DAI 22.

Applying the model with field data using transfer learning can significantly alter the importance of features, as reflected by the changes in feature scores shown by the bars (model before transfer learning) compared to the lines (model after transfer learning) in Fig. 5.11. This change also observed by Wang et al. (2023b). This shift occurs because remote sensing features are highly influenced by environmental conditions during data acquisition, which can lead to varying selections of disease-sensitive features across different studies. Understanding and validating these sensitive features

under ideal conditions, as defined by physical models, is crucial for model refinement. Transfer learning thus enhances the model's accuracy for specific tasks by adjusting feature weights according to real-world data.

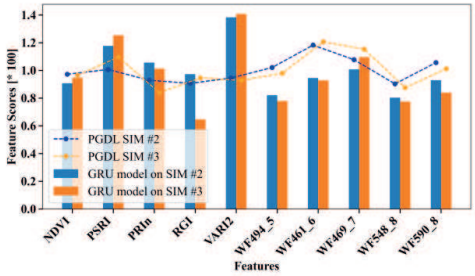


Fig. 5.11 *Feature importance for GRU model before and after transfer learning for monitoring maize leaf spot disease index (DI)*

Table 5.7 Model performance for monitoring maize leaf spot disease index (DI) across different disease stages in the 2021 and 2023 test set

Models	Datasets	2021						2023					
		R^2	RMSE	MAE	rRMSE	Intercept	Slope	R^2	RMSE	MAE	rRMSE	Intercept	Slope
GBDT	Early	0.55	0.10	0.08	27.87%	0.14	0.63	-0.05	0.05	0.04	34.65%	0.13	0.18
	Mild	0.81	0.07	0.06	17.08%	0.08	0.83	0.45	0.05	0.04	19.16%	0.11	0.58
	Moderate	0.72	0.09	0.08	20.56%	0.09	0.93	0.65	0.08	0.06	17.79%	0.17	0.59
	Severe	0.60	0.13	0.11	19.79%	0.29	0.60	0.24	0.14	0.10	21.73%	0.34	0.48
GRU model	Early	0.55	0.10	0.08	27.89%	0.13	0.63	-0.07	0.05	0.04	34.90%	0.14	0.10
	Mild	0.78	0.07	0.06	18.01%	0.10	0.83	0.64	0.05	0.04	18.16%	0.11	0.62
	Moderate	0.68	0.09	0.09	22.03%	0.10	0.92	0.54	0.07	0.06	16.28%	0.15	0.62
	Severe	0.63	0.12	0.10	18.95%	0.31	0.63	0.33	0.14	0.10	21.54%	0.43	0.34
PGDL-GRU SIM #1	Early	0.61	0.10	0.07	25.76%	0.13	0.64	0.48	0.04	0.03	23.71%	0.02	0.77
	Mild	0.78	0.07	0.06	18.01%	0.10	0.83	0.68	0.04	0.03	15.93%	0.00	0.99
	Moderate	0.72	0.09	0.08	20.56%	0.09	0.93	0.68	0.07	0.05	15.84%	-0.01	1.02
	Severe	0.68	0.11	0.09	17.61%	0.07	0.76	0.50	0.12	0.10	19.15%	-0.08	1.09
PGDL-GRU SIM #2	Early	0.76	0.08	0.06	20.20%	0.14	0.65	0.70	0.03	0.02	18.07%	-0.01	1.05
	Mild	0.79	0.07	0.06	17.73%	0.10	0.82	0.79	0.04	0.03	12.97%	0.01	0.97
	Moderate	0.79	0.07	0.07	17.76%	0.07	0.92	0.76	0.06	0.05	13.66%	0.00	1.03
	Severe	0.80	0.09	0.07	13.92%	0.09	0.77	0.76	0.09	0.07	13.38%	0.08	0.92
PGDL-GRU SIM #3	Early	0.73	0.08	0.06	21.41%	0.14	0.64	0.63	0.03	0.02	20.07%	0.02	0.83
	Mild	0.81	0.07	0.06	16.77%	0.09	0.82	0.73	0.04	0.03	14.63%	0.01	0.95
	Moderate	0.76	0.08	0.07	19.05%	0.06	0.91	0.81	0.05	0.04	12.30%	-0.04	1.05
	Severe	0.72	0.11	0.09	16.48%	0.03	0.85	0.70	0.10	0.07	14.84%	0.12	0.85

5.4 Discussion

5.4.1 Insights gained from simulation methods

Selecting an appropriate simulation method is crucial for the development of PGDL models. In this study, we used three different simulation methods (Table 5.2). **SIM #1**: A simulated dataset was generated using evenly spaced C_{ab} values coupled with the PROSPECT-D and LESS models. C_{ab} was chosen as a variable for simulation because of its established correlation with disease in previous studies (Hornero et al., 2021). This method allows for large-scale data generation without the need for additional field measurements. However, while C_{ab} correlates with disease, the relationship with the DI is complex. Our sensitivity analysis highlights how variations in target variables influence spectral signatures, showing that C_{ab} alone provides limited insight into the spectral variability associated with disease spread progression. Furthermore, crop disease processes are multifaceted, involving diverse physiological indicators such as vegetation temperature, chlorophyll fluorescence, photosynthetic energy downregulation, and other photosynthetic pigments (Hernandez-Clemente et al., 2019). Although C_{ab} is a key component of photosynthetic pigments, it cannot fully represent the complexities of disease dynamics.

SIM #2: A simulated dataset was generated using ASD measured spectra from diseased leaves and the LESS model. This method most closely resembles UAV-collected data because it reduces the cumulative errors introduced by coupling multiple physical models. However, it requires ground-based spectroscopic measurements, which can be labor-intensive and difficult to obtain in agricultural experiments.

SIM #3: A simulated dataset was generated using mixed spectra from diseased endmembers and the LESS model. This approach simplifies the data collection process compared to SIM #2. However, the simulations are idealized and do not perfectly replicate leaf spectra, as it ignores elements such as leaf veins, in addition to diseased and healthy pixels. Overall, SIM #2 and SIM #3 incorporating real disease spectral data reduce cumulative errors from RTM coupling and improve similarity to UAV data.

The consistency between simulations and UAV hyperspectral data highlights the alignment of these methods, particularly in simulations using real disease spectral information (SIM #2 and SIM #3). The magnitude of the correlation between UAV-collected spectra and DI was lower than that between simulated spectra and DI (Fig. 5.5). This discrepancy is likely attributed to the difference in sample sizes—while the UAV dataset included 1,968 observations (492 plots × 4 time points in the 2021), the simulated datasets were substantially larger in SIM #2 and SIM #3. Despite this, the relationship patterns observed in UAV data align with those in SIM #2 and SIM #3, supporting their effectiveness in explaining DI. The sensitive wavelengths identified (400–700 nm for positive correlation and near 750 nm for negative correlation) align with findings in the literature. For instance, Mahlein et al. (2013) showed that the reflectance of disease-infected leaves (*Cercospora* leaf spot, sugar beet rust, and powdery mildew) was higher in the green and red regions of the spectrum (500–700

nm) compared to healthy sugar beet leaves, while it decreased in the 700–900 nm range. Similarly, Zarco-Tejada et al. (2018) observed that the reflectance in the 400–450 nm range increased with disease severity, while the reflectance in the 750–790 nm range decreased. This is attributed to the disruption of photosynthetic pigments and crop structure caused by disease, with the 400–500 nm range corresponding to absorption centers of photosynthetic pigments, and the 750 nm region reflecting changes in crop structure (Hernandez-Clemente et al., 2019). Overall, the sensitivity analysis (Fig. 5.5a) supports the use of simulation-pretrained DL models for analyzing UAV-collected hyperspectral spectra.

5.4.2 Effectiveness of PGDL

PGDL offers a promising approach to enhance model generalization across different disease stages by integrating multiple data sources. Specifically, models trained with disease-related simulation data (PGDL SIM #2 and SIM #3) were enhanced by incorporating three types of data. (1) **Simulations** generated by RTMs is cost-effective compared to real-world observations and serves as a valuable tool for PGDL pre-training. Our results showed that prior knowledge from synthetic data significantly improves PGDL performance compared to directly applying a data-driven model to field data. (2) **Leaf-scale spectra** capture detailed disease information, offering higher sensitivity and accuracy in disease assessment. However, the sparse data acquisition methods struggle to capture the spatial diversity of disease occurrence. (3) **Canopy-scale spectra** collected by UAV are ideal for rapid and efficient disease monitoring, though they can be influenced by canopy structure and environmental factors. To leverage the strengths of these data types, PGDL integrates simulations to enrich the dataset, uses leaf-scale observations to constrain the model, and applies UAV data to enhance model accuracy.

Compared with physically-based methods, PGDL addresses the inherent limitations of RTMs through transfer learning. The RTMs, while grounded in biophysical principles, are simplifications of complex ecosystem processes. Their effectiveness often suffer from limited retrieval accuracy in real-world applications (Combal et al., 2003). Their performance is further constrained by the need for high-quality, noise-free spectral inputs, which is rarely achievable with real-world UAV or satellite sensors. PGDL overcomes these challenges by fine-tuning on field data, enabling the model to adapt to sensor noise and real-world variability. This transfer learning strategy enhances robustness to both model simplifications and spectral imperfections.

In contrast to purely data-driven approaches, PGDL also improves generalizability and reduces reliance on large volumes of labeled training data. Data-driven models such as GBDT and GRU often exhibit low sensitivity to early disease stages. These models tend to optimize for overall accuracy and may prioritize the more distinguishable mild, moderate, and severe stage symptoms (Kamilaris and Prenafeta-Boldú, 2018). As a result, early-stage detection is frequently compromised. PGDL, by contrast, enhances early-stage recognition by leveraging prior knowledge. Furthermore, traditional data-driven methods require extensive labeled datasets, but PGDL mitigates this need

through pretraining on synthetic data. This is especially beneficial in scenarios with limited field coverage or at the early disease stage, where acquiring ground truth is more challenging. For example, in 2023, due to reduced plot size and sparse early-stage infection, data-driven models exhibited poor performance, particularly during early disease onset. Similar findings were reported by Wang et al. (2023b), who demonstrated that RTM-guided ML improved the monitoring of cover crop traits using airborne hyperspectral imaging with fewer field samples. Likewise, Qin et al. (2024) observed that hybrid approaches combining RTMs and ML exhibited greater stability across varying training sample sizes in grassland leaf area index mapping.

Furthermore, our findings demonstrate the potential of PGDL for monitoring maize leaf spot, showing significant performance improvements. By combining the strengths of physically-based and data-driven methods, PGDL benefits from well-validated prior knowledge provided by the physical models, though these simulations remain imperfect. The incorporation of transfer learning can help overcome these limitations. Transfer learning enables a model to leverage knowledge from source tasks in different domains (Pan et al., 2011). In our study, transfer learning was straightforward, as the feature space of simulations and UAV data aligned. Thus, PGDL proves to be an effective solution for maize disease monitoring.

5.4.3 Limitations and future work

While this study demonstrates the effectiveness of PGDL in monitoring maize leaf spot by integrating simulations, leaf-scale, and canopy-scale data, several limitations remain that could be addressed in future research.

First, although the LESS model simulation generates hyperspectral images from the 400–2500 nm wavelength range, our study was limited to using hyperspectral data from the visible and near infrared (VNIR) region (400–900 nm) due to the UAV-mounted sensor used in our experiment. Reflectance in the shortwave infrared (SWIR) range, however, is known to be crucial for understanding water absorption in plant leaves, which is linked to disease development (Gold et al., 2020a; Huang et al., 2015; Meng et al., 2020). Additionally, vegetation temperature has proven to be an important indicator of crop health and transpiration rates (Lu et al., 2020), while LiDAR data can complement spectral data by addressing spectral confusion and improving model performance (Yu et al., 2021a). Sun-induced fluorescence (SIF), which provides insights into photosynthetic activity, is also a valuable indicator for disease detection (Buschmann et al., 2000; Jones and Schofield, 2008; Moya and Cerovic, 2004). These multimodal remote sensing data could also be simulated within the LESS model. Future studies that include SWIR, LiDAR, and SIF data are likely to enhance the model's disease monitoring capabilities.

Another limitation is the simplification in the simulation process. In our study, all leaf within a maize plant was assigned to the same spectral curve, which does not fully capture the complex, layered nature of maize leaf spot progression. Disease severity is often more pronounced in the lower parts of the plant, with upper leaves showing less visible damage (Liu et al., 2022). Future research should consider a more detailed

simulation approach, where different spectral curves are assigned to different canopy layers. This would enhance the realism of simulated data and improve disease monitoring accuracy. At the same time, the trade-off between model complexity and computational cost should be carefully considered.

5.5 Conclusions

This study demonstrates the effectiveness of PGDL for monitoring maize leaf spot by combining physically-based modeling with data-driven approaches. The results highlight that simulation methods play a critical role in ensuring the consistency between simulated data and UAV hyperspectral data, as well as in enhancing the accuracy of the PGDL model. Specifically, simulations incorporating real disease spectral characteristics (SIM #2 and SIM #3) yielded the most accurate representations of disease progression, closely aligning with spectra obtained from UAV hyperspectral imagery. Moreover, PGDL showed robust generalization across various disease stages, including early stages and low DI levels, with particularly strong performance when trained with SIM #2 and SIM #3 data. This success can be attributed to the integration of simulation data, leaf-scale spectra, and canopy-scale spectra, which collectively improved the model's ability to capture the multifaceted nature of disease progression. Finally, the PGDL pretraining phase enabled the model to capture critical spectral response patterns linked to maize leaf spot through feature importance analysis. These results highlight the potential of PGDL for accurate and early detection of crop diseases. Future work will focus on refining early-stage detection and extending the framework to other crop-disease systems.

5.6 Supplementary information

Additional tables and figures supporting this chapter are available online. They can be accessed via the QR code or at the following URL: PhD-thesis/chapter5-tgrs-supplymentary.pdf at main · Briya1990/PhD-thesis

6

A synergistic UAV-driven deep learning and epidemic modeling framework for dynamic spatiotemporal prediction of maize leaf spot

This chapter is based on:
Bai, Y., Kooistra, L., Liu, Q., Yu, X., Jia, T., Zhu, Y., Jiang, T., Jiang, T., Li, S., Tekinerdogan, B., Duan, C., Jin, X. (2025). A synergistic UAV-driven deep learning and epidemic modeling framework for dynamic spatiotemporal prediction of maize leaf spot. One earth (Submitted)

Abstract

Leaf spot is a serious yield-reducing disease of maize (*Zea mays*) in many parts of the world where this crop is cultivated. Timely prediction of leaf spot disease dynamics is critical for shifting agriculture from reactive control to preventive management. Although remote sensing (RS) enables large-scale disease monitoring, its application to spatiotemporal prediction remains limited. Here, we introduce the RS-DeepSpread model, a novel Synergistic RS-Deep Learning with Epidemic framework that integrates an RS-driven deep learning with a stochastic epidemic spread model to predict the spatiotemporal progression of maize leaf spot. The core concept of RS-DeepSpread lies in the complementarity between the two components: RS-based deep learning generates the initial disease probability maps, while the epidemic model iteratively refines these predictions by disease spread. As a first step, we benchmarked three RS-deep learning architectures—multi-layer perceptron (MLP), long short-term memory (LSTM), and gated recurrent unit (GRU)—to determine the optimal hyperspectral-driven predictor of maize leaf spot. The GRU model achieved the highest performance across two growing seasons (2021: overall accuracy (OA) = 79.07%; 2023: OA = 85.00%). We then used GRU outputs as initial conditions for the epidemic model, forming the RS-DeepSpread system. Results show that RS-DeepSpread yields improved accuracy (2021: quadratic weighted kappa (QWK) = 92.54%, OA = 85.37%; 2023: QWK = 89.71%, OA = 91.67%) and lower underestimation (2021: 5.36%; 2023: 3.97%) and overestimation rates (2021: 8.93%; 2023: 3.97%). Moreover, this framework predicted epidemic rate peaks up to three days earlier than field observations. These findings demonstrate that integrating epidemic modeling with an RS-deep learning algorithm trained by hyperspectral imagery offers a solution for timely and spatially explicit prediction of crop disease dynamics.

6.1 Introduction

Maize (*Zea mays* L.), one of the world's most important staple crops, is particularly vulnerable to fungal diseases. Among these, maize leaf spot (MLS) diseases are a significant threat to global maize production. . For example, leaf spots caused by *Curvularia lunata* (*Curvularia* Leaf Spot), by *Bipolaris maydis* (Southern Leaf Blight), and by the polycyclic pathogens *Cercospora Zeina* (gray leaf spot) are well known (Crous et al., 2006; Tehon and Daniels, 1925). These diseases reduce the functional leaf area available for photosynthesis and thereby limit yield. For example, yield reductions from MLS have been reported in the range of about 11 % to 69 % depending on hybrid and environment (Dai et al., 2024; Ngoko et al., 2002; Ward et al., 1999). Some extreme losses up to ~79 % have also been documented (Cardwell et al., 1997). While chemical control remains an effective strategy for managing disease, the excessive use of pesticides raises serious concerns for environmental health and food safety (Zhou et al., 2025). As a result, there is an urgent need for approaches that can determine where and when pesticide applications are truly necessary. Achieving this goal hinges on accurately modeling the spatiotemporal dynamics of disease spread at scale. In this regard, remote sensing (RS) methods that respond to MLS infection (e.g., Jia et al. (2023)) could help to monitor and mitigate the progress of MLS outbreaks.

Recent progress in RS technologies offers new potential to enhance disease monitoring by providing timely, non-destructive, and spatially explicit observations. Among these, hyperspectral imaging stands out due to its higher spectral resolution, which enables the detection of subtle physiological changes in woody crops, such as pigment degradation, altered water status, and structural modifications, before visible symptoms appear (Zarco-Tejada et al., 2018; Zarco-Tejada et al., 2021). These pre-symptomatic signals can be disentangled from abiotic stress responses using spectral–physiological trait linkages and feature selection approaches within machine learning (ML) frameworks. For example, Camino et al. (2022) demonstrated that ML models can exploit the relative importance of specific narrow bands to discriminate disease-induced spectral changes from other stressors, enhancing early detection capabilities. Hyperspectral sensors have been deployed on ground-based systems (Almoujahed et al., 2025), UAVs (Zeng et al., 2024), airborne (Eugenio et al., 2021) and satellite platforms (Poblete et al., 2023b)—offering multi-scale imagery that supports both early detection and continuous tracking of disease developmental level. UAV-based hyperspectral imaging combines high spatial, spectral, and temporal resolution, enabling rapid, field-wide, site-specific disease monitoring (Zhang et al., 2024). This enables real-time tracking of disease dynamics, facilitating spatiotemporal monitoring of disease progression at the canopy scale. However, spectral signals are often influenced by confounding factors such as soil background, canopy architecture, and environmental variability, which can compromise the specificity of RS-based disease monitoring (El-baki et al., 2025). As a result, many RS-based disease models remain limited in specificity across heterogeneous agricultural landscapes.

To interpret RS data more effectively, deep learning models have been increasingly adopted due to their ability to learn complex, nonlinear relationships. For example, Wu et al. (2021) proposed a cost-effective method for early pine wilt diagnosis using UAV imagery and You Only Look Once version 3 (YOLOv3), while Qin et al. (2021) introduced SCANet (spatial-context-attention network), an attention-based network, to detect pine nematode disease with superior accuracy compared to DeepLabV3+, DenseNet, and HRNet. Despite their high performance, deep learning models face key limitations: they often lack interpretability, are sensitive to noisy or imbalanced datasets, and their predictive reliability varies across studies (Shahi et al., 2023). These limitations arise from the black-box nature of deep learning and its dependency on large volumes of high-quality training datasets (Dehghan-Shoar et al., 2023).

To improve model specificity and predictive capacity, Camino et al. (2021) proposed a pioneering strategy that involves integrating RS with epidemic modeling. This hybrid approach leverages the strengths of both methods: RS provides a spatially explicit baseline of disease status, while the epidemic spread model offers mechanistic insights into pathogen dispersal, host connectivity, and environmental influence. Camino et al. (2021) coupled spatial epidemiological models using high-resolution hyperspectral imagery and ML algorithms to monitor the spread of *Xylella fastidiosa* in almond orchards. Their approach enabled the detection of asymptomatic but infected trees that were missed by field inspections, highlighting the potential of integrating spread modeling and RS data for improving detection sensitivity. However, this work focused on a single aerial campaign (time-point assessments) and binary classification (infected vs. healthy), without modeling the full spatiotemporal progression of disease severity.

To address this gap, in this study, we propose a novel *Synergistic RS–deep learning and epidemic* framework (RS-DeepSpread) to capture the spatiotemporal progression of MLS. This framework combines a remote sensing-driven deep learning (RS-deep learning) model with a stochastic epidemic spread model. For that, we developed an RS-deep learning model trained on hyperspectral features to classify disease severity at the canopy scale. We then coupled RS-deep learning with a stochastic iterative epidemic spread model to simulate the spatiotemporal progression of MLS across the field. Finally, we assessed which model performed best in predicting MLS severity by using ground observations across both spatial and temporal dimensions.

6.2 Materials and methods

6.2.1 Study area and data collection

6.2.1.1 Experimental design

Field experiments were conducted in Xinxiang City, Henan Province, China (35.30° N, 113.93° E), located on the North Henan Plain (Yubei Plain). Maize is the dominant crop in this region, which is characterized by a warm temperate continental monsoon climate. Hot and humid summers provide favorable conditions for the development and spread of MLS.

Experiments were carried out in 2021 and 2023 (Fig. 6.1). In 2021, the trial included

492 plots, each measuring 1.25 × 1.8 m and planted with a single maize genotype. Each plot contained 24 plants arranged in four rows with 60 cm row spacing and 22.5 cm plant spacing. Sowing took place on May 30, 2021. In total, 246 genotypes were tested under two pathogen treatments. To induce MLS, plots in treatment 1 were inoculated with *Bipolaris maydis* (southern leaf blight), and those in treatment 2 with *Curvularia lunata* (Curvularia leaf spot)—both major pathogens affecting maize in China. Inoculation was performed on the evening of August 2, at the maize big trumpet stage. A water-suspended spore solution (1×10^5 spores mL^{-1}) was prepared and evenly sprayed using a handheld sprayer.

In 2023, two independent experimental repeats (repeat 1 and repeat 2) were established. Each repeat comprised 60 plots arranged in three east–west rows of 20 plots (3 × 20 = 60). Each plot measured 4.0 × 4.8 m, and each row contained the same set of 20 genotypes. The outer rows in both repeats were inoculated with *Curvularia lunata*, while the central rows were inoculated with *Bipolaris maydis*. The remaining inner rows were left uninoculated and served as healthy controls. The inoculation procedure and timing were consistent with 2021, conducted on the evening of August 16 during the big trumpet stage.

Across both years, maize was grown at a density of approximately 75,000 plants ha^{-1}. Standard agronomic management—including fertilization, irrigation, and weed control—was applied uniformly based on recommendations from local agricultural experts (Xu et al., 2017). These practices ensured consistent soil fertility and moisture conditions across experimental plots, minimizing confounding effects on disease development.

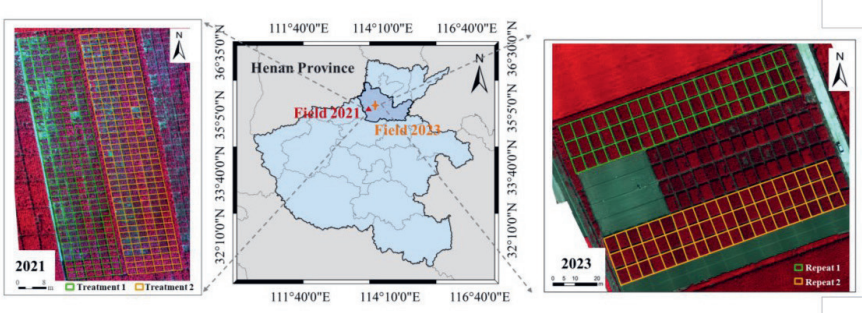


Fig. 6.1. *Overview of the field experiments conducted in 2021 and 2023. The experimental site on the left corresponds to the 2021 trial, and the site on the right to the 2023 trial. Plot boundaries are outlined with yellow and green polygons. Below each field layout, a false-color composite (NIR-R-G) of the corresponding UAV-based hyperspectral orthomosaic is shown, with the Near-Infrared (852.12 nm), red (649.01 nm), and green (552.08 nm) bands displayed in the red, green, and blue channels, respectively. The data was acquired on 27 August 2021 and 29 August 2023.*

6.2.1.2 Visual inspections

Visual inspections were conducted to quantify MLS severity for each plot following

the initial appearance of symptoms (Table 6.1, Fig. 6.2). The assessment of disease severity involved four main steps: sample collection, leaf disease index evaluation, plot-level disease index (DI) calculation, and disease severity categorization. During sample collection, three plants were randomly selected per plot in 2021, and five plants per plot in 2023 to account for the larger plot size. For each plant, three representative leaves were determined—the leaf above the ear, the ear leaf, and the leaf below the ear—and photographed in the field for subsequent evaluation of the leaf disease index. The leaf disease index was visually assessed by three experienced phytopathologists based on the percentage of the leaf surface exhibiting lesions, with scores assigned to one of six severity classes: 0 (0%), 1 (0–5%), 3 (6–25%), 5 (26–50%), 7 (51–75%), and 9 (76–100%), respectively. These scores were aggregated to compute the DI using equation (1).

$$DI = \sum_{i=0}^{n}\left(X_i \cdot S_i\right) / \sum_{i=0}^{n}\left(X_i \cdot S_{\max}\right) \times 100 \quad (1)$$

Where S_i represents the scores of leaf disease index, and S_{max} is the highest score of the leaf disease index, which in this study is 9; i denotes the degree of disease severity (0–n); X_i is the number of leaves assigned to severity class i.

Finally, each plot was then assigned to one of four disease severity categories: early (DI ⩽ 30%), mild (30% < DI ⩽ 50%), moderate (50% < DI ⩽ 70%), and severe (DI > 70%), respectively.

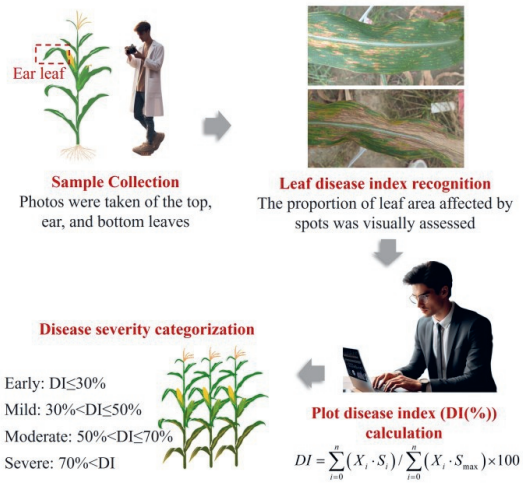


Fig. 6.2. *Flow chart of disease severity categorization.*

6.2.1.3 Hyperspectral images collection and preprocessing

Hyperspectral imaging was conducted on the same dates as the field campaigns (Table 6.1), under predominantly clear skies to maintain consistency between aerial and visual inspections. A Pika L hyperspectral camera (Resonon, Bozeman, MT, USA) mounted on a DJI Matrice 600 Pro UAV (DJI, Shenzhen, China) was used for image

collection. The UAV, equipped with an RTK-GNSS module, provided centimeter-level positional accuracy. All flights were conducted at an altitude of 50 m and a speed of 1.5 m/s between 10:00 and 14:00 local time to minimize variations caused by solar angle and illumination.

The Pika L sensor captures 150 contiguous bands within the 400–1000 nm spectral range, with an effective spectral resolution of 2.1 nm (after combining adjacent bands) and a full width at half maximum (FWHM) of 3.3 nm. Its 17 mm focal length offers an instantaneous field of view (IFOV) of 1.47 mrad and a field of view (FOV) of 30.8°, yielding a ground spatial resolution of approximately 0.5 cm at the flight altitude.

Raw hyperspectral images were first radiometrically calibrated to convert digital numbers into radiance. This process corrected for sensor-specific responses by applying a pixel-wise gain cube and a dark-noise offset cube automatically selected by the system. Specifically, this calibration was performed using equation (2):

$$Radiance = (RawData - offset) \times gain \quad (2)$$

Geometric correction was then performed by co-registering the hyperspectral images with simultaneously acquired high-resolution RGB data. Ground control points (GCPs) distributed across the field were incorporated to ensure accurate spatial alignment. To account for ambient illumination, radiance values were further normalized to reflectance using a 60% gray reference panel. The panel was placed on a flat, unobstructed area of the field and included in each flight mission. Finally, average reflectance spectra were calculated for each plot, yielding plot-level reflectance data for subsequent analysis.

Table 6.1 Dates of infection and experiment data acquisition

Year	Infection date	Visual inspections and hyperspectral imaging acquisition (days after infection, DAI)
2021	2 August	20 August (DAI 18)； 27 August (DAI 25)； 2 September (DAI 31)； 8 September (DAI 37)
2023	16 August	29 August (DAI 13),1 September (DAI 16)； 5 September (DAI 20), 9 September (DAI 24)； 12 September (DAI 27), 16 September (DAI 31), 22 eptember (DAI 37), 25 September (DAI 40)

6.2.2 Hyperspectral features extraction and analysis

6.2.2.1 Biophysical parameters and spectral features

Average canopy reflectance spectra were calculated for each experimental plot and used to derive a series of hyperspectral features. Spectral data between 400 nm and 900 nm (117 bands) were retained to avoid the low signal-to-noise ratio commonly found near the sensor's spectral limits.

Biophysical parameters including chlorophyll content (C_{ab}), carotenoid content (C_{ar}), equivalent water thickness (C_w), dry matter content (C_m), and anthocyanin content (A_{nth}) were retrieved through inversion of the PROSAIL radiative transfer model. PROSAIL combines the PROSPECT-D leaf optical model, which simulates leaf-level biochemical and structural properties, with the SAIL canopy model, which describes canopy-level radiative transfer. This model was selected because the maize canopy was fully closed

and could be approximated as a homogeneous turbid medium.

A hybrid RTM–deep learning inversion strategy was adopted to estimate biophysical parameters from simulated and measured hyperspectral spectra. The input parameter ranges for PROSAIL were determined from published optical property datasets (i.e., LOPEX and ANGERS (Feret et al., 2008)) and study (Nie et al., 2023) (Table 6.2). The simulated spectra (with ~1 nm sampling) were resampled to match the spectral response function of the PikaL hyperspectral sensor, ensuring consistent spectral resolution. Specifically, we averaged the simulated PROSAIL bands to align with Pika L's channel grid.

A multilayer perceptron (MLP) regression model (Bourlard and Morgan, 1994) was trained on these simulated spectra to predict all five biophysical parameters simultaneously. The architecture of this MLP was shown in Fig. S6.1. To mitigate the ill-posed nature of the inversion, field-measured leaf area index (LAI) values obtained using a SUNSCAN instrument (Delta-T Devices, Cambridge, UK) were incorporated as an additional input for MLP. The input layer of MLP contained the same number of nodes as the number of PikaL bands plus one additional node representing LAI. The hidden layers applied successive 2:1 compression ratios, and the output layer comprised five nodes corresponding to the five target biophysical parameters. The network employed ReLU activation functions and a dropout rate of 0.2 to mitigate overfitting.

Model performance for C_{ab} and A_{nth} was validated using field measurements obtained with a Dualex Scientific+ sensor (Force-A, Orsay, France) following (Bai et al., 2024a). For each sampled plot, five plants were randomly selected, and for each plant, three leaves (ear leaf, the first leaf above the ear, and the first leaf below the ear) were measured. The average of Dualex readings grouped by plot was used to compare with the inversions. Model accuracy was assessed using the coefficient of determination (R^2) and root mean square error (RMSE) (Fig. S6.2).

Table 6.2 Inputs for PROSAIL simulation

Model	Variable	Acronym	Range	Steps	Units
PROSPECT-D (leaf level)	Chlorophyll content	C_{ab}	1-100	5	μg/cm^2
	Carotenoid content	C_{ar}	0-26	1	μg/cm^2
	Anthocyanin content	A_{nth}	0-20	1	μg/cm^2
	Brown pigment content	C_{brown}	0.2	*N/A*	*N/A*
	Equivalent water thickness	C_w	0-0.08	0.01	cm
	Dry matter content	C_m	0-0.04	0.01	g/cm^2
	Leaf structure parameter	N	1-1.5	0.1	*N/A*
SAIL (canopy level)	Leaf area index	LAI	1-5	0.3	*N/A*
	Hot-spot size parameter	Hspot	0.25	*N/A*	mm^{-1}
	Solar zenith angle	SZA	65	*N/A*	Degree
	Observed zenith angle	OZA	0	*N/A*	Degree
	Relative azimuth angle	RAA	0	*N/A*	Degree
	Average leaf inclination angle	ALA	30-50	10	Degree

From the averaged reflectance spectra, a set of hyperspectral vegetation indices (VIs) and wavelet features (WFs) was calculated. A total of 69 VIs were computed from visible–NIR bands, sensitive to pigments, water, nitrogen, canopy structure, and cover characteristics (Table S6.1). To complement these indices, we extracted WFs, which simultaneously encode spectral position and scale and are known to be sensitive to disease (Zhang et al., 2014). WFs were extracted using the continuous wavelet transform (CWT) with the Mexican Hat mother wavelet, following the method outlined by Cheng et al. (2010). For each spectrum, coefficients were derived across scales 3 to 8.

6.2.2.2 Feature analysis

To identify the most significant features associated with MLS progression, the disease development was categorized into four groups—early, mild, moderate, and severe—based on the disease severity assessed on the final visual inspection. A one-way analysis of variance (ANOVA) was then performed across these four groups at each observation date. Statistical significance was determined according to the following p-value thresholds: $p < 0.001$ was considered very highly significant, $0.001 \leqslant p < 0.01$ was considered highly significant, $0.01 \leqslant p < 0.05$ was considered significant, and $p \geqslant 0.05$ was regarded as not significant. Features showing significant differences ($p < 0.05$) across more than two consecutive time points were considered consistently responsive to disease progression and retained for further analysis.

To minimize redundancy and multicollinearity among hyperspectral features, variance inflation factor (VIF) analysis was applied. For each feature, the VIF was computed by regressing it against all other narrow-band indices using equation (3).

$$VIF = 1/(1-R^2) \tag{3}$$

where R^2 is the coefficient of determination of the regression. Features with VIF $\leqslant$ 10 were retained to reduce inter-correlation (Hair Jr et al., 2010), while those with VIF > 10 were deemed highly collinear. In each correlated group, spectral information entropy was calculated to quantify the spectral information richness, and only the feature with the highest entropy —indicating maximal spectral information richness—was selected for further analysis.

6.2.3 Modeling approaches for predicting MLS severity

To predict MLS severity, we employed three deep learning models (Section 6.2.2.1) and an RS-DeepSpread framework (Section 6.2.2.2). All models were trained and validated using datasets from 2021 and 2023 growing seasons, respectively. For each year, hyperspectral imagery and disease severity classes from DAI 31 were used exclusively for testing, while data from other sampling dates were used for training. The deep learning models were driven by 11 hyperspectral features selected as described in Section 6.2.1. These comprised one chlorophyll-related feature (Cab) and five wavelet features (WF494,5, WF461,6, WF469,7, WF548,8, and WF590,8), together with five VIs (PSRI, RGI, PRIn,VARI2, NDVI). To enable daily-scale disease severity prediction, the selected hyperspectral features were temporally reconstructed using logistic growth functions fitted to the training data. This interpolation approach

was chosen because the logistic function naturally captures the sigmoid-like dynamics typical of crop physiological processes and disease progression (Woodhouse, 2006).

6.2.3.1 RS-deep learning

Deep learning models were trained using hyperspectral data from sample plots and time points. These models were used to predict both the daily disease severity class and the corresponding class probabilities. Three types of deep learning architectures were considered for classification: an MLP, a long short-term memory (LSTM) network, and a gated recurrent unit (GRU) model. The best-performing model from this stage was used in the integrated modeling framework (Section 6.2.2.3).

All three networks shared the same overall structure: a core network (MLP, LSTM, or GRU), followed by an attention mechanism, and finally a classification layer. First, the normalized hyperspectral features were fed into the core network. The outputs from this layer passed through an attention module, which calculated feature-level weights. The core network outputs and attention-weighted features were concatenated and fed into a fully connected classification layer to predict disease severity classes. The classification layer used softmax activation with cross-entropy loss to predict the probability distribution over four disease severity classes (early, mild, moderate, and severe). After obtaining the probability vector from the softmax, the model selects the class with the highest probability as its final prediction.

MLP is a basic network composed of multiple layers of artificial neurons. Given that the spectral input data consisted of 10 features, the MLP architecture in this study was designed with three hidden dense layers containing 10, 20, and 40 neurons, respectively. Each layer employed a rectified linear unit (ReLU) activation function to introduce nonlinearity.

The LSTM unit can learn long-term dependencies by maintaining an internal memory of past inputs, making it well-suited for handling the temporal patterns present in hyperspectral data (Graves, 2013). An LSTM unit uses three gating mechanisms—input gate, forget gate, and output gate—to regulate the flow of information through the network. These gates determine which information is added to, removed from, or passed through the memory cell at each time step. Specifically: The input gate (i_t) controls how much new information is written to the cell state, the forget gate (f_t) decides how much of the previous cell state should be retained, and the output gate (o_t) determines how much of the cell state is exposed to the output. The LSTM equations governing these gates and the cell state update are defined in equations (4)-(8):

$$i_t = \sigma\left(W_i \cdot \left[h_{t-1}, x_t\right] + b_i\right) \quad \text{(input gate)} \quad (4)$$

$$f_t = \sigma\left(W_f \cdot \left[h_{t-1}, x_t\right] + b_f\right) \quad \text{(forget gate)} \quad (5)$$

$$o_t = \sigma\left(W_o\left[h_{t-1}, x_t\right] + b_o\right) \quad \text{(output gate)} \quad (6)$$

$$C_t = f_t * C_{t-1} + i_t * \tanh\left(W_C \cdot \left[h_{t-1}, x_t\right] + b_C\right) \quad (7)$$

$$h_t = o_t * \tanh\left(C_t\right) \quad (8)$$

Here, x_t, h_t and c_t represent the input, hidden state, and cell state at time step t, respectively. W and b denote the learnable weights and biases for each gate. The

sigmoid (σ) and hyperbolic tangent (tanh) functions introduce nonlinearity and ensure gated control over information flow.

The GRU unit, designed for sequential data, includes an update gate and a reset gate (Chen et al., 2019). The update gate focuses on integrating new information into the hidden layer, while the reset gate disregards less important information. The formulas are given as in equations (9)-(12):

$$z_t = \sigma\left(W_z \cdot \left[h_{t-1}, x_t\right]\right) \quad \text{(Update gate)} \quad (9)$$

$$r_t = \sigma\left(W_r \cdot \left[h_{t-1}, x_t\right]\right) \quad \text{(Reset gate)} \quad (10)$$

$$\tilde{h}_t = \tanh\left(W \cdot \left[r_t * h_{t-1}, x_t\right]\right) \quad \text{(New memory cell)} \quad (11)$$

$$h_t = \left(1 - z_t\right) * h_{t-1} + z_t * \tilde{h}_t \quad (12)$$

where, h_{t-1} represents the output from the previous time step, x_t is the current input, [ ] denotes concatenation, W_z, W_r, and W represent the learning weights for the update gate, reset gate, and new memory cell, respectively, σ and tanh are sigmoid and tanh activation functions, respectively, while $\tilde{h}_t$ represents the output of the new memory cell, and h_t denotes the output at the current time step.

All models were trained using the Adam optimizer with a learning rate of 0.001 and a batch size of 500. The training process spanned up to 10,000 epochs with early stopping based on the best validation accuracy. A hold-out validation set was used to evaluate model generalizability under real-world class distributions. The model achieving the highest validation accuracy was checkpointed and used for subsequent inference. To address the class imbalance issue inherent in the disease classification task, class weights were incorporated into the loss function during training.

6.2.3.2 RS-DeepSpread

In this study, we propose an RS-DeepSpread model integrating the RS deep learning model and the epidemic spread model (Fig. 6.3). The core idea behind RS-DeepSpread is twofold: (1) the RS-deep learning model provides spatially explicit disease probability estimates that serve as the initial condition for the epidemic model, and (2) the epidemic model iteratively refines these initial estimates to account for spatial and temporal disease dynamics. The integration allows RS-DeepSpread to combine spectral–physiological sensitivity from hyperspectral data with epidemiological process dynamics, providing a synergistic and data-driven prediction framework.

The epidemic spread model follows a stochastic optimization framework adapted from Parnell et al. (2011). This spread model estimates the probability of disease severity changes for unsampled plots through an iterative algorithm that improves initial random disease map accuracy by minimizing an objective function. Here, the initial random disease map of the spread model initiated by the RS deep learning model provides spatially explicit disease probability estimates. This initialization provided a more informed starting point for the epidemic spread simulation, as opposed to random or uniform initialization. In this study, the model assumes two biological constraints

consistent with field observations and prior epidemiological knowledge: (1) disease severity transitions unidirectionally from low to high, and (2) infected plots do not recover over time.

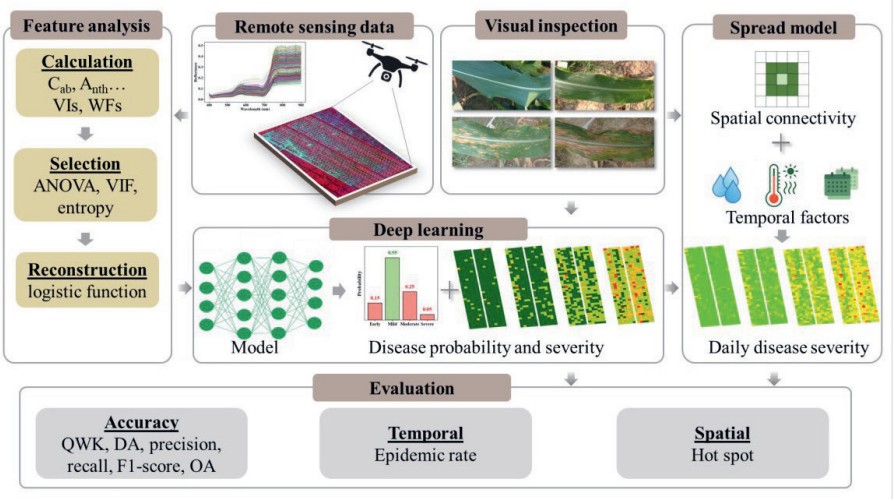


Fig. 6.3. *RS-DeepSpread framework daily prediction of maize leaf spot severity. Inputs included UAV-based hyperspectral features and field visual inspections, while outputs were daily disease severity maps. Abbreviations: Cab, chlorophyll content; Anth, anthocyanin content; VIs, vegetation indices; WFs, wavelet features; ANOVA, analysis of variance; VIF, variance inflation factor; QWK, weighted kappa coefficient; DA, directional accuracy; OA, overall accuracy*

The RS-DeepSpread consists of two phases: initialization (Steps 1–4) and iterative optimization (Steps 5–8), as outlined below.

1. **Graph construction:** All plots in the field were mapped using high-resolution UAV imagery and treated as nodes in a graph. Each node was connected to its eight neighboring plots to form the edges, thereby establishing spatial connectivity.
2. **Disease status assignment:** The probability of disease status changes was directly assigned to plots at sampled time points using visual inspection data—classified as 1 if disease severity increased and 0 if the disease severity remained unchanged. For unsampled time points, the probability of disease status change for each plot was initialized using RS-deep learning outputs, providing a continuous prior disease probability map.
3. **Epidemic rate estimation:** The epidemic rate *r(t)*, reflecting the temporal rate of disease severity increase. It was modeled as a function of temperature and humidity using a linear regression approach, as proposed by Van der Plank (2013). The regression equation was (13):

$$r(t) = a \cdot T + b \cdot H + c \qquad (13)$$

where T and H represent the average temperature (°C) and relative humidity (%) over each observation interval. In this study, daily temperature and humidity data were obtained from a local meteorological station. The regression coefficients

used were a=0.0219, b=0.0057, and c=−0.8785.

4. **Initial objective function (OF):** The OF is a metric quantifying the difference between the estimated disease map and observed field data. Cross-entropy loss was selected as the OF, as it is one of the most commonly used metrics for measuring the difference between predicted probabilities and true labels in multi-class classification tasks. Only sampled time points were used to calculate the OF. Here, the RS-deep learning estimations serve as the initial estimated disease map.
5. **Dispersal probability calculation:** The probability of pathogen spread between plots was modeled using circuit theory. The effective pathogen dispersion between plots was the effective distances ($deff_{ij}$) between node pairs across the graph. The effective distance between any two nodes (plots) i and j was defined as the resistance distance on the graph, where each edge was treated as a resistor. The conductance G_{ij}, representing the dispersal probability, was computed as equation (14):

$$G_{ij}(t) = P_i(t) \cdot \exp\left(-\alpha \cdot d_{ij}\right) \cdot \frac{P_{\text{edge}_{ij}}(t)}{\sum_{j=1}^{8} P_{\text{edge}_{ij}}(t)} \tag{14}$$

where $P_i(t)$ represents the probability of disease increase for plot i at time point t; $P_{edge_{ij}}$ denotes the probability of pathogen dispersal across edge ij, calculated as the area of a rectangular trapezoid with a height of 1 and bases corresponding to P_i and P_j, respectively; d_{ij} is the Euclidean distance between plots i and j; and α is the distance decay coefficient (α>0) in the negative exponential dispersal kernel, estimated during a later stage of the algorithm.

6. **Probability update**: A plot at an unsampled time point t was randomly selected, and its disease increase probability $P_i(t)$ was updated. This update was informed by the effective distances to its neighboring plots, their current disease probabilities, the epidemic rate, and the duration of disease progression, according to the function equation (15).

$$P_i^{k\to k+1}(t+1) = \{1 - \exp\left[-\sum_{j\neq i} P_j(t) \cdot \exp\left(-\beta \cdot deff_{ij}\right)\right]\} \cdot \exp(r(t) \cdot t) \tag{15}$$

In this context, $deff_{ij}$ represents the effective distance between plot i and j, and β is the distance decay coefficient (β>0), which was estimated during a later stage of the algorithm. The term $r(t)$ denotes the epidemic rate at time t, reflecting the speed of disease progression.

7. **Recalculate OF:** Following the update, the objective function was recalculated using the updated disease map.
8. **Acceptance criterion**: If the updated OF was lower than in the previous iteration, the change was accepted. Otherwise, the previous values of the map and OF were retained.

For training this model, we set a stopping criterion. The algorithm was allowed to run for up to 2000 iterations, or until an early stopping condition was met. Specifically, training was terminated if the OF did not decrease by at least 0.01 over 20 consecutive iterations. To get the optimal values of parameters α and β, a grid search was conducted by repeating the training. The combination that leads to the estimated map with the lowest OF was selected.

6.2.4 Evaluation

6.2.4.1 Classification performance

Disease severity classification is an ordinal classification problem, where labels (disease severity levels) follow a natural order (e.g., early → mild → moderate → severe). Unlike nominal classification, ordinal prediction must account not only for whether a prediction is correct, but also how far an incorrect prediction deviates from the true class. Therefore, both order-aware and conventional metrics were employed to comprehensively evaluate model performance.

To assess the agreement between predicted and observed severity levels while penalizing large deviations, we utilized the Quadratic Weighted Kappa (QWK)(Warrens, 2012). It is defined as equation (16):

$$\mathrm{QWK} = 1 - \frac{\sum_{i,j} w_{ij} O_{ij}}{\sum_{i,j} w_{ij} E_{ij}} \tag{16}$$

where O_{ij} is the observed confusion matrix between true class i and predicted class j, E_{ij} is the expected confusion matrix under random agreement, and w_{ij} is the quadratic weight defined equation (17) with k being the total number of classes.

$$w_{ij} = \frac{(i-j)^2}{(k-1)^2} \tag{17}$$

QWK ranges from -1 to 1, with 1 representing perfect agreement, 0 representing random agreement, and negative values indicating systematic disagreement. This metric emphasizes larger misclassifications, making it particularly suitable for assessing disease severity predictions where the difference between mild and severe infection is critical.

Monitoring the temporal dynamics of disease progression is essential for timing fungicide applications. To evaluate the model's ability to capture these trends (e.g., identifying whether the infection is expanding or stable between observation dates), we calculated the Mean Directional Accuracy (MDA)(Blaskowitz and Herwartz, 2011). The MDA quantifies whether the model tends to correctly estimate the observed disease progression between two observation dates (e.g., DAI 31–DAI 25 in 2021; DAI 31–DAI 27 in 2023). For each sample i, the observed and predicted changes in disease severity were computed as:

$$\Delta y_i = y_i - y_{\mathrm{ref},i} \tag{18}$$

$$\Delta \hat{y}_i = \hat{y}_i - y_{\mathrm{ref},i} \tag{19}$$

where $y_{ref,i}$ and y_i denote the reference and target disease severity classes at two time

points, and $\hat{y}_i$ represents the model-predicted class at the target date.

$$MDA = \frac{1}{N}\sum_{i=1}^{N}\mathbf{1}_{\mathrm{sgn}(\Delta y_i)=\mathrm{sgn}(\Delta \hat{y}_i)} \tag{20}$$

where 1 is the indicator function and *sgn* is the sign function. A high MDA indicates the model is reliable for tracking disease expansion over time.

To assess whether the model consistently underestimates or overestimates the rate of disease development, we analyzed the bias in the predicted changes relative to the observed changes. We calculated the underestimation rate (Underestimation) and the overestimation rate (Overestimation) to quantify the trade-off between biological risk and economic cost.

Underestimation is defined as the frequency with which the observed disease progression exceeds the predicted progression:

$$Underestimation = \frac{1}{N}\sum_{i=1}^{N}\mathbf{1}_{\Delta y_i > \Delta \hat{y}_i} \tag{21}$$

Overestimation is defined as the frequency with which the predicted disease progression exceeds the observed progression:

$$Overestimation = \frac{1}{N}\sum_{i=1}^{N}\mathbf{1}_{\Delta y_i > \Delta \hat{y}_i} \tag{22}$$

In addition to order-aware metrics, conventional classification metrics—including precision, recall, F1-score, and overall accuracy (OA)—were computed at both class-specific and weighted-average levels. Weighted averages accounted for class imbalance by assigning weights proportional to the number of samples per class (Haibo and Yunqian, 2013). Model performance was evaluated using independent test datasets from 2021 and 2023 growing seasons.

6.2.4.2 Temporal analysis

To evaluate each model's ability to capture disease progression over time, we analyzed the temporal indicator: the epidemic rate *r(t)*. It is a key epidemiological indicator reflecting the average daily rate of disease progression. It reflects the combined influence of host susceptibility, pathogen aggressiveness, and environmental conditions during the epidemic. By quantifying how rapidly disease severity changes over time, *r(t)* provides a dynamic measure of outbreak intensity. Typically, plant disease development follows a sigmoidal (logistic) growth pattern. During the initial phase**,** infection is limited and disease severity increases slowly, resulting in a low epidemic rate. In the exponential phase, disease expansion accelerates rapidly under favorable environmental conditions such as optimal temperature, high humidity, and canopy closure; *r(t)* rises sharply and reaches its peak. In the late phase, disease progression slows as host tissues become fully infected or necrotic, leading to a gradual decline in *r(t)*.

In this study, we computed *r(t)* from both field-observed and model-predicted severity data and plotted epidemic rate curves for each growing season as (23). These curves were used to identify the timing of epidemic peaks and to compare disease

spread trajectories across models.

$$r = \frac{1}{t_2 - t_1} ln(x_2 - x_1) \tag{23}$$

6.2.4.3 Spatial analysis

To further characterize spatial clustering, we employed hotspot analysis based on the Getis–Ord G_i* statistic (Ord and Getis, 1995). This technique identifies statistically significant clusters (hot and cold spots) by considering each plot's disease severity value within the context of its spatial neighbors. Hot spot analysis is a powerful tool to characterize the dynamics of plant disease propagation and to understand the epidemiology at a regional scale (Tian et al., 2023).

Disease severity categories—early, mild, moderate, and severe—were assigned values of 0, 1, 2, and 3, respectively. The hotspots were quantified using the Getis-Ord G_i* statistic as equation (24):

$$G_i^*(d) = \frac{\sum_{j=1}^{n} w_{i,j}(d)x_j - \bar{X}\sum_{j=1}^{n} w_{i,j}}{S\sqrt{\frac{n\sum_{j=1}^{n} w_{ij}^2 - W_i^2}{n-1}}} \tag{24}$$

where x_j is the disease severity value for plot j, $w_{i,j}$ is the spatial weight between plots i and j, and n is the total number of plots, $\bar{x}$ is the mean value, and S is the standard deviation. The G_i* statistic returns a z-score (standard deviation) for each plot in the image to identify clustered and random patterns separately. The resulting z-scores indicate the statistical significance of clustering at three confidence levels: 90% ($|z| \geqslant 1.65$), 95% ($|z| \geqslant 1.96$), and 99% ($|z| \geqslant 2.58$). Plots with significantly high z-scores were defined as hotspots, while those with significantly low z-scores were defined as cold spots. Based on z-score magnitude, the study area was categorized into seven spatial classes: very hot spot, hot spot, warm spot, not significant spot, cool spot, cold spot, and very cold spot. All spatial analysis was performed using ArcGIS 10.3 (Environmental Systems Research Institute, Redlands, CA, USA).

6.3 Results

6.3.1 Assessment of RS features to track different disease progression at canopy level

The average reflectance spectra were analyzed for plots classified as severe during the final visual inspection, showing a consistent increase with days after infection (DAI) (Fig. 6.4). Reflectance values rose consistently as infection advanced. In particular, spectral changes in the blue (450–485 nm), green (495–570 nm), red (625–685 nm), and red-edge ($\approx$ 705 nm) regions reflected the degradation of chlorophyll pigments with increasing DAI.

The most sensitive hyperspectral features were identified based on VIF and information entropy analysis. These included indices associated with chlorophyll content (C_{ab}) and representative wavelet features ($WF_{494,5}$, $WF_{461,6}$, $WF_{469,7}$, $WF_{548,8}$, and $WF_{590,8}$). Additional selected indices were related to carotenoid and chlorophyll

content (PSRI, RGI), xanthophyll and photosynthetic efficiency (PRI_n), anthocyanins ($VARI_2$), and canopy structural traits (NDVI).

The temporal dynamics of these key hyperspectral features were evaluated at the plot level to determine whether they could effectively distinguish different disease progression, as defined by the final visual inspection (Fig. 6.5). Overall, the selected features exhibited significant differences among disease stages after DAI 18 in both 2021 and 2023. PSRI and $VARI_2$ showed highly significant differences ($p < 0.001$) on DAI 24 in 2023. Among these features, C_{ab} displayed a decreasing trend with increasing DAI, indicating chlorophyll degradation. In contrast, PSRI and PRI_n increased with DAI, reflecting stress-induced pigment changes, while $VARI_2$ and NDVI showed a consistent decline, corresponding to reduced anthocyanin expression and canopy greenness.

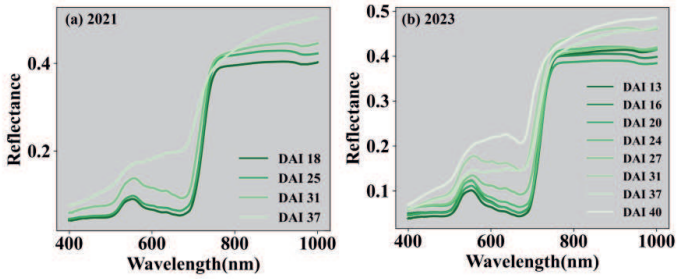


Fig. 6.4. *Average canopy reflectance spectra of plots that were classified as severe (left: 26 plots in 2021, right: 47 plots in 2023) during the last visual inspection, shown as a function of days after infection (DAI).*

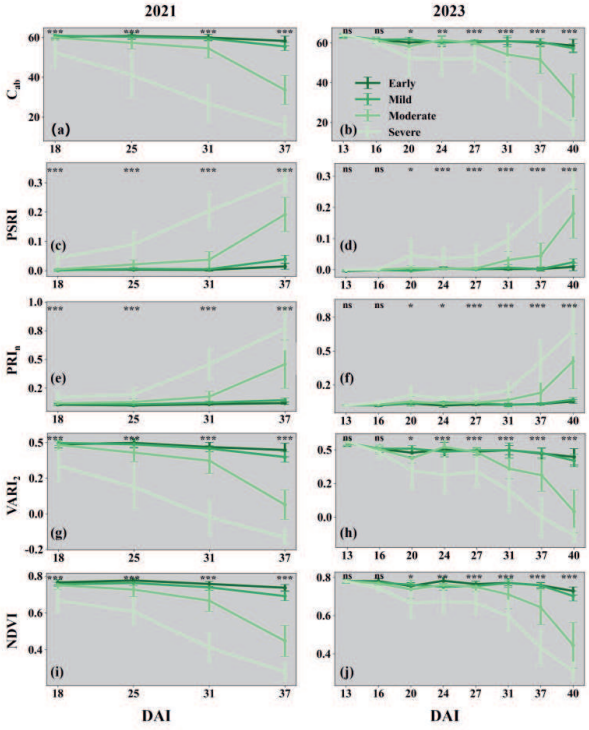


Fig. 6.5. *Temporal changes of key hyperspectral features across different disease progression levels (plots exhibiting distinct final severity classes during the last visual inspection) at multiple observation dates for 2021 (left) and 2023 (right). Error bars indicate the 95% confidence intervals. Asterisks denote statistical significance from one-way ANOVA: *** very highly significant ($p < 0.001$), ** highly significant ($0.001 \leqslant p < 0.01$), * significant ($0.01 \leqslant p < 0.05$), and ns not significant ($p \geqslant 0.05$).*

6.3.2 Prediction performance of individual models

The prediction performance of various models was evaluated using MLS datasets from two independent test years (Fig. 6.6, Table S6.2, Table S6.3, Fig. S6.3, and Fig. S6.4. Among the RS-deep learning models, the GRU consistently demonstrated the highest performance across both years for both order-aware and conventional classification metrics. Therefore, the GRU model was selected as the RS component in the construction of the RS-DeepSpread model.

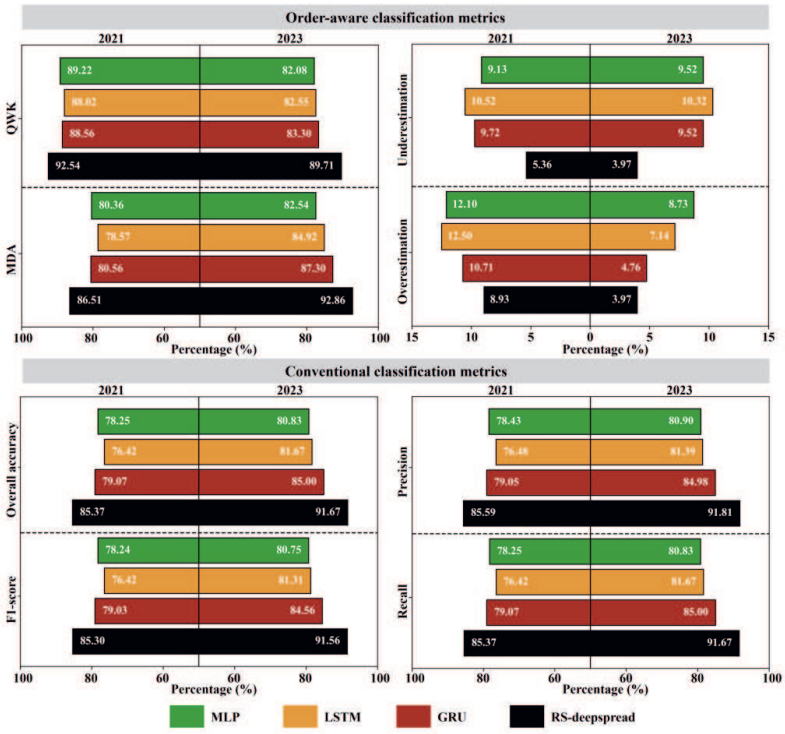


Fig.6.6. *Performance comparison among different models with order-aware and conventional classification metrics on the 2021 and 2023 test sets. Order-aware metrics (top row) include QWK (weighted kappa coefficient), MDA (Mean Directional Accuracy), underestimation, and overestimation rates. Conventional metrics (bottom row) include overall accuracy, F1-score, precision, and recall.*

The RS-DeepSpread model, which couples UAV-derived RS predictions with the epidemic spread module, consistently outperformed all individual RS-deep learning models (MLP, LSTM, and GRU) in both years. For order-aware classification metrics, RS-DeepSpread achieved the highest QWK values of 92.54 in 2021 and 89.71 in 2023, and the highest MDA of 86.51% and 92.86%, respectively. It also yielded the lowest overestimation rates (8.93% in 2021 and 3.97% in 2023) and underestimation rates (5.36% in 2021 and 3.97% in 2023). For conventional classification metrics, the RS-DeepSpread model achieved the highest overall accuracy (85.37%), along with the best weighted average precision (85.59%), recall (85.37%), and F1-score (85.30%) in 2021. The RS-DeepSpread model maintained improved performance in 2023, achieving an overall accuracy of 91.67%, and the highest weighted averages for precision (91.81%), recall (91.67%), and F1-score (91.56%). These results highlight the advantage of combining spatial-temporal epidemic dynamics with high-resolution UAV data.

6.3.3 Temporal epidemic prediction of MLS epidemics

To assess the temporal dynamics of MLS development, we compared the predicted

epidemic progression across models using the epidemic rate (r) over time, benchmarked against field observations. The temporal trajectories of $r(t)$ derived from field observations, the GRU model, and the RS-DeepSpread framework exhibit generally consistent trends (Fig. 6.7). All models successfully anticipated the timing of the epidemic change-rate peak earlier than the field observations. In 2021, the field-observed peak occurred at DAI 31, while the RS-DeepSpread and RS-deep learning models predicted it at DAI 28 and DAI 27, respectively. Similarly, in 2023, the observed peak appeared at DAI 24, and all models consistently predicted it at DAI 21, indicating an enhanced capacity for early epidemic detection.

To further elucidate the hyperspectral feature evolution around the epidemic peak, we constructed two matrices: a temporal similarity variation matrix (Fig. 6.7 b, e) and a similarity change-rate matrix (Fig. 6.7 c, f). The temporal similarity matrix, based on cosine similarity, quantified the day-to-day stability of hyperspectral feature patterns across DAI periods, while the change-rate matrix—computed as the absolute difference between consecutive days—captured the temporal gradient of spectral evolution. In 2023, hyperspectral features showed extremely high similarity (approaching 1.0, deep red) during DAI 13–19 (Fig. 6.7e), indicating minimal spectral variation at the early, latent stage of disease development. Similarity gradually decreased during DAI 20–40 (transitioning from red to blue), reflecting the expanding heterogeneity of canopy spectra as the disease progressed. The maximum rate of similarity change occurred around DAI 20 (Fig. 6.7f), marking the onset of rapid spectral transformation associated with the shift from the latent to the expansion stage of infection. This early spectral response implied that hyperspectral features enabled the detection of epidemic progression earlier than visual inspection. A similar temporal pattern was observed in 2021 (Fig. 6.7 b, c), demonstrating the efficacy of UAV-based hyperspectral sensing for tracking the temporal dynamics of MLS epidemics.

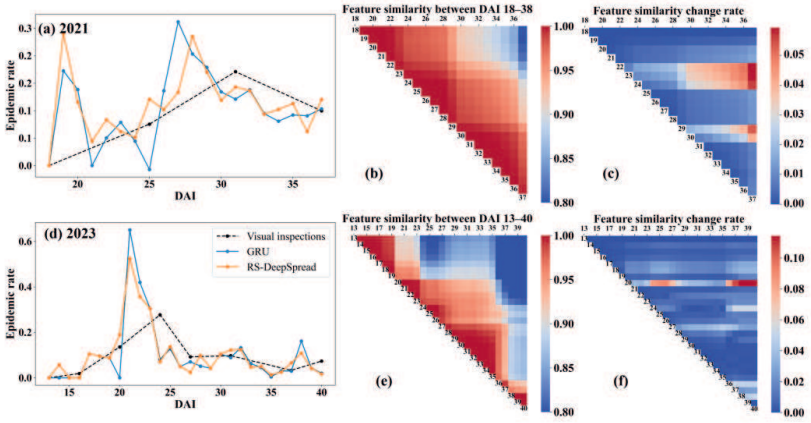


Fig.6.7. *Temporal dynamics of MLS epidemics and evolution of hyperspectral feature patterns. (a) and (d) show the epidemic rate r(t) from field observations, the GRU model, and the RS-DeepSpread framework. (b) and (e) present heatmaps of temporal*

similarity among hyperspectral feature vectors across DAI periods in 2021 and 2023. (c) and (f) illustrate the temporal change rate of feature similarity, reflecting the evolution speed of canopy spectral characteristics during epidemic progression.

6.3.4 Spatial prediction mapping

Hotspot analysis of model predictions revealed distinct spatial clustering patterns of MLS severity (Fig. 6.8), where hot spots and cold spots represent areas of severe and early-stage infection, respectively. Both models reproduced hotspot distributions broadly consistent with those observed through visual inspections, demonstrating their ability to capture the overall spatial pattern of disease occurrence. To quantitatively assess the spatial prediction accuracy, we compared the hotspot difference maps between model-predicted and visually observed disease severity. The RS-DeepSpread model achieved a higher proportion of correct estimations (63.82% in 2021 and 78.33% in 2023) and a lower rate of underestimation (14.43% in 2021 and 10.83% in 2023) compared with the GRU model (Fig. 6.8k). These results highlight that RS-DeepSpread yields *improved performance* for predicting MLS severity.

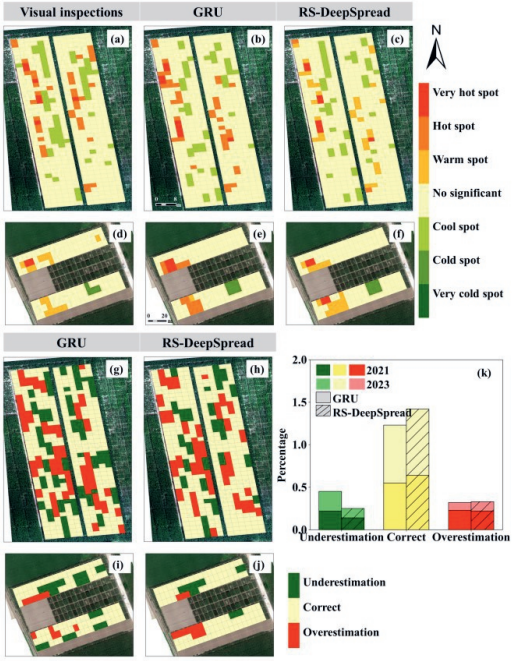


Fig. 6.8. *Spatial hotspots of predicted MLS severity for the 2021 and 2023 test sets. Hot spots and cold spots are defined based on the z-score of predicted disease severity. Hot spots (red areas) indicate regions of higher predicted disease severity (severe), while cold spots (green areas) indicate regions of lower predicted severity (early). (a–f) show the spatial distribution of disease severity derived from visual inspections (a, d), the GRU model (b, e), and the RS-DeepSpread model (c, f). (g–j) present the spatial differences in z-scores between GRU and visual inspections (g, i), and between RS-*

DeepSpread and visual inspections (h, j). (k) summarizes the percentage of underestimation, correct estimation, and overestimation cases based on the z-score statistics.

6.4 Discussion

6.4.1 Hyperspectral features response to MLS

Hyperspectral features derived from radiative transfer model inversions, together with VIs and WFs effectively enabled the detection of MLS. Based on VIF analysis and information entropy evaluation, the most parsimonious and representative hyperspectral features were identified. Our results indicated that chlorophyll-related indices, pigment indicators, the xanthophyll index, and photosynthetic efficiency indices all contributed to MLS detection. Specifically, chlorophyll degradation increased as disease symptoms intensified (Fig. 6.5 a, b). This observation aligns with findings that inoculated maize plants exhibit reduced chlorophyll under both lethal leaf spot (Li et al., 2022) and macrospora leaf spot infections (Bermúdez-Cardona et al., 2015). WFs near 500 nm were also highly responsive to MLS, likely because this spectral region captures variations in pigment composition such as chlorophyll and accessory pigments. However, chlorophyll degradation is not unique to MLS and may also be induced by other biotic or abiotic stressors (Hernandez-Clemente et al., 2019). Therefore, successful discrimination of MLS symptoms requires integrating pigment-related indices with additional plant physiological traits to distinguish disease effects from confounding factors such as water stress.

Regarding hyperspectral indices incorporated into the RS-deep learning, PSRI and $VARI_2$ exhibited clear distinctions across disease progression stages. The PSRI, sensitive to carotenoid and chlorophyll balance, has been widely validated for detecting leaf diseases such as spikelet rot in rice (Xue et al., 2023), fire blight in pear (Bagheri, 2020), and tar spot complex in maize (Loladze et al., 2019). $VARI_2$, associated with anthocyanin content, also proved effective, consistent with prior findings that anthocyanin levels gradually increase as foliar symptoms worsen (Zarco-Tejada et al., 2018). Additionally, the PRI_n index, a variant of the photochemical reflectance index (PRI), reflects variations in xanthophyll cycle pigments and total pigment pool size, thus serving as an indicator of light-use efficiency and photosynthetic performance (Gamon et al., 1992). The reduction in light transmittance and photosynthetic activity caused by pathogen infection and colonization leads to decreased fluorescence emission, making PRI_n a sensitive indicator for detecting MLS.

6.4.2 The complementarity of RS-deep learning and the epidemic spread model

Traditionally, epidemic spread models and RS–deep learning models have been viewed as fundamentally distinct paradigms—representing theory-driven and data-driven approaches, respectively. Epidemic models, grounded in disease development principles, offer the potential to extrapolate beyond observed conditions (Kraemer et al., 2025). In contrast, RS-deep learning models excel in flexibility and adaptability, enabling the discovery of complex or nonlinear relationships hidden within RS data (Zhu et al., 2017). Rather than being mutually exclusive, these two frameworks are

inherently complementary.

In this study, we synergistically combined the two modeling paradigms in two ways. First, the RS-deep learning model enhanced the parameterization of the epidemic spread model. In conventional epidemic frameworks, the probability of disease state transitions at unsampled time points is difficult to infer from first principles and is often initialized with uniform distributions (Parnell et al., 2011). This introduces uncertainty and strong dependence on sparse visual inspection data. Within the RS-DeepSpread framework, these transition probabilities were informed by outputs from the RS-deep learning, providing data-driven parameter initialization. This integration contributed to the model's stable and temporally consistent forecasting of epidemic rate peaks—arriving three days earlier in both 2021 and 2023 (Fig. 6.7). Notably, the intervals of visual inspections differed between years—approximately seven days in 2021 versus three days in 2023—resulting in fewer reference points and greater prediction uncertainty in 2021. The robust performance of RS-DeepSpread under these conditions suggests reduced dependence on dense ground observations, underscoring its potential for scalable and timely disease monitoring.

Second, the epidemic spread model constrained uncertainties inherent in the RS-deep learning predictions through iterative optimization informed by both field observations and epidemiological drivers such as temperature, humidity, and time. RS-deep learning operates in high-dimensional feature spaces and is sensitive to noise, data imbalance, and spectral variability. For instance, disease datasets often exhibit strong imbalance, with mild cases vastly outnumbering severe ones (Liu et al., 2025). Since disease severity typically increases with DAI, missing late-stage samples (e.g., DAI 40) disproportionately removes severe cases, reducing predictive accuracy. The epidemic spread model, guided by epidemiological laws, counteracts this limitation. During the course of an epidemic, the number of diseased plants generally increases over time, while the overall severity is a function of the initial inoculum, the rate of spread, and the duration of the epidemic. The spread rate itself depends on pathogen virulence, host resistance, and environmental conditions such as temperature and humidity (Dalal and Singh, 2017; Minogue and Fry, 1983). By embedding these constraints, RS-DeepSpread consistently outperformed the RS–deep learning model alone—improving QWK by up to 7.63%, increasing correct classification rate by up to 10.32%, and reducing overestimation and underestimation by 12.50% and 5.56%, respectively. These improvements were further corroborated by the hotspot analysis results (Fig. 6.8), which demonstrated more spatially coherent and accurate disease severity mapping. These results highlight that integrating epidemiological dynamics allows the hybrid model to correct inconsistencies, reduce biases, and stabilize predictions.

Ultimately, the RS-DeepSpread framework bridges physically based modeling with data-driven learning under noisy and incomplete observations. Such hybrid or physics-guided learning systems are gaining traction across disciplines, including earth system science (Liu et al., 2024a), engineering (Howland and Dabiri, 2019), and medical diagnostics (Bhouri et al., 2021). In such synergistic systems, data-driven models enrich

and extend the capabilities of physical models, while benefiting in return from physically plausible constraints rooted in natural science.

6.4.3 Limitations and future directions

Hyperspectral features can capture the spatiotemporal progression of disease severity, forming the foundation for remote sensing–based disease prediction (Bai et al., 2024a). This capability motivates further exploration into the mechanisms underlying spectral responses to infection dynamics. Although the proposed model can predict disease severity for dates without direct hyperspectral acquisition (Fig. 6.6), several questions remain unresolved and warrant further investigation. Specifically, how far in advance can disease progression be accurately forecast? How many temporal observations are required to achieve robust predictive performance? And which key growth stages contribute most critically to model accuracy? Addressing these questions will require additional time-series data across diverse disease development scenarios to refine temporal disease prediction.

This study represents an attempt at coupling epidemic spread models with RS-deep learning for disease prediction. While the proposed framework demonstrates clear benefits, there remains considerable room for deeper integration (Reichstein et al., 2019). From a systems modeling perspective, a key area for improvement lies in model parameterization. Epidemic models often depend on parameters that are difficult to estimate directly from first principles (Capaldi et al., 2012). Machine learning offers a potential solution by learning parameter relationships that best represent observed field dynamics. For instance, hyperspectral measurements in the shortwave infrared (SWIR) and thermal infrared (TIR) regions could be used to infer environmental variables such as canopy temperature and humidity (Gerhards et al., 2019)—factors that strongly influence pathogen development and spread. Integrating such data-driven parameterizations could enhance the realism and adaptability of the epidemic component.

Finally, model generalization and scalability remain important challenges. The current experiment was conducted at a localized, small-scale level. While the approach shows promise and offers conceptual guidance for broader applications, its scalability to regional or national levels remains to be validated. In real-world agricultural disease management, there is a pressing need for large-scale, spatially and temporally continuous predictions (Nkwocha and Chandel, 2025). Addressing this need will require future research to extend the model across wider spatial and temporal domains, ensuring it can support practical decision-making in pest and disease prevention.

6.5 Conclusions

This study introduces a novel synergistic framework that integrates UAV-based hyperspectral remote sensing with an epidemic spread model to predict the spatiotemporal dynamics of MLS. The integrated model achieved substantial improvements in prediction accuracy and early-warning performance, while reducing both underestimation and overestimation rates across two independent growing seasons.

Throughout the study period, the model consistently predicted the peak of disease progression earlier than field observations. These results demonstrate the potential of hybrid RS–epidemic modeling to advance dynamic crop disease prediction and support data-driven decision-making in precision agriculture. The proposed RS-DeepSpread framework offers a scalable and transferable foundation for developing proactive, reliable disease monitoring systems applicable to a broad range of crop–pathogen systems. Future work will focus on expanding temporal data coverage and validating model scalability across diverse agroecological regions.

6.6 Supplementary information

Additional tables and figures supporting this chapter are available online. They can be accessed via the QR code or at the following URL: PhD-thesis/chapter6-Supplementary .pdf at main · Briya1990/PhD-thesis



Summary

7.1 Main findings

In this thesis, different aspects related to unmanned aerial vehicle (UAV) collected data and radiative transfer model (RTM) simulations applied to monitoring maize disease were evaluated. These aspects ranged from understanding the canopy spectra response mechanism, including integration of RTMs and machine learning, to developing a disease-sensitive index. In this chapter, the results obtained for each of the individual topics are summarized (Section 7.1), and further considerations are made, including projections with respect to possible future scientific and operational developments in this research domain (Section 7.2).

7.1.1 What are the current applications, challenges, and perspectives in monitoring crop diseases using hyperspectral remote sensing?

Hyperspectral remote sensing can capture crop disease characteristics through spectral and spatial features. The four criteria (diversity, robustness, relevance, and parsimony) for spectral feature selection can be applied to detect and differentiate plant disease. The supervised classification methods and physically based approaches are proposed to monitor plant diseases using hyperspectral remote sensing. The capacity to utilize these spectral features makes imaging spectroscopy an invaluable tool in monitoring various crop diseases.

Utilizing hyperspectral remote sensing for plant disease monitoring can be categorized into five distinct applications: assessing disease incidence or severity, discriminating among stressors, monitoring disease symptoms at the early stage, and discriminating crop resistance in breeding programs. Recent and considerable advances in hyperspectral sensors and data analysis methods have yielded powerful tools for monitoring plant diseases at high spatial and temporal resolutions.

Advantages:

- Hyperspectral sensor can generate distinct spectral signature for plant disease, consisting of reflectance measurements in hundreds of contiguous wavelength channels.
- Narrow wavebands in hyperspectral data exhibit high sensitivity to subtle plant changes induced by diseases, enabling the differentiation of various disease types and early detection of asymptomatic stage.
- Hyperspectral images for plant disease monitoring holds great potential for enhancing both accuracy and transferability of local findings to larger scale.
- Differences between symptoms induced by pathogens and those caused by different types of stress in plants can be discriminated using hyperspectral approaches.
- Hyperspectral remote sensing can dynamically monitor the occurrence and development of crop diseases at a large scale.

Challenges:

- The study of monitoring plant diseases exists disconnects between the foliar and canopy scales.

- There remains a lack of relevant theories and standards for the sensitivity and robustness of the selected spectral features to target plant disease.
- Hyperspectral datasets for plant diseases present unique challenges, such as limited data from controlled experimental scenarios and difficulties in obtaining large-scale samples of diseased crops.
- Factors such as soil, plant structure, and phenology add layers of complexity when interpreting remote sensing data for plant disease monitoring.

7.1.2 Can a disease-specific index monitor early maize leaf-spot?

Chapter 3 introduces a new disease spectral index, the Disease Sensitive Index (DSI), designed for canopy-scale maize leaf disease monitoring. The DSI was developed based on an analysis of the spectral response mechanisms of simulation data using PROSPECT-D and LESS. We also evaluated the performance of the DSI using both simulation data and UAV-collected images.

In the case of simulation data, the DSI showed a strong correlation with chlorophyll content, while its sensitivity to planting space (PS) alterations was notably low (Fig. 3.7). For UAV-collected images, the DSI was highly statistically significant ($p < 0.001$) in differentiating disease severity (Fig. 3.9). When comparing DSI with the disease index (DI) for maize fields infected with rust, DSI outperformed other indices, demonstrating the lowest RMSE and highest R^2 values ($R^2 = 0.69$, RMSE = 0.13) (Fig. 3.10). Similarly, when examining the relationship between VIs and DI in maize leaf spot-infected fields, the DSI also achieved the highest accuracy, with the highest R^2 value ($R^2 = 0.62$) (Fig. 3.11). Temporal multispectral imagery from Site A showed distinct patterns in differentiating resistance and susceptibility to leaf spot disease (Fig. 3.12), with DSI showing a consistently significant difference ($|\text{effect sizes}| \geq 0.8$) from DAI 12. Likewise, at Site C, DSI revealed substantial differences in distinguishing infected from healthy areas starting from DAI 10 (Fig. 3.13).

Overall, our findings confirm that the DSI is both a practical and effective tool for early-stage monitoring of maize rust and leaf spot diseases. The results highlight the DSI's scalability and adaptability across diverse environments, underscoring its potential as a reliable solution for early-stage disease detection. This makes it a valuable tool for both monitoring disease onset and informing decision-making in breeding experiments and farm-level disease control strategies.

7.1.3 How and when do remote sensing features respond to maize leaf spot disease?

Chapter 4 explores the sensitivity of biophysical and spectral features as indicators of maize adaptation to leaf spot disease. Using high-resolution UAV hyperspectral imaging, we tracked the maize response over 30 days post-infection. This analysis included hyperspectral features, biophysical parameters derived from the PROSAIL model, spectral reflectance, vegetation indices (VIs), and wavelet features (WFs). We also assessed the effectiveness of these features for machine learning models across different sites and times.

Our results showed that WFs provided the earliest indicator of disease onset, detecting changes as soon as 6 days after infection (DAI). VIs followed, with responses

detectable by DAI 8, and changes in chlorophyll content became evident by DAI 10. For example, compared to DAI 0 measurements (Fig. 4.7), the change in chlorophyll content first increased and then gradually decreased. The accumulation of chlorophyll content in infected areas lagged behind healthy areas, with a notable difference in the chlorophyll content change rate observed from DAI 10 onward. However, spectral reflectance in the 400–900 nm wavelength range was prone to noise, and no significant continuous changes in response to the disease were observed during the monitoring period.

VIs responded to the disease by DAI 8, with the normalized photochemical reflectance index (PRIn), related to xanthophyll and photosynthetic efficiency, showing continuous changes until DAI 30 (Table 4.5). The PRIn remained close to zero in healthy areas at DAI 0 but sharply increased in infected areas after DAI 15. WFs, particularly $WF_{586,6}$, $WF_{590,7}$, and $WF_{590–598,8}$ (located within the yellow edge region, 550–650 nm), exhibited the earliest response at DAI 6. Changes in $WF_{590,8}$ in infected areas consistently preceded those in healthy areas. Although WFs responded rapidly to disease onset, the trends were noisy and discontinuous, particularly at the early stages of infection (Fig. 4.10), suggesting instability at the early stages.

The performance of our maize resistance classification models demonstrated both complementarity and redundancy among biophysical and spectral features (Fig. 4.14). These diverse features were complementary at the early stages of infection, improving accuracy when integrated. Specifically, models incorporating chlorophyll content, VIs, and WFs outperformed models based on spectral features or VIs alone, with a maximum overall accuracy difference of 9.36%. However, as the disease progressed, the complementarity of these features diminished, indicating information redundancy during the mild and early severe stages.

Overall, our findings underscore the value of temporal response analysis in understanding the spectral characteristics of crops and pathogens. The effectiveness of our classification models, which combine biophysical and spectral features, highlights their complementary role during the early and severe stages of disease infection. This research reveals for the first time the redundancy of information at the mild and early severe stages, confirmed through continuous observation. Our methodology and key findings offer valuable insights for future disease monitoring research.

7.1.4 Can a physical model-guided deep learning approach improve early-stage detection of maize leaf spot by leveraging the generalization strengths of physical models?

Chapter 5 introduces a novel approach—Physical Model-Guided Deep Learning (PGDL)—which integrates the strengths of physical models with deep learning for more robust disease monitoring. This study developed PGDL by evaluating three simulation methods based on RTMs: canopy spectrum simulations with evenly spaced chlorophyll contents (SIM #1), measured leaf disease spectra (SIM #2), and mixed endmember spectra (SIM #3). PGDL models were pre-trained on these simulations and applied to UAV-collected field data using transfer learning.

We evaluated three modeling techniques for predicting DI from UAV-collected data across multiple years. The modeling approaches can be categorized into three groups: (1) physically-based methods that estimate DI solely from simulation data (SIM #2 and SIM #3); (2) data-driven methods, including traditional machine learning and deep learning models; and (3) the PGDL approach, which uses a gated recurrent unit (GRU)-attention model pre-trained on simulations (SIM #1, SIM #2, and SIM #3) and applies it to field data using transfer learning.

The best performance was achieved with PGDL using SIM #2 ($R^2 = 0.85$ in 2021, $R^2 = 0.93$ in 2023), followed by PGDL with SIM #3 ($R^2 = 0.82$ in 2021, $R^2 = 0.92$ in 2023). The lowest RMSE was observed with PGDL using SIM #2 and SIM #3 (RMSE = 0.08 in 2021, RMSE = 0.06 in 2023), indicating that prior knowledge combined with measured disease data significantly enhanced DI monitoring accuracy.

To assess the models' generalization for DI monitoring over time, we compared their performance across different disease stages. While data-driven models showed similar performance to PGDL at the mild and moderate stages, they struggled at the early and severe stages, especially during the early stage (Fig. 5.7, Table 5.6). The key advantage of PGDL models (SIM #2 and SIM #3) is their ability to detect disease early, which is crucial for timely intervention and improving management outcomes.

Overall, this study demonstrates the effectiveness of PGDL for monitoring maize leaf spot by combining physically-based modeling with data-driven approaches. The results highlight that simulation methods play a critical role in the quality of simulated data and the accuracy of PGDL models. Specifically, using real disease spectral information (SIM #2 and SIM #3) provided the most accurate disease progression representation and strong generalization across different disease stages. This success can be attributed to integrating synthetic, leaf-scale, and canopy-scale data, which enhanced the model's ability to capture diverse aspects of disease progression. In conclusion, this study offers a novel tool for disease monitoring in precision agriculture, laying the groundwork for early disease detection and more efficient crop management strategies.

7.1.5 Can hyperspectral remote sensing predict maize leaf-spot disease progression in both space and time?

Chapter 6 proposes the RS-DeepSpread model, which integrates a hyperspectral remote sensing–based deep learning model with an epidemic spread model (Fig. 6.3). The concept behind RS-DeepSpread is two-fold: first, the remote sensing deep learning model generates spatially explicit probability maps of disease occurrence that serve as initial conditions for the epidemic model; second, the epidemic spread model iteratively refines these estimates to capture the spatiotemporal dynamics of disease progression.

Firstly, three remote sensing–deep learning architectures—multi-layer perceptron (MLP), long short-term memory (LSTM), and gated recurrent unit (GRU)—were evaluated to identify the optimal configuration for hyperspectral disease prediction. The GRU model achieved the highest performance across two growing seasons and was therefore selected as the deep learning component of the integrated RS-DeepSpread framework.

Building upon the GRU predictions and the epidemic laws embedded in the spread model, the RS-DeepSpread framework was developed and rigorously tested. It consistently outperformed all standalone RS–deep learning models in both 2021 and 2023. Specifically, RS-DeepSpread achieved the highest quadratic weighted kappa (QWK) values (92.54 in 2021 and 89.71 in 2023) and correct classification rates (86.51% and 92.86%), along with the lowest overestimation (8.93% and 3.97%) and underestimation (5.36% and 3.97%) rates. For conventional metrics, RS-DeepSpread attained the highest overall accuracies (85.37% in 2021 and 91.67% in 2023) and superior weighted average precision, recall, and F1-scores in both years. These results demonstrated the effectiveness of combining spatiotemporal epidemic dynamics with high-resolution UAV hyperspectral data.

To further evaluate temporal predictive capability, we compared the modeled epidemic progression rates (r) over time with field observations. The RS-DeepSpread framework reproduced the observed trends well and successfully anticipated the peak in the epidemic change rate approximately three days earlier than field measurements (Fig. 6.7), highlighting its potential for early disease warning.

Overall, the RS-DeepSpread model substantially enhanced prediction accuracy compared with standalone deep learning models, confirming the added value of integrating mechanistic epidemic modeling with data-driven hyperspectral analysis for spatiotemporal prediction of maize leaf-spot disease.

7.2 Reflection and outlook

In this section, considerations initiated in Section 7.1 are further extended, seeking to bridge the gap between current and future scientific and operational developments related to the main topics of this thesis.

7.2.1 VIs for monitoring disease

Vegetation indices (VIs) play a foundational role in disease monitoring. As reviewed in Chapter 2, VIs are among the earliest and most widely used hyperspectral features for detecting crop stress. They effectively capture physiological, biochemical, and structural leaf changes induced by fungal and bacterial infections. For example, the photochemical reflectance index (PRI), which reflects xanthophyll cycle activity, has been used to quantify the disease index (DI) of yellow rust (Puccinia striiformis) in wheat; when applied to independent spectral measurements, PRI achieved an R^2 of 0.97 (Huang et al., 2007). Similarly, Tian et al. (2023) developed $RIBI_{nir}$, a near-infrared (NIR)-based index that enhances the subtle spectral responses caused by *Magnaporthe oryzae* infection. $RIBI_{nir}$ delivered high classification accuracy for healthy versus infected samples at both leaf-level greenhouse conditions (81.41%) and field conditions (86.36%).

However, VIs have limitations. Canopy reflectance is influenced by many confounding factors—soil optical properties, atmospheric effects, canopy geometry, and sun-sensor geometry—which can obscure a direct link between a VI and a single biophysical variable (e.g., biomass). Traditional ratio-based indices like normalized

difference vegetation index (NDVI), simple ratio (SR), or photochemical reflectance index (PRI) are particularly sensitive to soil brightness: in bright soils they respond strongly, but in very dark soils or water backgrounds their sensitivity can drop dramatically (Chen and Yang, 2020; Gao et al., 2000). For example, NDVI may remain nearly constant whether a leaf covers 1% or 100% of a dark surface, causing ambiguity.

Many VIs also share strong mathematical relationships. Indices based on red and near-infrared (NIR) bands — such as difference vegetation index (DVI), enhanced vegetation index (EVI), two-band enhanced vegetation index (EVI_2), and near-infrared reflectance of vegetation (NIRv) — exhibit correlations because as LAI increases, NIR reflectance tends to rise while red reflectance falls. NIRv is closely tied to DVI and can represent parameters like FPAR (fraction of absorbed photosynthetically active radiation) combined with photon escape probability. EVI and EVI_2 are, in effect, scaled or corrected versions of DVI (Jiang et al., 2008), while NDVI introduces a non-linear denominator (NIR + Red) that alters sensitivity. The soil-adjusted vegetation index (SAVI) offers a more unified framework: by introducing a correction factor to account for soil background, it reduces soil brightness effects (Huete et al., 2002).

To address these constraints, future research should emphasize spectral feature fusion, spectral feature analysis, and spectral feature selection. Spectral feature fusion integrates data across different sensor types, providing a more comprehensive depiction of disease-induced changes. Pathogen infections simultaneously modify multiple physiological processes—photosynthetic rate, stomatal conductance, leaf energy dissipation, chlorophyll fluorescence emission, and pigment concentrations (Hernandez-Clemente et al., 2019) —none of which can be adequately captured by a single sensor. For example, thermal infrared data are needed to infer vegetation temperature linked to stomatal regulation and transpiration-driven cooling, whereas fluorescence, pigment-related, and water-related responses require spectroscopy across visible to short-wave infrared wavelengths. Combining these complementary measurements enhances sensitivity to diverse disease mechanisms.

Accurate disease prediction also relies on rigorous analysis and selection of hyperspectral features. Correlation analysis helps identify features most directly linked to disease progression, while feature selection reduces redundancy and mitigates model overfitting. For instance, Hornero et al. (2021) selected five optimal hyperspectral features—combined with biochemical parameters retrieved using radiative transfer modeling—to classify oak decline symptoms, achieving up to 82% accuracy. Tian et al. (2021) further demonstrated that only two to four VIs were sufficient to distinguish asymptomatic and early rice blast infection stages, with classification accuracies exceeding 65% and 80%, respectively. These findings reinforce that feature quality fundamentally determines model quality. However, feature selection remains challenging because different diseases and infection stages may yield different spectral optimal feature sets, underscoring the need for a standardized framework for feature selection in disease monitoring.

In summary, no single VI is universally optimal. Effective disease monitoring

requires selecting features aligned with instrument characteristics, disease biology, and hyperspectral sensitivity, with an emphasis on extracting the most informative and physiologically meaningful features.

7.2.2 Hybrid modelling approach for monitoring disease

Machine learning has become a cornerstone of monitoring disease using hyperspectral remote sensing. As reviewed in Chapter 2, citation trends since 2012 show the growing frequency and popularity of machine learning in this domain. However, despite its successes, several pitfalls limit the broader impact of machine learning in monitoring disease. Risks of naïve extrapolation, sampling bias, neglect of confounding factors, and misinterpretation of correlation as causation can lead to unreliable conclusions (Caldwell et al., 2014; Reichstein and Beer, 2008). Furthermore, purely data-driven machine learning models struggle to generalize beyond the observed data range and often lack interpretability—highlighting the need for integration with physically grounded approaches.

Deep learning extends machine learning by effectively modeling sequential and spatial data, with transformative success in computer vision, speech recognition, and control systems (LeCun et al., 2015), as well as in physics (Baldi et al., 2014), chemistry (Schütt et al., 2017) and biology (Alipanahi et al., 2015). Its application in disease monitoring is growing. For instance, Zhang et al. (2019d) proposed a deep learning framework for detecting yellow rust in winter wheat using high-resolution hyperspectral UAV imagery. By jointly exploiting spectral and spatial information through multiple Inception–ResNet layers, the model outperformed a random forest classifier, highlighting the capability of deep architectures to capture subtle disease signals and suggesting the need for validation on broader datasets and more efficient hyperspectral data-processing algorithms. Similarly, Sheenam et al. (2023) developed a VGG19-based system trained on images of healthy and diseased wheat plants. After fine-tuning, the model achieved strong accuracy, precision, recall, and F1 scores in classifying key wheat diseases including powdery mildew, yellow rust, and leaf rust, further illustrating the promise of deep learning for reliable crop disease detection.

Nevertheless, transferring deep learning methods from computer vision to remote sensingbased disease monitoring remains challenging. Unlike standard RGB images, hyperspectral and multispectral data consist of hundreds of spectral bands, each with unique statistical and spatial dependencies. These data often violate the assumption of independent and identically distributed samples, complicating training and inference. Additionally, multi-sensor data fusion is nontrivial due to differences in geometry, spatial/temporal resolution, and physical meaning. Observational sequences are further affected by missing data, noise, and systematic gaps caused by cloud cover or acquisition issues. Key barriers to deep learning adoption in monitoring disease using remote sensing include limited labeled data, high computational demands, and the need for interpretability and physical consistency (Reichstein et al., 2019). To overcome these challenges, hybrid modelling—integrating physical process models with machine learning—offers a promising pathway. Traditionally, physical and data-driven

modelling were viewed as distinct paradigms: theory-based versus data-based. Yet they are inherently complementary. Physical models provide interpretability, mechanistic understanding, and extrapolation potential, whereas machine learning offers flexibility, adaptiveness, and the ability to uncover latent patterns.

There are many promising opportunities in combining optical sensing and epidemiological modeling for crop-disease monitoring. On one hand, remote sensing can inform epidemiological models. Non-destructive, spatially explicit disease quantification from optical sensing provides rich data for parameterizing process-based models. The predictive power of epidemic model is fundamentally limited by the amount and quality of parameterization data. Traditional data collection methods (manual scouting or limited sampling) are often costly, slow, and subject to human bias (Mikaberidze et al., 2025). Using remote sensing with high revisit frequency, we can repeatedly monitor disease patterns across large spatial grids, with greater sampling density and more replicate plots than would be feasible with manual inspection. This would dramatically improve our capacity to estimate spatial spread parameters (e.g. dispersal kernels, infection pressure from source areas) (Saubin et al., 2021), and unify these observations with environmental and host-pathogen metadata to better understand how dispersal and reproduction depend on host genotype, pathogen, and environment (Farber et al., 2019; Karisto et al., 2018).

On the other hand, epidemiological modeling can inform remote-sensing interpretation. Disease classification from optical sensing often reduces to deciding whether a location is diseased (or how severe the disease is) based on spectral signals. But these signals may be ambiguous or noisy. Epidemiological models can supply context: for example, a simple weather-based risk model may confirm that conditions are favorable for disease at given locations, lending higher confidence to weak or ambiguous sensor signals. More powerful still, spatial or spatiotemporal epidemic models capture the fact that disease often clusters at multiple scales: the chance of infection at a site is higher if its neighbours are already infected (Madden et al., 2018). In practice, static or dynamic models of disease spread (e.g., incorporating dispersal kernels, infection probabilities, spatiotemporal correlations) can be combined with remote-sensing outputs. As a result, one can move beyond pixel-level classification to a probabilistic, process-aware interpretation of sensor data, improving detection robustness and reducing false positives/negatives.

Hybrid models not only improve predictive performance but also enhance consistency and credibility. Importantly, embedding physical constraints acts as a natural regularization mechanism, preventing overfitting in limited-sample regimes (Reichstein et al., 2019). This aligns with ongoing advances toward explainable AI (Angelov et al., 2021) and the integration of logic-based reasoning within deep neural architectures (Zhang, 2023). In the context of remote sensing based disease monitoring, such physics-aware machine learning frameworks hold particular promise for developing interpretable, generalizable, and biologically consistent disease prediction systems.

7.2.3 Large-scale disease monitoring

Remote sensing technologies now enable researchers and farmers to obtain high-resolution, multi-spectral imagery of agricultural landscapes, offering a bird's-eye view of crop health and growth (Malamiri et al., 2021). In this thesis we have shown successful field-scale disease monitoring using UAV imagery; however, large-scale monitoring—observing and analysing extensive geographic areas—is vital for managing widespread crop disease outbreaks.

While UAV imagery offers high spatial resolution and flexible data acquisition, it is often limited in terms of spatial coverage and operational accessibility (Guo et al., 2021b). In contrast, satellite imagery provides broad spatial coverage, but often lacks the fine resolution needed to capture subtle variation in crop health (Prins and Van Niekerk, 2021). Moreover, satellite data may suffer from atmospheric interference, cloud cover, and limited temporal/spatial resolution—all of which can reduce accuracy and reliability in agricultural monitoring (Mwinuka et al., 2022).

To overcome the limitations of using either UAV or satellite data alone, researchers are increasingly using data-fusion techniques—integrating information from multiple imaging sources to create a combined dataset that leverages the strengths of each (Zhang et al., 2023). Multi-platform monitoring frameworks are now widely applied in precision agriculture. For example, (Revill et al., 2020) used Sentinel-2 MSI data for winter-wheat LAI modelling, and found that UAV-derived models yielded far better accuracy (R^2 = 0.80 vs 0.29; normalized RMSE 11% vs 17%). By calibrating the satellite data in a two-stage method using averaged UAV predictions, they improved satellite LAI retrieval to R^2 = 0.88 and normalized RMSE = 8%. In another study, Mazzia et al. (2020) used UAV multispectral data to refine satellite-based vineyard vigour classification: satellite imagery alone lacked discriminative power due to background–vegetation mixing, but training a deep model on UAV data enabled satellite imagery to reach comparable discrimination levels.

Researchers have proposed several methods for integrating multi-scale datasets. One approach is calibration or correction: high-resolution UAV data are used to correct satellite data. For instance, Zhang et al. (2019c) derived band-wise correction coefficients from UAV multispectral data to retrieve SPAD (leaf chlorophyll) values from Sentinel-2 imagery, improving R^2 from 0.61 to 0.91. Another method is up-scaling: Liu et al. (2024b) up-scaled UAV data to satellite pixel size, and used regression-fitted satellite models corrected by UAV data—the corrected model achieved R^2 = 0.787 (an improvement of 0.157) and RMSE = 2.043.

A third method is imagery fusion for parameter retrieval: Allu and Mesapam (2025) used Brovey and principal component analysis (PCA) fusion to combine UAV and satellite data, thereby leveraging UAV's spatial detail and Sentinel-2's spectral breadth; their results showed strong correlations (high R^2) between fused imagery VIs and UAV reference data. The spatio-temporal fusion study by Li et al. (2023) also demonstrated how daily synthetic imagery at high spatial resolution can better represent object boundaries and spatial texture compared to standard fusion methods.

These case studies illustrate how UAV data has often been used to enhance satellite-based retrievals or classification frameworks. Despite the growing application of multi-platform data fusion in agriculture, its use for large-scale disease monitoring remains relatively rare. Therefore, for comprehensive crop-disease surveillance, we propose that the future lies in the coordinated integration of airborne/UAV and satellite-based hyperspectral technologies. This combined approach promises improved accuracy, scalability and efficiency in monitoring crop health across variable scales.

References

Abdulridha, J., Ampatzidis, Y., Ehsani, R., de Castro, A.I. (2018). Evaluating the performance of spectral features and multivariate analysis tools to detect laurel wilt disease and nutritional deficiency in avocado. *Computers and Electronics in Agriculture, 155*, 203-211

Abdulridha, J., Ampatzidis, Y., Kakarla, S.C., Roberts, P. (2020). Detection of target spot and bacterial spot diseases in tomato using UAV-based and benchtop-based hyperspectral imaging techniques. *Precision Agriculture, 21*, 955-978

Adão, T., Hruška, J., Pádua, L., Bessa, J., Peres, E., Morais, R., Sousa, J.J. (2017). Hyperspectral imaging: a review on UAV-based sensors, data processing and applications for agriculture and forestry. *Remote Sensing, 9*, 1110

Ahrens, C.W., Andrew, M.E., Mazanec, R.A., Ruthrof, K.X., Challis, A., Hardy, G., Byrne, M., Tissue, D.T., Rymer, P.D. (2020). Plant functional traits differ in adaptability and are predicted to be differentially affected by climate change. *Ecology and Evolution, 10*, 232-248

Al-Saddik, H., Laybros, A., Billiot, B., Cointault, F. (2018). Using image texture and spectral reflectance analysis to detect yellowness and esca in grapevines at leaf-level. *Remote Sensing, 10*

Alipanahi, B., Delong, A., Weirauch, M.T., Frey, B.J. (2015). Predicting the sequence specificities of DNA-and RNA-binding proteins by deep learning. *Nature Biotechnology, 33*, 831-838

Alisaac, E., Behmann, J., Kuska, M.T., Dehne, H.W., Mahlein, A.K. (2018). Hyperspectral quantification of wheat resistance to Fusarium head blight: comparison of two Fusarium species. *European Journal of Plant Pathology, 152*, 869-884

Allu, A.R., Mesapam, S. (2025). Fusion of Satellite and UAV Imagery for Crop Monitoring. *ISPRS Annals of the Photogrammetry, Remote Sensing and Spatial Information Sciences, X-G-2025*, 71-79

Almoujahed, M.B., Apolo-Apolo, O.E., Whetton, R.L., Kazlauskas, M., Kriaučiūnienė, Z., Šarauskis, E., Mouazen, A.M. (2025). Field-based hyperspectral imaging for detection and spatial mapping of fusarium head blight in wheat. *European Journal of Agronomy, 164*, 127485

Anderegg, J., Hund, A., Karisto, P., Mikaberidze, A. (2019). In-field detection and quantification of septoria tritici blotch in diverse wheat germplasm using spectral-temporal features. *Frontiers in Plant Science, 10*, 1355

Angelov, P.P., Soares, E.A., Jiang, R., Arnold, N.I., Atkinson, P.M. (2021). Explainable artificial intelligence: an analytical review. *Wiley Interdisciplinary Reviews: Data Mining Knowledge Discovery, 11*, e1424

Apan, A., Held, A., Phinn, S., Markley, J. (2004). Detecting sugarcane 'orange rust' disease using EO-1 Hyperion hyperspectral imagery. *International Journal of Remote Sensing, 25*, 489-498

Appeltans, S., Guerrero, A., Nawar, S., Pieters, J., Mouazen, A.M. (2020). Practical recommendations for hyperspectral and thermal proximal disease sensing in potato and leek fields. *Remote Sensing, 12*, 1939

Aragon, B., Johansen, K., Parkes, S., Malbeteau, Y., Al-Mashharawi, S., Al-Amoudi, T., Andrade, C.F., Turner, D., Lucieer, A., McCabe, M.F. (2020). A calibration procedure for field and UAV-based uncooled thermal infrared instruments. *Sensors, 20*, 3316

References

Asner, G.P., Martin, R.E. (2008). Spectral and chemical analysis of tropical forests: Scaling from leaf to canopy levels. *Remote Sensing of Environment, 112*, 3958-3970

Atzberger, C. (2013). Advances in remote sensing of agriculture: context description, existing operational monitoring systems and major information needs. *Remote Sensing, 5*, 949-981

Bagheri, N. (2020). Application of aerial remote sensing technology for detection of fire blight infected pear trees. *Computers and Electronics in Agriculture, 168*, 105147

Bagheri, N., Mohamadi-Monavar, H., Azizi, A., Ghasemi, A. (2018). Detection of Fire Blight disease in pear trees by hyperspectral data. *European Journal of Remote Sensing, 51*, 1-10

Bai, Y., Jin, X. (2024). Hyperspectral approaches for rapid and spatial plant disease monitoring. *Trends in Plant Science, 29*, p711-712

Bai, Y., Nie, C., Yu, X., Gou, M., Liu, S., Zhu, Y., Jiang, T., Jia, X., Liu, Y., Nan, F. (2024a). Comprehensive analysis of hyperspectral features for monitoring canopy maize leaf spot disease. *Computers and Electronics in Agriculture, 225*, 109350

Bai, Y., Nie, C., Yu, X., Gou, M., Liu, S., Zhu, Y., Jiang, T., Jia, X., Liu, Y., Nan, F., Li, L., Tekinerdogan, B., Song, Y., Liu, Q., Jin, X. (2024b). Comprehensive analysis of hyperspectral features for monitoring canopy maize leaf spot disease. *Computers and Electronics in Agriculture, 225*, 109350

Baldi, P., Sadowski, P., Whiteson, D. (2014). Searching for exotic particles in high-energy physics with deep learning. *Nature Communications, 5*, 4308

Baret, F., Champion, I., Guyot, G., Podaire, A. (1987). Monitoring wheat canopies with a high spectral resolution radiometer. *Remote Sensing of Environment, 22*, 367-378

Baret, F., Guyot, G. (1991). Potentials and limits of vegetation indices for LAI and APAR assessment. *Remote Sensing of Environment, 35*, 161-173

Baret, F., Houlès, V., Guérif, M. (2007). Quantification of plant stress using remote sensing observations and crop models: the case of nitrogen management. *Journal of Experimental Botany, 58*, 869-880

Bauriegel, E., Giebel, A., Geyer, M., Schmidt, U., Herppich, W.J.C., agriculture, e.i. (2011). Early detection of Fusarium infection in wheat using hyper-spectral imaging*, 75*, 304-312

Behmann, J., Steinrücken, J., Plümer, L. (2014). Detection of early plant stress responses in hyperspectral images. *ISPRS Journal of Photogrammetry and Remote Sensing, 93*, 98-111

Belwalkar, A., Poblete, T., Longmire, A., Hornero, A., Hernández-Clemente, R., Zarco-Tejada, P.J.J.R.S.o.E. (2022). Evaluation of SIF retrievals from narrow-band and sub-nanometer airborne hyperspectral imagers flown in tandem: Modelling and validation in the context of plant phenotyping. *Remote Sensing of Environment, 273*, 112986

Berger, K., Atzberger, C., Danner, M., D'Urso, G., Mauser, W., Vuolo, F., Hank, T. (2018). Evaluation of the PROSAIL model capabilities for future hyperspectral model environments: a review study. *Remote Sensing, 10*, 85

Berger, K., Machwitz, M., Kycko, M., Kefauver, S.C., Van Wittenberghe, S., Gerhards, M., Verrelst, J., Atzberger, C., van der Tol, C., Damm, A., Rascher, U., Herrmann, I., Paz, V.S., Fahrner, S., Pieruschka, R., Prikaziuk, E., Buchaillot, M.L., Halabuk, A., Celesti, M., Koren, G., Gormus, E.T., Rossini, M., Foerster, M., Siegmann, B., Abdelbaki, A., Tagliabue, G., Hank, T., Darvishzadeh, R., Aasen, H., Garcia, M., Pôças, I., Bandopadhyay, S., Sulis, M., Tomelleri, E., Rozenstein, O., Filchev, L., Stancile, G., Schlerf, M. (2022). Multi-sensor spectral synergies for crop stress detection and monitoring in the optical domain:

A review. *Remote Sensing of Environment, 280*, 113198

Bhadra, S., Sagan, V., Sarkar, S., Braud, M., Mockler, T.C., Eveland, A.L. (2024). PROSAIL-Net: A transfer learning-based dual stream neural network to estimate leaf chlorophyll and leaf angle of crops from UAV hyperspectral images. *ISPRS Journal of Photogrammetry and Remote Sensing, 210*, 1-24

Bhouri, M.A., Costabal, F.S., Wang, H., Linka, K., Peirlinck, M., Kuhl, E., Perdikaris, P. (2021). COVID-19 dynamics across the US: A deep learning study of human mobility and social behavior. *Computer Methods in Applied Mechanics and Engineering, 382*, 113891

Blackburn, G.A. (1999). Relationships between spectral reflectance and pigment concentrations in stacks of deciduous broadleaves. *Remote Sensing of Environment, 70*, 224-237

Blaskowitz, O., Herwartz, H. (2011). On economic evaluation of directional forecasts. *International Journal of Forecasting, 27*, 1058-1065

Bock, C.H., Poole, G.H., Parker, P.E., Gottwald, T.R. (2010). Plant Disease Severity Estimated Visually, by Digital Photography and Image Analysis, and by Hyperspectral Imaging. *Critical Reviews in Plant Sciences, 29*, 59-107

Boegh, E., Soegaard, H., Broge, N., Hasager, C., Jensen, N., Schelde, K., Thomsen, A. (2002). Airborne multispectral data for quantifying leaf area index, nitrogen concentration, and photosynthetic efficiency in agriculture. *Remote Sensing of Environment, 81*, 179-193

Bos, L., Parlevliet, J. (1995). Concepts and terminology on plant/pest relationships: toward consensus in plant pathology and crop protection. *Concepts and terminology on plant/pest relationships: toward consensus, 33*, 69-102

Botha, E.J., Leblon, B., Zebarth, B.J., Watmough, J. (2010). Non-destructive estimation of wheat leaf chlorophyll content from hyperspectral measurements through analytical model inversion. *International Journal of Remote Sensing, 31*, 1679-1697

Bourlard, H.A., Morgan, N. (1994). Multilayer Perceptrons. *Connectionist Speech Recognition: A Hybrid Approach* (pp. 59-80): Springer

Boyd, L.A., Ridout, C., O'Sullivan, D.M., Leach, J.E., Leung, H. (2013). Plant–pathogen interactions: disease resistance in modern agriculture. *Trends in Genetics, 29*, 233-240

Brest, C.L., Goward, S.N. (1987). Deriving surface albedo measurements from narrow band satellite data. *International Journal of Remote Sensing, 8*, 351-367

Broge, N.H., Thomsen, A.G., Andersen, P., Benes, T. (2003). Comparison of selected vegetation indices as indicators of crop status. In

Buschmann, C., Langsdorf, G., Lichtenthaler, H.K. (2000). Imaging of the Blue, Green, and Red Fluorescence Emission of Plants: An Overview. *Photosynthetica, 38*, 483-491

Calderon, R., Navas-Cortes, J.A., Lucena, C., Zarco-Tejada, P.J. (2013). High-resolution airborne hyperspectral and thermal imagery for early, detection of Verticillium wilt of olive using fluorescence, temperature and narrow-band spectral indices. *Remote Sensing of Environment, 139*, 231-245

Calderon, R., Navas-Cortes, J.A., Zarco-Tejada, P.J. (2015). Early detection and quantification of verticillium wilt in olive using hyperspectral and thermal imagery over large areas. *Remote Sensing, 7*, 5584-5610

Caldwell, P.M., Bretherton, C.S., Zelinka, M.D., Klein, S.A., Santer, B.D., Sanderson, B.M. (2014). Statistical significance of climate sensitivity predictors obtained by data mining. *Geophysical Research Letters, 41*, 1803-1808

References

Camarero, J.J., Olano, J.M., Alfaro, S.J.A., Fernández-Marín, B., Becerril, J.M., García-Plazaola, J.I. (2012). Photoprotection mechanisms in Quercus ilex under contrasting climatic conditions. *Flora-Morphology, Distribution, Functional Ecology of Plants, 207*, 557-564

Camino, C., Araño, K., Berni, J.A., Dierkes, H., Trapero-Casas, J.L., León-Ropero, G., Montes-Borrego, M., Roman-Écija, M., Velasco-Amo, M.P., Landa, B.B., Navas-Cortes, J.A., Beck, P.S.A. (2022). Detecting Xylella fastidiosa in a machine learning framework using Vcmax and leaf biochemistry quantified with airborne hyperspectral imagery. *Remote Sensing of Environment, 282*, 113281

Camino, C., Calderon, R., Parnell, S., Dierkes, H., Chemin, Y., Roman-Ecija, M., Montes-Borrego, M., Landa, B.B., Navas-Cortes, J.A., Zarco-Tejada, P.J., Beck, P.S.A. (2021). Detection of Xylella fastidiosa in almond orchards by synergic use of an epidemic spread model and remotely sensed plant traits. *Remote Sensing of Environment, 260*, 112420

Cao, Z., Yao, X., Liu, H., Liu, B., Cheng, T., Tian, Y., Cao, W., Zhu, Y. (2019). Comparison of the abilities of vegetation indices and photosynthetic parameters to detect heat stress in wheat. *Agricultural and Forest Meteorology, 265*, 121-136

Capaldi, A., Behrend, S., Berman, B., Smith, J., Wright, J., Lloyd, A.L. (2012). Parameter estimation and uncertainty quantication for an epidemic model. *Mathematical biosciences engineering*, 553

Cardwell, K.F., Schulthess, F., Ndemah, R., Ngoko, Z. (1997). A systems approach to assess crop health and maize yield losses due to pests and diseases in Cameroon. *Agriculture, Ecosystems & Environment, 65*, 33-47

Carter, G.A., Knapp, A.K.J.A.j.o.b. (2001). Leaf optical properties in higher plants: linking spectral characteristics to stress and chlorophyll concentration*, 88*, 677-684

Casadevall, A. (2008). Evolution of intracellular pathogens. *Annual Review of Microbiology, 62*, 19-33

Chakraborty, S., Newton, A.C. (2011a). Climate change, plant diseases and food security: an overview. *Plant Pathology, 60*, 2-14

Chakraborty, S., Newton, A.C.J.P.p. (2011b). Climate change, plant diseases and food security: an overview. *Plant Pathology, 60*, 2-14

Chandrakar, V., Pandey, N., Keshavkant, S. (2018). Plant Responses to Arsenic Toxicity: Morphology and Physiology. In M. Hasanuzzaman, K. Nahar, & M. Fujita (Eds.), *Mechanisms of Arsenic Toxicity and Tolerance in Plants* (pp. 27-48). Singapore: Springer Singapore

Chang, Q., Liu, J., Wang, Q., Han, L., Liu, J., Li, M., Huang, L., Yang, J., Kang, Z. (2013). The effect of Puccinia striiformis f. sp. tritici on the levels of water-soluble carbohydrates and the photosynthetic rate in wheat leaves. *Physiological and Molecular Plant Pathology, 84*, 131-137

Charach, A., Dashti, B., Carson, P., Booker, L., Lim, C.G., Lillie, E., Yeung, E., Ma, J., Raina, P., Schachar, R. (2011). AHRQ Comparative Effectiveness Reviews. *Attention Deficit Hyperactivity Disorder: Effectiveness of Treatment in At-Risk Preschoolers; Long-Term Effectiveness in All Ages; and Variability in Prevalence, Diagnosis, and Treatment*. Rockville (MD): Agency for Healthcare Research and Quality (US)

Chemura, A., Mutanga, O., Dube, T. (2017). Separability of coffee leaf rust infection levels with machine learning methods at Sentinel-2 MSI spectral resolutions. *Precision Agriculture, 18*, 859-881

Chen, C., Song, M. (2019). Visualizing a field of research: A methodology of systematic scientometric reviews. *PLoS One, 14*, e0223994

Chen, G., He, Y.N., De Santis, A., Li, G.S., Cobb, R., Meentemeyer, R.K. (2017). Assessing the impact of emerging forest disease on wildfire using Landsat and KOMPSAT-2 data. *Remote Sensing of Environment, 195*, 218-229

Chen, J., Saimi, A., Zhang, M., Liu, Q., Ma, Z. (2022a). Epidemic of wheat stripe rust detected by hyperspectral remote sensing and its potential correlation with soil nitrogen during latent period. *Life, 12*, 1377

Chen, J.X., Jiang, D., Zhang, Y. (2019). A hierarchical bidirectional GRU model with attention for EEG-based emotion classification. *IEEE Access, 7*, 118530-118540

Chen, Q., Zheng, B., Chen, T., Chapman, S.C. (2022b). Integrating a crop growth model and radiative transfer model to improve estimation of crop traits based on deep learning. *Journal of Experimental Botany, 73*, 6558-6574

Chen, X., Vierling, L., Deering, D. (2005). A simple and effective radiometric correction method to improve landscape change detection across sensors and across time. *Remote Sensing of Environment, 98*, 63-79

Chen, X., Yang, Y. (2020). Observed earlier start of the growing season from middle to high latitudes across the Northern Hemisphere snow-covered landmass for the period 2001–2014. *Environmental Research Letters, 15*, 034042

Cheng, T., Rivard, B., Sánchez-Azofeifa, G.A., Feng, J., Calvo-Polanco, M. (2010). Continuous wavelet analysis for the detection of green attack damage due to mountain pine beetle infestation. *Remote Sensing of Environment, 114*, 899-910

Cogato, A., Meggio, F., De Antoni Migliorati, M., Marinello, F. (2019). Extreme Weather Events in Agriculture: A Systematic Review. *Sustainability, 11*, 2547

Comar, A., Burger, P., De Solan, B., Baret, F., Daumard, F., Hanocq, J.-F. (2012). A semi-automatic system for high throughput phenotyping wheat cultivars in-field conditions: description and first results. *Functional Plant Biology, 39*, 914-924

Combal, B., Baret, F., Weiss, M., Trubuil, A., Macé, D., Pragnere, A., Myneni, R., Knyazikhin, Y., Wang, L. (2003). Retrieval of canopy biophysical variables from bidirectional reflectance: Using prior information to solve the ill-posed inverse problem. *Remote Sensing of Environment, 84*, 1-15

Cronin, P., Ryan, F., Coughlan, M. (2008). Undertaking a literature review: a step-by-step approach. *British Journal of Nursing, 17*, 38-43

Crous, P.W., Groenewald, J.Z., Groenewald, M., Caldwell, P., Braun, U., Harrington, T.C. (2006). Species of Cercospora associated with grey leaf spot of maize. *Studies in Mycology, 55*, 189-197

Dai, Z., Pi, Q., Liu, Y., Hu, L., Li, B., Zhang, B., Wang, Y., Jiang, M., Qi, X., Li, W. (2024). ZmWAK02 encoding an RD-WAK protein confers maize resistance against gray leaf spot. *New Phytologist, 241*, 1780-1793

Dalal, P.K., Singh, J.K. (2017). Role of modeling in insect pest and disease management. *Journal of Entomology Zoology studies, 5*, 1773-1777

Damm, A., Cogliati, S., Colombo, R., Fritsche, L., Genangeli, A., Genesio, L., Hanus, J., Peressotti, A., Rademske, P., Rascher, U., Schuettemeyer, D., Siegmann, B., Sturm, J., Miglietta, F. (2022). Response times of remote sensing measured sun-induced chlorophyll fluorescence, surface temperature and vegetation indices to evolving soil water limitation in a crop canopy. *Remote Sensing of Environment, 273*, 112957

References

Damm, A., Paul-Limoges, E., Haghighi, E., Simmer, C., Morsdorf, F., Schneider, F.D., van der Tol, C., Migliavacca, M., Rascher, U. (2018). Remote sensing of plant-water relations: an overview and future perspectives. *Journal of Plant Physiology, 227*, 3-19

Darvishzadeh, R., Atzberger, C., Skidmore, A.K., Abkar, A.A. (2009). Leaf area index derivation from hyperspectral vegetation indicesand the red edge position. *International Journal of Remote Sensing, 30*, 6199-6218

Dash, J., Curran, P. (2004). The MERIS terrestrial chlorophyll index. *International Journal of Remote Sensing, 25*, 5403– 5413

Datt, B. (1999). Visible/near infrared reflectance and chlorophyll content in Eucalyptus leaves. *International Journal of Remote Sensing, 20*, 2741-2759

De Castro, A.I., Ehsani, R., Ploetz, R., Crane, J.H., Abdulridha, J. (2015). Optimum spectral and geometric parameters for early detection of laurel wilt disease in avocado. *Remote Sensing of Environment, 171*, 33-44

Dehghan-Shoar, M.H., Orsi, A.A., Pullanagari, R.R., Yule, I.J. (2023). A hybrid model to predict nitrogen concentration in heterogeneous grassland using field spectroscopy. *Remote Sensing of Environment, 285*, 12

Devadas, R., Lamb, D.W., Simpfendorfer, S., Backhouse, D. (2009). Evaluating ten spectral vegetation indices for identifying rust infection in individual wheat leaves. *Precision Agriculture, 10*, 459-470

Dhami, N., Kim, S.K., Paudel, A., Shrestha, J., Rijal, T. (2015a). A review on threat of gray leaf spot disease of maize in Asia. *Journal of Maize Research and Development, 1*, 71-85

Dhami, N.B., Kim, S., Paudel, A., Shrestha, J., Rijal, T.R. (2015b). A review on threat of gray leaf spot disease of maize in Asia. *Journal of Maize Research and Development, 1*, 71-85

Dutta, A., Tyagi, R., Chattopadhyay, A., Chatterjee, D., Sarkar, A., Lall, B., Sharma, S. (2024). Early detection of wilt in Cajanus cajan using satellite hyperspectral images: Development and validation of disease-specific spectral index with integrated methodology. *Computers and Electronics in Agriculture, 219*

El-baki, M.S.A., Ibrahim, M., Elsayed, S., Yaseen, Z.M., El-Fattah, N.G.A. (2025). Water status and plant traits of dry bean assessment using integrated spectral reflectance and RGB image indices with artificial intelligence. *Scientific Reports, 15*, 16808

Eugenio, F.C., da Silva, S.D.P., Fantinel, R.A., De Souza, P.D., Felippe, B.M., Romua, C.L., Elsenbach, E.M. (2021). Remotely Piloted Aircraft Systems to Identify Pests and Diseases in Forest Species: The global state of the art and future challenges. *IEEE Geoscience Remote Sensing Magazine, 10*, 320-333

Ex, E. (2009). ENVI EX user's guide. *ITT Visual Information Solutions*

Farber, D.H., De Leenheer, P., Mundt, C.C.J.J.o.b. (2019). Dispersal kernels may be scalable: Implications from a plant pathogen. *Journal of Biogeography, 46*, 2042-2055

Feng, J., Li, D., Gu, J., Cao, X., Shang, R., Zhang, X., Jiao, L. (2022a). Deep Reinforcement Learning for Semisupervised Hyperspectral Band Selection. *IEEE Transactions on Geoscience and Remote Sensing, 60*

Feng, W., Shen, W., He, L., Duan, J., Guo, B., Li, Y., Wang, C., Guo, T. (2016). Improved remote sensing detection of wheat powdery mildew using dual-green vegetation indices. *Precision Agriculture, 17*, 608-627

Feng, Z., Song, L., Duan, J., He, L., Zhang, Y., Wei, Y., Feng, W. (2022b). Monitoring wheat powdery

mildew based on hyperspectral, thermal infrared, and rgb image data fusion. *Sensors, 22*, 33

Feret, J.-B., François, C., Asner, G.P., Gitelson, A.A., Martin, R.E., Bidel, L.P.R., Ustin, S.L., le Maire, G., Jacquemoud, S. (2008). PROSPECT-4 and 5: Advances in the leaf optical properties model separating photosynthetic pigments. *Remote Sensing of Environment, 112*, 3030-3043

Féret, J.B., Gitelson, A., Noble, S.D., Jacquemoud, S. (2017). PROSPECT-D: Towards modeling leaf optical properties through a complete lifecycle. *Remote Sensing of Environment, 193*, 204-215

Fernandez, C.I., Leblon, B., Haddadi, A., Wang, K., Wang, J. (2020). Potato late blight detection at the leaf and canopy levels based in the red and red-edge spectral regions. *Remote Sensing, 12*, 1292

Fiorani, Fabio, Schurr, Ulrich (2013). Future scenarios for plant phenotyping. *Annual Review of Plant Biology, 64*, 267-291

Fisher, M.C., Henk, D.A., Briggs, C.J., Brownstein, J.S., Madoff, L.C., McCraw, S.L., Gurr, S.J. (2012). Emerging fungal threats to animal, plant and ecosystem health. *Nature, 484*, 186-194

Fu, P., Zhang, W., Yang, K., Meng, F. (2020). A novel spectral analysis method for distinguishing heavy metal stress of maize due to copper and lead: RDA and EMD-PSD. *Ecotoxicology and Environmental Safety, 206*, 111211

Galieni, A., D'Ascenzo, N., Stagnari, F., Pagnani, G., Xie, Q., Pisante, M. (2021). Past and future of plant stress detection: an overview from remote sensing to positron emission tomography. *Frontiers in Plant Science, 11*, 609155

Gamon, J.A., Huemmrich, K.F., Wong, C.Y.S., Ensminger, I., Garrity, S., Hollinger, D.Y., Noormets, A., Penuelas, J. (2016). A remotely sensed pigment index reveals photosynthetic phenology in evergreen conifers. *Proceedings of the National Academy of Sciences of the United States of America, 113*, 13087-13092

Gamon, J.A., Peñuelas, J., Field, C.B. (1992). A narrow-waveband spectral index that tracks diurnal changes in photosynthetic efficiency. *Remote Sensing of Environment, 41*, 35-44

Gao, X., Huete, A.R., Ni, W., Miura, T. (2000). Optical–biophysical relationships of vegetation spectra without background contamination. *Remote Sensing of Environment, 74*, 609-620

Garcia-Ruiz, F., Sankaran, S., Maja, J.M., Lee, W.S., Rasmussen, J., Ehsani, R.J.C., Agriculture, E.i. (2013). Comparison of two aerial imaging platforms for identification of Huanglongbing-infected citrus trees*, 91*, 106-115

Gastellu-Etchegorry, J.P., Lauret, N., Yin, T., Landier, L., Kallel, A., Malenovský, Z., Bitar, A.A., Aval, J., Benhmida, S., Qi, J., Medjdoub, G., Guilleux, J., Chavanon, E., Cook, B., Morton, D., Chrysoulakis, N., Mitraka, Z. (2017). DART: recent advances in remote sensing data modeling with atmosphere, polarization, and chlorophyll fluorescence. *IEEE Journal of Selected Topics in Applied Earth Observations and Remote Sensing, 10*, 2640-2649

Gerhards, M., Schlerf, M., Mallick, K., Udelhoven, T. (2019). Challenges and Future Perspectives of Multi-/Hyperspectral Thermal Infrared Remote Sensing for Crop Water-Stress Detection: A Review. *Remote Sensing, 11*, 1240

Gitelson, A., Merzlyak, M., Zur, Y., Stark, R., Gritz, U. (2001). Non-destructive and remote sensing techniques for estimation of vegetation status. *Papers in Natural Resources, 1*, 273

Gitelson, A., Merzlyak, M.N. (1994). Spectral reflectance changes associated with autumn senescence of Aesculus hippocastanum L. and Acer platanoides L. leaves. Spectral features and relation to chlorophyll estimation. *Journal of Plant Physiology, 143*, 286-292

Gitelson, A.A., Viña, A., Ciganda, V., Rundquist, D.C., Arkebauer, T.J. (2005). Remote estimation of canopy chlorophyll content in crops. *Geophysical Research Letters, 32*, L08403

Gold, K.M., Townsend, P.A., Chlus, A., Herrmann, I., Couture, J.J., Larson, E.R., Gevens, A.J. (2020a). Hyperspectral measurements enable pre-symptomatic detection and differentiation of contrasting physiological effects of late blight and early blight in potato. *Remote Sensing, 12*, 286

Gold, K.M., Townsend, P.A., Herrmann, I., Gevens, A.J. (2020b). Investigating potato late blight physiological differences across potato cultivars with spectroscopy and machine learning. *Plant Science, 295*, 110316

Gomiero, T., Pimentel, D., Paoletti, M.G. (2011). Environmental impact of different agricultural management practices: conventional vs. organic agriculture. *Critical Reviews in Plant Sciences, 30*, 95-124

Gonçalves, R., Figueiredo, J., Pedro, E., Meirelles, W., Leite, R., Sauer, A., Paccola, L. (2013). Etiology of Phaeosphaeria leaf spot disease of maize. *Journal of Plant Pathology*

Govender, M., Govender, P., Weiersbye, I., Witkowski, E., Ahmed, F. (2009). Review of commonly used remote sensing and ground-based technologies to measure plant water stress. *Water Sa, 35*

Graves, A. (2013). Generating sequences with recurrent neural networks. *arXiv preprint arXiv:*. 1308.0850

Guo, A., Huang, W., Dong, Y., Ye, H., Ma, H., Liu, B., Wu, W., Ren, Y., Ruan, C., Geng, Y. (2021a). Wheat yellow rust detection using uav-based hyperspectral technology. *Remote Sensing, 13*, 123

Guo, X., Wang, M., Jia, M., Wang, W. (2021b). Estimating mangrove leaf area index based on red-edge vegetation indices: A comparison among UAV, WorldView-2 and Sentinel-2 imagery. *International Journal of Applied Earth Observation and Geoinformation, 103*, 102493

Guo, Z., Ni, Y., Gao, H., Ding, G., Zeng, Y. (2024). A dual-branch selective attention capsule network for classifying kiwifruit soft rot with hyperspectral images. *Scientific Reports, 14*, 10664

Haagsma, M., Page, G.F.M., Johnson, J.S., Still, C., Waring, K.M., Sniezko, R.A., Selker, J.S. (2020). Using hyperspectral imagery to detect an invasive fungal pathogen and symptom severity in pinus strobiformis seedlings of different genotypes. *Remote Sensing, 12*, 4041

Haboudane, D., Miller, J.R., Tremblay, N., Zarco-Tejada, P.J., Dextraze, L. (2002). Integrated narrow-band vegetation indices for prediction of crop chlorophyll content for application to precision agriculture. *Remote Sensing of Environment, 81*, 416-426

Haibo, H., Yunqian, M. (2013). Assessment Metrics for Imbalanced Learning. *Imbalanced Learning: Foundations, Algorithms, and Applications* (pp. 187-206): IEEE

Hair Jr, J.F., Black, W.C., Babin, B.J., Anderson, R.E. (2010). Multivariate data analysis. *Multivariate data analysis* (pp. 785-785). London: Prentice Hall

He, L., Qi, S.L., Duan, J.Z., Guo, T.C., Feng, W., He, D.X. (2021). Monitoring of wheat powdery mildew disease severity using multiangle hyperspectral remote sensing. *IEEE Transactions on Geoscience and Remote Sensing, 59*, 979-990

Hernandez-Clemente, R., Hornero, A., Mottus, M., Penuelas, J., Gonzalez-Dugo, V., Jimenez, J.C., Suarez, L., Alonso, L., Zarco-Tejada, P.J. (2019). Early diagnosis of vegetation health from high-resolution hyperspectral and thermal imagery: lessons learned from empirical relationships and radiative transfer modelling. *Current Forestry Reports, 5*, 169-183

Hernández-Clemente, R., Kolari, P., Porcar-Castell, A., Korhonen, L., Mõttus, M.J.I.T.o.G., Sensing,

R. (2016). Tracking the seasonal dynamics of boreal forest photosynthesis using EO-1 Hyperion reflectance: Sensitivity to structural and illumination effects*, 54*, 5105-5116

Hillnhuetter, C., Mahlein, A.-K., Sikora, R.A., Oerke, E.-C. (2012). Use of imaging spectroscopy to discriminate symptoms caused by Heterodera schachtii and Rhizoctonia solani on sugar beet. *Precision Agriculture, 13*, 17-32

Hornero, A., Hernandez-Clemente, R., North, P.R.J., Beck, P.S.A., Boscia, D., Navas-Cortes, J.A., Zarco-Tejada, P.J. (2020). Monitoring the incidence of Xylella fastidiosa infection in olive orchards using ground-based evaluations, airborne imaging spectroscopy and Sentinel-2 time series through 3-D radiative transfer modelling. *Remote Sensing of Environment, 236*, 111480

Hornero, A., Zarco-Tejada, P.J., Quero, J.L., North, P.R.J., Ruiz-Gomez, F.J., Sanchez-Cuesta, R., Hernandez-Clemente, R. (2021). Modelling hyperspectral- and thermal-based plant traits for the early detection of Phytophthora-induced symptoms in oak decline. *Remote Sensing of Environment, 263*, 112570

Howland, M.F., Dabiri, J.O. (2019). Wind Farm Modeling with Interpretable Physics-Informed Machine Learning. *Energies, 12*, 2716

Huang, J., Liao, H., Zhu, Y., Sun, J., Sun, Q., Liu, X.J.C., agriculture, e.i. (2012a). Hyperspectral detection of rice damaged by rice leaf folder (Cnaphalocrocis medinalis)*, 82*, 100-107

Huang, L.-S., Ju, S.-C., Zhao, J.-L., Zhang, D.-Y., Qi, H., Teng, L., Yang, F., Yan, Z. (2015). Hyperspectral measurements for estimating vertical infection of yellow rust on winter wheat plant. *International Journal of Agriculture and Biology, 17*, 1237-1242

Huang, L., Liu, Y., Huang, W., Dong, Y., Ma, H., Wu, K., Guo, A. (2022). Combining Random Forest and XGBoost Methods in Detecting Early and Mid-Term Winter Wheat Stripe Rust Using Canopy Level Hyperspectral Measurements. *Agriculture-Basel, 12*

Huang, L., Wu, K., Huang, W., Dong, Y., Ma, H., Liu, Y., Liu, L. (2021). Detection of fusarium head blight in wheat ears using continuous wavelet analysis and PSO-SVM. *Agriculture, 11*, 998

Huang, L., Zhang, H., Ruan, C., Huang, W., Hu, T., Zhao, J. (2020). Detection of scab in wheat ears using in situ hyperspectral data and support vector machine optimized by genetic algorithm. *International Journal of Agricultural and Biological Engineering, 13*, 182-188

Huang, L.S., Zhao, J.L., Zhang, D.Y., Yuan, L., Dong, Y.Y., Zhang, J.C. (2012b). Identifying and Mapping Stripe Rust in Winter Wheat using Multi-temporal Airborne Hyperspectral Images. *International Journal of Agriculture and Biology, 14*, 697-704

Huang, W., Guan, Q., Luo, J., Zhang, J., Zhao, J., Liang, D., Huang, L., Zhang, D. (2014). New Optimized Spectral Indices for Identifying and Monitoring Winter Wheat Diseases. *IEEE Journal of Selected Topics in Applied Earth Observations and Remote Sensing, 7*, 2516-2524

Huang, W., Lamb, D.W., Niu, Z., Zhang, Y., Liu, L., Wang, J. (2007). Identification of yellow rust in wheat using in-situ spectral reflectance measurements and airborne hyperspectral imaging. *Precision Agriculture, 8*, 187-197

Huete, A., Didan, K., Miura, T., Rodriguez, E.P., Gao, X., Ferreira, L.G. (2002). Overview of the radiometric and biophysical performance of the MODIS vegetation indices. *Remote Sensing of Environment, 83*, 195-213

Iordache, M.-D., Mantas, V., Baltazar, E., Pauly, K., Lewyckyj, N. (2020). A machine learning approach to detecting pine wilt disease using airborne spectral. *Remote Sensing, 12*

Jia, X., Yin, D., Bai, Y., Yu, X., Song, Y., Cheng, M., Liu, S., Bai, Y., Meng, L., Liu, Y. (2023). Monitoring maize leaf spot disease using multi-source UAV imagery. *Drones, 7*, 650

Jiang, Z., Huete, A.R., Didan, K., Miura, T. (2008). Development of a two-band enhanced vegetation index without a blue band. *Remote Sensing of Environment, 112*, 3833-3845

Jin, S., Sun, X., Wu, F., Su, Y., Li, Y., Song, S., Xu, K., Ma, Q., Baret, F., Jiang, D., Ding, Y., Guo, Q. (2021a). Lidar sheds new light on plant phenomics for plant breeding and management: Recent advances and future prospects. *ISPRS Journal of Photogrammetry and Remote Sensing, 171*, 202-223

Jin, X., Jie, L., Wang, S., Qi, H.J., Li, S.W. (2018). Classifying wheat hyperspectral pixels of healthy heads and fusarium head blight disease using a deep neural network in the wild field. *Remote Sensing, 10*, 395

Jin, X., Zarco-Tejada, P.J., Schmidhalter, U., Reynolds, M.P., Hawkesford, M.J., Varshney, R.K., Yang, T., Nie, C., Li, Z., Ming, B. (2020). High-throughput estimation of crop traits: a review of ground and aerial phenotyping platforms. *IEEE Geoscience and Remote Sensing Magazine, 9*, 200-231

Jin, X., Zarco-Tejada, P.J., Schmidhalter, U., Reynolds, M.P., Hawkesford, M.J., Varshney, R.K., Yang, T., Nie, C., Li, Z., Ming, B., Xiao, Y., Xie, Y., Li, S. (2021b). High-Throughput Estimation of Crop Traits: A Review of Ground and Aerial Phenotyping Platforms. *IEEE Geoscience and Remote Sensing Magazine, 9*, 200-231

Joalland, S., Screpanti, C., Varella, H.V., Reuther, M., Schwind, M., Lang, C., Walter, A., Liebisch, F. (2018). Aerial and ground based sensing of tolerance to beet cyst nematode in sugar beet. *Remote Sensing, 10*, 787

Jomova, K., Valko, M. (2013). Health protective effects of carotenoids and their interactions with other biological antioxidants. *European Journal of Medicinal Chemistry, 70*, 102-110

Jones, H., Schofield, P. (2008). Thermal and other remote sensing of plant stress. *General and Applied Plant Physiology, 34*, 19-32

Kamilaris, A., Prenafeta-Boldú, F.X. (2018). Deep learning in agriculture: A survey. *Computers and Electronics in Agriculture, 147*, 70-90

Karisto, P., Hund, A., Yu, K., Anderegg, J., Walter, A., Mascher, F., McDonald, B.A., Mikaberidze, A. (2018). Ranking quantitative resistance to Septoria tritici blotch in elite wheat cultivars using automated image analysis. *Phytopathology, 108*, 568-581

Karniadakis, G.E., Kevrekidis, I.G., Lu, L., Perdikaris, P., Wang, S., Yang, L. (2021). Physics-informed machine learning. *Nature Reviews Physics, 3*, 422-440

Kattenborn, T., Fassnacht, F.E., Schmidtlein, S. (2019). Differentiating plant functional types using reflectance: which traits make the difference? *Remote Sensing in Ecology Conservation, 5*, 5-19

Khan, I.H., Liu, H., Li, W., Cao, A., Wang, X., Liu, H., Cheng, T., Tian, Y., Zhu, Y., Cao, W., Yao, X. (2021). Early detection of powdery mildew disease and accurate quantification of its severity using hyperspectral images in wheat. *Remote Sensing, 13*, 3612

Kokaly, R.F., Clark, R.N. (1999). Spectroscopic Determination of Leaf Biochemistry Using Band-Depth Analysis of Absorption Features and Stepwise Multiple Linear Regression. *Remote Sensing of Environment, 67*, 267-287

Kraemer, M.U., Tsui, J.L.-H., Chang, S.Y., Lytras, S., Khurana, M.P., Vanderslott, S., Bajaj, S., Scheidwasser, N., Curran-Sebastian, J.L., Semenova, E. (2025). Artificial intelligence for modelling infectious disease epidemics. *Nature, 638*, 623-635

Kranner, I., Minibayeva, F.V., Beckett, R.P., Seal, C.E. (2010). What is stress? Concepts, definitions and applications in seed science. *New Phytologist, 188*, 655-673

Kruse, F.A., Lefkoff, A.B., Boardman, J.W., Heidebrecht, K.B., Shapiro, A., Barloon, P., Goetz, A.F. (1993). The spectral image processing system (SIPS)—interactive visualization and analysis of imaging spectrometer data. *Remote Sensing of Environment, 44*, 145-163

Kuai, J., Sun, Y., Zhou, M., Zhang, P., Zuo, Q., Wu, J., Zhou, G. (2016). The effect of nitrogen application and planting density on the radiation use efficiency and the stem lignin metabolism in rapeseed (Brassica napus L.). *Field Crops Research, 199*, 89-98

Kumar, R., Hooda, K., Olakh, D., Kaur, H., Malik, V.K., Kumar, S. (2014). Research Article Reaction of QPM inbred lines against Maydish Leaf Blight (MLB) and Charcol Rot. *Electronic Journal of Plant Breeding, 4(4): 1280-1283 (Dec 2013), 4*, 1280-1283

Kurihara, J., Koo, V.-C., Guey, C.W., Lee, Y.P., Abidin, H. (2022). Early detection of basal stem rot disease in oil palm tree using unmanned aerial vehicle-based hyperspectral imaging. *Remote Sensing, 14*, 799

Lacoste, C., Nansen, C., Thompson, S., Moir-Barnetson, L., Mian, A., McNee, M., Flower, K.C. (2015). Increased susceptibility to aphids of flowering wheat plants exposed to low temperatures. *Environmental Entomology, 44*, 610-618

Langenkämper, D., Mogstad, A.A., Hansen, I.M., Baussant, T., Bergsagel, Ø., Nilssen, I., Frost, T.K., Nattkemper, T.W. (2022). Exploring time series of hyperspectral images for cold water coral stress response analysis. *PLoS One, 17*, e0272408

Leach, N., Coops, N.C., Obrknezev, N. (2019). Normalization method for multi-sensor high spatial and temporal resolution satellite imagery with radiometric inconsistencies. *Computers Electronics in Agriculture, 164*, 104893

LeCun, Y., Bengio, Y., Hinton, G. (2015). Deep learning. *Nature, 521*, 436-444

Leong, D., Teo, K., Rangarajan, S., Lopez-Jaramillo, P., Avezum Jr, A., Orlandini, A. (2018). World Population Prospects 2019. Department of Economic and Social Affairs Population Dynamics. New York (NY): United Nations; 2019 (https://population. un. org/wpp/Download/, accessed 20 September 2020). The decade of healthy ageing. Geneva: World Health Organization. *World, 73*, 362k2469

Li, D.-C., Liu, C.-W., Hu, S.C. (2011). A fuzzy-based data transformation for feature extraction to increase classification performance with small medical data sets. *Artificial Intelligence in Medicine, 52*, 45-52

Li, X., Lee, W.S., Li, M., Ehsani, R., Mishra, A.R., Yang, C., Mangan, R.L. (2012). Spectral difference analysis and airborne imaging classification for citrus greening infected trees. *Computers and Electronics in Agriculture, 83*, 32-46

Li, Y., Yan, W., An, S., Gao, W., Jia, J., Tao, S., Wang, W. (2023). A Spatio-Temporal Fusion Framework of UAV and Satellite Imagery for Winter Wheat Growth Monitoring. *Drones, 7*, 23

Li, Y., Yang, K., Han, Q., Gao, W., Zhang, J., Wu, B. (2021). A new method that combines spectral indexes and Naive Bayes to distinguish heavy metal pollution in crops. *Remote Sensing Letters, 12*, 666-673

Li, Z., Ma, X., Xin, H. (2017). Feature engineering of machine-learning chemisorption models for catalyst design. *Catalysis Today, 280*, 232-238

Lin, F., Guo, S., Tan, C., Zhou, X., Zhang, D. (2020). Identification of rice sheath blight through

spectral responses using hyperspectral images. *Sensors, 20*, 6243

Liu, F., Xiao, Z. (2020). Disease spots identification of potato leaves in hyperspectral based on locally adaptive 1D-CNN. In, *2020 IEEE International Conference on Artificial Intelligence and Computer Applications (ICAICA)* (pp. 355-358)

Liu, H., Guo, F., Chen, X., Wu, B.M. (2022). Temporal Progress and Spatial Patterns of Northern Corn Leaf Blight in Corn Fields in China. *Phytopathology®, 112*, 1936-1945

Liu, J., Wang, X., Chen, Q. (2025). A Lightweight Framework for Protected Vegetable Disease Detection in Complex Scenes. *Food Science Nutrition, 13*, e70200

Liu, L., Dong, Y., Huang, W., Du, X., Ma, H. (2020a). Monitoring Wheat Fusarium Head Blight Using Unmanned Aerial Vehicle Hyperspectral Imagery. *Remote Sensing, 12*, 3811

Liu, L., Zhou, W., Guan, K., Peng, B., Xu, S., Tang, J., Zhu, Q., Till, J., Jia, X., Jiang, C., Wang, S., Qin, Z., Kong, H., Grant, R., Mezbahuddin, S., Kumar, V., Jin, Z. (2024a). Knowledge-guided machine learning can improve carbon cycle quantification in agroecosystems. *Nat Commun, 15*, 357

Liu, L.Y., Dong, Y.Y., Huang, W.J., Du, X.P., Ren, B.Y., Huang, L.S., Zheng, Q., Ma, H.Q. (2020b). A disease index for efficiently detecting wheat fusarium head blight using sentinel-2 multispectral imagery. *IEEE Access, 8*, 52181-52191

Liu, M., Zhang, Z., Liu, X., Yao, J., Du, T., Ma, Y., Shi, L. (2020c). Discriminant Analysis of the Damage Degree Caused by Pine Shoot Beetle to Yunnan Pine Using UAV-Based Hyperspectral Images. *Forests, 11*, 1258

Liu, R., Jia, K., Li, H., Zhang, J. (2024b). Using Unmanned Aerial Vehicle Data to Improve Satellite Inversion: A Study on Soil Salinity. *Land, 13*, 1438

Liu, X., Liu, L., Hu, J., Guo, J., Du, S. (2020d). Improving the potential of red SIF for estimating GPP by downscaling from the canopy level to the photosystem level. *Agricultural and Forest Meteorology, 281*, 107846

Liu, Z., Qi, J., Wang, N., Zhu, Z., Luo, J., Liu, L., Tang, J., Cheng, J. (2018). Hyperspectral discrimination of foliar biotic damages in rice using principal component analysis and probabilistic neural network. *Precision Agriculture, 19*, 973-991

Llanes, A., Andrade, A., Alemano, S., Luna, V. (2018). Metabolomic approach to understand plant adaptations to water and salt stress. *Plant metabolites and regulation under environmental stress* (pp. 133-144): Elsevier

Loey, M., ElSawy, A., Afify, M. (2020). Deep Learning in Plant Diseases Detection for Agricultural Crops. *International Journal of Service Science, Management, Engineering, and Technology, 11*, 41-58

Loladze, A., Rodrigues, F.A., Toledo, F., San Vicente, F., Gérard, B., Boddupalli, M.P. (2019). Application of Remote Sensing for Phenotyping Tar Spot Complex Resistance in Maize. *Frontiers in Plant Science, Volume 10 - 2019*, 00552

Lopez-Lopez, M., Calderon, R., Gonzalez-Dugo, V., Zarco-Tejada, P.J., Fereres, E. (2016). Early detection and quantification of almond red leaf blotch using high-resolution hyperspectral and thermal imagery. *Remote Sensing, 8*, 276

Lu, Y., Xu, K., Zhang, L., Deguchi, M., Shishido, H., Arie, T., Pan, R., Hayashi, A., Shen, L., Akita, S.J.A.n. (2020). Multimodal plant healthcare flexible sensor system. *ACS Nano, 14*, 10966-10975

Luo, L., Chang, Q., Wang, Q., Huang, Y. (2021). Identification and severity monitoring of maize dwarf mosaic virus infection based on hyperspectral measurements. *Remote Sensing, 13*, 4560

Ma, L., Liu, Y., Zhang, X., Ye, Y., Yin, G., Johnson, B.A. (2019). Deep learning in remote sensing applications: A meta-analysis and review. *ISPRS Journal of Photogrammetry and Remote Sensing, 152*, 166-177

Machwitz, M., Pieruschka, R., Berger, K., Schlerf, M., Aasen, H., Fahrner, S., Jiménez-Berni, J., Baret, F., Rascher, U. (2021). Bridging the Gap Between Remote Sensing and Plant Phenotyping—Challenges and Opportunities for the Next Generation of Sustainable Agriculture. *Frontiers in Plant Science, 12*

Madden, L., Hughes, G., Moraes, W.B., Xu, X.-M., Turechek, W. (2018). Twenty-five years of the binary power law for characterizing heterogeneity of disease incidence. *Phytopathology, 108*, 656-680

Mahlein, A.-K., Alisaac, E., Al Masri, A., Behmann, J., Dehne, H.-W., Oerke, E.-C. (2019). Comparison and combination of thermal, fluorescence, and hyperspectral imaging for monitoring fusarium head blight of wheat on spikelet scale. *Sensors, 19*, 2281

Mahlein, A.-K., Steiner, U., Hillnhuetter, C., Dehne, H.-W., Oerke, E.-C. (2012). Hyperspectral imaging for small-scale analysis of symptoms caused by different sugar beet diseases. *Plant Methods, 8*

Mahlein, A.K., Kuska, M.T., Behmann, J., Polder, G., Walter, A. (2018). Hyperspectral Sensors and Imaging Technologies in Phytopathology: State of the Art. In J.E. Leach, & S.E. Lindow (Eds.), *Annual Review of Phytopathology* (pp. 535-558)

Mahlein, A.K., Rumpf, T., Welke, P., Dehne, H.W., Pluemer, L., Steiner, U., Oerke, E.C. (2013). Development of spectral indices for detecting and identifying plant diseases. *Remote Sensing of Environment, 128*, 21-30

Mahlein, A.K., Steiner, U., Dehne, H.W., Oerke, E.C. (2010). Spectral signatures of sugar beet leaves for the detection and differentiation of diseases. *Precision Agriculture, 11*, 413-431

Malamiri, H.R.G., Aliabad, F.A., Shojaei, S., Morad, M., Band, S.S. (2021). A study on the use of UAV images to improve the separation accuracy of agricultural land areas. *Computers Electronics in Agriculture, 184*, 106079

Malenovský, Z., Mishra, K.B., Zemek, F., Rascher, U., Nedbal, L. (2009). Scientific and technical challenges in remote sensing of plant canopy reflectance and fluorescence. *Journal of Experimental Botany, 60*, 2987-3004

Marshall, M., Thenkabail, P., Biggs, T., Post, K. (2016). Hyperspectral narrowband and multispectral broadband indices for remote sensing of crop evapotranspiration and its components (transpiration and soil evaporation). *Agricultural and Forest Meteorology, 218-219*, 122-134

Martinelli, F., Scalenghe, R., Davino, S., Panno, S., Scuderi, G., Ruisi, P., Villa, P., Stroppiana, D., Boschetti, M., Goulart, L.R., Davis, C.E., Dandekar, A.M. (2015). Advanced methods of plant disease detection: a review. *Agronomy for Sustainable Development, 35*, 1-25

Martinez, E.L., Fernandez, F.J.B. (2019). Chapter 4 - Economics of Production, Marketing and Utilization. In S.O. Serna-Saldivar (Ed.), *Corn (Third Edition)* (pp. 87-107). Oxford: AACC International Press

Marzougui, A., Ma, Y., Zhang, C., McGee, R.J., Coyne, C.J., Main, D., Sankaran, S. (2019). Advanced imaging for quantitative evaluation of aphanomyces root rot resistance in lentil. *Frontiers in Plant Science, 10*, 383

Maschler, J., Atzberger, C., Immitzer, M. (2018). Individual Tree Crown Segmentation and Classification of 13 Tree Species Using Airborne Hyperspectral Data. *Remote Sensing, 10*, 1218

Mazzia, V., Comba, L., Khaliq, A., Chiaberge, M., Gay, P. (2020). UAV and machine learning based

refinement of a satellite-driven vegetation index for precision agriculture. *Sensors, 20*, 2530

Meng, R., Lv, Z., Yan, J., Chen, G., Zhao, F., Zeng, L., Xu, B. (2020). Development of spectral disease indices for southern corn rust detection and severity classification. *Remote Sensing, 12*, 3233

Meroni, M., Busetto, L., Colombo, R., Guanter, L., Moreno, J., Verhoef, W. (2010). Performance of spectral fitting methods for vegetation fluorescence quantification. *Remote Sensing of Environment, 114*, 363-374

Merzlyak, M.N., Gitelson, A.A., Chivkunova, O.B., Rakitin, V.Y. (1999). Non-destructive optical detection of pigment changes during leaf senescence and fruit ripening. *Physiologia Plantarum, 106*, 135-141

Mikaberidze, A., Cruz, C., Zerihun, A., Barreto, A., Beck, P., Calderón, R., Camino, C., Campbell, R.E., Delalieux, S.K., Fabre, F. (2025). Opportunities and challenges in combining optical sensing and epidemiological modelling. *Phytopathology*

Minhas, P.S., Rane, J., Pasala, R.K. (2017). Abiotic Stresses in Agriculture: An Overview. In P.S. Minhas, J. Rane, & R.K. Pasala (Eds.), *Abiotic Stress Management for Resilient Agriculture* (pp. 3-8). Singapore: Springer Singapore

Minogue, K., Fry, W. (1983). Models for the spread of disease: model description. *Phytopathology, 73*, 1168-1173

Mishra, P., Polder, G., Vilfan, N. (2020). Close Range Spectral Imaging for Disease Detection in Plants Using Autonomous Platforms: a Review on Recent Studies. *Current Robotics Reports, 1*, 43-48

Morkunas, I., Woźniak, A., Mai, V.C., Rucińska-Sobkowiak, R., Jeandet, P. (2018). The role of heavy metals in plant response to biotic stress. In, *Molecules* (p. 2320)

Mou, L., Saha, S., Hua, Y., Bovolo, F., Bruzzone, L., Zhu, X.X. (2022). Deep Reinforcement Learning for Band Selection in Hyperspectral Image Classification. *IEEE Transactions on Geoscience and Remote Sensing, 60*

Moya, I., Cerovic, Z.G. (2004). Remote sensing of chlorophyll fluorescence: instrumentation and analysis. In G.C. Papageorgiou, & Govindjee (Eds.), *Chlorophyll a Fluorescence: A Signature of Photosynthesis* (pp. 429-445). Dordrecht: Springer Netherlands

Mwinuka, P.R., Mourice, S.K., Mbungu, W.B., Mbilinyi, B.P., Tumbo, S.D., Schmitter, P. (2022). UAV-based multispectral vegetation indices for assessing the interactive effects of water and nitrogen in irrigated horticultural crops production under tropical sub-humid conditions: A case of African eggplant. *Agricultural Water Management, 266*, 107516

Ngoko, Z., Cardwell, K., Marasas, W., Wingfield, M., Ndemah, R., Schulthess, F. (2002). Biological and physical constraints on maize production in the Humid Forest and Western Highlands of Cameroon. *European Journal of Plant Pathology, 108*, 893-902

Nguyen, C., Sagan, V., Maimaitiyiming, M., Maimaitijiang, M., Bhadra, S., Kwasniewski, M.T. (2021). Early detection of plant viral disease using hyperspectral imaging and deep learning. *Sensors, 21*, 742

Nie, C., Shi, L., Li, Z., Xu, X., Yin, D., Li, S., Jin, X. (2023). A comparison of methods to estimate leaf area index using either crop-specific or generic proximal hyperspectral datasets. *European Journal of Agronomy, 142*, 126664

Nkwocha, C.L., Chandel, A.K. (2025). Towards an End-to-End Digital Framework for Precision Crop Disease Diagnosis and Management Based on Emerging Sensing and Computing Technologies: State over Past Decade and Prospects. *Computers*

Nutter, F.W., Esker, P.D., Netto, R.A.C. (2006). Disease assessment concepts and the advancements made in improving the accuracy and precision of plant disease data. *European Journal of Plant Pathology, 115*, 95-103

Oerke, E.-C., Herzog, K., Toepfer, R. (2016). Hyperspectral phenotyping of the reaction of grapevine genotypes to Plasmopara viticola. *Journal of Experimental Botany, 67*, 5529-5543

Oerke, E.C. (2020). Remote Sensing of Diseases. *Annual Review of Phytopathology, 58*, 225-252

Osco, L.P., Junior, J.M., Ramos, A.P.M., de Castro Jorge, L.A., Fatholahi, S.N., de Andrade Silva, J., Matsubara, E.T., Pistori, H., Gonçalves, W.N., Li, J. (2021). A review on deep learning in UAV remote sensing. *International Journal of Applied Earth Observation Geoinformation, 102*, 102456

Osdaghi, E., Young, A.J., Harveson, R.M. (2020). Bacterial wilt of dry beans caused by Curtobacterium flaccumfaciens pv. flaccumfaciens: a new threat from an old enemy. *Molecular Plant Pathology, 21*, 605-621

Ouyang, Z.-T., Gao, Y., Xie, X., Guo, H.-Q., Zhang, T.-T., Zhao, B. (2013). Spectral discrimination of the invasive plant Spartina alterniflora at multiple phenological stages in a saltmarsh wetland. *PLoS One, 8*, e67315

Paini, D.R., Sheppard, A.W., Cook, D.C., De Barro, P.J., Worner, S.P., Thomas, M.B. (2016). Global threat to agriculture from invasive species. *Proceedings of the National Academy of Sciences of the United States of America, 113*, 7575-7579

Pan, S.J., Yang, Q. (2010). A Survey on Transfer Learning. *IEEE Transactions on Knowledge and Data Engineering, 22*, 1345-1359

Pan, W., Liu, N.N., Xiang, E.W., Yang, Q. (2011). Transfer learning to predict missing ratings via heterogeneous user feedbacks. In, *Proceedings of the Twenty-Second International Joint Conference on Artificial Intelligence, Barcelona, Catalonia, Spain* (p. 2318)

Parnell, S., Gottwald, T., Irey, M., Luo, W., Van Den Bosch, F. (2011). A stochastic optimization method to estimate the spatial distribution of a pathogen from a sample. *Phytopathology, 101*, 1184-1190

Paux, E., Lafarge, S., Balfourier, F., Derory, J., Charmet, G., Alaux, M., Perchet, G., Bondoux, M., Frederic, B., Barillot, R., Ravel, C., Sourdille, P., Gouis, J. (2022). Breeding for Economically and Environmentally Sustainable Wheat Varieties: An Integrated Approach from Genomics to Selection. *Biology, 11*, 149

Penuelas, J., Baret, F., Filella, I. (1995). Semi-empirical indices to assess carotenoids/chlorophyll a ratio from leaf spectral reflectance. *Photosynthetica, 31*, 221-230

Peters, R.D., Noble, S.D. (2024). A new dataset of leaf optical traits to include biophysical parameters in addition to spectral and biochemical assessment. *Remote Sensing of Environment, 315*, 114424

Plascyk, J.A., Gabriel, F.C. (1975). The fraunhofer line discriminator mkii-an airborne instrument for precise and standardized ecological luminescence measurement. *IEEE Transactions on Instrumentation and Measurement, 24*, 306-313

Poblete, T., Camino, C., Beck, P.S.A., Hornero, A., Kattenborn, T., Saponari, M., Boscia, D., Navas-Cortes, J.A., Zarco-Tejada, P.J. (2020). Detection of Xylella fastidiosa infection symptoms with airborne multispectral and thermal imagery: Assessing bandset reduction performance from hyperspectral analysis. *ISPRS Journal of Photogrammetry and Remote Sensing, 162*, 27-40

Poblete, T., Navas-Cortes, J.A., Camino, C., Calderon, R., Hornero, A., Gonzalez-Dugo, V., Landa, B.B., Zarco-Tejada, P.J. (2021). Discriminating Xylella fastidiosa from Verticillium dahliae infections in

olive trees using thermal- and hyperspectral-based plant traits. *ISPRS Journal of Photogrammetry and Remote Sensing, 179*, 133-144

Poblete, T., Navas-Cortes, J.A., Hornero, A., Camino, C., Calderon, R., Hernandez-Clemente, R., Landa, B.B., Zarco-Tejada, P.J. (2023a). Detection of symptoms induced by vascular plant pathogens in tree crops using high-resolution satellite data: Modelling and assessment with airborne hyperspectral imagery. *Remote Sensing of Environment, 295*, 113698

Poblete, T., Navas-Cortes, J.A., Hornero, A., Camino, C., Calderon, R., Hernández-Clemente, R., Landa, B.B., Zarco-Tejada, P.J. (2023b). Detection of symptoms induced by vascular plant pathogens in tree crops using high-resolution satellite data: Modelling and assessment with airborne hyperspectral imagery. *Remote Sensing of Environment, 295*, 113698

Prabhakar, M., Prasad, Y.G., Desai, S., Thirupathi, M., Gopika, K., Rao, G.R., Venkateswarlu, B. (2013). Hyperspectral remote sensing of yellow mosaic severity and associated pigment losses in Vigna mungo using multinomial logistic regression models. *Crop Protection, 45*, 132-140

Prins, A.J., Van Niekerk, A. (2021). Crop type mapping using LiDAR, Sentinel-2 and aerial imagery with machine learning algorithms. *Geo-spatial Information Science, 24*, 215-227

Qi, J., Jiang, J., Zhou, K., Xie, D., Huang, H. (2023). Fast and accurate simulation of canopy reflectance under wavelength-dependent optical properties using a semi-empirical 3d radiative transfer model. *Journal of Remote Sensing, 3*, 0017

Qi, J., Xie, D., Yin, T., Yan, G., Gastellu-Etchegorry, J.-P., Li, L., Zhang, W., Mu, X., Norford, L.K. (2019). LESS: LargE-Scale remote sensing data and image simulation framework over heterogeneous 3D scenes. *Remote Sensing of Environment, 221*, 695-706

Qin, G.X., Wu, J., Li, C.B., Meng, Z.Y. (2024). Comparison of the hybrid of radiative transfer model and machine learning methods in leaf area index of grassland mapping. *Theoretical and Applied Climatology, 155*, 2757-2773

Qin, J., Wang, B., Wu, Y., Lu, Q., Zhu, H. (2021). Identifying Pine Wood Nematode Disease Using UAV Images and Deep Learning Algorithms. *Remote Sensing, 13*, 162

Ranum, P., Pena-Rosas, J.P., Garcia-Casal, M.N. (2014). Global maize production, utilization, and consumption. *Annals of the New York Academy of Sciences, 1312*, 105-112

Reichstein, M., Beer, C. (2008). Soil respiration across scales: The importance of a model–data integration framework for data interpretation. *Journal of Plant Nutrition Soil Science, 171*, 344-354

Reichstein, M., Camps-Valls, G., Stevens, B., Jung, M., Denzler, J., Carvalhais, N., Prabhat (2019). Deep learning and process understanding for data-driven Earth system science. *Nature, 566*, 195-204

Reisig, D.D., Godfrey, L.D. (2010). Remotely sensing arthropod and nutrient stressed plants: a case study with nitrogen and cotton aphid (hemiptera: aphididae). *Environmental Entomology, 39*, 1255-1263

Rembold, F., Carnicelli, S., Nori, M., Ferrari, G.A. (2000). Use of aerial photographs, Landsat TM imagery and multidisciplinary field survey for land-cover change analysis in the lakes region (Ethiopia). *International Journal of Applied Earth Observation, 2*, 181-189

Ren, Y., Huang, W., Ye, H., Zhou, X., Ma, H., Dong, Y., Shi, Y., Geng, Y., Huang, Y., Jiao, Q., Xie, Q. (2021a). Quantitative identification of yellow rust in winter wheat with a new spectral index: Development and validation using simulated and experimental data. *International Journal of Applied Earth Observation and Geoinformation, 102*

Ren, Y., Ye, H.C., Huang, W.J., Ma, H.Q., Guo, A.T., Ruan, C., Liu, L.Y., Qian, B.X. (2021b). A new

spectral index for the quantitative identification of yellow rust using fungal spore information. *Big Earth Data, 5*, 201-216

Revill, A., Florence, A., MacArthur, A., Hoad, S., Rees, R., Williams, M. (2020). Quantifying Uncertainty and Bridging the Scaling Gap in the Retrieval of Leaf Area Index by Coupling Sentinel-2 and UAV Observations. In, *Remote Sensing*

Reynolds, D., Baret, F., Welcker, C., Bostrom, A., Ball, J., Cellini, F., Lorence, A., Chawade, A., Khafif, M., Noshita, K., Mueller-Linow, M., Zhou, J., Tardieu, F. (2019). What is cost-efficient phenotyping? Optimizing costs for different scenarios. *Plant Science, 282*, 14-22

Reynolds, G.J., Windels, C.E., MacRae, I.V., Laguette, S. (2012). Remote sensing for assessing rhizoctonia crown and root rot severity in sugar beet. *Plant Disease, 96*, 497-505

Richardson, A.D., Hufkens, K., Milliman, T., Aubrecht, D.M., Chen, M., Gray, J.M., Johnston, M.R., Keenan, T.F., Klosterman, S.T., Kosmala, M. (2018). Tracking vegetation phenology across diverse North American biomes using PhenoCam imagery. *Scientific Data, 5*, 1-24

Rocha, A.D., Groen, T.A., Skidmore, A.K. (2019). Spatially-explicit modelling with support of hyperspectral data can improve prediction of plant traits. *Remote Sensing of Environment, 231*, 111200

Rouse, J.W., Haas, R.H., Schell, J.A., Deering, D.W. (1974). Monitoring vegetation systems in the Great Plains with ERTS. *NASA Special Publication, 351*, 309

Saubin, M., De Mita, S., Zhu, X., Sudret, B., Halkett, F. (2021). Impact of ploidy and pathogen life cycle on resistance durability. *Peer Community Journal, 1*

Schütt, K.T., Arbabzadah, F., Chmiela, S., Müller, K.R., Tkatchenko, A. (2017). Quantum-chemical insights from deep tensor neural networks. *Nature Communications, 8*, 13890

Shahi, T.B., Xu, C.-Y., Neupane, A., Guo, W. (2023). Recent Advances in Crop Disease Detection Using UAV and Deep Learning Techniques. *Remote Sensing, 15*, 2450

Sheenam, S., Khattar, S., Verma, T. (2023). Automated wheat plant disease detection using deep learning: a multi-class classification approach. In, *2023 3rd International Conference on Intelligent Technologies (CONIT)* (pp. 1-5): IEEE

Shi, Y., Huang, W., Zhou, X. (2017). Evaluation of wavelet spectral features in pathological detection and discrimination of yellow rust and powdery mildew in winter wheat with hyperspectral reflectance data. *Journal of Applied Remote Sensing, 11*, 026025

Singh, V., Sharma, N., Singh, S. (2020). A review of imaging techniques for plant disease detection. *Artificial Intelligence in Agriculture, 4*, 229-242

Skoneczny, H., Kubiak, K., Spiralski, M., Kotlarz, J. (2020). Fire blight disease detection for apple trees: hyperspectral analysis of healthy, infected and dry leaves. *Remote Sensing, 12*, 2101

Sterling, A., Di Rienzo, J.A. (2022). Prediction of south american leaf blight and disease-induced photosynthetic changes in rubber tree, using machine learning techniques on leaf hyperspectral reflectance. *Plants, 11*, 329

Stuckens, J., Verstraeten, W.W., Delalieux, S., Swennen, R., Coppin, P. (2009). A dorsiventral leaf radiative transfer model: Development, validation and improved model inversion techniques. *Remote Sensing of Environment, 113*, 2560-2573

Stutsel, B., Johansen, K., Malbéteau, Y.M., McCabe, M.F. (2021). Detecting plant stress using thermal and optical imagery from an unoccupied aerial vehicle. *Frontiers in Plant Science, 12*, 734944

Sun, L., Wang, W., Jia, C., Liu, X. (2021a). Leaf area index remote sensing based on Deep Belief

Network supported by simulation data. *International Journal of Remote Sensing, 42*, 7637-7661

Sun, Q., Li, L., Guo, F., Zhang, K., Dong, J., Luo, Y., Ma, Z. (2021b). Southern corn rust caused by Puccinia polysora Underw: a review. *Phytopathology Research, 3*, 25

Suzuki, N., Rivero, R.M., Shulaev, V., Blumwald, E., Mittler, R. (2014). Abiotic and biotic stress combinations. *New Phytologist, 203*, 32-43

Tehon, L., Daniels, E. (1925). Notes on the parasitic fungi of Illinois—II. *Mycologia, 17*, 240-249

Terentev, A., Dolzhenko, V., Fedotov, A., Eremenko, D. (2022a). Current state of hyperspectral remote sensing for early plant disease detection: a review. *Sensors, 22*, 757

Terentev, A., Dolzhenko, V., Fedotov, A., Eremenko, D. (2022b). Current state of hyperspectral remote sensing for early plant disease detection: a review*, 22*, 757

Thenkabail, P.S., Enclona, E.A., Ashton, M.S., Van Der Meer, B. (2004). Accuracy assessments of hyperspectral waveband performance for vegetation analysis applications. *Remote Sensing of Environment, 91*, 354-376

Thenkabail, P.S., Smith, R.B., De Pauw, E. (2000). Hyperspectral vegetation indices and their relationships with agricultural crop characteristics. *Remote Sensing of Environment, 71*, 158-182

Thomas, S., Kuska, M.T., Bohnenkamp, D., Brugger, A., Alisaac, E., Wahabzada, M., Behmann, J., Mahlein, A.-K. (2018). Benefits of hyperspectral imaging for plant disease detection and plant protection: a technical perspective. *Journal of Plant Diseases and Protection, 125*, 5-20

Tian, L., Wang, Z., Xue, B., Li, D., Zheng, H., Yao, X., Zhu, Y., Cao, W., Cheng, T. (2023). A disease-specific spectral index tracks Magnaporthe oryzae infection in paddy rice from ground to space. *Remote Sensing of Environment, 285*, 113384

Tian, L., Xue, B., Wang, Z., Li, D., Yao, X., Cao, Q., Zhu, Y., Cao, W., Cheng, T. (2021). Spectroscopic detection of rice leaf blast infection from asymptomatic to mild stages with integrated machine learning and feature selection. *Remote Sensing of Environment, 257*, 112350

van der Tol, C., Rossini, M., Cogliati, S., Verhoef, W., Colombo, R., Rascher, U., Mohammed, G. (2016). A model and measurement comparison of diurnal cycles of sun-induced chlorophyll fluorescence of crops. *Remote Sensing of Environment, 186*, 663-677

van der Tol, C., Verhoef, W., Timmermans, J., Verhoef, A., Su, Z. (2009). An integrated model of soil-canopy spectral radiances, photosynthesis, fluorescence, temperature and energy balance. *Biogeosciences, 6*, 3109-3129

Vanegas, F., Bratanov, D., Powell, K., Weiss, J., Gonzalez, F. (2018). A Novel Methodology for Improving Plant Pest Surveillance in Vineyards and Crops Using UAV-Based Hyperspectral and Spatial Data. *Sensors, 18*

Vaswani, A. (2017). Attention is all you need. *Advances in neural information processing systems*

Vergara-Diaz, O., Kefauver, S.C., Elazab, A., Nieto-Taladriz, M.T., Araus, J.L. (2015). Grain yield losses in yellow-rusted durum wheat estimated using digital and conventional parameters under field conditions. *The Crop Journal, 3*, 200-210

Verrelst, J., Camps-Valls, G., Muñoz-Marí, J., Rivera, J.P., Veroustraete, F., Clevers, J.G.P.W., Moreno, J. (2015). Optical remote sensing and the retrieval of terrestrial vegetation bio-geophysical properties – A review. *ISPRS Journal of Photogrammetry and Remote Sensing, 108*, 273-290

Verrelst, J., Rivera-Caicedo, J.P., Reyes-Muñoz, P., Morata, M., Amin, E., Tagliabue, G., Panigada, C., Hank, T., Berger, K. (2021). Mapping landscape canopy nitrogen content from space using PRISMA data.

ISPRS Journal of Photogrammetry and Remote Sensing, 178, 382-395

Viera-Torres, M., Sinde-Gonzalez, I., Gil-Docampo, M., Bravo-Yandun, V., Toulkeridis, T. (2020). Generating the baseline in the early detection of bud rot and red ring disease in oil palms by geospatial technologies. *Remote Sensing, 12*, 3229

Virlet, N., Sabermanesh, K., Sadeghi-Tehran, P., Hawkesford, M.J. (2016). Field Scanalyzer: An automated robotic field phenotyping platform for detailed crop monitoring. *Functional Plant Biology, 44*, 143-153

Wahabzada, M., Mahlein, A.-K., Bauckhage, C., Steiner, U., Oerke, E.-C., Kersting, K. (2016). Plant Phenotyping using Probabilistic Topic Models: Uncovering the Hyperspectral Language of Plants. *Scientific Reports, 6*

Wang, D., Vinson, R., Holmes, M., Seibel, G., Bechar, A., Nof, S., Tao, Y. (2019). Early detection of tomato spotted wilt virus by hyperspectral imaging and outlier removal auxiliary classifier generative adversarial nets (OR-AC-GAN). *Scientific Reports, 9*, 4377

Wang, J., Shi, L., Fu, Y., Si, H., Liu, Y., Qiao, H. (2023a). Mapping Wheat Take-All Disease Levels from Airborne Hyperspectral Images Using Radiative Transfer Models. *Remote Sensing, 15*

Wang, S., Guan, K., Zhang, C., Jiang, C., Zhou, Q., Li, K., Qin, Z., Ainsworth, E.A., He, J., Wu, J., Schaefer, D., Gentry, L.E., Margenot, A.J., Herzberger, L. (2023b). Airborne hyperspectral imaging of cover crops through radiative transfer process-guided machine learning. *Remote Sensing of Environment, 285*, 113386

Ward, J.M., Stromberg, E.L., Nowell, D.C., Nutter Jr, F.W. (1999). Gray leaf spot: a disease of global importance in maize production. *Plant Disease, 83*, 884-895

Warrens, M.J. (2012). Some Paradoxical Results for the Quadratically Weighted Kappa. *Psychometrika, 77*, 315-323

Weiss, M., Jacob, F., Duveiller, G. (2020). Remote sensing for agricultural applications: A meta-review. *Remote Sensing of Environment, 236*, 111402

Wilson, P.D., Sagan, C. (1995). Spectrophotometry and organic matter on Iapetus: 1. Composition models. *Journal of Geophysical Research: Planets, 100*, 7531-7537

Woodhouse, I.H. (2006). Predicting backscatter-biomass and height-biomass trends using a macroecology model. *IEEE Transactions on Geoscience remote sensing, 44*, 871-877

Wu, B., Liang, A., Zhang, H., Zhu, T., Zou, Z., Yang, D., Tang, W., Li, J., Su, J. (2021). Application of conventional UAV-based high-throughput object detection to the early diagnosis of pine wilt disease by deep learning. *Forest Ecology and Management, 486*, 118986

Wu, C., Niu, Z., Tang, Q., Huang, W. (2008). Estimating chlorophyll content from hyperspectral vegetation indices: Modeling and validation. *Agricultural and Forest Meteorology, 148*, 1230-1241

Xia, T., Zhang, C., Yang, K., Fu, P., Wang, M. (2022). Application of an innovative narrow band vegetation index to corn leaves to explore the characteristics of corn spectra under Cu2+stress. *Remote Sensing Letters, 13*, 579-587

Xiao, Y., Dong, Y., Huang, W., Liu, L., Ma, H. (2021). Wheat fusarium head blight detection using uav-based spectral and texture features in optimal window size. *Remote Sensing, 13*, 2437

Xu, X., He, P., Zhang, J., Pampolino, M.F., Johnston, A.M., Zhou, W. (2017). Spatial variation of attainable yield and fertilizer requirements for maize at the regional scale in China. *Field Crops Research, 203*, 8-15

References

Xuan, G., Li, Q., Shao, Y., Shi, Y. (2022). Early diagnosis and pathogenesis monitoring of wheat powdery mildew caused by blumeria graminis using hyperspectral imaging. *Computers and Electronics in Agriculture, 197*, 106921

Xue, B., Tian, L., Wang, Z., Wang, X., Yao, X., Zhu, Y., Cao, W., Cheng, T. (2023). Quantification of rice spikelet rot disease severity at organ scale with proximal imaging spectroscopy. *Precision Agriculture, 24*, 1049-1071

Yan, J., Tan, B.C. (2019). Maize biology: From functional genomics to breeding application. *J Integr Plant Biol, 61*, 654-657

Yan, Y., Deng, L., Liu, X., Zhu, L. (2019). Application of UAV-based multi-angle hyperspectral remote sensing in fine vegetation classification. *Remote Sensing, 11*, 2753

Yang, K., Ryu, Y., Dechant, B., Berry, J.A., Hwang, Y., Jiang, C., Kang, M., Kim, J., Kimm, H., Kornfeld, A., Yang, X. (2018). Sun-induced chlorophyll fluorescence is more strongly related to absorbed light than to photosynthesis at half-hourly resolution in a rice paddy. *Remote Sensing of Environment, 216*, 658-673

Yang, P. (2022). Exploring the interrelated effects of soil background, canopy structure and sun-observer geometry on canopy photochemical reflectance index. *Remote Sensing of Environment, 279*, 113133

Yu, K., Anderegg, J., Mikaberidze, A., Karisto, P., Mascher, F., McDonald, B.A., Walter, A., Hund, A. (2018). Hyperspectral canopy sensing of wheat septoria tritici blotch disease. *Frontiers in Plant Science, 9*, 1195

Yu, R., Li, S., Zhang, B., Zhang, H. (2022). A Deep Transfer Learning Method for Estimating Fractional Vegetation Cover of Sentinel-2 Multispectral Images. *IEEE Geoscience and Remote Sensing Letters, 19*

Yu, R., Luo, Y., Zhou, Q., Zhang, X., Wu, D., Ren, L. (2021a). A machine learning algorithm to detect pine wilt disease using UAV-based hyperspectral imagery and LiDAR data at the tree level. *International Journal of Applied Earth Observation and Geoinformation, 101*, 102363

Yu, R., Luo, Y.Q., Li, H.A., Yang, L.Y., Huang, H.G., Yu, L.F., Ren, L.L. (2021b). Three-Dimensional Convolutional Neural Network Model for Early Detection of Pine Wilt Disease Using UAV-Based Hyperspectral Images. *Remote Sensing, 13*, 22

Yuan, L., Pu, R.L., Zhang, J.C., Wang, J.H., Yang, H. (2016). Using high spatial resolution satellite imagery for mapping powdery mildew at a regional scale. *Precision Agriculture, 17*, 332-348

Zarco-Tejada, P.J., Berjon, A., Lopez-Lozano, R., Miller, J.R., Martin, P., Cachorro, V., Gonzalez, M.R., de Frutos, A. (2005). Assessing vineyard condition with hyperspectral indices: Leaf and canopy reflectance simulation in a row-structured discontinuous canopy. *Remote Sensing of Environment, 99*, 271-287

Zarco-Tejada, P.J., Camino, C., Beck, P.S.A., Calderon, R., Hornero, A., Hernandez-Clemente, R., Kattenborn, T., Montes-Borrego, M., Susca, L., Morelli, M., Gonzalez-Dugo, V., North, P.R.J., Landa, B.B., Boscia, D., Saponari, M., Navas-Cortes, J.A. (2018). Previsual symptoms of Xylella fastidiosa infection revealed in spectral plant-trait alterations. *Nature Plants, 4*, 432-439

Zarco-Tejada, P.J., González-Dugo, V., Berni, J.A.J. (2012). Fluorescence, temperature and narrow-band indices acquired from a UAV platform for water stress detection using a micro-hyperspectral imager and a thermal camera. *Remote Sensing of Environment, 117*, 322-337

Zarco-Tejada, P.J., González-Dugo, V., Williams, L.E., Suárez, L., Berni, J.A.J., Goldhamer, D., Fereres, E. (2013). A PRI-based water stress index combining structural and chlorophyll effects: Assessment using diurnal narrow-band airborne imagery and the CWSI thermal index. *Remote Sensing of Environment, 138*, 38-50

Zarco-Tejada, P.J., Poblete, T., Camino, C., Gonzalez-Dugo, V., Calderon, R., Hornero, A., Hernandez-Clemente, R., Roman-ecija, M., Velasco-Amo, M.P., Landa, B.B., Beck, P.S.A., Saponari, M., Boscia, D., Navas-Cortes, J.A. (2021). Divergent abiotic spectral pathways unravel pathogen stress signals across species. *Nature Communications, 12*, 6088

Zeng, T., Wang, Y., Yang, Y., Liang, Q., Fang, J., Li, Y., Zhang, H., Fu, W., Wang, J., Zhang, X. (2024). Early detection of rubber tree powdery mildew using UAV-based hyperspectral imagery and deep learning. *Computers Electronics in Agriculture, 220*, 108909

Zeng, Y., Hao, D., Huete, A., Dechant, B., Berry, J., Chen, J.M., Joiner, J., Frankenberg, C., Bond-Lamberty, B., Ryu, Y., Xiao, J., Asrar, G.R., Chen, M. (2022). Optical vegetation indices for monitoring terrestrial ecosystems globally. *Nature Reviews Earth & Environment, 10*, 1038

Zhan, Z., Qin, Q., Ghulan, A., Wang, D. (2007). NIR-red spectral space based new method for soil moisture monitoring. *Science in China Series D: Earth Sciences, 50*, 283-289

Zhang, H., Li, J., Liu, Q., Lin, S., Huete, A., Liu, L., Croft, H., Clevers, J.G., Zeng, Y., Wang, X.J.M.i.E., Evolution (2022). A novel red-edge spectral index for retrieving the leaf chlorophyll content*, 13*, 2771-2787

Zhang, J.-C., Pu, R.-l., Wang, J.-h., Huang, W.-j., Yuan, L., Luo, J.-h. (2012a). Detecting powdery mildew of winter wheat using leaf level hyperspectral measurements. *Computers and Electronics in Agriculture, 85*, 13-23

Zhang, J., Huang, W., Li, J., Yang, G., Luo, J., Gu, X., Wang, J. (2011). Development, evaluation and application of a spectral knowledge base to detect yellow rust in winter wheat. *Precision Agriculture, 12*, 716-731

Zhang, J., Huang, Y., Pu, R., Gonzalez-Moreno, P., Yuan, L., Wu, K., Huang, W. (2019a). Monitoring plant diseases and pests through remote sensing technology: A review. *Computers and Electronics in Agriculture, 165*, 104943

Zhang, J., Pu, R., Huang, W., Yuan, L., Luo, J., Wang, J. (2012b). Using in-situ hyperspectral data for detecting and discriminating yellow rust disease from nutrient stresses. *Field Crops Research, 134*, 165-174

Zhang, J., Pu, R., Huang, W., Yuan, L., Luo, J., Wang, J.J.F.C.R. (2012c). Using in-situ hyperspectral data for detecting and discriminating yellow rust disease from nutrient stresses*, 134*, 165-174

Zhang, J., Wang, B., Zhang, X., Liu, P., Dong, Y., Wu, K., Huang, W. (2018). Impact of spectral interval on wavelet features for detecting wheat yellow rust with hyperspectral data. *International Journal of Agricultural and Biological Engineering, 11*, 138-144

Zhang, J., Yuan, L., Pu, R., Loraamm, R.W., Yang, G., Wang, J. (2014). Comparison between wavelet spectral features and conventional spectral features in detecting yellow rust for winter wheat. *Computers and Electronics in Agriculture, 100*, 79-87

Zhang, J.C., Pu, R.L., Huang, W.J., Yuan, L., Luo, J.H., Wang, J.H. (2012d). Using in-situ hyperspectral data for detecting and discriminating yellow rust disease from nutrient stresses. *Field Crops Research, 134*, 165-174

Zhang, K., Zhang, F., Wan, W., Yu, H., Sun, J., Del Ser, J., Elyan, E., Hussain, A. (2023). Panchromatic and multispectral image fusion for remote sensing and earth observation: Concepts, taxonomy, literature review, evaluation methodologies and challenges ahead. *Information Fusion, 93*, 227-242

Zhang, L. (2023). Combining neural networks with logic rules. *International Journal of Computational Intelligence Applications, 22*, 2350015

Zhang, N., Pan, Y., Feng, H., Zhao, X., Yang, X., Ding, C., Yang, G. (2019b). Development of Fusarium head blight classification index using hyperspectral microscopy images of winter wheat spikelets. *Biosystems Engineering, 186*, 83-99

Zhang, N., Yang, G., Pan, Y., Yang, X., Chen, L., Zhao, C. (2020). A review of advanced technologies and development for hyperspectral-based plant disease detection in the past three decades. *Remote Sensing, 12*, 3188

Zhang, S., Zhao, G., Lang, K., Su, B., Chen, X., Xi, X., Zhang, H. (2019c). Integrated Satellite, Unmanned Aerial Vehicle (UAV) and Ground Inversion of the SPAD of Winter Wheat in the Reviving Stage*, 19*, 1485

Zhang, X., Han, L., Dong, Y., Shi, Y., Huang, W., Han, L., González-Moreno, P., Ma, H., Ye, H., Sobeih, T. (2019d). A Deep Learning-Based Approach for Automated Yellow Rust Disease Detection from High-Resolution Hyperspectral UAV Images. In, *Remote Sensing* (p. 1554)

Zhang, Y., Hui, J., Qin, Q., Sun, Y., Zhang, T., Sun, H., Li, M. (2021). Transfer-learning-based approach for leaf chlorophyll content estimation of winter wheat from hyperspectral data. *Remote Sensing of Environment, 267*

Zhang, Z., Huang, L., Wang, Q., Jiang, L., Qi, Y., Wang, S., Shen, T., Tang, B.-H., Gu, Y. (2024). UAV hyperspectral remote sensing image classification: A systematic review. *IEEE Journal of Selected Topics in Applied Earth Observations Remote Sensing Applications: Society and Environment*

Zhou, L., Nie, C., Su, T., Xu, X., Song, Y., Yin, D., Liu, S., Liu, Y., Bai, Y., Jia, X., Jin, X. (2023). Evaluating the canopy chlorophyll density of maize at the whole growth stage based on multi-scale UAV image feature fusion and machine learning methods. *Agriculture, 13*, 895

Zhou, Q., Yu, L., Zhang, X., Liu, Y., Zhan, Z., Ren, L., Luo, Y. (2022). Fusion of UAV hyperspectral imaging and LiDAR for the early detection of EAB stress in Ash and a new EAB detection index-NDVI. *Remote Sensing, 14*, 2428

Zhou, W., Li, M., Achal, V. (2025). A comprehensive review on environmental and human health impacts of chemical pesticide usage. *Emerging Contaminants, 11*, 100410

Zhu, H., Lin, C., Liu, G., Wang, D., Qin, S., Li, A., Xu, J.-L., He, Y. (2024). Intelligent agriculture: deep learning in UAV-based remote sensing imagery for crop diseases and pests detection. *Frontiers in Plant Science, 15*, 1435016

Zhu, X.X., Tuia, D., Mou, L., Xia, G.-S., Zhang, L., Xu, F., Fraundorfer, F. (2017). Deep learning in remote sensing: A comprehensive review and list of resources. *IEEE Geoscience Remote Sensing Magazine, 5*, 8-36

Zhuang, F., Qi, Z., Duan, K., Xi, D., Zhu, Y., Zhu, H., Xiong, H., He, Q. (2020). A comprehensive survey on transfer learning. *Proceedings of the IEEE, 109*, 43-76

Zibrat, U., Susic, N., Knapic, M., Sirca, S., Strajnar, P., Razinger, J., Voncina, A., Urek, G., Stare, B.G. (2019). Pipeline for imaging, extraction, pre-processing, and processing of time-series hyperspectral data for discriminating drought stress origin in tomatoes. *MethodsX, 6*, 399-408



Summary

The emergence and spread of crop diseases pose not only a severe threat to food security, but also undermine the sustainability of agricultural ecosystems and the economic well-being of farmers. Achieving efficient and precise early detection of disease has thus become a critical challenge for modern precision agriculture. With the rapid advancement and adoption of technologies such as hyperspectral remote sensing, unmanned aerial vehicles (UAVs), and artificial intelligence models, researchers are increasingly able to assess crop health from the leaf to the canopy, and across both spatial and temporal scales. However, despite promising progress, the complex spectral mechanisms underlying disease response remain poorly understood. Moreover, data-driven models can achieve high accuracy in disease monitoring, but often lack physical constraints, leading to overfitting and poor generalization.

In response to these gaps, this doctoral study unfolds across five interlinked dimensions—symptom characterization, hyperspectral feature extraction, index development, model fusion, and spatiotemporal extension—to build a robust monitoring system specifically tailored for maize leaf spot disease. Chapter 2 reviews recent advances in hyperspectral remote sensing for crop disease monitoring; Chapter 3 investigates the temporal sensitivity of multi-source hyperspectral features; Chapter 4 proposes a novel canopy-scale disease sensitive index Chapters 5 and 6 introduce two integrative frameworks: PGDL (physical model-guided deep learning) and RS-DeepSpread (*Synergistic RS–deep learning and epidemic* framework). Through this comprehensive approach, the study aims to enable early disease detection.

Chapter 2 reviews hyperspectral remote sensing in crop disease monitoring. The chapter begins by describing the observable spectral symptoms of major crop diseases, then delves into key hyperspectral features—such as spectral–textural traits, pigment absorption, solar-induced chlorophyll fluorescence, and temporal dynamics. It then examines the detection algorithms in use, spanning traditional statistical methods, machine-learning approaches, and physically-based frameworks. The strengths of these methods—early disease detection, stressor differentiation, resistance assessment and large-scale monitoring—are highlighted. The chapter concludes by proposing future directions: integrating physical models with deep learning, enhancing the robustness and sensitivity of features, and developing open-access shared datasets to accelerate global progress in disease monitoring.

Chapter 3 introduces the Disease Sensitive Index (DSI), a novel canopy-scale metric specifically designed to detect early maize leaf diseases. The DSI exhibits strong responsiveness to pigment variation, rather than plant spacing, thereby offering the ability to isolate early disease onset. We applied this index to multispectral UAV data collected over multiple years and sites, demonstrating its robustness ($R^2 = 0.69$ in 2021 and $R^2 = 0.62$ in 2022 for disease-index estimation). Time-series analysis of vegetation indices revealed that the DSI can identify infection onset as early as 10 days post-infection. These findings suggest that the DSI is a promising tool for precision agriculture, enabling reliable early maize leaf spot monitoring.

Chapter 4 investigates how sensitive UAV-based hyperspectral features are to maize

leaf spot disease. We tracked maize over 30 days post-infection using high-resolution UAV hyperspectral imaging, extracting biophysical parameters (via the PROSAIL model) and spectral features (reflectance, vegetation indices, and wavelet features). We found that wavelet features detected disease as early as day 6 after infection, followed by VIs at day 8 and changes in chlorophyll content at day 10. Classification models combining chlorophyll content, VIs, and wavelet features performed best, achieving up to 9.36 % higher accuracy than models using only VIs or spectra in early and severe stages. In mild and early severe stages, however, spectral-only models reached 86.21 % accuracy. These findings show that multi-source features are complementary in early and severe stages of disease but become redundant in the mild and early severe stages.

Chapter 5 introduces a PGDL framework to improve UAV-based hyperspectral monitoring of maize leaf spot disease. We first generate three types of radiative transfer simulations — (1) uniformly varied chlorophyll content, (2) measured disease leaf spectra, and (3) mixed endmember spectra — to serve as physically informed priors. We then train deep neural networks using these simulations and transfer them to UAV-collected hyperspectral data across four disease stages (early, mild, moderate, severe). Our results show that simulations based on real diseased leaf spectra (SIM #2 and SIM #3) align closely with UAV measurements (R^2 ~0.97–0.99). In disease-index retrieval, the PGDL models, especially when pre-trained on SIM #2, outperform both purely data-driven and physically based approaches (early stage: R^2 = 0.76 in 2021, 0.70 in 2023). This study demonstrates that PGDL enhances early disease detection.

Chapter 6 presents the RS-DeepSpread framework, a novel integration of remote-sensing-driven deep learning and stochastic epidemic modelling for spatiotemporal monitoring of maize leaf spot disease. We combined the deep-learning component predictive output with a stochastic epidemic spread model. RS-DeepSpread significantly outperformed the standalone deep network: in 2021 it achieved quadratic weighted kappa (QWK) = 92.54 % and overall accuracy (OA) = 85.37 %, and in 2023 QWK = 89.71 % and OA = 91.67 %. Moreover, it reduced under- and over-estimation rates (2021: 5.36 % under, 8.93 % over; 2023: 3.97 % each) and forecasted epidemic peak timing up to three days earlier than field observations. These results demonstrate that coupling remote-sensing deep learning with epidemic modelling offers a promising solution for timely, spatially explicit prediction of disease dynamics, supporting a shift from reactive to preventive disease management.

Acknowledgment

First and foremost, I extend my deepest gratitude to my supervisors, Xiuliang Jin, Bedir Tekinerdogan, and Qingzhi Liu. Your exceptional guidance, constant encouragement, and boundless patience have elevated this thesis and my academic journey in ways I could never have imagined. Your fresh ideas, engaging discussions, and shared fieldwork trips turned research into a meaningful adventure — thank you for making a lasting difference.

To my collaborators, Lammert Kooistra and Carlos Camino: thank you sincerely. Your partnership not only enriched this project scientifically but also made it enjoyable and insightful. The good times in Wageningen, brimming with laughter and shared curiosity, will remain unforgettable.

I'd like to recognise all of the co-authors for your vital contributions. Your ideas, inspiring conversations, and research outputs have been invaluable — especially Pablo J. Zarco-Tejada and Peñuelas Josep. I greatly admire the care and dedication with which you approached the revisions of our article.

To my colleagues at the Information Technology Department (INF): I am very grateful. A special mention to Claudia Ravestein, Marieke Moller, and Laura Simon for your generous assistance during my PhD process. And to all INF PhD students — Laura Jansen, Mar Ariza-Sentís, Mingya Qu, Mingzhu Du, Kaiwen Wang, Zhen Cao, Dongxiao Zou, Lirong Lu— thank you for sharing insight, providing clarifying walks through tough problems, and treasuring the small moments of sunshine together. Your involvement has been indispensable.

My gratitude also goes to all colleagues at the Chinese Academy of Agricultural Sciences (CAAS). Thank you for your wisdom and support: Chengwei Nie, Dangmeng Yin, Fan Fan, Yang Song, Jing Yu, Shuaibing Liu, Xun Yu, Xiao Jia, Yadong Liu, Fei Nan, Tiantian Jiang, Yanqin Zhu — and all my other brothers and sisters there.

To my friends in Wageningen: thank you for your companionship, encouragement and help. You sparked research inspiration, enriched the daily moments of life, and brightened my memories. Especially Tianyi Jia, Yang Li, Chengjie Yang, Zihan Liu, Jun Liu, Qiuhong Huang, Yan Li, and my badminton partners Mingyang Ding and Jiaoyi Qu. There are so many of you and I'm truly grateful.

Finally, to my family: I am profoundly grateful to my parents for their unwavering encouragement and the values they instilled, which have kept me fortunate and hopeful about the future. My deep thanks go to my parents-in-law, who lovingly cared for my son so that our little family could embark fully on this endeavor. To my son, Changle, thank you for growing up healthy and bright. A special tribute goes to my husband, Minyang Xu— your boundless understanding and trust have made all of this possible.

Short biography



Yali Bai was born on July 17, 1990 in Henan Province, China. Yali earned her Bachelor's degree in Geo-information Science from Henan Chengjian College in 2013. Immediately after graduation, she returned to her hometown to join China Resources Gas Co., Ltd., where she worked in human-resources management for five years—a role outside her academic discipline, yet one which she embraced and from which she developed strong organisational, interpersonal and leadership skills.

In 2018, driven by a desire to broaden her horizons and deepen her technical knowledge, she returned to academia. After a dedicated three-month period of studying higher mathematics and preparing for entrance examinations, she began her MSc in Surveying and Mapping Engineering at Wuhan University (2018–2021). Her research focused on smart agriculture and quantitative remote sensing, culminating in a master's thesis titled "Hyperspectral-based Monitoring of Rice Blast Disease".

Following the completion of her master's degree, Yali entered a joint PhD programme through the Graduate School of the Chinese Academy of Agricultural Sciences (GSCAAS) and Wageningen University & Research. She conducted research both at the Crop Phenotyping Innovation Group at CAAS and at the Information Technology Group at Wageningen University in the Netherlands. Her doctoral research explores the integration of remote-sensing technologies, Unmanned Aerial Vehicle (UAV) systems and machine-learning methods within maize leaf spot monitoring—an innovative interdisciplinary endeavour that combines geospatial science, computer science and agricultural engineering.

Looking to the future, Yali aspires to expand her understanding of macroeconomics to better grasp the mechanisms of global systems, and to work with large-scale language models and other frontier artificial-intelligence technologies. Throughout her journey, she upholds the philosophy: Change brings circulation, and circulation brings attainment. As a lifelong learner, she firmly believes in the power of growth and the potential for transformation across disciplines and geographies.

Publications

From this thesis:

Bai, Y., Jin, X. (2024). Hyperspectral approaches for rapid and spatial plant disease monitoring. *Trends in Plant Science, 29*, 711-712

Bai, Y., Nie, C., Yu, X., Gou, M., Liu, S., Zhu, Y., Jiang, T., Jia, X., Liu, Y., Nan, F. (2024). Comprehensive analysis of hyperspectral features for monitoring canopy maize leaf spot disease. *Computers Electronics in Agriculture, 225*, 109350

Bai, Y., Zarco-Tejada, P.J., Peñuelas, J., McCabe, M.F., Hawkesford, M.J., Atzberger, C., Poblete, T., Kumar, L., Reynolds, M.P., Nie, C. (2025). Hyperspectral Remote Sensing for Monitoring Crop Disease: Applications, challenges, and perspectives. *IEEE Geoscience and Remote Sensing Magazine*,2-26

Bai, Y., Kooistra, L., Liu, Q., Yu, X., Jia, T., Zhu, Y., Jiang, T., Jiang, T., Li, S., Tekinerdogan, B., Duan, C., Jin, X. (2025). Physical model-guided deep learning for enhanced monitoring maize leaf spot. *IEEE Transactions on Geoscience and Remote Sensing* (Under review)

Bai, Y., et al. (2025) A novel disease sensitive index (DSI) for monitoring early maize leaf disease using PROSPECT-D and LESS models. *Smart Agricultural Technology* (Under review).

Bai, Y., et al. (2025) RS-DeepSpread: A synergistic UAV hyperspectral–deep learning and epidemic modeling framework for spatiotemporal prediction of maize leaf spot. *One earth* (Submitted).

Contributions outside of this thesis:

Jia, X., Yin, D., **Bai, Y.**, Yu, X., Song, Y., Cheng, M., Liu, S., Bai, Y., Meng, L., Liu, Y. (2023). Monitoring maize leaf spot disease using multi-source UAV imagery. *Drones*, 7, 650

Nan, F., Song, Y., Yu, X., Nie, C., Liu, Y., **Bai, Y**., Zou, D., Wang, C., Yin, D., Yang, W. (2023). A novel method for maize leaf disease classification using the RGB-D post-segmentation image data. *Frontiers in Plant Science, 14*, 1268015

Zhu, Y., Fan, F., Zhang, Z., Yu, X., Jiang, T., Li, L., Liu, Y., **Bai, Y.**, Tang, Z., Liu, S. (2025). How to Better Use Canopy Height in Soybean Biomass Estimation. *Agriculture, 15*, 1024

Liu, Z., Guo, J., Li, C., Wang, L., Gao, D., **Bai, Y.**, Qin, F. (2025). Effective Cultivated Land Extraction in Complex Terrain Using High-Resolution Imagery and Deep Learning Method. *Remote Sensing, 17*, 9

Jiang, T., Li, L., Zhang, Z., Yu, X., Zhu, Y., Li, L., Liu, Y., Bai, Y., Tang, Z., Liu, S. (2025). YOLO-light-pruned: A lightweight model for monitoring maize seedling count and leaf age using near-ground and UAV RGB images. *Artificial Intelligence in Agriculture*

Yali Bai
Wageningen School of Social Sciences (WASS)
Completed Training and Supervision Plan

Name of the learning activity	Department/Institute	Year	ECTS*
A) Project related competences			
A1 Managing a research project			
WASS PhD Introduction	WASS	2023	1
Writing research proposal	WASS, INF, WUR	2024	6
'Counting maize tassels from field RGB image by a three-step method '	The International Association of Chinese Professionals in Geographic Information Sciences (CPGIS) 30th Anniversary Greetings, Beijing	2022	1
'A novel disease sensitive index (DSI) for monitoring early maize leaf disease'	Association of American Geographers (AAG) 2024 Annual Meeting, Honolulu	2024	1
'Utilization of synthetic minority oversampling technique and transfer learning for improving rice and wheat LAI estimation'	Computers and Electronics in Agriculture	2024	1
Scientific writing	Wageningen in'to Languages	2024	1.8
A2 Integrating research in the corresponding discipline			
Research Methodology from research question to research proposal	WASS	2024	4
Umich data science python	University of Michigan	2022	6.3
Remote Sensing Image Acquisition, Analysis and Applications	University of New South Wales, Sydney	2022	0.8
The 3rd PhenoRob - Wageningen Workshop	PE&RC	2024	0.3
Summer school -'Digital plant phenotyping and agri-food robotics'	PE&RC	2024	1.5
B) General research related competences			
B1 Placing research in a broader scientific context			
Remote Sensing for Environmental Sciences	PE&RC	2025	1.5
Self-Driving Cars	University of Toronto	2022	5
B2 Placing research in a societal context			
Making an Impact	WGS	2024	1
C) Career related competences/personal development			
C1 Employing transferable skills in different domains/careers			
Scientific Integrity	WGS	2024	0.6
Total			**32.8**

*One credit according to ECTS is on average equivalent to 28 hours of study load

The research in this thesis was financially supported by the **National Key R&D Program of China (Young Scientist Program)**: *"Development of New Technologies for Maize Phenotyping and Genotyping and Application of Genome-wide Selection for Drought Tolerance"* (Grant No. **2023YFD1202500**).

Cover design by Google Gemini Pro

Printed by www.proefschriftmaken.nl

